LOW TEMPERATURE SORPTION-ENHANCED HYDROGEN PRODUCTION FROM NATURAL GAS USING VARIABLE-VOLUME, BATCH-MEMBRANE REACTORS

A Dissertation
Presented to
The Academic Faculty

by

David Milton Anderson

In Partial Fulfillment
of the Requirements for the Degree
Doctor of Philosophy in the
School of Mechanical Engineering

Georgia Institute of Technology
December 2015

LOW TEMPERATURE SORPTION-ENHANCED HYDROGEN PRODUCTION FROM NATURAL GAS USING VARIABLE-VOLUME, BATCH-MEMBRANE REACTORS

Approved by:

Dr. Andrei G. Fedorov
School of Mechanical Engineering
Georgia Institute of Technology

Dr. Peter A. Kottke
School of Mechanical Engineering
Georgia Institute of Technology

Dr. Michael A. Filler
School of Chemical and Biomolecular Engineering
Georgia Institute of Technology

Dr. William J. Wepfer
School of Mechanical Engineering
Georgia Institute of Technology

Dr. Christopher W. Jones
School of Chemical and Biomolecular Engineering
Georgia Institute of Technology

Date Approved: July 31, 2015

Be conservative by sticking to well-established physical principles, but probe them by exposing their most radical conclusions.

- Niels Bohr [1]

ACKNOWLEDGEMENTS

I'd like to acknowledge the support and encouragement of a number of individuals, without whom this dissertation would certainly not have been possible. Beginning with my graduate research advisor Professor Andrei Fedorov – I could not have asked for a better advisor, mentor and friend over the past 5 years, and I look forward to continuing our personal and professional relationship for years to come. Also from the MITf lab, I'd like to thank our research engineer Peter Kottke and my fellow graduate student Thomas Yun; together with Andrei we formed quite a team working on portable/distributed catalytic hydrogen production, and our spirited and intellectually challenging weekly meetings will remain as one of my fondest memories of graduate school.

Continuing with others at Georgia Tech, I'd like to thank the remaining members of my PhD reading committee: Professors Michael Filler, Christopher Jones and William Wepfer. Each committee member provided valuable feedback throughout the process and was instrumental in helping me produce the highest quality dissertation possible. In building my reactor testbed, J.D. Huggins and the machine room staff (Louis Boulanger and Steven Sheffield) were invaluable resources in helping design and fabricate parts. Mohamed Nasr was instrumental in developing the LabVIEW data acquisition and pressure control scheme used to operate the testbed reactor. Lastly, I'd like to thank Mack Bowers for his encouragement and friendship.

Finally, I'd like to acknowledge the support of my family and friends who sustained me through the many challenges associated with pursuing a PhD. My wife Allison was a constant source of support and encouragement, and I will forever be grateful for her steadfast belief in me. I'd also like to thank my parents, Emery and Carolyn, for their support and my son Luke for helping me develop perspective and balance as a researcher.

TABLE OF CONTENTS

Page

LIST OF TABLES

Page

LIST OF FIGURES

Page

LIST OF SYMBOLS AND ABBREVIATIONS

Symbols

A_c	cross-sectional area
$[B]$	diffusion coefficient matrix for Maxwell-Stefan diffusive flux
Bi	Biot number
c_j	concentration of species j
$c_{p,b}$	specific heat of porous bed
$\bar{c}_{p,j}$	specific heat of gaseous species j
d	sorbent/catalyst layer thickness
D_{mem}	membrane permeability
$\mathcal{D}_{eff,j}$	effective mass diffusivity of species j in a mixture
$\mathcal{D}_{AB}$	binary mass diffusivity of species$A$ and B
e	error
$E_{a,i}$	activation energy for reaction i
f	recycle fraction
h	convective heat transfer coeff.
H	reactor height
ΔH_i	heat of reaction i
$J_{H_2,perm}$	H_2 permeation flux through selective membrane
$J_{z,j}$	diffusive flux of species j in the z-direction
k	thermal conductivity
k_i	rate constant for reaction i
k_{ldf}	linear driving force adsorption coefficient
k_V	valve coefficient
K	equilibrium constant
m	mass
$\dot{n}$	molar flow rate
N	number of moles
N_s	number of species
P	pressure

$P_{H_2}^{\infty}$	membrane permeate-side H_2 partial pressure
q_{CO_2}	adsorbed quantity of CO_2 per unit mass of sorbent
$\bar{q}$	characteristic value of CO_2 loading in timescale analysis
Q	heat input from system to surroundings
$\bar{r}_{CH_4}$	characteristic rate of CH_4 consumption in timescale analysis
r_{CO_2}	fraction of CO_2 adsorbed from the gas phase
r_i	rate of reaction i
r_{MFC}	ratio of analyte to carrier gas as controlled by MFC
r_{MS}	ratio of analyte to carrier gas as detected by MS
R_u	universal gas constant
S_h	volumetric generation of heat due to reaction and/or adsorption
S_j	volumetric production rate of species j due to catalytic reaction
t	time
T	temperature
T_0	target reactor operating temperature
U^P	piston velocity
V	volume
v_m	molar average velocity
W	work done by system on surroundings
x_j	mole fraction of species j
X_{CH_4}	fuel conversion
z	axial coordinate position in transport-kinetic model

Greek Symbols

α	thermal diffusivity
δ	membrane thickness

ε	extent of reaction
$\bar{\varepsilon}$	composite porosity
η	efficiency
ν_{ij}	stoichiometric coefficient of the j^{th} component of reaction i
ρ	density
τ	tortuosity
τ_k	timescale of a process k
ϕ	catalyst mass fraction

Subscripts

0	initial
ads	adsorption
atm	atmospheric
c	critical
cat	catalyst
d	dead (volume)
des	desorption
$diff$	diffusion
eq	equilibrium
H	heater
i	reaction i
int	interface
j	species j
max	maximum
mem	membrane
min	minimum
$perm$	permeation
R	reduced
rxn	reaction
s	solid
$sorb$	sorbent
T	total
th	thermal
$trans$	transport
∞	infinity

Superscripts

eff	effective
$''$	per unit area

Abbreviations

APCI	Air Products and Chemicals, Inc.
CHAMP	CO_2/H_2 Active Membrane Piston
HTC	hydrotalcite
LHV	lower heating value
LUB	length of unused bed
MFC	mass flow controller
MS	mass spectrometer
PSA	pressure swing adsorption
RKDP	Runge-Kutta Dormand-Prince
RM	reverse methanation reaction
RMTZ	reaction mass transfer zone
S/C Ratio	steam to carbon ratio
SCCM	flowrate in cm^3/min at STP
SE	sorption-enhanced
SMR	steam methane reforming
STP	standard temperature and pressure
WGS	water-gas shift reaction

SUMMARY

Natural gas is an attractive fuel choice for distributed power generation due to the availability of a well-developed production and distribution infrastructure worldwide, including both intra-continental compressed gas pipeline network and inter-continental liquefied delivery. With its favorable 4:1 hydrogen to carbon ratio, natural gas also has compelling potential to become an economically viable "transition" fossil fuel to a low carbon energy future. This doctoral dissertation proposes a novel approach to producing hydrogen – the ultimate clean, carbon-free fuel – from natural gas for use in fuel cell vehicles and residential fuel cell based power generations with possibility for energy efficient on-board/on-site CO_2 capture.

A variable-volume batch membrane reactor, termed CHAMP-SORB, is comprehensively investigated, aiming to dramatically reduce the operating temperature and steam to methane feed ratios to levels that enable economically feasible hydrogen production at the point-of-use. In the CHAMP-SORB reactor, a batch of steam and methane is introduced into a piston-cylinder reaction chamber, where a steam reforming catalytic reaction occurs that produces H_2 and CO_2. To circumvent thermodynamic limitations and produce a purified H_2 stream, both reaction products are continuously removed from the reactor by (*i*) selective H_2 permeation through a dense palladium-silver membrane, and (*ii*) selective CO_2 uptake onto a solid porous adsorbent. Unique aspects of the CHAMP-SORB reactor are (*i*) that optimal conditions for reaction, H_2 permeation, and CO_2 adsorption are maintained by dynamic modulation of reactor volume; and (*ii*) non-fully reacted fuel and residual reaction bi-products such as CO and H_2 can be recycled via regenerative fuel processing as part of the cyclic operation, thus further improving fuel utilization and energy efficiency.

A series of first principle models with increasing complexity, including (*i*) a purely thermodynamic analysis of the CHAMP-SORB operating cycle to define optimal reactor temperature and feed composition, (*ii*) a purely kinetic model in the absence of any transport limitations to define the ideal limit on the rate of achieving high fuel conversion and hydrogen yield efficiency, and (*iii*) a comprehensive heat/mass transport-kinetics model were developed to understand the fundamental physical and chemical principles governing the CHAMP-SORB reactor process. A complimentary experimental study was also performed to investigate the combined reaction/separation processes in CHAMP-SORB and validate the fundamental understanding of the key operating principles revealed through modeling efforts. As a result, this work has produced a number of new insights on the fundamental trade-offs associated with hydrogen production in multi-functional reactors enhanced via membrane/sorption product separation as well as established a set of engineering guidelines that can be broadly applied to distributed H_2 production from steam reforming of hydrocarbon fuels.

CHAPTER 1

INTRODUCTION

Although abundant petroleum and coal have enabled the production of affordable primary power and transportation fuels over the past century, the recent emergence of natural gas as a significant fossil fuel resource has dramatically changed the energy landscape [2]. With its favorable hydrogen-to-carbon ratio coupled with recently developed techniques to tap vast reserves that were previously not economically viable, natural gas has been touted by many as a bridge fuel to a low-carbon energy future and as a potential means to minimize dependence on foreign oil for transportation fuel [3, 4]. To make full use of this promising resource, new chemical conversion processes that are optimized for natural gas feedstock must be developed. A process that can efficiently produce hydrogen in a small-scale, distributed fashion by steam reforming of natural gas is one such technology that would have a far-reaching impact, as it could eliminate the requirement for a large-scale hydrogen delivery infrastructure and aid the diffusion of hydrogen-powered technology into society [5, 6]. Such a process could effectively utilize the existing natural gas distribution infrastructure and would pair well with localized natural gas production from shale gas wells [2].

Hydrogen production from natural gas feedstock via the steam-methane reforming (SMR) process is a mature industrial technology [7, 8]; yet adapting this process for distributed production has proven problematic. Owing to the strongly endothermic nature of the process, reaction temperatures in excess of 900°C are traditionally employed in large-scale SMR reactors to overcome the thermodynamic limitations of the process. For

a distributed reactor system, a maximum operating temperature below 500°C is desired to improve safety and reduce material cost and preheating energy requirements. Furthermore, in a conventional large-scale fuel processing plant, multiple sequential unit operations are required after the primary reforming reaction step to first consume unwanted CO and create additional H_2 through the water gas shift (WGS) reaction, and then purify the H_2 product using various separation techniques [9]. In addition to resulting in an excessively large footprint, with decreasing system size the sequential unit operation approach has an increasingly deleterious effect on performance because the relative impact of system losses and cost of balance-of-plant components become more pronounced [10]. Lastly, although the stoichiometry of the overall SMR process only requires a 2:1 molar H_2O to CH_4 feed (S/C ratio), industrial SMR processes frequently operate at S/C ratios of between 3-6:1 to enhance CH_4 conversion and to minimize catalyst coking [9]. In distributed applications, operating at S/C ratios closer to 2:1 are desired as excess steam is less readily available, is energetically costly, and reduces the volumetric H_2 yield density.

Combined reaction-separation approaches are a promising means to overcome the SMR process scale-down limitations [11-17]. By Le Chatelier's principle, *in situ* removal of H_2 and/or CO_2 from the reactor shifts equilibrium toward greater fuel conversion and H_2 yield, potentially producing a suitable level of conversion at much lower temperature and allowing removal of subsequent WGS and purification unit operations. To this end, this dissertation focuses on the advancement of the CO_2/H_2 Active Membrane Piston (CHAMP) variable volume, batch-membrane reactor concept to incorporate selective CO_2 adsorption and enable distributed H_2 production from natural gas feedstock. The

CHAMP reactor, operating in a cycle similar to the Internal Combustion (IC) engine, has proven capable of dynamically maintaining optimal reaction conditions for transport of reactants to the catalyst, reaction kinetics at the catalyst, and H_2 membrane separation. Specifically, as fuel is depleted and reactor pressure is reduced due to permeation, strategic compression using the ”active” piston is employed to increase the concentration of the remaining fuel and hydrogen, thereby providing additional driving force for reaction and permeation. Because the residence time and thermodynamic state (pressure and temperature) in the variable-volume batch reactor can be actively controlled to allow reaction and separation to proceed at an enhanced rate and to a desired level of completion, the CHAMP offers flexibility for various desired H_2 throughputs not possible with traditional large-scale steady-state flow reactors. Previously, theoretical and experimental studies on CHAMP performance were carried out using only H_2 separation and with methanol (CH_3OH) as feedstock due to its relatively low reaction temperature, which established the fundamental feasibility and promise of the approach [18, 19].

This work extends the original CHAMP reactor concept further by (*i*) incorporating CO_2 adsorption to complement the H_2 membrane separation and (*ii*) reforming CH_4 as opposed to CH_3OH. This enhanced reactor concept, termed CHAMP-SORB, incorporates sorbent regeneration steps in its operating cycle, thereby preventing eventual saturation of the sorbent and enabling CH_4 conversion enhancement for repeated cyclic operation. In particular, the active regeneration steps will deviate from the traditional pressure swing adsorption (PSA) process, as partial pressure of the adsorbed species is reduced by expanding the reactor volume as opposed to purging a fixed bed with an inert sweep gas.

Regenerating the sorbent through this method is desirable because it minimizes dilution of CO_2 during desorption, making it more energy efficient to capture.

The remainder of this work is organized as follows. Chapter 2 provides an overview of the steam methane reforming reaction mechanism and presents the typical industrial arrangement for large-scale, centralized hydrogen production via SMR. Attention is drawn to aspects of the industrial process that are not conducive to distributed H_2 production, and an outline of the desired specifications for a distributed system is presented. Most notably, reduced reaction temperature (400-500°C), multifunctional components to minimize reactor footprint, and minimal use of steam in excess of the stoichiometric 2:1 H_2O:CH_4 feed ratio required by the SMR process are identified as key technological drivers, which motivates a search for innovative process and reactor design concepts. Lastly, several state-of-the-art techniques, namely sorption-enhanced SMR and membrane SMR reactors, designed to meet these distributed system requirements are discussed.

Having outlined the requirements for distributed H_2 production in Chapter 2, Chapter 3 proceeds by investigating in a general sense (*i.e.*, without consideration of reactor design) the separation requirements to achieve suitable fuel conversion/H_2 yield levels in the desired SMR operating temperature range. Once these separation requirements are established, an enhanced version of the CHAMP reactor that incorporates CO_2 adsorption (CHAMP-SORB) is introduced. The CHAMP-SORB cycle is analyzed thermodynamically to establish the fundamental limits of reactor performance for the entire operating cycle, including the filling, reaction/permeation/adsorption, exhaust, and CO_2 desorption steps.

In Chapter 4, having established the thermodynamic viability of the CHAMP-SORB approach, the CHAMP-SORB concept is experimentally demonstrated, establishing its capability to perform SMR at 400°C and a 2:1 S/C ratio. Each sub-function (e.g. Pd/Ag membrane selective H_2 permeation, CO_2 adsorption, CH_4/H_2O preheating/reactor filling, and catalyst reduction/activity verification) of the reactor is tested independently to characterize the performance of each of the key CHAMP-SORB components. The performance of the reactor is then experimentally assessed for the main, reaction step of the CHAMP-SORB cycle.

Chapter 5 complements the experimental work of the previous chapter by developing an ideal kinetic model and using the testbed results to verify the model accuracy. The verified model is then used to investigate scenarios that cannot be experimentally observed with the laboratory scale prototype reactor, namely the performance of the CHAMP-SORB reactor when the dead volume of the valves/piping is small relative to the working volume of the cylinder. The ideal kinetic model is also used to conduct timescale analysis to develop operation regime maps and provide an understanding of the interplay between reaction, permeation and adsorption rates.

Chapter 6 develops a first-principle transport-kinetic model that accounts for spatial gradients in species concentration and temperature that are expected to arise as the CHAMP-SORB is scaled-up. Using timescale analysis as a guide, two reactor sizes are analyzed and compared to illustrate the impact of transient species transport and temperature non-uniformity on reactor performance. The comprehensive model simulations demonstrate that an approach commonly used in conventional sorption-assisted SMR reactors when the catalyst is uniformly distributed within the porous media

region of the CHAMP-SORB reactor results in substantial spatial variations in reaction rates due to concentration and temperature gradients and thus sub-optimal catalyst utilization, which can dramatically reduce the overall reactor performance. It is shown that for the membrane reactors enhanced with CO_2 sorption, stratifying the sorbent-catalyst packed bed such that the catalyst is in intimate contact with the membrane surface these transport limitations can be mitigated.

Lastly, Chapter 7 concludes by summarizing the key findings of the study and discussing recommended directions of future research efforts. An explicit statement is made that captures the original contributions of this doctoral dissertation to fundamental science and general engineering practice in the field of distributed hydrogen production and methane steam reforming.

CHAPTER 2

DISTRIBUTED HYDROGEN PRODUCTION FROM STEAM METHANE REFORMING

The overarching goal of this work is to develop an energy efficient and scalable method of producing hydrogen at the point of use for fuel cell vehicles and residential power applications. Distributed hydrogen production, also known as forecourt production, is a promising approach to overcome one of the primary barriers to a sustainable hydrogen economy [20-24]: the present lack of a large-scale hydrogen delivery infrastructure [25]. Because the distribution of hydrogen is both costly and technically challenging, at present roughly 95% of worldwide hydrogen production is captive (*i.e.*, production and usage are collocated) [26]. Implementation of efficient, small-scale hydrogen production from methane, the primary component of natural gas, at the point of use would allow application of this captive production strategy for residential co-generation [5, 6] and vehicle refueling stations [27]. To understand the challenges associated with this strategy, it is instructive to first briefly discuss the established large-scale industrial processes and consider the difficulties of scaling-down a similar approach for distributed hydrogen production.

2.1 Industrial Scale Centralized Steam Methane Reforming

Steam methane reforming (SMR) is an industrially mature technology that is the primary route of hydrogen production worldwide from natural gas, accounting for 95% of the hydrogen produced in the United States [7, 8]. The SMR process consists of the

strongly endothermic reverse methanation (RM) reaction, equation (2.1), and moderately exothermic water gas shift (WGS) reaction, equation (2.2):

$$CH_4 + H_2O \rightleftharpoons 3H_2 + CO \quad (\Delta H_{298K} = 206.1\ kJ/mol) \tag{2.1}$$

$$CO + H_2O \rightleftharpoons H_2 + CO_2 \quad (\Delta H_{298K} = -41.2\ kJ/mol) \tag{2.2}$$

The combined reaction (SMR) is endothermic and stoichiometrically defines the maximum H_2 yield for a given quantity of CH_4:

$$CH_4 + 2H_2O \rightleftharpoons 4H_2 + CO_2 \ (\Delta H_{298K} = 164.9\ kJ/mol) \tag{2.3}$$

The reactions described in equations (2.1) – (2.3) occur in parallel, typically over a nickel catalyst [28]. Figure 2.1 illustrates the standard layout of a large-scale, centralized SMR plant.

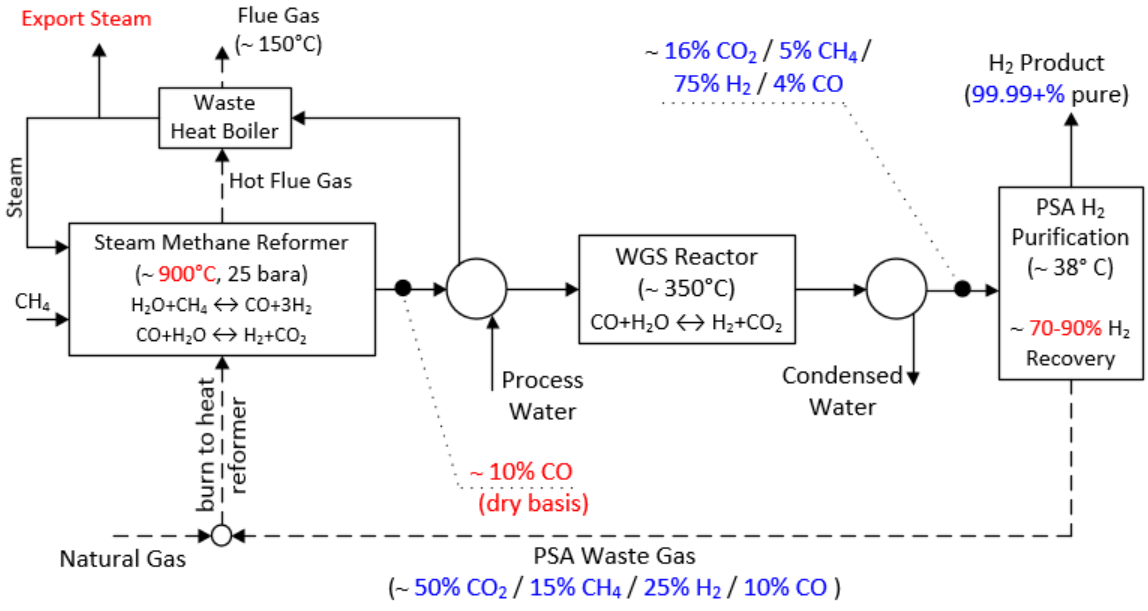

Figure 2.1: Industrial steam methane reforming process (adapted from [29])

Because reverse methanation is endothermic while the WGS reaction is exothermic and both reactions are equilibrium limited for typical reactor conditions, it is impossible to achieve complete conversion of CH_4 into CO_2 and H_2 in a single stage of a conventional continuous flow reactor [9]. To shift the equilibrium of the strongly endothermic reverse methanation reaction in a favorable direction of greater hydrogen yield, large-scale industrial steam reformers utilize an initial reactor stage (labeled "Steam Methane Reformer" in Figure 2.1) that operates at a highly elevated temperature in a range of 800-900°C. The reformer is also fed with excess of steam (H_2O), *i.e.*, a high steam to carbon (S/C) molar ratio, to promote further CH_4 conversion and to minimize catalyst coking. While the stoichiometry of the combined reaction, given by equation (2.3), requires a S/C ratio of only 2, industrial SMR processes typically operate at a S/C ratio of between 3 and 6.

Because of the high operating temperature of the initial SMR reactor stage, which is thermodynamically unfavorable for conversion of CO to CO_2 via the exothermic WGS reaction, the effluent gas from a single stage reactor typically contains an unacceptably large amount of CO (8-10% on a dry basis) [7, 8]. To substantially reduce the CO concentration and to produce additional H_2, one or two subsequent low-temperature reactors are utilized with conditions favorable for the exothermic WGS reaction. For applications where extremely pure hydrogen is required, such as PEM fuel cells where CO concentrations above $20\ ppm$ can poison the Pt catalyst [30], additional product purification of residual carbon monoxide from the effluent of the low temperature WGS reactor is achieved via pressure swing adsorption (PSA), membrane separation, or catalytic fine cleanup by preferential oxidation. With numerous sequential unit

operations, including intermediate heat exchangers for thermal management of the reagent/product streams between active (reaction/separation) units, as well as a need for high temperature operating conditions, it is clear that industrial SMR is capital intensive, technologically complex and challenging, and requires a large footprint; yet, it is currently the most cost-effective method of commercial scale hydrogen production [3].

2.2 Requirements for Distributed Hydrogen Production via SMR Process

On-site, localized production of hydrogen from methane at lower (and dynamically variable) throughputs, which can be used in conjunction with the current natural gas distribution infrastructure, places stringent demand on the complexity/cost, energy (thermal) efficiency and footprint of the fuel processing strategy. Simply reducing the size of the conventional industrial approach is impractical because of the excessive operating temperature (with associated cost and thermal efficiency penalty) and at best linear footprint reduction with production capacity for multi-unit equipment (with possible "non-scalable" component bottlenecks). Thus, to effectively implement SMR processes in smaller-scale distributed applications, the following process attributes are favorable for scale down:

- Lower operating temperature (below 500℃) to reduce material cost and preheating energy requirements;
- Multifunctional components (*e.g.*, combined reaction/separation step, elimination of dedicated low temperature WGS reactors) to reduce the overall system complexity and footprint;
- Operation at lower S/C ratio (ideally the stoichiometric 2:1 ratio) to improve thermal efficiency, to increase volumetric H_2 yield density, and to avoid use of excess steam, which may not be as readily available as it would be in a large-scale industrial plant.

2.3 State of the Art Processes to Meet Distributed SMR Requirements

Combined reaction-separation processes are an attractive means to reduce the required SMR operating temperature and increase the practicality of on-site hydrogen generation [31, 32]. By Le Chatelier's principle, selective removal of H_2 and/or CO_2 from the reactor shifts equilibrium toward greater fuel conversion and H_2 yield, thereby circumventing the thermodynamic equilibrium limitations of the SMR process. This results in a suitable level of conversion that can be achieved at much lower temperature, and even potential removal of subsequent WGS and PSA purification steps. Moreover, the *in situ* removal of the reversible reactions' products enhances the forward reaction kinetics by increasing instantaneous concentrations of the reagents, which can further reduce the required reactor volume for a given H_2 yield, thus increasing the power density. Two SMR reaction-separation processes that have been extensively investigated are packed-bed catalytic H_2 membrane reactors [13, 14, 17, 33] and CO_2 sorption-enhanced reactors [6, 11, 12, 15, 16, 34-37]. Relatively little attention has been paid to reactor systems that incorporate combined H_2 membrane separation and *in situ* CO_2 sorption, with the exception of the work by the Tsotsis research group at University of Southern California [38-40] and research efforts on a fluidized bed sorption-enhanced membrane reactor for Tokyo Gas Company [41-43]. The work of the Tsotsis group experimentally demonstrated the sorption-enhanced membrane reactor only for the low temperature WGS reaction; utility of this approach for the overall SMR process was investigated only through modeling of a fixed bed reactor consisting of two concentric tubes separated by a membrane with the outer (feed) shell containing SMR catalyst + CO_2 sorbent and the inner shell carrying sweep gas and permeated H_2. This model

accounted for the coupling of reaction kinetics with the transient loading of the CO_2 sorbent; however mass transport was only handled using an axial dispersion coefficient. Radial gradients in concentration due to H_2 permeation across the membrane, which would be important in scaling up of the reactor, were not considered. Tokyo Gas Company achieved an important practical result by building a pilot fluidized bed reactor combining membrane separation with CO_2 adsorption [41]; however, this reactor system still operated at rather high temperatures (550℃) and utilized an excess amount of steam (at a 2.7:1 S/C ratio) to shift reaction equilibrium for improved conversion.

2.3.1 Sorption-enhanced SMR (SE-SMR) process

The first investigation of a sorption-enhanced reactor to reduce the operating temperature of the SMR process was performed by Air Products and Chemicals, Inc. (APCI) in the mid 1990's [12]. Figure 2.2 conceptually illustrates the APCI's SE-SMR process.

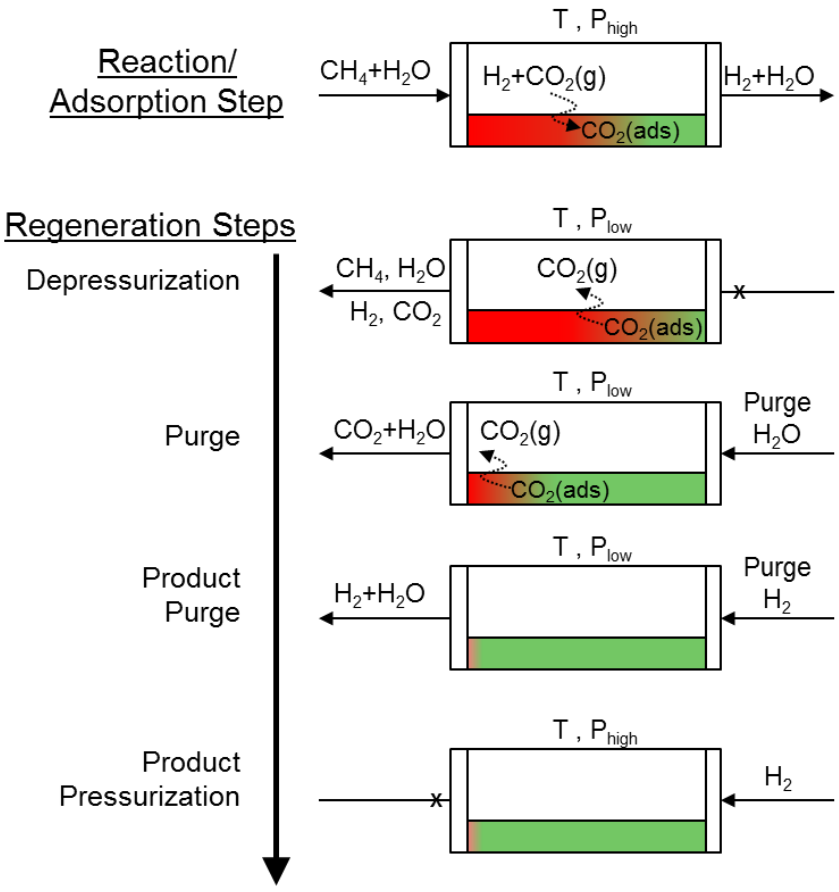

Figure 2.2: Sorption-enhanced SMR process (adapted from [44]). The catalyst/sorbent bed is depicted as green when the sorbent has low CO_2 loading and as red when the sorbent is saturated and can no longer adsorb more CO_2.

As shown in Figure 2.2, there is an axial gradient in CO_2 loading within the flow-through reactor, ranging from fully saturated sorbent at the reactor inlet to sorbent with essentially zero CO_2 loading at the reactor outlet. The SE-SMR process is inherently unsteady; as time progresses the location at which the sorbent transitions from saturated to lightly loaded with CO_2 propagates down the reactor flow path until it reaches the outlet. At this point, termed "breakthrough," the sorbent cannot adsorb any more of the CO_2 created by the SMR reactions, and as a result CO_2 can be detected in the reactor effluent. Figures 2.3a and 2.3c illustrate the time evolution of the local CO_2 loading per

unit sorbent mass (q_{CO_2}) and gas-phase CO_2 mole fraction, respectively, during the reaction/adsorption step of an SE-SMR process. Once the sorbent is fully saturated, high levels of pure H_2 yield can no longer be achieved and the sorbent must be regenerated by depressurizing and purging the system, as illustrated in the lower portion of Figure 2.2. During the desorption process, aided by reverse-direction flow of purge gas, the boundary between saturated and unloaded sorbent propagates in the reverse direction as shown in Figure 2.3b.

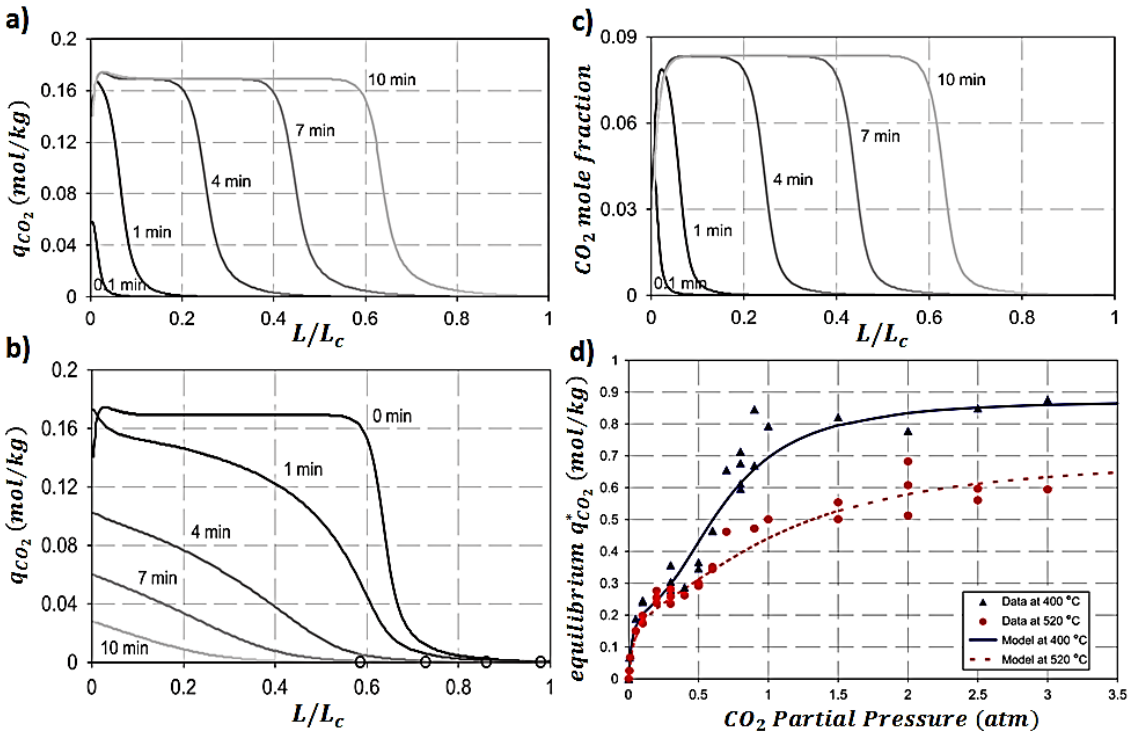

Figure 2.3: Typical behavior of a SE-SMR reactor, including temporal evolution of the spatial CO_2 loading distribution during the a) reaction/adsorption and b) regeneration steps, respectively. Also shown are the c) the temporal evolution of the gas-phase CO_2 mole fraction during the reaction/adsorption step, and d) the equilibrium CO_2 sorbent loading as a function of CO_2 partial pressure (sorption isotherms) at 400°C and 520°C. The SE-SMR reactor shown is operated at 490°C and 1.5 bar total pressure with a 4:1 H_2O to CH_4 feed ratio (reproduced from [45]).

There are two primary locations in a sorption-enhanced reactor where reactions occur, called "reaction mass transfer zones" (RMTZs). The first RMTZ is stationary and is located at the inlet of the reactor, where the inlet mixture of CH_4 and H_2O react to produce some amount of CO_2, CO and H_2 until the reacting mixture reaches the equilibrium composition that would be achieved in a reactor with no CO_2 adsorption. In the second RMTZ, the mixture leaving the first RMTZ (at pre-CO_2 adsorption equilibrium composition) reaches a sorbent region with lower CO_2 loading. At this axial location in the reactor, the CO_2 present in the gas mixture can be adsorbed, allowing further removal of CO_2 from the reaction space and creating conditions favorable for additional conversion of CH_4 even at low temperatures (~400-500°C). The second RMTZ propagates axially along the length of the reactor as the sorbent becomes increasingly loaded with CO_2. The movement of the second RMTZ zone through the reactor, coinciding with the region where the local sorbent loading with CO_2 (q_{CO_2}) and gas phase CO_2 mole fraction (x_{CO_2}) transition from high (saturated) to low (near zero) values, can be seen in Figures 2.3a and 2.3c.

The data presented in Figure 2.3 is useful in illustrating some of the limitations of the SE-SMR strategies. First, although the maximum possible sorbent loading $q^*_{CO_2}$ is approximately $0.65\ mol/kg$ at 520°C (according to the sorption isotherm shown in Figure 2.3d), the actual loading achieved during the SE-SMR process (at a lower temperature of 490°C, which favors greater CO_2 sorption capacity) is shown to be only $0.17\ mol/kg$ in Figure 2.3a. This is because the partial pressure of CO_2 leaving the first RMTZ, which represents the highest CO_2 concentration in the reactor, is limited by the equilibrium composition without CO_2 removal. For a feed with high steam content of 4:1

S/C ratio and an operating temperature of 490°C, the equilibrium mole fraction of CO_2 is only $ca.\ x_{CO_2} = 0.08$. With a total pressure in the reactor of $1.5\ atm$, this results in a maximum CO_2 partial pressure (the driving force for CO_2 adsorption) of only $0.12\ atm$. According to the sorption isotherms presented in Figure 2.3d, at this low value of a driving partial pressure the equilibrium CO_2 loading is much lower than the maximum value of $0.65\ mol/kg$, meaning that a large portion of the sorbent capacity is unutilized. A secondary limitation of the SE-SMR continuous flow reactor process is the fact that, due to non-instantaneous adsorption kinetics and axial species diffusion, CO_2 breakthrough occurs before the full axial length of sorbent is utilized. This results in an underutilized region of sorbent near the exit of the SE-SMR reactor, called the "length of unused bed" (LUB) [46]. Inefficient catalyst utilization near the inlet of the reactor is also prevalent in fixed bed SE-SMR reactors, as heat and mass transfer rates are highest at this location due to momentum, concentration and boundary layer development, yet the reaction rate quickly becomes locally limited by rapid saturation of the sorbent with CO_2.

In practice multiple SE-SMR reactors are used in parallel, yet out of phase with one another, to produce a quasi-steady H_2 output (allowing for reactors with saturated sorbent beds to regenerate while others maintain H_2 production). Reactors incorporating CO_2 sorption produce an improvement in CH_4 conversion at temperatures below 500°C; however, high S/C ratios (and thus large quantities of readily available steam) are required to achieve suitably high conversion and catalyst stability [12, 15, 45].

2.3.2 Membrane SMR reactors

Similar to sorption-enhanced SMR reactors, the fundamental operating principle behind membrane SMR reactors is to shift the reaction equilibrium and enhance the

forward reaction rate by selective removal of one of the products of the (reversible) reaction. Unlike SE-SMR reactors, however, rather than through adsorption onto a solid sorbent material, product removal is achieved via permeation through a selective membrane designed to allow preferential transport of the desired species. In particular, for hydrocarbon fuel reforming reactors aimed at producing fuel cell-grade H_2, use of a selectively permeable membrane is desirable as it provides a purified stream of hydrogen and can be used to eliminate downstream separation steps. Numerous types of hydrogen selective materials – including microporous alumina, zeolites, perovskites, and dense metallic membranes – have been investigated for membrane steam reforming reactors [47-52]. Most materials involve a tradeoff between *permeability* (*i.e.*, the magnitude of hydrogen flux rate at a given partial pressure/ concentration differential) and *selectivity* (*i.e.*, the preference for the desired species to permeate the membrane relative to that of undesired species). For example, alumina has high permeability and low selectivity, perovskites are very selective to H_2 yet their permeability is typically quite low, and zeolites typically have both moderate permeability and selectivity. Of the aforementioned group of selectively permeable materials, only dense metallic membranes such as palladium or palladium alloys offer both extremely high (potentially infinite) H_2 selectivity with high permeability [53-55]. The main limitation of Pd-based membranes is their high cost, which has been a strong driver to development of ultra-thin, yet mechanically stable high area implementations [55-57], as well as composite formulations with minimal Pd content [58-60].

Figure 2.4 presents a conceptual schematic of an annular membrane reactor for low temperature SMR and illustrates the performance benefit as compared to what can be

achieved without a selectively permeable hydrogen membrane. Due to the endothermic nature of the overall SMR process the CH_4 conversion increases monotonically with temperature; however, as illustrated in Figure 2.4b significantly higher levels of conversion can be achieved when membrane-assisted selective H_2 removal is employed, as compared to the maximum (equilibrium) values that are possible without membrane separation. Le Chatelier's principle predicts that because the SMR process produces more moles of products than the number of moles of reactants consumed during the reaction, higher fuel conversion is favored at lower pressure. Figure 2.4c shows that for a traditional (non-membrane) reactor this is the case, yet the opposite occurs for membrane reactors as the dominant component in the product mixture (H_2 has a 3-4 to 1 ratio relative to CO or CO_2) is removed from the reactor and does not inhibit the forward reaction process.

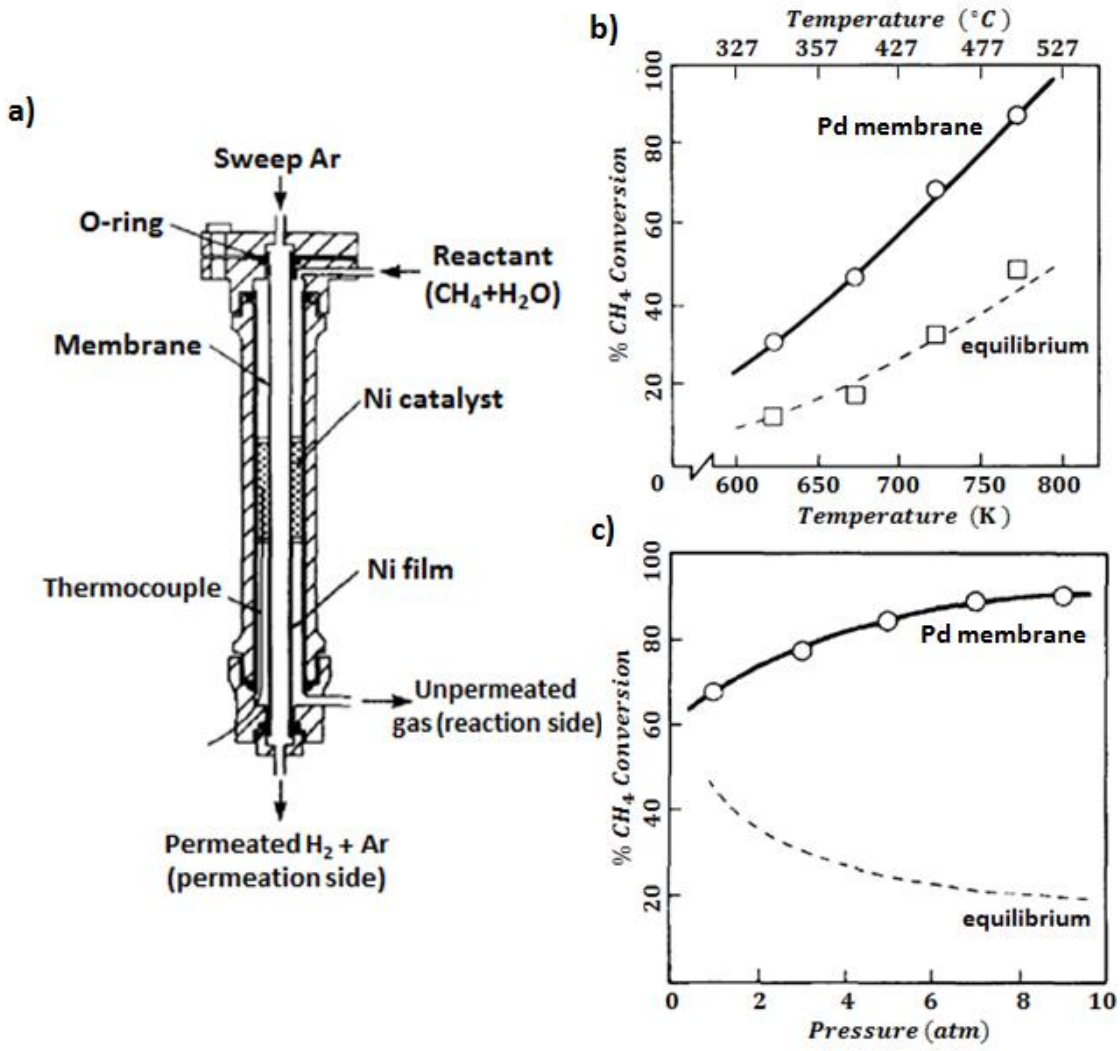

Figure 2.4: Membrane reactor for low temperature SMR: a) reactor schematic, b) CH_4 conversion versus temperature for a 3:1 molar H_2O/CH_4 feed ratio, and c) impact of operating pressure on CH_4 conversion with a 3:1 S/C feed ratio at 500°C operating temperature (reproduced from [33]).

2.4 Introduction to the CHAMP Reactor Concept

The CO_2/H_2 Active Membrane Piston (CHAMP) concept is a variable volume batch-membrane reactor recently proposed for hydrogen production via steam reforming of hydrocarbons [61]. The CHAMP operates in a cycle similar to the Internal Combustion (IC) engine, aiming to dynamically maintain the optimal conditions (pressure,

temperature, and residence time) for (*i*) transport of reactants to the catalyst, (*ii*) reaction kinetics at the catalyst, and (*iii*) selective permeation of H_2 through a membrane. In particular, to counteract the effects of fuel depletion and reduction in reactor pressure due to H_2 permeation, strategic compression of the CHAMP reactor volume is utilized to increase the concentration of the remaining fuel and hydrogen, thereby providing additional driving force for reaction and permeation. A schematic of the baseline embodiment of the CHAMP reactor is presented in Figure 2.5.

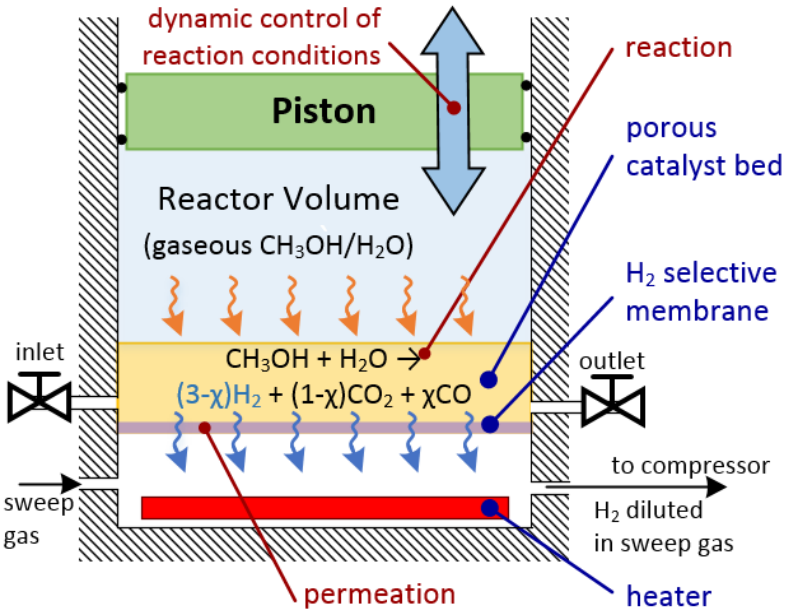

Figure 2.5: Baseline embodiment of CHAMP reactor for H_2 production via methanol steam reforming coupled to membrane hydrogen removal

Initial studies of the CHAMP reactor, utilizing methanol as a potential on-vehicle feedstock, demonstrated advantageous performance as compared to a traditional packed-bed continuous flow reactor in terms of the CHAMP's ability to overcome heat and mass transport limitations as well as to match transient H_2 product yield with its demand

without sacrificing conversion or yield efficiency [18, 19]. Figure 2.6 illustrates the modified embodiment of a CHAMP-class reactor which incorporates CO_2 adsorption and is the main focus of this doctoral dissertation. The porous bed on top of the membrane, containing only catalyst for the steam reforming reaction in the baseline CHAMP reactor shown in Figure 2.5, now includes a mixture of catalyst with a porous, CO_2-selective solid adsorbent. As carbon dioxide is produced via the SMR reaction, it is adsorbed onto the surface of this material (forming physi/chemi-sorbed complex CO_2-S as illustrated in Figure 2.6).

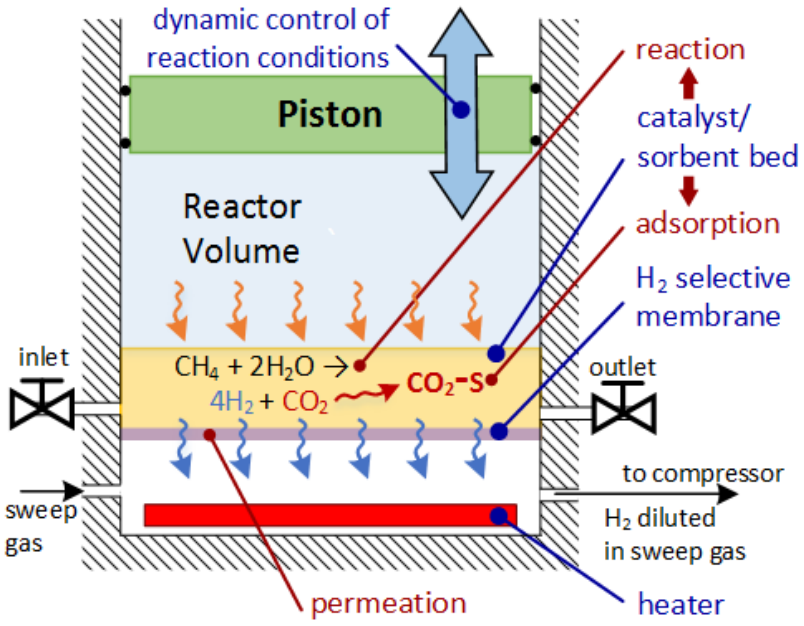

Figure 2.6: Schematic of a CHAMP-class reactor enhanced with a selective CO_2 sorbtion for H_2 production from the steam methane reforming reaction (proposed CHAMP-SORB concept).

In addition to favorable shift in equilibrium and enhanced conversion of the SMR reaction, the formation of CO which is a poison to H_2-selective membrane, via the

reverse WGS reaction given by equation (2.2), is effectively mitigated in CHAMP-SORB by the incorporation of a selective-CO_2 adsorbent. Figure 2.6 shows that, in addition to the physical phenomena of reaction and permeation that are critical features to the original, baseline CHAMP concept, adsorption is an additional process that will dramatically influence the performance of the CHAMP-SORB reactor, in particular providing the thermodynamic conditions that enable operation at much lower reaction temperatures and stoichiometric 2:1 feed S/C ratios to meet the demands of distributed H_2 production.

2.5 Concluding Remarks

This chapter discussed the large-scale, centralized production of H_2 from the steam methane reforming process and outlined limitations that provide significant impediments to for its adaptation for smaller scale, distributed production. Specific requirements for distributed process were introduced, and two state of the art concepts (sorption-enhanced SMR and membrane-enhanced SMR) to reduce the SMR reaction temperature were reviewed. Lastly, a CHAMP-class membrane reactor enhanced with selective CO_2 sorbent, termed CHAMP-SORB, was introduced that marries the advantages of SE-SMR and membrane SMR approaches in a novel semi-batch process. In Chapter 3, the performance limits of this CHAMP-SORB approach are assessed using thermodynamic analysis to establish an envelope of feasible operating conditions and to quantify its utility for low temperature SMR at near stoichiometric steam to carbon ratio in the fuel.

CHAPTER 3

THERMODYNAMIC ANALYSIS

In this chapter, the separation requirements are investigated to meet the target operating temperature and steam to carbon (S/C) ratio values for distributed SMR. Once the separation requirements are established, the operating cycle(s) of enhanced CHAMP reactor with CO_2 sorption (CHAMP-SORB) are introduced and carefully analyzed from a thermodynamic perspective to assess its viability as a concept for low temperature SMR.

3.1 CO_2/H_2 Separation Requirements for Low Temperature SMR

Before considering a specifics of the cyclic operation of CHAMP-SORB class of reactors that can achieve low temperature SMR with *in situ* separation of reaction products, it is useful to first establish the degree of separation required to achieve high CH_4 conversion at low temperature in a general sense (*i.e.*, irrespective of reactor type). During a combined reaction/permeation/adsorption process, the initial number of moles of each species *j*, N_j^0, evolves to a final value N_j according to species conservation:

$$N_j = N_j^0 + \left(1 - r_j\right)\Sigma_i \varepsilon_i \nu_{ij} - N_{j,perm} \tag{3.1}$$

where r_j is the fraction of produced species *j* that is adsorbed from the gas phase of the reactor, ε_i is the extent of reaction *i*, ν_{ij} is the stoichiometric coefficient of the j^{th} component of reaction *i*, and $N_{j,perm}$ is the number of moles of species *j* that permeates out from the reactor. The parameter r_j is non-zero for $j = CO_2$ only when considering CO_2 sorption, while the parameter $N_{j,perm}$ is non-zero for $j = H_2$ only for the case of hydrogen removal through membrane separation. Specifying zero permeation of all non-

hydrogen species implies use of a membrane that is infinitely selective to hydrogen, such as for example palladium-based membranes.

If the reactions proceed to equilibrium, the reverse methanation, equation (2.1), and water gas shift, equation (2.2), reactions must satisfy the following constraints:

$$K_{RM}(T) = \frac{x_{H_2}^3 x_{CO}}{x_{CH_4} x_{H_2O}} \cdot \left[\frac{P_T}{P_{ref}}\right]^2 \tag{3.2}$$

$$K_{WGS}(T) = \frac{x_{H_2} x_{CO_2}}{x_{CO} x_{H_2O}} \tag{3.3}$$

where x_j is the mole fraction of species j, and K_{RM} and K_{WGS} are the equilibrium constants for the reverse methanation and water gas shift reactions, respectively. These equilibrium constants are determined as function of the reaction temperature using empirical correlations given by Twigg [62]. Lastly, if a selectively permeable H_2 membrane is present, the final H_2 partial pressure in the reactor must be equal to the hydrogen partial pressure on the permeate side of the membrane ($P_{H_2}^{\infty}$). In the case of no membrane, this constraint reduces to a vanishing rate of H_2 permeation, *i.e.*:

$$\begin{gathered} P_{H_2}^{\infty} = x_{H_2} \cdot P_T \text{ (with membrane)} \\ or \\ N_{H_2,perm} = 0 \text{ (without membrane)} \end{gathered} \tag{3.4}$$

3.1.1 Impact of hydrogen removal alone on equilibrium conversion

Figure 3.1 shows the equilibrium CH_4 conversion at various pressures as a function of temperature of an initially pure methane-steam mixture with S/C ratio of 2. For cases with a membrane, the H_2 partial pressure on the permeate side of the membrane is held constant at $0.2\ bar$ by an inert sweep gas or consumption in an appropriate (electro)

chemical device. Without a membrane, reaction temperatures in excess of 700°C are required to achieve a conversion of greater than 90%, while the same can be achieved at less than 500°C with a membrane reactor at 5 bar reaction pressure.

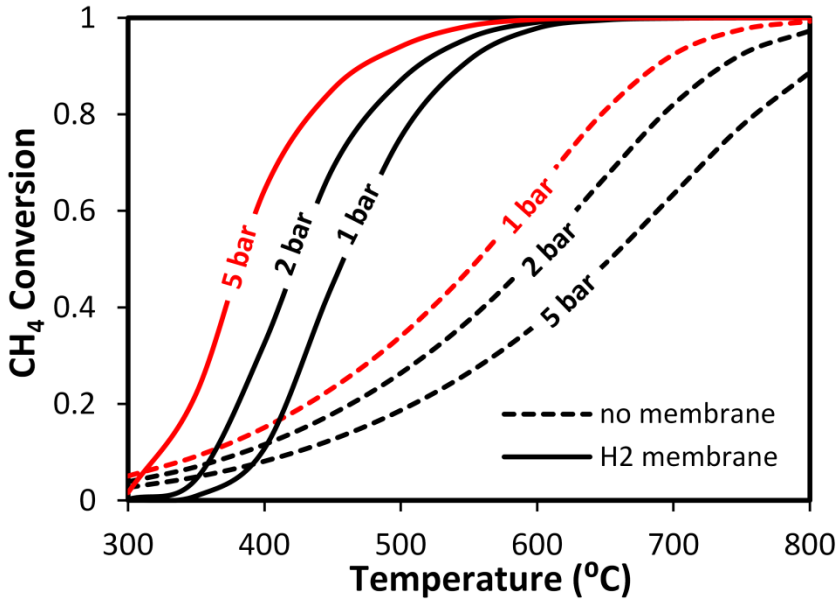

Figure 3.1: Equilibrium CH_4 conversion for a reactor with (solid lines) and without (dashed lines) a selectively permeable H_2 membrane at various operating pressures (assumed uniform within the reactor).

It is important to note that without a membrane, conversion decreases with increasing pressure, as is expected from Le Chatelier's principle because an increasing number of moles result from the overall reaction. In contrast, with a membrane conversion increases with increasing pressure because of the additional removal of H_2 from the reaction chamber at higher pressures due to increased driving force for permeation across the membrane. This is important because it enables operation at higher pressure to increase the volumetric H_2 yield density without hurting the final achievable CH_4 conversion. Also when coupled with CO_2 adsorption, as will be introduced in Section 3.1.2, operating at

higher pressure with H_2 removal enables a higher CO_2 partial pressure and thus more favorable conditions for increased quantity of CO_2 adsorption. While increased reaction pressure is always favorable for equilibrium conversion with a membrane, the maximum pressure is limited by the mechanical strength of the membrane; for the purpose of this paper, this limit is arbitrarily set to be $5\ bar$.

At very low temperatures, the conversion without a membrane actually exceeds that of the membrane case. This is an artifact of setting the equilibrium hydrogen partial pressure on the retentate side to a fixed value equal to that of the permeate side. At low temperatures, so little hydrogen is produced by the chemical reactions that in order to satisfy equation (3.4), hydrogen from the retentate side must actually permeate into the reactor ($i.e.,\ N_{H_2,perm} < 0$) to achieve equilibrium. The additional back-permeated hydrogen inhibits the equilibrium extent of the reactions and reduces the conversion as compared to the case without a membrane.

3.1.2 Equilibrium conversion enhancement with CO_2 sorption

Figure 3.2 illustrates the supplemental increase in CH_4 conversion which can be achieved by incorporating CO_2 adsorption. Calculations are made at $5\ bar$ pressure for the case with a membrane and $1\ bar$ without a membrane, because each represents the highest possible conversion without sorption within the pressure range considered. For each case, methane conversion with removal (r) of 50% and 90% of the produced CO_2 is plotted. With 90% CO_2 removal and H_2 separation via membrane, it is possible to achieve 90% CH_4 conversion at temperatures below 400°C. In contrast, without a membrane even removing a large fraction of the produced CO_2 does not result in conversions close to 90% in the temperature range considered (up to 600°C).

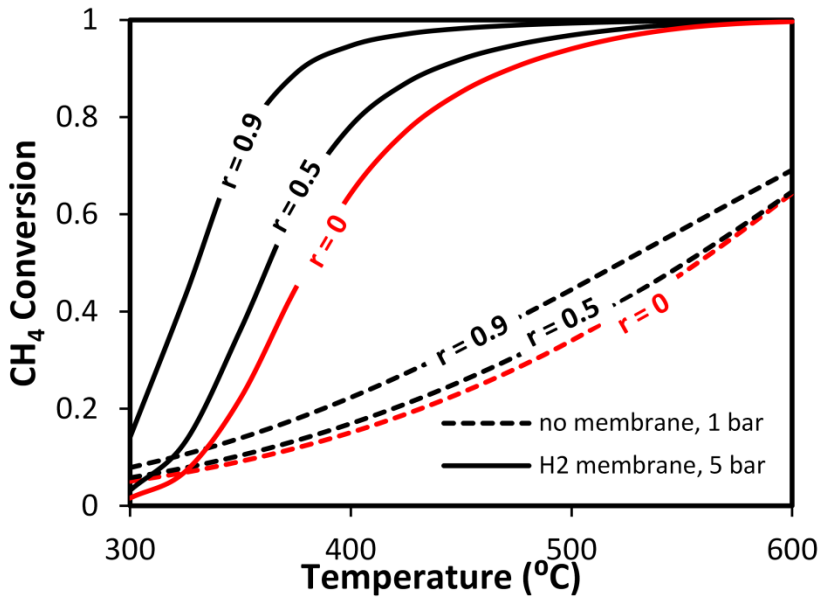

Figure 3.2: CH_4 conversion enhancement by removal of CO_2 via adsorption both with (solid lines) and without (dashed lines) hydrogen separation via a membrane

Comparing the magnitude of conversion enhancement associated with CO_2 removal with and without a hydrogen permeable membrane, it is clear there is a synergistic effect in combining CO_2 sorption with H_2 removal. The use of a hydrogen membrane also appears to have a more significant impact on achievable conversion at a given temperature than CO_2 removal; this is to be expected because 3-to-4 molecules of H_2 are produced per molecule of CH_4 consumed while less than 1 molecule of CO_2 is produced (with the exact value of H_2 and CO_2 production depending on the extent of reverse methanation vs. WGS reaction). A key result of SMR thermodynamic equilibrium analysis is that both a hydrogen permeable membrane and CO_2 sorption are required for the CHAMP reactor to achieve a desirable conversion level (>90%) with methane as feedstock at temperatures as low as 400°C.

3.2 CHAMP Reactor with CO_2 Sorption: CHAMP-SORB Cycle

The equilibrium calculations for sorption requirements in Section 3.1 are general and made without consideration for how CO_2 is removed from the system or the type of reactor (batch or continuous flow). This section describes a particular embodiment of a modified CHAMP reactor, termed CHAMP-SORB (first illustrated in Figure 2.6 of the previous chapter), which can facilitate low temperature hydrogen production via SMR with selective CO_2 adsorption incorporated. It also discusses how the sorption isotherm's shape will impact the reactor performance and identifies the most appropriate sorbent option that matches with batch-mode operation of the CHAMP-SORB reactor.

Figure 3.3 illustrates the steps of the proposed cyclic CHAMP-SORB reactor with CO_2 adsorption. In contrast to the basic CHAMP embodiment [19], which utilizes only one intake and one reaction/exhaust stroke, the CHAMP-SORB reactor operates in a four-stroke cycle. Proceeding clockwise from top left in Figure 3.3, the reactor is first filled with a mixture of CH_4 and H_2O, as well as recycled products from the previous cycle (if desired). The mixture then undergoes the steam-methane reforming reaction, which is enhanced by permeation of H_2 through the palladium-silver membrane and adsorption of CO_2. During this step, the piston moves downward to maintain constant pressure as selected species are removed from the gas phase via adsorption and permeation, and the temperature is maintained by heating (not shown) the sorbent/catalyst mixture layer. After the SMR reaction has proceeded sufficiently, the exhaust valve opens and the downstroke is completed to fully exhaust the chamber. As denoted by the dotted line, part or all of the exhaust gases can be recycled to the filling

upstroke of the next CHAMP cycle if losses of residual hydrogen and unconverted methane upon exhaust are to be minimized. Section 3.4.2 will show that this recycling has a positive impact on thermal efficiency of the reactor, but can come at a significant cost to volumetric H_2 yield density.

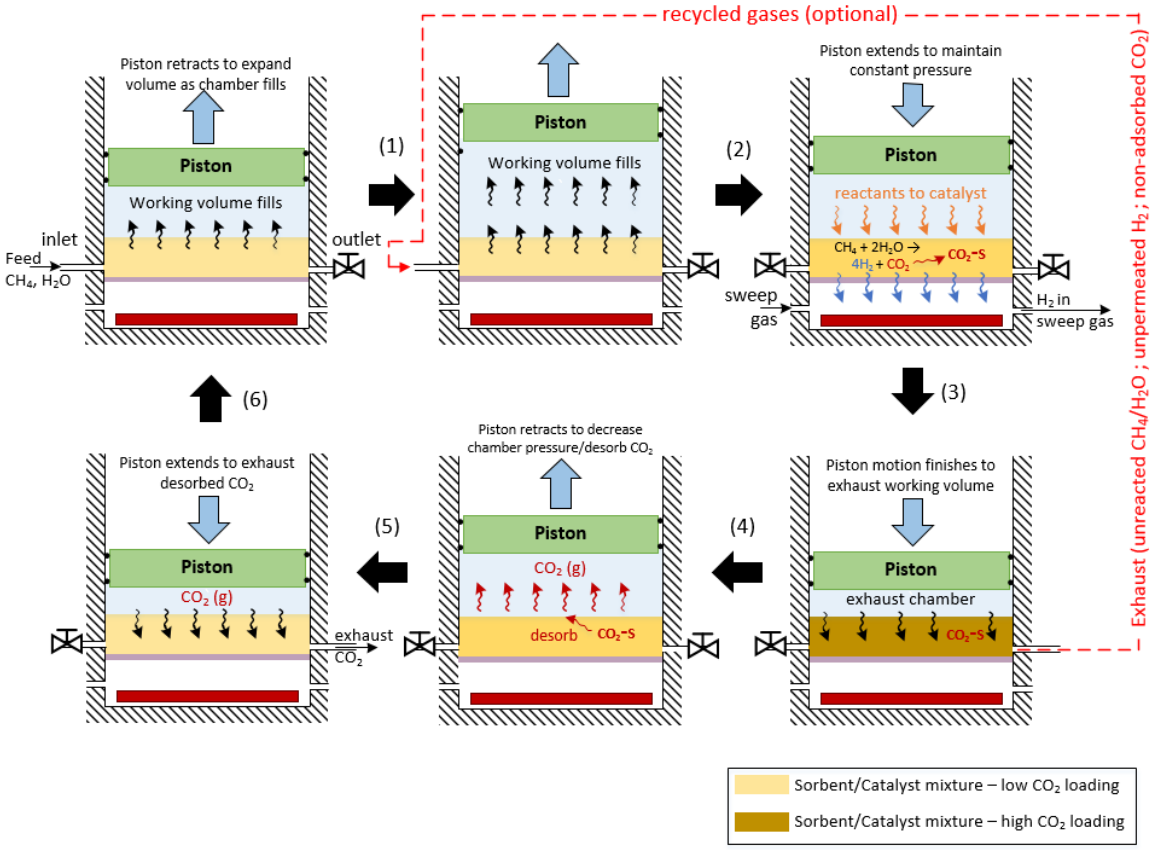

Figure 3.3: Schematic of CHAMP-SORB reactor cycle. The reactor utilizes four strokes per cycle: (a) retracting piston to fill the reactor, (b) extending piston to produce H_2 via SMR at constant pressure and then opening valve to exhaust products, (c) retracting piston to desorb CO_2 and (d) extending piston to desorb and produce a purified CO_2 as the final product.

Once the chamber is exhausted, a second upward stroke expands the chamber volume to reduce pressure and to facilitate desorption of CO_2, with heat addition to maintain

temperature during the endothermic desorption process. Lastly, a second downstroke exhausts the desorbed CO_2 from the reaction chamber, allowing it to be captured if desired. Note that CO_2 may not be fully removed during the desorption step and this sorbent loading will then be carried over to the start of the subsequent cycle.

To model the cyclic performance of the CHAMP-SORB reactor, species conservation is solved at each of the states (1) – (6) labeled in Figure 3.3. It is assumed that the reaction, permeation, adsorption, and desorption steps all proceed fully to equilibrium and that sufficient heat is added to maintain isothermal conditions. It is also assumed that the filling processes (6) – (1) – (2) is sufficiently fast that no CO_2 adsorption/desorption or SMR reaction occurs during this step. Similarly, no change in sorbent loading is assumed to occur during the CO_2 exhaust step (5) – (6). Lastly, the system is modeled as if the reactor chamber can be completely exhausted (i.e., neglecting any dead volume) at states (4) and (6) when the volume of the gas is fully compressed and piston stops reaching the top of the sorbent/catalyst mixture layer; this assumption is strictly valid in the limit of an infinitely thin layer of sorbent, but as the sorbent volume increases (e.g., in scaling up the reactor to desired productivity, the amount of gas contained within the porous sorbent voids may become significant.

In addition to solving the species balance, it is necessary to determine the required heat and work inputs for each step of the process to enable calculation of the overall thermal efficiency as a function of key process variables (temperature, pressure, S/C ratio, sorbent mass and recycle fraction). In doing so it is assumed that all expansion or compression steps are frictionless, quasi-equilibrium processes. The volume expansion during desorption step is assumed to occur slowly enough that the CO_2 loading of the

sorbent remains in equilibrium with the surrounding gas. Appendix A details the full set of equations and solution procedure for the species balance at each state (1) – (6), along with calculations of the required heat and boundary work inputs for each process.

3.3 Sorbent Considerations

3.3.1 Impact of sorption isotherm shape on CHAMP-SORB performance

Because the sorbent loading from a previous cycle is carried over to the next, the amount of CO_2 removed by adsorption during the reaction process (2) – (3) is equivalent to the amount desorbed during the volume expansion process (4) – (5). This removed quantity of CO_2, $N_{CO_2,des}$, is equal to the product of the mass of sorbent (m_{sorb}) and the change in sorbent loading (q_{CO_2}, units of $[mol/kg]$) between state 3 (with high loading at "low" reaction temperature $T_3 = T_{rxn}$ and "high" adsorption pressure $P_3 = P_{ads}$) and state 5 (with low loading at "high" desorption temperature $T_5 = T_{des}$ and "low" desorption pressure $P_5 = P_{des}$).

$$N_{CO_2,des} = m_{sorb}\left[q_{CO_2}(T_{rxn}, P_{ads}) - q_{CO_2}(T_{des}, P_{des})\right] \tag{3.5}$$

The shape of the adsorption isotherm will then have significant impact on the achievable CO_2 removal and the effective sorbent utilization. To illustrate this impact, Figure 3.4 shows two isotherms with identical saturation capacity at high CO_2 pressure and the same slope in the low-pressure Henry's region at a given temperature. The bottom isotherm is a classic Type I Langmuir isotherm while the top isotherm is Type IV by Brunauer classification [63], with two inflection points and a concave up region at moderate pressure which is often used to represent a multi-layer adsorption behavior. To achieve a desired sorbent utilization under isothermal conditions, the pressure in the

chamber for the Langmuir isotherm must be brought lower (P^*_{des}) than would be required for the sorbent with the Type IV isotherm (P_{des}). Alternatively, if the same desorption pressure ($e.g., P_{des}$) were desired for the Langmuir isotherm, combined temperature/pressure swing would have to be utilized ($T_{des} > T_{rxn}$) in order to achieve the same amount of CO_2 desorption.

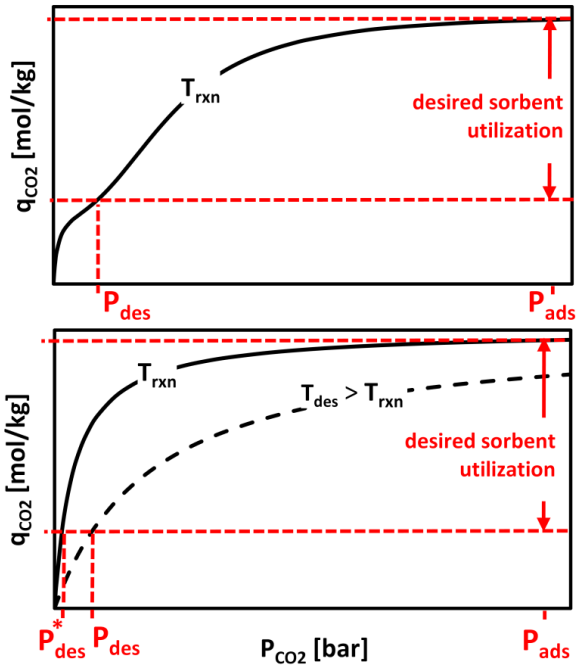

Figure 3.4: Illustration of impact of isotherm type on sorbent utilization and required reactor pressure and temperature. Type IV (top figure) isotherm allows a higher CO_2 pressure (P_{des}) during the desorption stage than the Type I (bottom figure) isotherm would require (P^*_{des}). The same desorption pressure can be achieved with the Type I isotherm only by incorporating a temperature swing between reaction and desorption.

Desorption pressure is critical for the cyclic CHAMP-SORB reactor, which relies on volume expansion alone to achieve the desired pressure swing. As such, the desorbed CO_2 remains in the reactor chamber, and the required expansion volume (state 5 in Figure 3.3) is related to the CO_2 desorption pressure by the ideal gas equation of state:

$$P_{des} = \frac{N_{CO_2,des}\, R_u T}{V_5} \tag{3.6}$$

As the required desorption pressure to achieve a desired sorbent utilization goes to zero, the required desorption volume approaches infinity. For distributed applications where a small footprint is required, a realistic practical limit on the desorption volume is that it matches the maximum volume of the system when filled with fuel at state 2. Comparing the isotherms of Figure 3.4, a sorbent with a Type IV isotherm is preferred for the batch reactors such as CHAMP-SORB because it leads to a less stringent low pressure requirement for adequate desorption than would be required for a Type I isotherm sorbent.

3.3.2 Comparison between CHAMP-SORB and traditional SE-SMR

Because the utility of a sorbent is lost when it becomes saturated, sorption-enhanced (SE) reaction processes are inherently transient whether a variable volume batch or fixed bed flow arrangement is used. The traditional approach to SE-SMR employs at least two fixed bed reactor units operating out of phase, with one regenerating while the other is producing hydrogen. When PSA is used for sorbent regeneration, CO_2 desorption is accomplished by reducing reactor pressure below that of the reaction/adsorption step, followed by flushing the chamber with a purge gas and then repressurizing with a portion of the H_2 product gas. During the purge and repressurization step, the flow is in the reverse direction to that of the reaction/adsorption step to push the CO_2 sorbent loading front towards the entrance of the reactor, ensuring that essentially pure H_2 product (on a dry basis) occupies the reactor volume at the end of desorption/regeneration phase, which is then pushed out the reactor when the flow direction is again switched and the

subsequent reaction step begins [44]. For applications where CO_2 sequestration is desired, steam has been proposed as the most suitable purge gas because it can be easily condensed out from the mixture; however it has been shown that an extremely high ratio of purge gas to desorbed CO_2 (greater than 60:1) is required to fully regenerate the sorbent [34]. A similar approach using temperature swing adsorption (TSA) at constant pressure as opposed to PSA has been proposed, but it still requires a significant amount of purge steam in a ~6:1 ratio with respect to H_2 product [6]. Accounting for the 1 to (3 or 4) ratio of CO_2 to H_2 produced by the overall SMR reaction, this equates to a roughly 20:1 ratio of purge gas to desorbed CO_2. As explained in the introduction section of this paper, this can be problematic for distributed and size-constrained applications where steam may be less readily available and its use would be detrimental from the reaction yield density prospective. Additionally, the energy required to generate steam in the ratios described above can dramatically lower the process energy efficiency.

The CHAMP-SORB offers additional benefits over the traditional SE-SMR process in that it does not require purge gas when desorbing the CO_2. Because the catalyst/sorbent mixture only fills a small portion of the reactor, it is possible to exhaust most of the gas by moving the piston to a position corresponding to minimum reactor volume. The purity of the H_2 product is ensured by membrane separation, so small amounts of residual CH_4, CO, and CO_2 carried over to a subsequent cycle are not an issue. The CHAMP-SORB does have a disadvantage, however, in that regeneration of the sorbent is limited by the presence of desorbed CO_2 in the reactor chamber. This limitation can be seen in the coupling of equations (3.5) and (3.6); as the volume is expanded, more CO_2 is desorbed according to the adsorption isotherm which in turn limits the reduction

in chamber pressure associated with the expansion process. Because the desorbed CO_2 remains in the chamber it is not possible to fully regenerate the sorbent in the CHAMP-SORB reactor when the reactor volume at the end of expansion/desorption step, which is capped by the initial volume occupied by the feed gas during the intake step. This is in contrast to a traditional PSA process, where the desorbed CO_2 is continuously exhausted from the reactor with a non-adsorbing purge species, and it is possible to fully regenerate the sorbent with sufficient purge gas flow.

The regeneration behavior of the CHAMP-SORB reactor has an interesting impact on the level of mass-based sorbent utilization, defined as the difference in loading between the adsorption and desorption steps and illustrated in Figure 3.4, as additional sorbent is incorporated in the reactor. If total reactor pressure is sufficiently high, the sorbent loading (per unit mass of sorbent) at the end of the reaction/adsorption step, $q_{CO_2}(T_{rxn}, P_{ads})$, remains nearly constant, regardless of sorbent mass, because the CO_2 partial pressure is high enough to fully saturate the sorbent. When the piston is moved to the system's maximum volume state to induce desorption, as more sorbent is present more CO_2 will be released into the gas phase according to equation (3.5) This in turn means that, as indicated by equation (3.6) the CO_2 pressure at the end of the desorption step will be higher as more sorbent is added to the reactor. The CO_2 desorption pressure and sorbent loading at state 5, $q_{CO_2}(T_{des}, P_{des})$, are linked by the adsorption isotherm, with loading monotonically increasing with pressure regardless of whether the isotherm is Type I or IV. As such, higher CO_2 desorption pressure corresponds to higher sorbent loading at the end of the desorption step (less complete desorption per unit mass) and thus lower specific sorbent utilization. There is therefore a diminishing returns

associated with increasing the sorbent mass, in that adding more sorbent results in a lower effective working capacity.

3.3.3 Selection of CO_2 sorbent

Having discussed the general impact of the sorption isotherm on the CHAMP-SORB performance, specific high temperature sorbents are now considered to determine the most appropriate option for this application based on the currently available materials as reported in the literature. In addition to the isotherm shape considerations, the sorbent must have sufficient CO_2 adsorption capacity at temperatures above 400°C and selectively adsorb CO_2 in presence of other gases, in particular water vapor. The sorbent must also have relatively fast kinetics and cyclic stability over many adsorption/desorption cycles. Several review papers outline the various sorbent options for SMR, including calcium oxides, lithium zirconate and hydrotalcites [29, 64]. Though possessing high CO_2 capacity, CaO has poor cyclic stability and is more suited for temperature swing adsorption, requiring high regeneration temperatures. Lithium zirconate similarly is more suited for TSA, and it also suffers from relatively slow kinetics which is not considered in this paper but is an important consideration. Hydrotalcites have lower CO_2 capacities than the other options, but they are well suited for PSA and have excellent cyclic stability and adequate kinetics in the 400-600°C temperature range.

The CO_2 adsorption properties of hydrotalcite-like compounds are sensitive to their preparation, in particular the Mg/Al ratio and degree of impregnation with alkali metals such as potassium or cesium carbonate [65]. Because the capacity is specific to the preparation method, many studies have reported variations in sorption capacity and other

characteristics [37, 66-70]. Of these, only one measured the sorption isotherm beyond a CO_2 pressure of $1\ bar$, most likely because higher CO_2 pressures are not relevant to conventional flow-through SMR reactors. However, data in this pressure range is critical for the CHAMP-SORB reactor, which can achieve high CO_2 partial pressure conditions as the CH_4 and H_2O are depleted by the SMR reaction and H_2 is removed from the reaction chamber via membrane permeation. The sorption isotherm reported by Lee *et al.* contains data up to $3\ bar$ and is of Type IV, owing to a proposed mechanism which combines monolayer adsorption with a multi-layer chemical complexation reaction [67]. Because it contains data at the required high CO_2 partial pressures, this isotherm is utilized in the CHAMP-SORB cyclic calculations that are reported next in Section 3.4.

3.4 Results and Discussion

Two key performance metrics for a small-scale distributed reactor, such as the CHAMP-SORB, are thermal (energy) efficiency and volumetric yield density. The thermal efficiency calculation is based on the ratio of heating values of the H_2 product to the CH_4 fuel, with the required heat and work inputs during all stages of the CHAMP-SORB cycle also accounted for (note that all calculations follow a sign convention that the work input is negative):

$$\eta_{th} = \frac{LHV_{H_2} \cdot N_{H_2,perm}}{LHV_{CH_4} \cdot N_{CH_4,1} + \Sigma Q_{in} - \Sigma W_{b,out}} \tag{3.7}$$

The energy required to increase the temperature and pressure of the initial mixture of liquid H_2O and gaseous CH_4 from a standard state (25°C, 1 bar) to the elevated reaction temperature and pressure are included in the heat and work components of equation (3.7) [71]. The energy penalty associating with generating steam can become a significant

factor in the overall thermal efficiency of the process, as the enthalpy of vaporization of one mole of liquid water at STP is *ca.* 20% of the endothermic heat of the reverse methanation reaction for one mole of CH_4 [34].

The hydrogen yield density is defined as the amount of H_2 permeated through the membrane in a given cycle divided by the maximum volume of the system. The maximum volume occurs at state (2) in Figure 3.3, because the reactor contains the largest amount of gas species at this point (as discussed in Section 3.2, the final volume of the low pressure desorption step is constrained to match this volume). Both the volume of gas and the solid volume of the sorbent are included when determining the maximum volume for the yield density calculation:

$$V_{\max} = V_2 = \Sigma_j N_{j,2} v_{j,2}(T_{rxn}, P_{rxn}) + (1 - \varepsilon_t) \cdot m_{sorb}/\rho_{sorb} \qquad (3.8)$$

where ε_t is the total porosity and ρ_{sorb} is the density of the hydrotalcite sorbent taken from Ding and Alpay [66], and $v_{j,2}$ is the specific volume of species j at the reaction (state 2) temperature and pressure.

Two additional metrics that are considered in assessing the CHAMP-SORB performance are hydrogen yield efficiency and CH_4 conversion. The yield efficiency is defined as the actual amount of H_2 permeated through the reactor divided by the maximum possible H_2 yield if all the carbon in the introduced CH_4 were oxidized to CO_2 (as opposed to some CO), which according to the stoichiometry of the overall SMR process is four times the number of moles of CH_4 fed. The CH_4 conversion is defined in a traditional sense of moles reacted divided by moles fed; however, it is important to note that when part of the exhaust gas mixture from the previous cycle is recycled, the moles of CH_4 fed only includes the quantity of new fuel that is added ($N_{CH_4,1}$), not the total

moles of fuel present after recycle ($N_{CH_4,2}$). As a result, the general expression for CH_4 conversion is:

$$X_{CH_4} = \frac{N_{CH_4,2} - N_{CH_4,3}}{N_{CH_4,1}} \tag{3.9}$$

3.4.1 CHAMP-SORB performance without fuel recycling

The first case considered is for baseline operation with no exhaust gas recirculation (recycling) from the previous cycle. If this is the case, states (1) and (2) in Figure 3.3 are identical (*i.e.* $N_{j,1} = N_{j,2}$). Figure 3.5 is a representative plot that shows how the thermal efficiency, hydrogen yield density, yield efficiency and conversion vary with S/C ratio at a fixed reaction temperature, pressure and mass of sorbent.

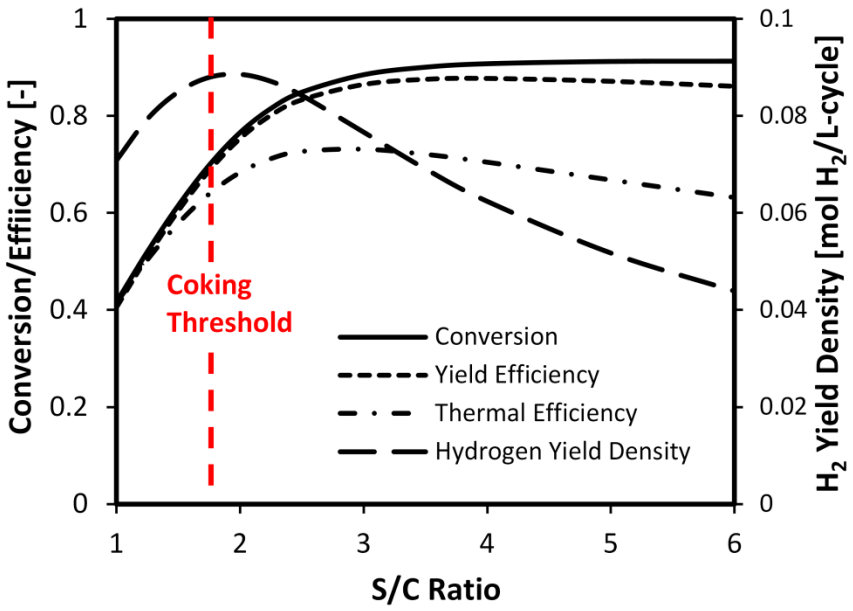

Figure 3.5: Impact of S/C ratio on conversion, yield efficiency, thermal efficiency and hydrogen yield density of CHAMP-SORB reactor. Calculations made with a sorbent mass of 1 $kg/(initial\ mol\ CH_4)$ at 400°C without any fuel regeneration.

As expected from the Le Chatelier's principle, operating with more steam has a favorable impact on CH_4 conversion. Conversion monotonically increases with S/C ratio, an effect that is particularly pronounced for S/C ratios less than 3. Yield efficiency, however, trends closely with CH_4 conversion at low S/C ratios but reaches a maximum and actually tails off at S/C ratios greater than 4. This is due to a dilution effect of excess steam in the reactor chamber: even as more H_2 is produced at higher levels of CH_4 conversion, the hydrogen partial pressure is reduced due to an accumulation of non-permeating, non-adsorbing species in the chamber such that the additional H_2 cannot permeate out of the reactor. The dilution effect at high S/C ratios has a more pronounced effect on the hydrogen yield density due an extra volume required for additional steam in the feed, with yield density tailing off significantly with additional steam above a S/C ratio of 2. Operating at low S/C ratios, where H_2O becomes the limiting reactant, is also detrimental to yield density. As such, the optimal S/C ratio for hydrogen yield density is approximately 2, which corresponds to the stoichiometry of the combined SMR reaction.

Determining the optimal S/C ratio for maximum thermal efficiency is not as straightforward as matching the stoichiometry of the combined SMR reaction for maximum yield density. The increase in conversion/yield efficiency with excess steam and the energetic penalty associated with generating steam are competing factors which lead to a maximum thermal efficiency at a S/C ratio of 2.8 for the conditions of Figure 3.5. Below this optimal S/C ratio, operating with additional steam is favorable because the lower heating value of the extra H_2 produced outweighs the extra energy input required to produce the steam. Operating above the optimal S/C ratio, however, decreases the overall cycle's thermal efficiency as the energetic cost of producing steam becomes

dominant. The tail off in thermal efficiency at higher than optimal S/C ratios is mitigated by the fact that the CH_4 conversion continues to increase, albeit at slower rates, with increased steam. As a result, the thermal efficiency penalty at high S/C ratios is not as pronounced as the reduction in hydrogen yield density.

Because the CHAMP-SORB reactor thermal efficiency and H_2 yield density analysis shows favorable operation at lower S/C ratios than typically found in industrial or sorption-enhanced SMR applications, it is important to consider the potential issue of catalyst deactivation through carbon deposition [72]. Carbon deposition on a catalyst can occur at high temperatures through the endothermic decomposition of methane ($CH_4 \rightleftharpoons C + 2H_2$) and at lower temperatures by the exothermic Boudouard reaction ($2CO \rightleftharpoons C + CO_2$) [73]. Methane decomposition is not likely at the lower CHAMP-SORB operating temperatures, but the possibility of low temperature carbon deposition through the Boudouard reaction is possible and more likely to occur at lower S/C ratios [11]. Snoeck *et al.* experimentally determined an expression for the "coking threshold" (*i.e.*, the ratio of CO_2 to CO concentrations above which the net rate of carbon formation becomes zero) on a Ni steam reforming catalyst which can be used to determine a critical S/C ratio below which there will be a risk of catalyst deactivation through coking [74]. For the conditions of Figure 3.5, this coking threshold corresponds to a S/C ratio of 1.75. This result suggests that it is possible to operate the CHAMP-SORB at S/C ratios low enough to optimize H_2 yield density without risking coking of the catalyst, however it is important to recognize that the actual coking threshold will depend on the catalyst and should be monitored in any future experiments with a CHAMP-SORB class reactor. While a S/C coking threshold of 1.75 is specific to the conditions of Figure 3.5, this

parameter is monitored during all calculations presented in the following sections and is determined to be sufficiently low in all of these cases to not be a limiting factor in optimization.

Figure 3.6 summarizes the simultaneous impact of varying the S/C ratio and amount of sorbent on the two key performance metrics, thermal efficiency and hydrogen yield density, at a temperature of 400°C and pressure of 5 bar. The solid curves in Figure 3.6a indicate lines of constant sorbent mass (per mole of CH_4 fed), while dashed curves are lines of constant S/C ratio. The same trend is seen as in Figure 3.5, with increasing thermal efficiency and yield density at S/C ratios less than 2, followed by a region of decreasing yield density but increasing thermal efficiency at intermediate S/C ratios, and finally decreasing both the yield density and thermal efficiency at high S/C ratios. It can also be seen in Figure 3.6a that the S/C ratio corresponding to maximum yield density (marked by circles in the plot) always occurs at or just slightly below 2 regardless of sorbent amount. This is in contrast to the S/C ratio corresponding to maximum thermal efficiency (marked by crosses), which decreases with increasing sorbent amount because the increased capacity to selectively remove CO_2 reduces the amount of required excess steam to enhance the conversion. The diminishing returns associated with including additional sorbent, the reasons for which were discussed in Section 3.3.2, can also be seen in Figure 3.6b and Figure 3.6c, as increasingly more sorbent is required to provide the same benefit in thermal efficiency and yield density. The thermal efficiency and yield density both increase with additional sorbent at low sorbent levels; however, at very high sorbent amounts (greater than 4 $kg/mole\ CH_4$), the yield density can actually decrease with increasing sorbent mass. This occurs specifically at low S/C ratios and is due to the

fact that the volume occupied by the sorbent becomes significant relative to the volume of gas in the reactor.

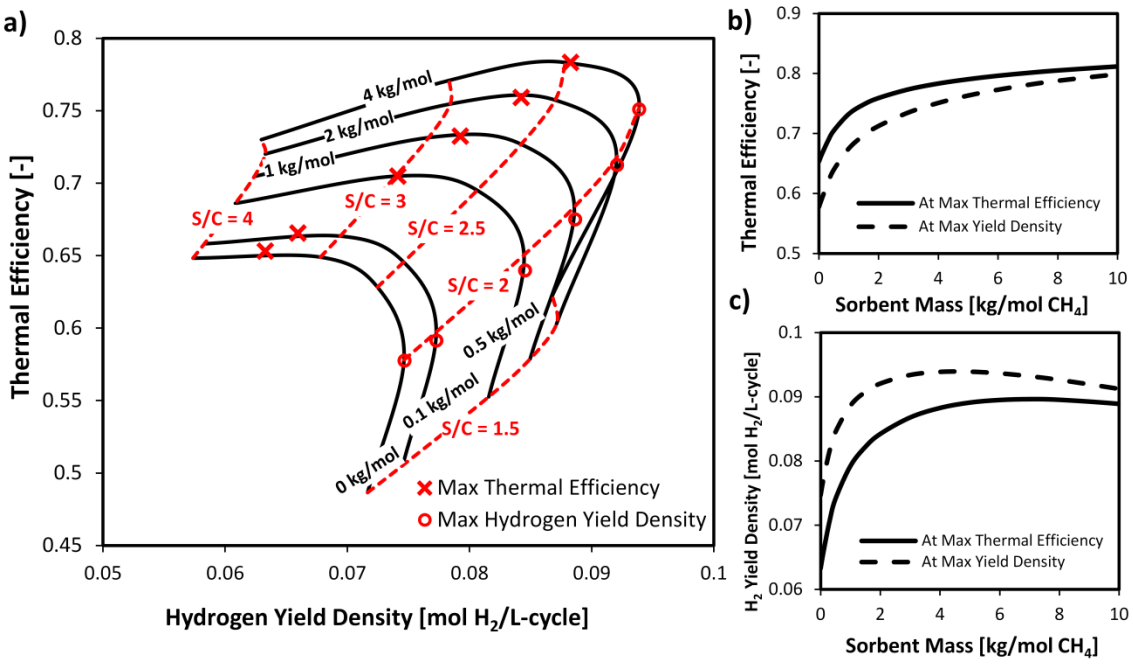

Figure 3.6: CHAMP-SORB reactor cyclic performance without regeneration: (a) Regime map for thermal efficiency versus cyclic hydrogen yield density at varying S/C ratios (---) and sorbent mass (—); (b) Thermal efficiency and (c) Hydrogen yield density as a function of sorbent loading with S/C ratios chosen to maximize each metric.

For each specific sorbent mass, the point corresponding to maximum thermal efficiency is labeled with an "x" and maximum yield density with an "o." The loci of these points are plotted on Figure 3.6b and Figure 3.6c, illustrating the impact of optimizing S/C ratio for thermal efficiency versus hydrogen yield density on each of these parameters, with additional data included beyond $4\ kg/mol$ of sorbent. While Figure 3.6b shows that thermal efficiency continues to monotonically increase with increasing amount of sorbent, according to Figure 3.6c hydrogen yield density eventually

tails off at high sorbent loadings regardless of whether the S/C ratio is chosen to maximize thermal efficiency or yield density.

3.4.2 CHAMP-SORB reactor performance with fuel recycling

At the end of the reaction/permeation/adsorption step, the residual gas in the reactor consists of some unreacted CH_4 as well as trace CO and unpermeated H_2. All of these are valuable, energy-carrying products, and because most of the hydrogen product is already separated from this mixture it is possible to recycle the residual gas from the CHAMP-SORB reactor exhaust to improve fuel utilization. To model this "closed-loop" mode of operation with product recycling, a recycle fraction (*f*), defined as the percentage of gas at the end of the reaction step that is recycled ($N_{j,2} = N_{j,1} + fN_{j,3}$), is introduced. The recycle fraction can take values between zero (no recycle) and unity (full recycle). In the case of full recycle, the reactor fully converts all CH_4 and H_2O introduced and outputs pure H_2 during the reaction step and pure CO_2 when the chamber is exhausted after the desorption step, resulting in a "closed-loop" operation.

Figure 3.7 illustrates the impact of increasing the recycle fraction for a CHAMP-SORB cycle at 400°C, $5\ bar$ with a specific sorbent mass of $1\ kg/mol\ CH_4$ while changing the S/C ratio. The thermal efficiency versus hydrogen yield density curve for $f = 0$ in Figure 3.7a matches its counterpart in Figure 3.6a, but as the recycle fraction is increased the curves gradually flatten out. The reason for this flattening is that the impact of lower conversion and hydrogen yield on thermal efficiency penalty at low S/C ratios is "softened" due to recycling of unconverted CH_4, as opposed to wasting it by exhausting without recycle. Similarly, the drop off in thermal efficiency at high S/C ratios is less severe with fuel recycling because a portion of the excess steam is carried

over from the previous cycle and less energy of vaporization is required to generate new steam. As the regeneration fraction is increased from 0 to 1, the general trend is that thermal efficiency increases while hydrogen yield density decreases due to the added volume occupied by the recycled gas and carried over through the cycle. This tradeoff is further illustrated in Figure 3.7b, which depicts thermal efficiency and corresponding hydrogen yield density as a function of recycle fraction where at all points the S/C ratio is chosen to optimize efficiency.

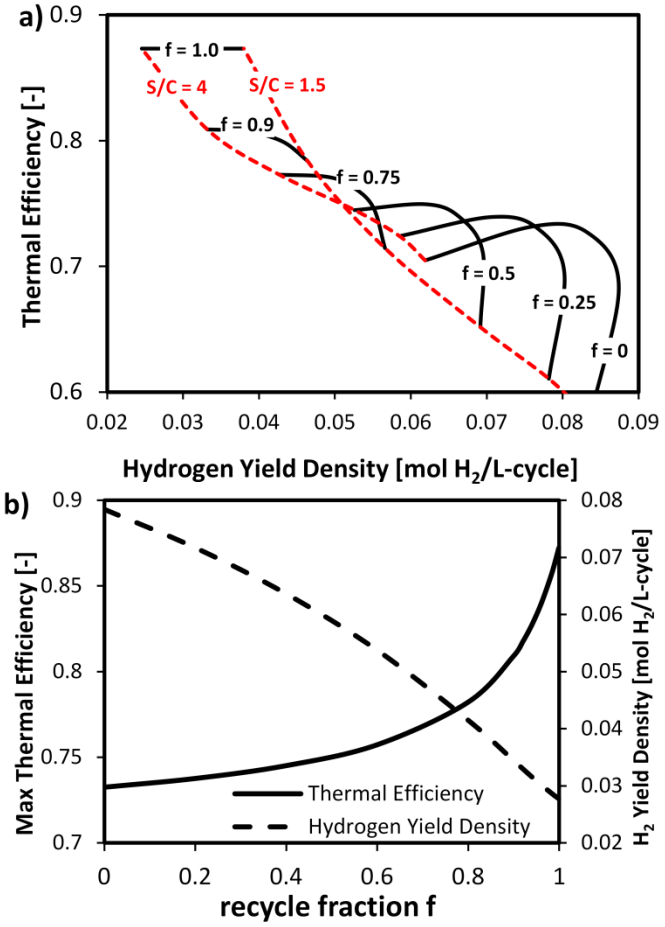

Figure 3.7: Impact of recycle fraction on CHAMP-SORB reactor thermal efficiency and hydrogen yield density: (a) Regime map for 1 $kg\ sorbent/mol\ CH_4$; (b) Maximum thermal efficiency with optimal S/C ratio as a function of recycle fraction and corresponding yield density tradeoff.

When the full amount of residual gas is carried over to the next cycle (*i.e.*, $f = 1.0$), the thermal efficiency becomes a constant value regardless of S/C ratio. This result can be understood by recognizing that the amount of gaseous CO_2, CO and H_2 must be equal at the beginning and end of the reaction/permeation/adsorption step – states (2) and (3), respectively, in Figure 3.3 – during cyclic operation because only CH_4 and H_2O are added to the reactor from one cycle to the next. To keep the CO quantity constant, the reverse methanation and WGS reactions must proceed to equal extents because carbon monoxide is neither permeated nor adsorbed out from the reaction chamber. As such, the net reaction must match that of the overall SMR process ($CH_4 + 2H_2O \rightleftharpoons 4H_2 + CO_2$), and therefore all the CO_2 and H_2 produced must be removed from the gas phase by adsorption and permeation, respectively, for their quantities to remain equivalent from state (2) to (3). Ultimately, this fixes the proportion of permeated H_2 to added (new fuel increment) CH_4 (4:1) and H_2O (2:1) for each CHAMP-SORB cycle, regardless of the operating S/C ratio after the recycled gas is introduced to the chamber at the start of the reaction/permeation/adsorption step. As a result, the thermal efficiency approaches a fixed value with full regeneration, as the heating value of CH_4 along with the heat required to preheat the fuel and maintain isothermal conditions during cyclic operation are always held in fixed proportion relative to the heating value of H_2 that is permeated from the reactor.

The reasoning above holds true regardless of sorbent mass, so it is expected that this constant thermal efficiency with full regeneration should remain unchanged with varying sorbent amount at a given reaction temperature and pressure. This is confirmed by the results in Figure 3.8, which is a regime map of thermal efficiency versus hydrogen yield

density for varying the sorbent mass and recycle fraction (with the S/C ratio implicitly varied at each data point to maximize thermal efficiency). The curve for 100% recycle is not plotted because the optimal S/C ratio for maximum thermal efficiency is arbitrary when the efficiency is constant, but the curve for 99.9% shows that the thermal efficiency reaches a constant value equal to that of Figure 3.7a for all non-zero sorbent amounts.

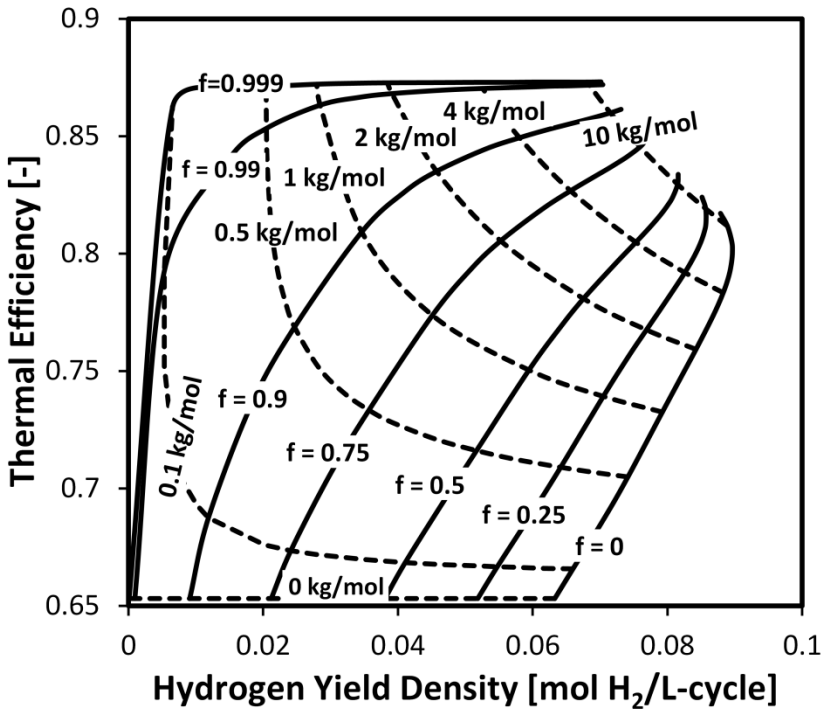

Figure 3.8: Regime map for CHAMP-SORB cyclic performance with exhaust recycling (all results are for different S/C ratios chosen to maximize thermal efficiency at each recycle fraction and sorbent mass combinations). Dashed lines represent foci of constant sorbent mass (per unit of added fuel) while solid lines represent foci of constant recycle fraction.

Moving along lines of constant recycle fraction in Figure 3.8, an increase in the sorbent amount increases both thermal efficiency and hydrogen yield density until the volume occupied by the sorbent becomes significant relative to the gas volume of the reactor chamber. Beyond this point additional sorbent continues to increase thermal

efficiency while hurting yield density, in agreement with previously observed trends. The sorbent mass at which hydrogen yield density is negatively impacted does grow, however, with increasing recycle fraction because the added volume of the recycled gases delays the deleterious effect of solid volume occupied by the sorbent. Another important result of Figure 3.8 is that the thermal efficiency's benefit of exhaust recycling is only present when there is some non-vanishing amount of sorbent. This is because without a sorbent to perturb the equilibrium state of the recycled gases, there is no conversion enhancement associated with recycling. Therefore, adding an increasing amount of exhaust gas in the absence of a sorbent only serves to decrease the hydrogen yield density while keeping thermal efficiency constant. Lastly, as more sorbent is added to the reactor an increasingly smaller fraction of residual products needs to be recycled in order to achieve the same thermal efficiency, while the associated hydrogen yield density penalty becomes lessened.

3.5 Conclusions

In this chapter, a thermodynamic cycle of a new class of variable volume batch-membrane reactor with integrated CO_2 sorption, termed CHAMP-SORB, was analyzed with focus on hydrogen production from methane feedstock with consideration given to constraints imposed by distributed applications if natural gas is used as a primary source of methane. It was shown that both H_2 and CO_2 separation are required to be able to achieve desirable conversion levels at temperatures as low as 400°C with low S/C ratios, which are desirable for greater thermal efficiency and hydrogen yield density. The CHAMP-SORB reactor has advantages over traditional SE-SMR approaches in that it does not require a purge gas for sorbent regeneration and is more scalable to different

hydrogen generation demands; however this comes with a constraint on maximum achievable sorbent utilization because the desorbed CO_2 remains in the reactor as the volume is expanded rather than is continuously purged as is in the case of continuous flow SE-SME reactors. A "closed-loop" mode of the CHAMP-SORB reactor operation with partial or full recycle of unreacted reaction products with recoverable energy content was introduced, which allows one to maximize thermal efficiency and provides a compelling option for applications involving CO_2 capture combined with power (H_2) generation.

Regime maps for the reactor quasi-equilibrium operation of the CHAMP-SORB reactor, with and without product recycle, were used in this chapter to explore the tradeoff between thermal efficiency and hydrogen yield density at a given temperature and pressure, as a function of sorbent mass, S/C ratio and recycle fraction. The analysis yielded the following fundamental insights and recommendations:

- The optimal S/C ratio in the feed that maximizes hydrogen yield density is approximately 2 regardless of sorbent mass. S/C ratios above 2 are desired for maximum thermal efficiency; however, with increasing sorbent mass less excess steam is required for optimal thermal efficiency because of the incremental equilibrium shift provided by the additional CO_2 sorption.
- There is a diminishing return on sorbent utilization and CH_4 conversion enhancement as more sorbent is added due to the nature of sorbent regeneration into a fixed volume environment of the batch reactor without use of an inert carrier gas. Further, initially increasing the sorbent amount increases both thermal efficiency and yield density of the variable-volume batch reactor, but eventually yield density suffers when the fraction of reactor volume occupied by adsorbent becomes significant relative to the gas volume.
- Increasing "degree of recycling", i.e., the fraction of unreacted reactants and un-separated products at the end of each cycle that is fed back to the reactor for the

next consecutive cycle, increases thermal efficiency of the process up to its maximum at 100% recycling, but there is an associated reduction in hydrogen yield density due to a carry-over volume associated with the recycled, rather than simply exhausted, product stream. Importantly, the improvement in process thermal efficiency is not only due to mitigation of a waste of unreacted fuel especially at low S/C ratios, but also owes to a decrease in the energy input required for extra steam production especially at high S/C ratios when the fuel conversion is intrinsically high.

- The thermal efficiency benefit of incorporating recycling is only present when CO_2 sorption is incorporated into the CHAMP reactor operation. As more sorbent is added, a lesser degree of recycling is required to achieve a desired level of thermal efficiency, albeit at the expense of simultaneous reduction in hydrogen yield density.
- As a the recycle fraction approaches unity, the thermal efficiency converges to a constant value, irrespective of either the sorbent mass or post-recycle S/C ratio, because H_2 and CO_2 are produced in a fixed proportion relative to the consumed CH_4 and H_2O.

Overall, thermodynamic analysis shows that CHAMP-SORB cycle is a viable option for low temperature distributed production of hydrogen via sorption-enhanced steam methane reforming. With this fundamental proof of thermodynamic viability and an established envelope of operating conditions resulting in an optimal performance of an ideal CHAMP-SORB reactor, subsequent chapters focus on experimental demonstration of the key step(s) of the CHAMP-SORB cycle and complimentary theoretical investigation of reaction/adsorption kinetics and heat/mass transfer effects to quantify the fundamental trade-offs of this new fuel processing approach under conditions relevant to practical applications.

CHAPTER 4

EXPERIMENTAL INVESTIGATION

In this chapter, results of an experimental investigation into CHAMP-SORB as a means to achieve low (down to 400^{o}C) temperature SMR at a S/C ratio of 2:1 are presented. The testbed apparatus if first described, followed by a presentation of experiments validating each of the reactor sub-functions. Lastly, performance data for a fully-functional CHAMP-SORB reactor is reported, focusing on the most important fuel reaction/hydrogen permeation/carbon dioxide adsorption step of the reactor cycle.

4.1 Experimental Apparatus

The P&ID of the experimental testbed apparatus is shown in Figure 4.1.

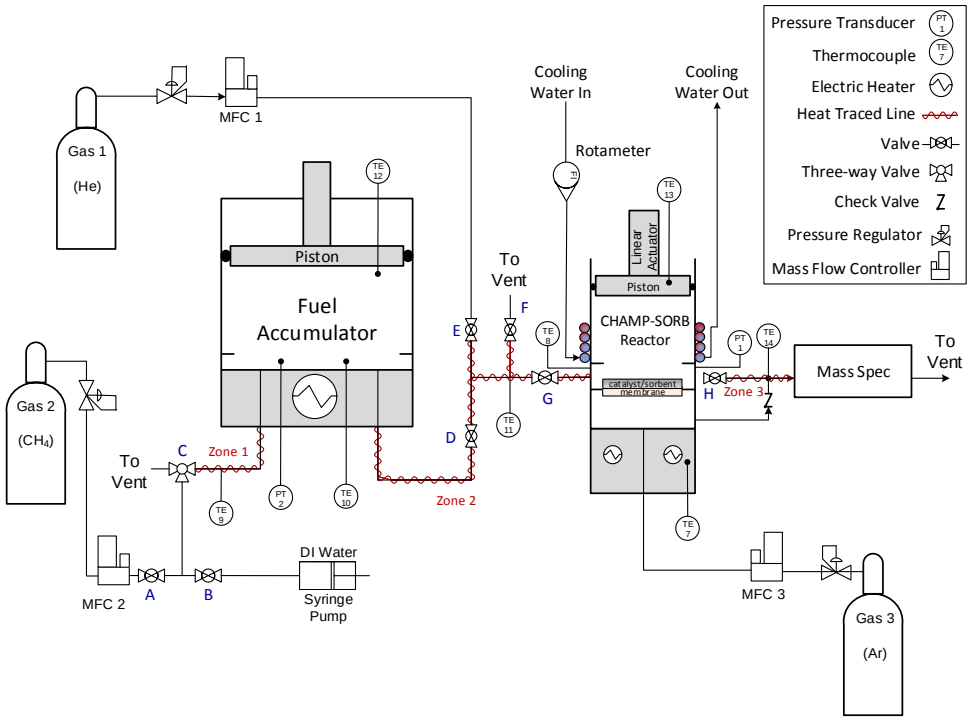

Figure 4.1: P&ID of CHAMP-SORB experimental testbed. The piping in zones 1-3 is insulated/heated with NiCr resistance heaters to ensure any steam remains superheated.

Engineering part and assembly-level drawings of the main components shown in the P&ID are provided in Appendix B. Figure 4.2 contains a picture of the experimental apparatus, with the physical parts labeled to show their correspondence to elements on the P&ID.

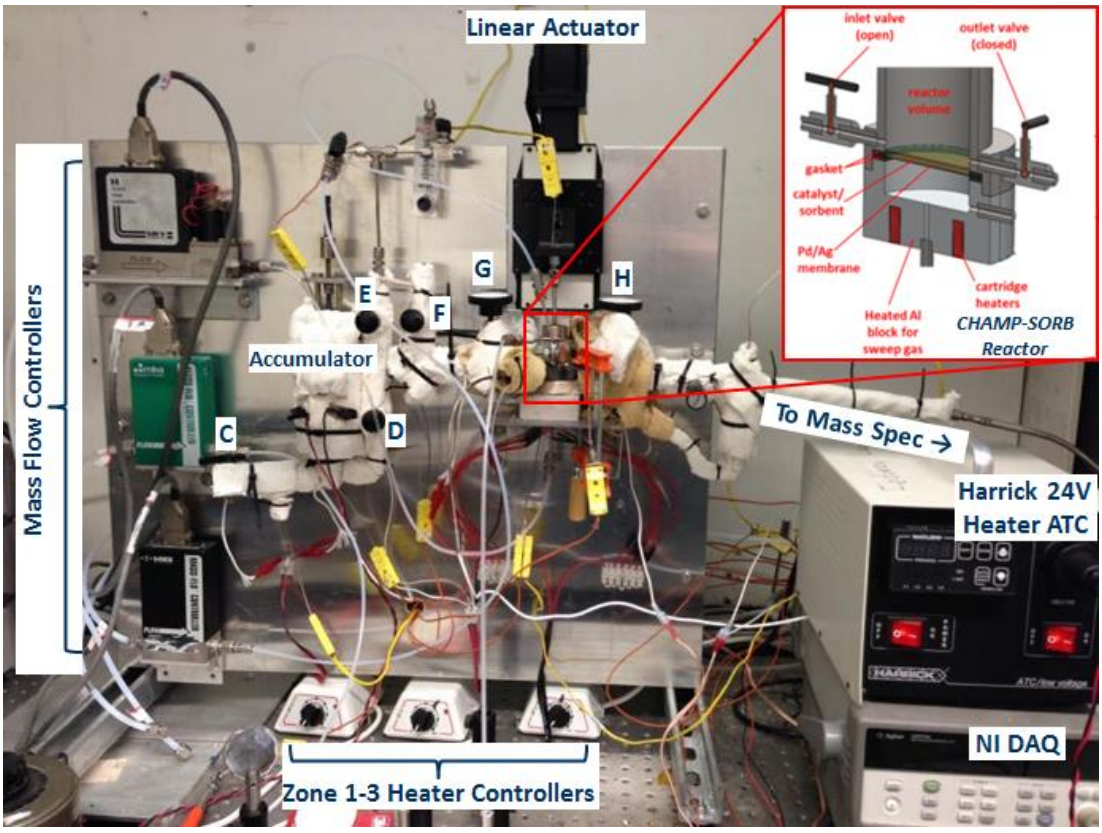

Figure 4.2: Experimental CHAMP-SORB testbed apparatus

The fuel accumulator, designed to hold and deliver a CH_4/steam mixture at the desired S/C ratio, and the CHAMP-SORB reactor were both constructed in a piston/cylinder arrangement out of 17-4 stainless steel. Because the reactor and accumulator are of a comparable volume to their inlet and outlet valves, the ratio of working volume (*i.e.* volume that can be swept by piston motion), to dead volume (*i.e.*

the volume occupied by valves, piping, etc.) must be considered. Figure 4.3 presents experimental data used to determine the dead volume of the testbed CHAMP-SORB reactor. The piston was moved via the linear actuator between its maximum and minimum displacement positions twice, and the pressure and temperature were continually recorded using a custom-written LabVIEW data acquisition program.

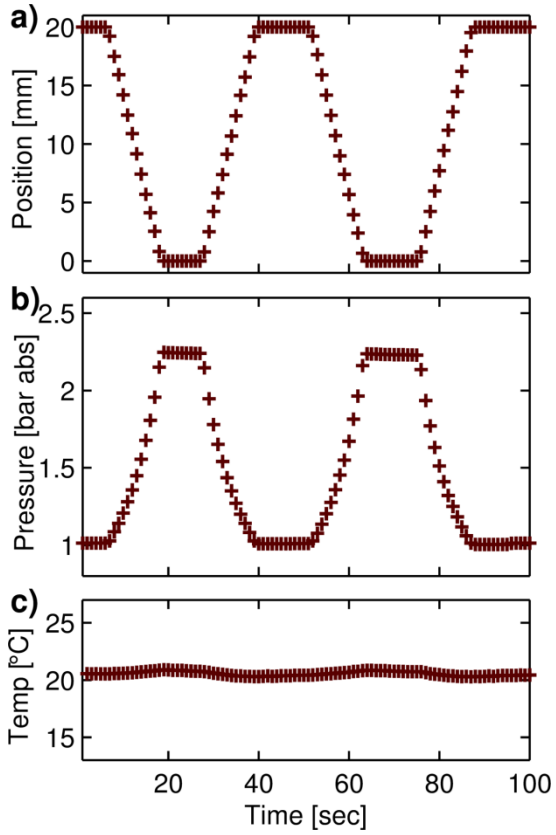

Figure 4.3: Experimental data for calculation of CHAMP-SORB testbed reactor dead volume

As the reactor volume was compressed, the pressure increased and temperature remained nearly constant (less than 0.1% deviation between the maximum and minimum recorded values in absolute temperature). Assuming that the system is closed (*i.e.* no

moles of gas escape from the reactor), the theoretical relationship between pressure and volume for an isothermal control volume can be determined using the ideal gas equation of state:

$$NR_uT = PV = constant \tag{4.1}$$

Using the known cross-sectional area of the reactor, the maximum volume occupied by the gas mixture can be expressed as $V_{max} = V_d + A_c\Delta x$, where the dead volume (V_d) is the volume of the reactor when the piston is at its minimum position and Δx is the distance spanned by the piston as it moves from its minimum to maximum displacement. As such, from equation (4.1) it follows that:

$$V_d = \left(\frac{P_{min}}{P_{max} - P_{min}}\right) A_c\Delta x \tag{4.2}$$

where P_{min} is the reactor pressure at maximum volume and P_{max} is the reactor pressure at minimum volume. Using the experimental data from Figure 4.3a, the maximum and dead volumes of the reactor were calculated to be 8.79 cm^3 and 3.97 cm^3, respectively. To verify the accuracy of this calculation, all the pressure and position data points from Figure 4.3a are plotted against one another on Figure 4.4 and compared to the predicted change in pressure by the ideal gas equation of state. The accumulator's maximum and minimum volumes were assessed using a similar technique and calculated to be 122.8 cm^3 and 36.3 cm^3, respectively.

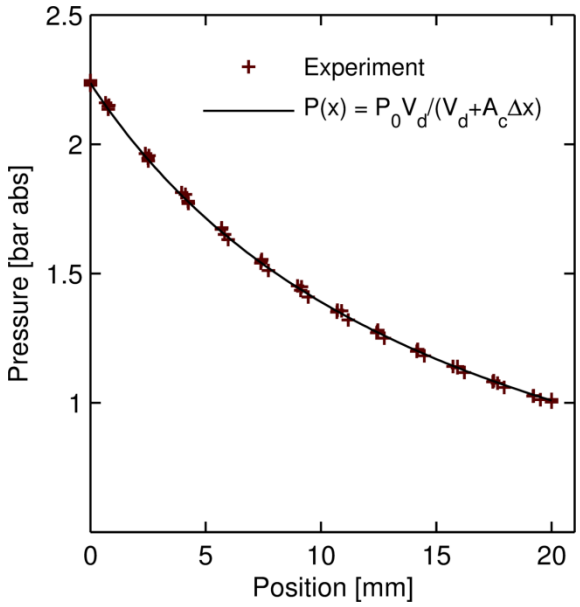

Figure 4.4: Relationship between position and pressure as measured experimentally vs. predicted by the ideal gas equation of state

Temperature and pressure were monitored in the locations indicated on the P&ID using K-type thermocouples (Omega Technologies) and high temperature miniature pressure transducers (Kulite Semiconductor Products). These probes were connected to an Agilent 34970A data acquisition/switch unit (DAQ) interfacing with a custom LabVIEW program to record temperature and pressure. Additionally, a NLS4-series linear actuator and a NSC-A1 stepper motor (Newmark Systems) were integrated in LabVIEW with closed-loop PID control to the reactor piston position. Effluent from the reactor was carried to a mass spectrometer (Hiden Analytical, HPR-20) for analysis using a sweep argon gas stream metered by mass flow controllers (MKS Instruments, 1179A series) with a precision of +/-1% of full scale.

The accumulator, CHAMP-SORB reactor and all lines/valves in between were thermally insulated using ceramic fiber insulation (Refractory Specialties Incorporated)

and heated by electric resistance heaters (Omega Technologies and Sun Electric Heater Company) to avoid condensation in any parts of the test loop. The membrane and catalyst/sorbent layer were heated to 400°C, controlled by a Harrick 24V automatic temperature controller. The piston of the CHAMP-SORB reactor was sealed against the cylinder bore using a perfluoroelastomer o-ring rated to a maximum temperature of 330°C, necessitating the use of cooling water metered through a rotameter (Cole-Palmer) at 1 $gallon/hr$ flowing through stainless steel tubing wrapped around the reactor cylinder to preserve the seal. The interface between the piston o-ring and the reactor cylinder wall was lubricated using high temperature Krytox XHT-1000 perfluoropolyether oil (DuPont).

4.2 Experimental Methods

4.2.1 Mass spectrometer calibration

To calculate the flowrate of an effluent from the CHAMP-SORB reactor, the mass spectrometer (MS) in Figure 4.1 was used in conjunction with an argon sweep gas at a known flowrate metered by a mass flow controller (MFC). Prior to conducting a reactor experiment, a gas mixture consisting of metered flows of both Ar and each expected analyte was sent to the MS for detection. The ratio of these flowrates was modified periodically by adjusting the MFC settings, creating a set of data for known MFC flow ratios and corresponding MS measurements. The raw data for a H_2 MS calibration run is presented in Figure 4.5.

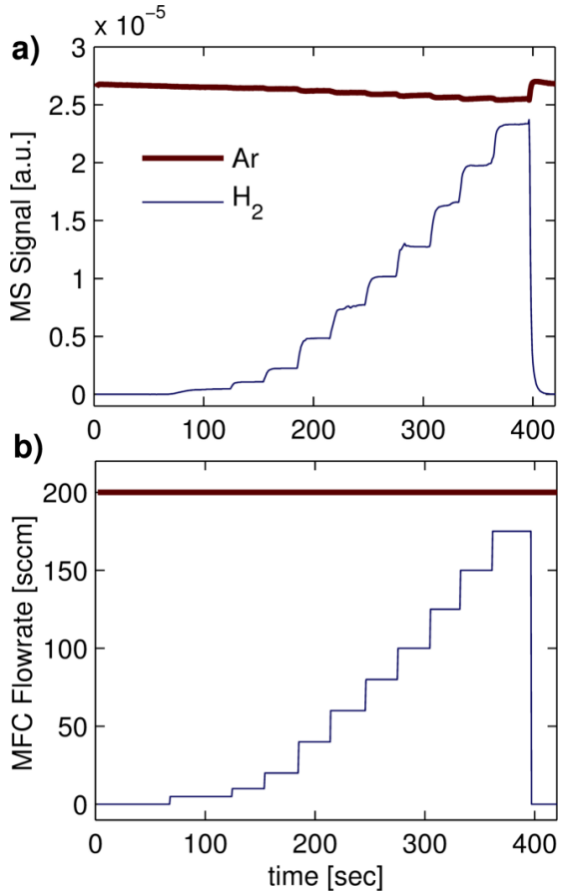

Figure 4.5: Raw experimental data for H_2 used in mass spectrometer calibration

The reported H_2 signal in Figure 4.5a is the increase in MS signal from a baseline reading of the H_2 signal when pure Ar gas was sent to the MS (although two orders of magnitude less than the Ar signal, this detected value is non-zero). Similarly, when utilizing experimental MS data to calculate the flowrate of any other analyte species, the MS signal of each analyte is also first adjusted to be relative to the analyte signal detected when pure sweep (Ar) gas is flowing to the spectrometer. This process accounts for baseline removal due to any small drift that may occur during the experimental process, and allows the least squares fitted line representing the MFC to MS ratio to pass through the origin.

During a calibration experiment, at each flow ratio the gas mixture was sent to the mass spectrometer for a minimum of 30 s. The ratio of the measured H_2 to Ar MS signal is extracted from the data by averaging over the final (stable) 15 seconds of data prior to switching to the next MFC flowrate ratio. The relationship between analyte to sweep gas MFC (known) flowrate ratio to MS signal ratio is reported in Figure 4.6.

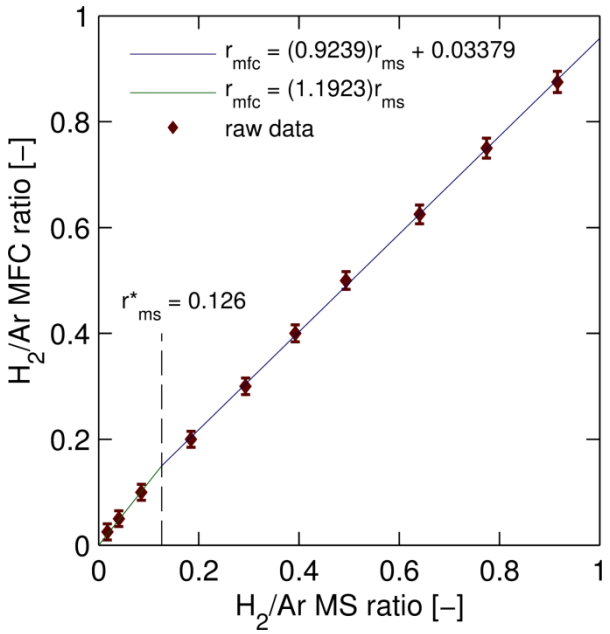

Figure 4.6: Metered H_2 to Ar MFC flowrate ratio vs. measured MS signal ratio. Least squares linear regression relating the two parameters is used in determining analyte flowrate during CHAMP-SORB experiments from MS data (the transition between segments of the piecewise fitted curve is marked with a vertical dashed line and labeled r^*_{MS})

Also shown in Figure 4.6 are two least squares regression lines; a piecewise relationship consisting of these two fitted curves are utilized because there is a change in the relationship between MS signal and MFC ratio at higher analyte flow values. For the H_2 calibration curve in Figure 4.6, this transition occurs above a MS signal ratio of $r^*_{MS} =$

0.126. Figure 4.7 reports calibration data and fitted least squares regression relationships for other tracked analytes.

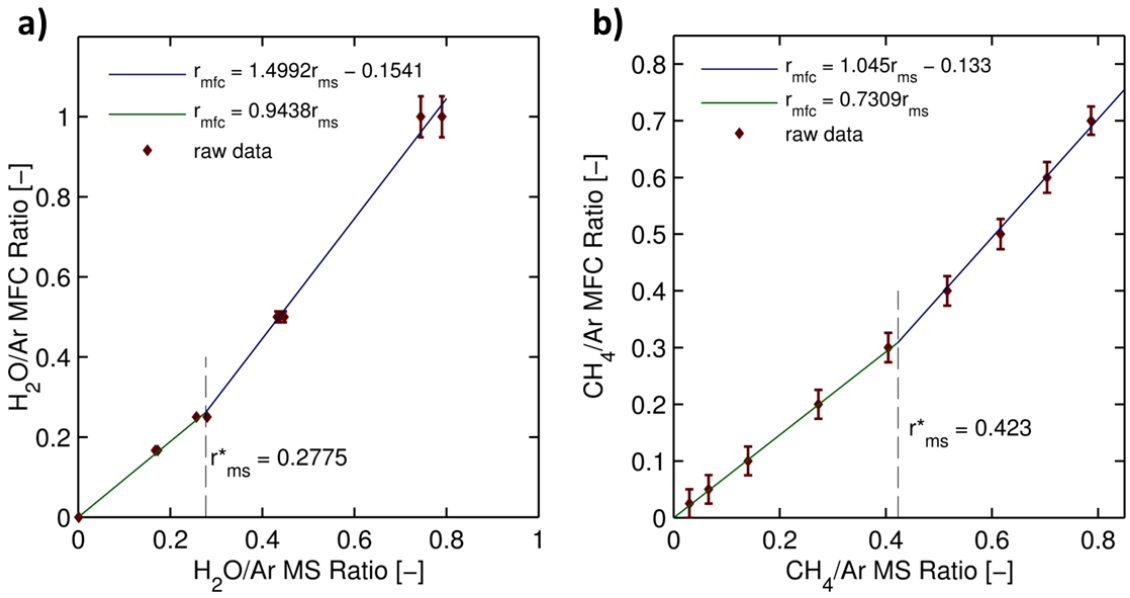

Figure 4.7: MS calibration and least squares fit lines for a) H_2O and b) CH_4

4.2.2 Typical sequence of CHAMP-SORB experiments

The following procedure was carried out to demonstrate the reaction/adsorption/ permeation step of the CHAMP-SORB reactor (refer to the P&ID in Figure 4.1 for valve labeling). During the entire experiment, a constant Ar flowrate of 200 $sccm$ was metered through MFC 3, flowing across the backside of the Pd/Ag membrane and to the mass spectrometer.

(1) Valves E, G and H were opened and the reactor piston was moved to minimum volume as 15 $sccm$ of helium flowed through the reactor to purge the system.

(2) Starting with the accumulator at the target operating pressure, the accumulator piston was moved downward to sweep a volume equal to that of the maximum volume of the CHAMP-SORB reactor (ensuring that after pressure equilibration

between the CHAMP-SORB reactor and the fuel accumulator, the system should be at the target pressure).

(3) Valves E and H were closed and valve D was opened to send fuel to the CHAMP-SORB reactor.

(4) The reactor piston was moved to maximum volume and the inlet valve G was closed, isolating the system at a final pressure equal to the target operating pressure.

(5) As the reaction/adsorption/permeation process occurred, the piston compressed the reactor volume to maintain constant pressure using closed loop feedback, and the mass spectrometer measured hydrogen production rate; simultaneously, valve D was closed and valves E & F were opened to purge the feed line with He.

(6) Valve H was slowly opened to send remaining contents inside the reactor to the mass spectrometer.

(7) Valve G was opened to send $15\ sccm$ of purge He to flush out remaining reactor contents.

4.2.3 Experimental uncertainties

The error bars in Figure 4.6 and Figure 4.7 are calculated using the uncertainty associated with the MFC measurements. In the case of H_2 and CH_4 calibration, the Ar flow was set at $200\ sccm$ for the duration of the test. An MFC with a maximum flowrate of $5000\ sccm$ was utilized, which has an accuracy of +/-1% of full scale, or $\pm\ 50\ sccm$. To substantially reduce experimental uncertainty, prior to conducting a calibration experiment the output of the MFC was sent to an Agilent ADM 1000 gas flow meter, and the MFC setting was adjusted until the target value of $200\ sccm$ was detected by the ADM 1000. At this flowrate, the ADM 1000 has an accuracy of $\pm\ 6\ sccm$. To verify there was no drift during the test, at the conclusion of the calibration experiment the Ar MFC output was again sent to the ADM 1000 to ensure the same target $200\ sccm$

reading was observed. In the H_2 and CH_4 calibration experiments, an MFC with a full scale of $500\ sccm$ was used to control the analyte flow, giving an accuracy of $\pm\ 6\ sccm$.

For the H_2O calibration experiment, the sweep Ar flow was controlled with the $500\ sccm$ full scale MFC, giving the same error as reported for the analyte in the H_2 or CH_4 calibration. The steam was introduced as liquid water, injected using a syringe pump (World Precision Instruments, SPI100i) with $\pm\ 0.05\ ml/hr$ accuracy (equivalent to $\pm\ 1.19\ sccm$ in vapor phase if recast using the density of an idea gas at standard temperature and pressure). Using these uncertainty values, a standard error propagation analysis was employed to calculate the error in MFC flowrate ratio for species i to Ar:

$$e_{r_{MFC}} = \sqrt{\left[\left(\frac{\partial r_{MFC}}{\partial \dot{n}_i}\right) e_{\dot{n}_i}\right]^2 + \left[\left(\frac{\partial r_{MFC}}{\partial \dot{n}_{Ar}}\right) e_{\dot{n}_{Ar}}\right]^2} \tag{4.3}$$

where the ratio of known flowrates metered by the mass flow controller $r_{MFC} = \dot{n}_i/\dot{n}_{Ar}$. Carrying out the partial differentiation of the equation describing r_{MFC}, equation (4.3) becomes:

$$e_{r_{MFC}} = \sqrt{\left[\left(\frac{1}{\dot{n}_{Ar}}\right) e_{\dot{n}_i}\right]^2 + \left[\left(-\frac{\dot{n}_i}{(\dot{n}_{Ar})^2}\right) e_{\dot{n}_{Ar}}\right]^2} \tag{4.4}$$

The variation in error bars for the experimental range of MFC flowrate ratios for the H_2O calibration is greater than the variation seen in the H_2 or CH_4 calibration. This is due to the difference in calibration experimental procedure for a liquid as opposed to a gas analyte; the syringe pump flowrate was held constant during the H_2O calibration experiment, to avoid transient behavior in the evaporator as liquid flowrates varied. To achieve different MFC flow ratios in the liquid calibration experiment, the Ar sweep gas flowrate, as opposed to the analyte flowrate, was modulated (in this particular case in the

range $100 - 500\ sccm$). This results in larger error bars at higher H_2O/Ar flowrate ratios in Figure 4.7a, as low values of Ar flow were required to achieve the desired flowrate ratio and the fixed $\pm 5\ sccm$ error was a larger percentage of the target flowrate. The experimental error in MS signal ratio is determined using an identical approach to that of equations (4.3) and (4.4); however, the error bars are not displayed on Figure 4.6 and Figure 4.7 because they are within the width of the marker lines due to the high accuracy of the MS readings.

The error in effluent flow rates calculated from the full CHAMP-SORB experiments is also calculated with an error propagation analysis. The general relationship between the detected signal ratio and the true (in this case, unknown) ratio of analyte to sweep gas flowrates is given by the least squares regression lines fitted from the calibration data (expressed in the general form $r_{MFC} = m_i r_{MS} + b$, where m_i and b are the slope and y-intercept, respectively, of the fitted data). It then follows that the flowrate of the unknown analyte relative to the known sweep gas flowrate is:

$$\dot{n}_i = \dot{n}_{Ar}(m_i r_{MS} + b) \tag{4.5}$$

Equation (4.5) is used in conjunction with the error propagation analysis to determine the experimental error of any effluent from the reactor as it is detected by the mass spectrometer:

$$e_{\dot{n}_i} = \sqrt{\left[\left(\frac{\partial \dot{n}_i}{\partial \dot{n}_{Ar}}\right) e_{\dot{n}_{Ar}}\right]^2 + \left[\left(\frac{\partial \dot{n}_i}{\partial r_{MS}}\right) e_{r_{MS}}\right]^2} \tag{4.6}$$

4.3 Component/Sub-Process Characterization and System Conditioning

Prior to each CHAMP-SORB reactor run, background experiments were conducted to characterize each of the CHAMP-SORB reactor key components and sub-functions (*i.e.*

reactor filling, permeation, adsorption and reaction). The procedures used and results of these experiments are described in detail in the following sections.

4.3.1 Reactor filling

Obtaining a batch of fuel mixture at the target total pressure with the appropriate S/C ratio (for this experiment a 2:1 ratio) is somewhat challenging due to the difference in phase at room temperature between H_2O (liquid) and CH_4 (gas). To accomplish this task, the accumulator was first heated to 200°C and filled with CH_4 at 1/3 of the target pressure. The filling process was comprised of first flowing CH_4 through the accumulator and out the downstream vent with the accumulator piston at minimum displacement (to flush out all non-CH_4 species), then closing the outlet valve and moving the accumulator piston to maximum displacement while opening connection of the accumulator to the pure CH_4 supply line. At this point, the heat tracing on the inlet line ("zone 1" in Figure 4.1) was turned off such that the temperature in the inlet line to the accumulator was approximately 25°C. Simultaneously, the heat tracing in "zone 2" was turned on to heat that portion of the line and outlet valve to 200°C.

After filling the accumulator with CH_4 at 1/3 the final target pressure, valve A was closed, valve B was opened, and the three way valve C was switched to a position such that any liquid water pumped was directed to the vent rather than the accumulator. This process ensured that the line was fully primed with water and that when valve C was subsequently switched to direct flow towards the accumulator, any additional quantity of water pumped by the syringe pump would cause an equal amount of water to enter the accumulator rather than to fill the piping connecting valves B and C. An amount of liquid H_2O corresponding to twice the number of moles of CH_4 in the accumulator (as

determined using the ideal gas equation of state) was then injected into the accumulator with the syringe pump. For a target final pressure of 5 bar with CH_4 in the accumulator initially at 1/3 this pressure, this required an injection of 30 mL liquid water at room temperature. Finally, valve C is closed and power is supplied to the zone 1 heater to vaporize the water. Figure 4.8 illustrates the rise in temperature and pressure (due to water vaporization) as zone 1 is heated to 200°C.

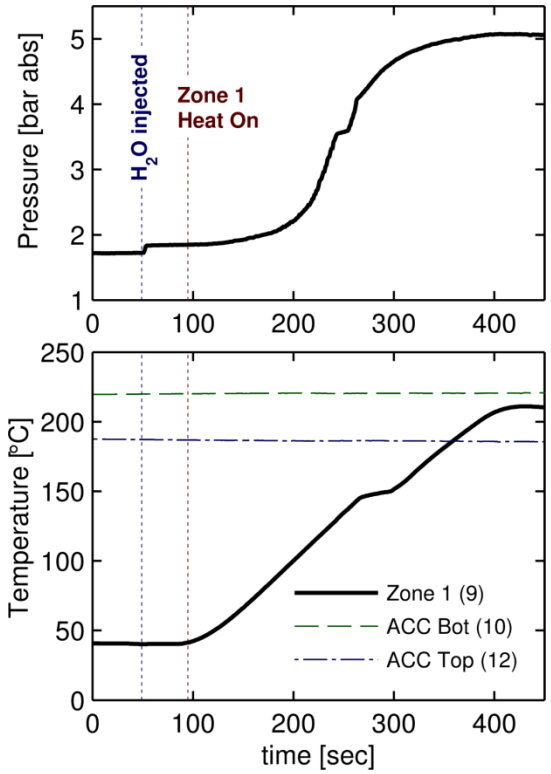

Figure 4.8: Transient response of a) the accumulator pressure, and b) the temperature measurements at "zone 1" and in the top and bottom of the accumulator during the vaporization of the injected liquid water.

The fact that the final pressure in the accumulator did in fact reach 5 bar, a value three times greater than the initial fill pressure of pure CH_4, provides confidence that the S/C ratio in the accumulator after following this filling process is the desired 2:1 value.

To further verify an accuracy of this approach of forming a mixture with a desired S/C ratio, a fraction of the mixture contained in the accumulator was sent to the CHAMP-SORB reactor for a brief (*ca.* 20 *s*) duration and then transmitted to mass spectrometer using the same flushing process outlined in steps (6) – (7) of the full test procedure (section 4.2.2). The CHAMP-SORB reactor was not fitted with any catalyst or sorbent during this experiment, so that the water-methane mixture would remain as supplied (*i.e.*, no change in species due to reaction or adsorption) and the S/C ratio could be tested using the mass spectrometer measurements. The results are presented in Figure 4.9.

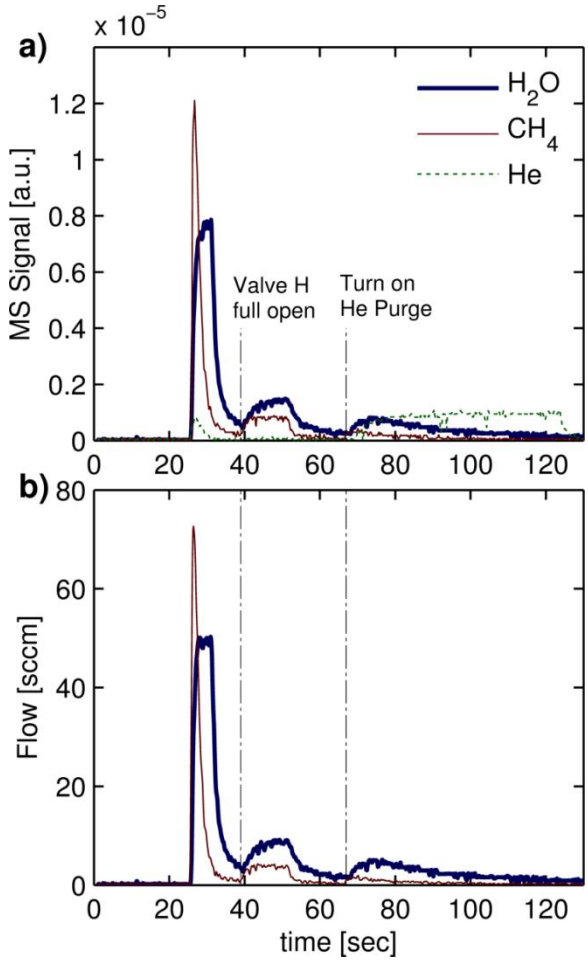

Figure 4.9: a) Measured MS signals and b) calculated H_2O and CH_4 flowrates from experiments designed to verify achievement of target S/C ratio in the accumulator

There is large spike in MS signal of H_2O and CH_4 when the outlet valve (H) is initially cracked due to the difference in pressure between the reactor (initially at $5\ bar$) and the sweep gas line (at atmospheric pressure). This initial spike is followed by two secondary peaks: first, when the outlet valve was fully opened, and secondly when He was swept through the reactor to purge out any contents that remain after pressure equilibration. The calculated CH_4 and H_2O flow rates reported in Figure 4.9 are then integrated in the time domain to determine total number of moles of each species present in the reactor. The potential range of values in the calculation of total moles of CH_4 or H_2O is determined by integration using the high and low bound values, as determined in the previously outlined error propagation analysis. The summary of three separate filling tests, using a single batch of fuel generated in the accumulator (the same batch used in obtaining data shown in Figure 4.8) is reported in Table 4.1. The error bounds on the S/C ratio for each experiment are calculated by integrating the molar flowrates at the high and low end of the tolerance and using these values to calculate the maximum and minimum possible S/C ratio.

Table 4.1: Calculated S/C ratio from fill test

Experiment	**S/C Ratio**	
	Nominal Value	**Uncertainty**
1	2.06 : 1	+/- 0.17
2	2.27 : 1	+/- 0.19
3	2.17 : 1	+/- 0.21
MEAN	**2.17 : 1**	**+/- 0.19**

The calculations in Table 4.1 show some spread in data between three separate reactor filling experiments from the same water-methane mixture batch prepared in the accumulator, with the mean S/C ratio being slightly above the target 2:1 value (2.17:1). However, the target (2:1) S/C ratio falls within the bounds of uncertainty around the experimentally observed mean value, and it is expected that the ratio of partial pressures (as determined using the pressure of pure methane in the accumulator prior to adding liquid water and heating above saturation temperature, along with the final pressure after heating) is a more accurate representation of the true S/C ratio because there is less error in the direct pressure transducer measurement than the error propagation of the indirect mass spectrometer measurement.

4.3.2 Membrane conditioning and permeability characterization

The H_2-selective membrane (Alfa Aesar, $50\ \mu m$ thick, 77% Pd/23% Ag) was conditioned by being wrapped in aluminum foil and heated to 650°C in a furnace for 3 hours prior to installation in the CHAMP-SORB reactor. After conditioning, the membrane was fitted in the CHAMP-SORB reactor, and the reactor was filled with inert He as quickly as possible to minimize exposure to potential contaminants and metal oxidants in the air. The reactor was then heated to the typical operating condition of 400°C filled with inert He at atmospheric pressure. The reactor inlet valve was subsequently opened and exposed to the H_2 tank regulated at $5\ bar$ total pressure, such that an initial gas mixture of four parts H_2 to one part He was achieved in the reactor upon equilibration. Argon sweep gas at a $200\ sccm$ flowrate was sent through the backside of the membrane to maintain a low permeate-side H_2 partial pressure and carry the permeated hydrogen to the mass spectrometer for detection. Once the inlet valve was

closed, the volume was held constant so that no more H_2 could enter the reactor, and as a result the reactor pressure decayed exponentially to a value approaching atmospheric pressure. Figure 4.10 reports the resulting rate of pressure decay observed in 5 separate experiments.

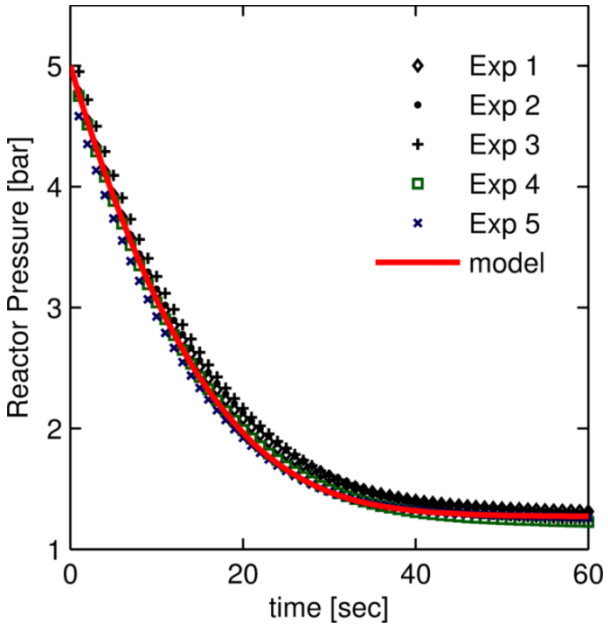

Figure 4.10: Reactor pressure decay as a result of H_2 permeation for 5 separate experiments. Solid line shows the modeled pressure decay rate using Sievert's law for hydrogen permeation using membrane permeance model from McLeod et al.[55]

Also shown in Figure 4.10 is the predicted pressure decay using Sievert's Law and a membrane permeability given by diffusion coefficient of $D_{mem} = 4.1 \times 10^{-5}\, exp\{-1387.9/T\}$ $[mol \cdot m/(m^2 \cdot s \cdot bar^{1/2})]$ as measured by McLeod et al. [55]. The prediction is obtained through the use of equations (4.7) and (4.8), where equation (4.7) relates the rate of pressure drop in the reactor (dP/dt, which is equal to the time rate of change in H_2 partial pressure dP_{H_2}/dt because the number of

moles of inert He remains constant) to the time rate of change in moles of H_2 (dN_{H_2}/dt) and is derived by taking the time derivative of the ideal gas equation of state with temperature T and volume V being held constant.

$$\frac{dP_{H_2}}{dt} = \left(\frac{R_u T}{V}\right)\frac{dN_{H_2}}{dt} \tag{4.7}$$

The time rate of change in number of moles of H_2 in the reactor is modeled using Sievert's Law [75, 76]:

$$\frac{dN_{H_2}}{dt} = -A_c \frac{D_{mem}}{\delta}\left[\left(P_{H_2}\right)^{1/2} - \left(P_{H_2}^{\infty}\right)^{1/2}\right] \tag{4.8}$$

The ordinary differential equation resulting from insertion of the expression for dN_{H_2}/dt back into equation (4.7) is then solved numerically as an initial value problem (with initial condition of $P_{H_2}\big|_{t=0} = 4\,bar$ to match the experimental test conditions). This solution is carried out in MATLAB using the built-in ode45 solver, an explicit Runge-Kutta Dorman-Prince (RKDP) scheme accurate to the order of $O(\Delta t^4)$ [77]. A permeate-side H_2 partial pressure value of $P_{H_2}^{\infty} = 0.1\,bar$ is chosen in the simulations to match the experimentally observed final total pressure in the reactor of approximately $1.1\,bar$ (due to inert He at atmospheric pressure and residual, unpermeated H_2 at $0.1\,bar$). The excellent match in pressure decay rate due to H_2 permeation between the experiments and simulations, with no adjustment or use of empirical factors, displayed in Figure 4.10 validates the applicability of Sievert's law to describe H_2 permeation in the CHAMP-SORB reactor and the use of McLeod et al.'s value of diffusivity as measure for Pd/Ag membrane permeance.

4.3.3 CO_2 adsorbent preparation and performance validation

The CO_2-selective sorbent was prepared by impregnating a base material of Pural MG 70 hydrotalcite (Sasol) with K_2CO_3 (Sigma Aldrich). The resulting sorbent was 78% by weight hydrotalcite, 22% by weight K_2CO_3. A batch of $25\ g$ of sorbent was produced as follows using the incipient wetness procedure [78]:

(1) $19.5\ g$ of Pural MG 70 was spread evenly in a porcelain bowl.
(2) $5.5\ g$ of K_2CO_3 was dissolved in $10\ mL$ of deionized water.
(3) Using a dropper, approximately half of the aqueous K_2CO_3 solution was added to the MG 70 powder and the wet powder was mixed and spread again evenly in the porcelain bowl.
(4) The remainder of the aqueous K_2CO_3 solution was added to the powder and mixed well.
(5) The wet powder was dried overnight in a fume hood at room temperature.
(6) After sitting overnight in a fume hood, the powder was fully dried by placing in an oven at 120°C for 6 hours.
(7) The dried mixture was brought from 120 to 400°C at a $3℃/min$ ramp rate, and then calcined at 400°C for 3 hours.
(8) The calcined sorbent was crushed and sieved to a diameter range of $0.124 - 0.297\ mm$.

To validate that the K_2CO_3-promoted hydrotalcite sorbent would adsorb CO_2 as intended, two experiments were conducted. The first of these was a test similar to the pressure decay experiment described in Section 4.3.2, where a gas mixture at roughly $5\ bar$ total pressure, comprised of an inert gas (in this case Ar) at atmospheric partial pressure with balance CO_2 (as opposed to H_2 in the permeation testing) is introduced into the testbed CHAMP-SORB reactor. For this experiment, the reactor is loaded with $0.25\ g$ of sorbent and heated to 400°C. The reactor is held at a constant volume and the pressure

decay is recorded and used to estimate the rate of CO_2 adsorption (using the ideal gas equation of state). There was a small leak of $0.07\ bar/min$ estimated when the reactor was filled with pure (inert) Ar at $5\ bar$, and measured to be the same rate both before and after the batch adsorption test. As a result, the pressure decay data presented in Figure 4.11 was adjusted for this constant decay rate, assuming that the same leak rate holds when reactor is filled with CO_2/Ar mixture to the same initial pressure. The batch CO_2 uptake experiment was conducted twice to ensure repeatability, and prior to each test the sorbent bed was purged with inert Ar gas for $15\ min$ (at which point no CO_2 was detected in the effluent to the mass spectrometer) to ensure that the sorbent was initially not loaded with any CO_2.

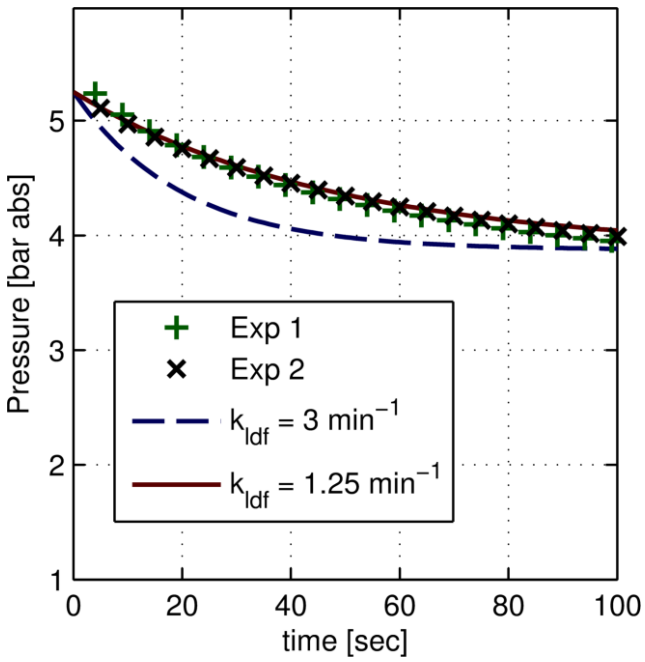

Figure 4.11: Reactor pressure decay during sorption CO_2 uptake – experiments and model predictions using various values of adsorption coefficient in linear driving force model

Also shown in Figure 4.11 are two predicted pressure decay curves for different linear driving force adsorption coefficients (k_{ldf}). Similar to the differential equation used to describe the change in reactor pressure (at constant volume and temperature) during the permeation experiment, according to the ideal gas equation of state the change in pressure during the batch CO_2 uptake experiment is expected to be of the following form:

$$\frac{dP_{CO_2}}{dt} = -\left(\frac{R_u T}{V}\right)\left[m_{sorb}\frac{dq_{CO_2}}{dt}\right] \tag{4.9}$$

For the batch CO_2 uptake experiment, the time rate of change in moles of CO_2 in the reactor is the product of the mass of the sorbent (m_{sorb}) and the time rate of change of CO_2 loaded on the sorbent per unit mass (dq_{CO_2}/dt). The rate of CO_2 adsorption (per unit mass of sorbent) can be modeled using the linear driving force approach:

$$\frac{dq_{CO_2}}{dt} = k_{ldf}\left[q_{eq} - q_{CO_2}\right] \tag{4.10}$$

where q_{CO_2} is the current loading of CO_2 per unit mass of sorbent and q_{eq} is the equilibrium loading of CO_2 at the current temperature and CO_2 partial pressure. At a temperature of 400°C, the linear driving force coefficient for the K_2CO_3-promoted hydrotalcite sorbent reported by Lee et al. is $3\ min^{-1}$ [67]. The relationship between equilibrium CO_2 loading and CO_2 partial pressure is also taken from Lee et al., and the initial value problem with these coupled ordinary differential equations (with an initial pressure $P_{CO_2}\big|_{t=0} = 4.25\ bar$ and initial sorbent loading $q_{CO_2}\big|_{t=0} = 0\ mol/kg$, to match experimental conditions) is again solved numerically in MATLAB using the ode45 RKDP numerical integration routine. The results of this numerical solution, for two possible k_{ldf} values, are shown in Figure 4.11. The reported value in the literature

of 3 min^{-1} overestimates the adsorption rate, but adjusting the linear driving force coefficient to 1.25 min^{-1} provides a match to the experimental data.

Because the measurements of pressure in the batch CO_2 uptake experiment only indirectly measure the CO_2 adsorption rate and are somewhat confounded by the slight leak in the system, a packed bed CO_2 adsorption experiment was also conducted to verify through direct measurement that the sorbent was in fact effective in capturing CO_2. The packed-bed experimental apparatus built for this experiment is illustrated in Figure 4.12.

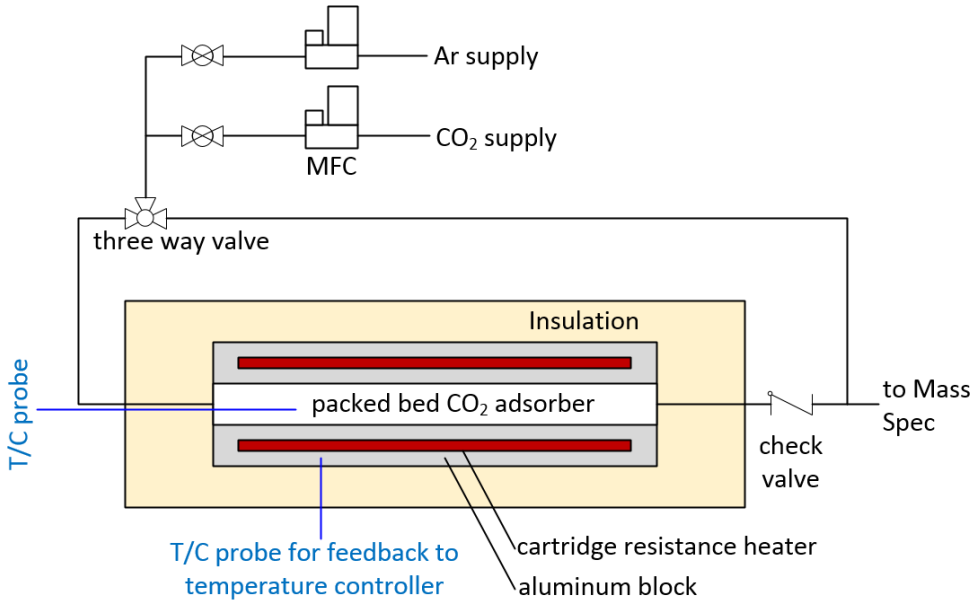

Figure 4.12: Experimental apparatus for packed bed CO_2 uptake experiment

The system consisted of ¼-inch stainless steel tube segment, surrounded by heated aluminum blocks and encased in rigid calcium silicate insulation. The tubular reactor was packed with sorbent and heated to 400°C using the Harrick 24V automatic temperature controller. Using mass flow controllers, a metered mixture of CO_2 (8 $sccm$) in inert Ar sweep gas (30 $sccm$) was first sent directly to the mass spectrometer, bypassing the

reactor, to detect the pure CO_2 MS signal. Once this baseline signal was established, the three way valve was switched such that the CO_2/Ar mixture was diverted to flow through the packed bed adsorber prior to reaching the mass spectrometer. The results of the packed bed CO_2 uptake experiment are shown in Figure 4.13.

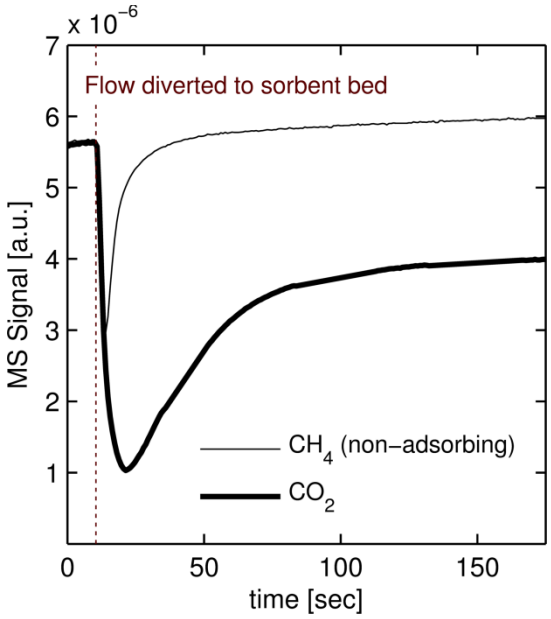

Figure 4.13: Reduction of MS signal of analyte (adsorbing CO_2 or non-adsorbing CH_4) due to flow diversion from bypass to through packed bed adsorber to confirm CO_2 adsorption

As can be seen by the drop in MS Signal for CO_2 once flow is diverted to the sorbent bed, there was a reduction in the relative amount of CO_2 that reached the mass spectrometer. Because the adsorber column is initially filled with inert Ar, the drop in CO_2 signal is partially due to the time required for the flowing CO_2-Ar mixture to displace that pure Ar. To identify how much of the detected reduction in CO_2 signal at the MS was due to the displacement effect, the same test procedure was carried out with a non-adsorbing species (CH_4) at the same $8\ sccm/30\ sccm$ analyte to carrier gas flow

ratio. Figure 4.13 illustrates that, although there was a drop in CH_4 MS signal at the moment of flow diversion to the adsorber bed, this drop was much shorter in duration than the time period during which the CO_2 signal drop is observed. Additionally, the CH_4 signal recovered fully to its pre-diverted value, while the CO_2 signal remained at approximately 2/3 of its initial value. The fact that the CO_2 signal did not fully vanish (i.e., indicative of complete CO_2 adsorption) after flowing through the packed bed column is likely because there was insufficient residence time in the reactor for complete adsorption; this is supported by the fact that the residence time (estimated to be *ca.* $25\ s$, as indicated by the duration of the drop in the MS signal of non-adsorbing CH_4 in Figure 4.13) is approximately half the intrinsic adsorption timescale ($\tau_{ads,intrinsic} \sim 1/k_{ldf}$, or $48\ s$ using the estimated k_{ldf} of $1.25\ min^{-1}$ from the batch adsorption experiment). Regardless of the incomplete adsorption, the experiment was successful in that its purpose was to obtain a direct, but strictly qualitative, confirmation that CO_2 was indeed being adsorbed (as opposed to the indirect pressure decay measurements obtained in the batch CO_2 uptake experiments).

4.3.4 Catalyst reduction and activity verification

The nickel on calcium aluminate catalyst (Alfa Aesar, HiFuel R110) is supplied in oxidized form, and prior to use in the CHAMP-SORB reactor must be reduced to convert the surface NiO to Ni. The supplier instructions state that the catalyst should be exposed to dry hydrogen at 600°C for a minimum of two hours. Because the CHAMP-SORB reactor, as designed for laboratory experiments, cannot reach a temperature this high (in order to maintain integrity of the seal material), the reduction procedure was carried out in the packed bed reactor as introduced in Figure 4.12. In this case, pure H_2 metered by a

mass flow controller was flowed through reactor filled this time with crushed catalyst as opposed to sorbent. Two means of verifying the reduction process were employed: 1) the catalyst temperature was monitored using a K-type thermocouple to look for a temperature rise due to initiation of the exothermic reduction process, and 2) the effluent of the packed bed was monitored for H_2O content (as H_2O will be the product of the reduction of NiO to Ni in the presence of dry H_2).

Figure 4.14 reports the time evolution of temperature and MS signal measurements obtained during the catalyst reduction procedure. When the H_2 flow was turned on, approximately $30\ s$ into data collection, both H_2 and H_2O were detected by the mass spectrometer. Simultaneously, the catalyst temperature rose from 600 to 608°C and the required output from the Harrick temperature controller to maintain the aluminum heater block at a constant value of 600°C was reduced by several percent (due to the heat generation from the exothermic catalyst reduction reaction).

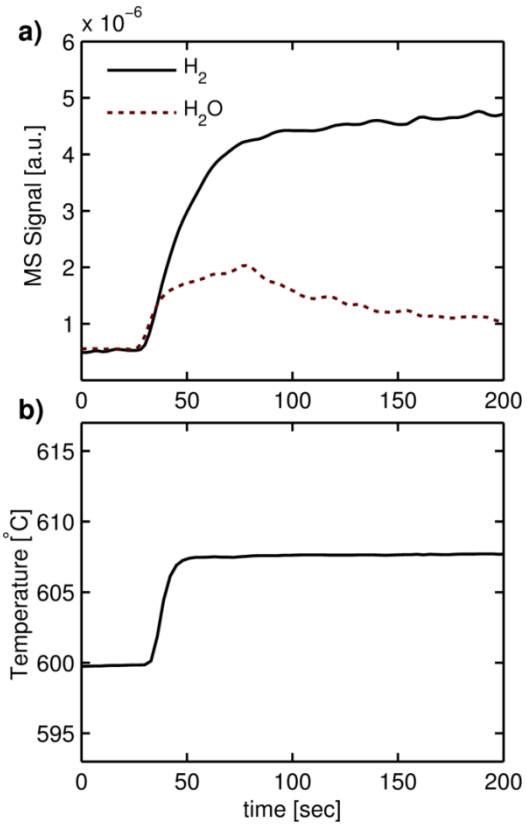

Figure 4.14: Measurements of a) effluent mass spectrometer signal and b) catalyst temperature during the catalyst reduction procedure. The presence of H_2O in the effluent and the rise in temperature (due to exothermic metal oxide reduction reaction) are the markers confirming successful reduction and activation of the catalyst.

Although not shown in Figure 4.14, the catalyst reduction was carried out for four hours, twice as long as the minimum duration specified by the supplier. Periodically during the reduction, the H_2 flow was shut off and each time the temperature measured in the catalyst gradually dropped to 600°C, then rose back to near 610°C when the H_2 flow was resumed. Once the reduction was complete, the second experiment was conducted to verify catalyst activity by first flushing the reactor with Ar, then replacing the H_2 feed with CH_4 and steam in a 2:1 S/C mass flow ratio, with water supplied through a syringe pump and evaporator to the packed bed reactor inlet. The results of this experiment, illustrated in Figure 4.15, confirm that all the expected products of the SMR process (H_2,

CO_2 and CO) are present in the effluent of the reactor. Similar to the packed bed adsorption experiment, the purpose of this test was to qualitatively confirm the occurrence of SMR (as opposed to a detailed characterization of the kinetics).

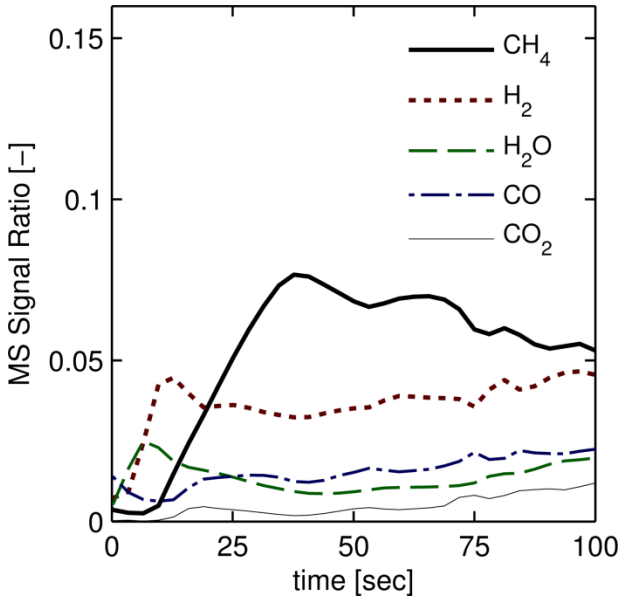

Figure 4.15: Packed bed reactor effluent with a 2:1 S/C ratio H_2O:CH_4 feed after catalyst reduction, confirming the presence of the expected products of the SMR process (H_2, CO_2, and CO).

4.4 Full CHAMP-SORB Reactor Performance

With the reactor sub-functions validated and materials conditioned and characterized, the following procedure was carried out to demonstrate the reaction/adsorption/ permeation step of the CHAMP-SORB reactor:

(1) With the CHAMP-SORB reactor at minimum volume and purged with inert He gas, the inlet valve was opened to send the H_2O and CH_4 fuel mixture in a 2:1 ratio to the reactor.
(2) The reactor was filled by moving the piston from minimum to maximum displacement, then the inlet valve was closed and the reaction/adsorption/permeation processes begin to occur.
(3) As the number of moles decreased in the reactor due to hydrogen permeation and carbon dioxide adsorption, the reactor volume was compressed by moving the piston downward to maintain constant pressure using closed loop feedback control, while the mass spectrometer continuously measured the rate of hydrogen permeation across the membrane.
(4) Once the hydrogen yield rate decreased to a negligible level, the outlet valve was slowly opened to send the non-permeated contents inside the CHAMP-SORB reactor to the mass spectrometer.
(5) After approximately $30\ s$, the inlet valve was opened (while keeping the outlet valve open) to send $15\ sccm$ of purge He to flush out remaining reactor contents into the mass spectrometer.

Results of a representative CHAMP-SORB experiment with the reactor loaded with $0.1\ g$ of catalyst and $0.25\ g$ of sorbent and operated at a nominal temperature of 400°C, pressure of $5\ bar$, and S/C ratio of 2:1 are reported in Figure 4.16. The corresponding steps from the test procedure are marked at the time at which they occur. During step (3), only H_2 was detected by the mass spectrometer because the reactor outlet valve was closed and only hydrogen can permeate across the membrane. When the outlet valve was opened, the mixture content of the reactor was sent to the mass spectrometer, providing a snapshot of the reactor contents at the end of the experiment. Figure 4.16a shows that when the outlet valve was opened at step (4), the reactor contained predominately CO_2 combined with some unreacted CH_4/H_2O and non-permeated H_2.

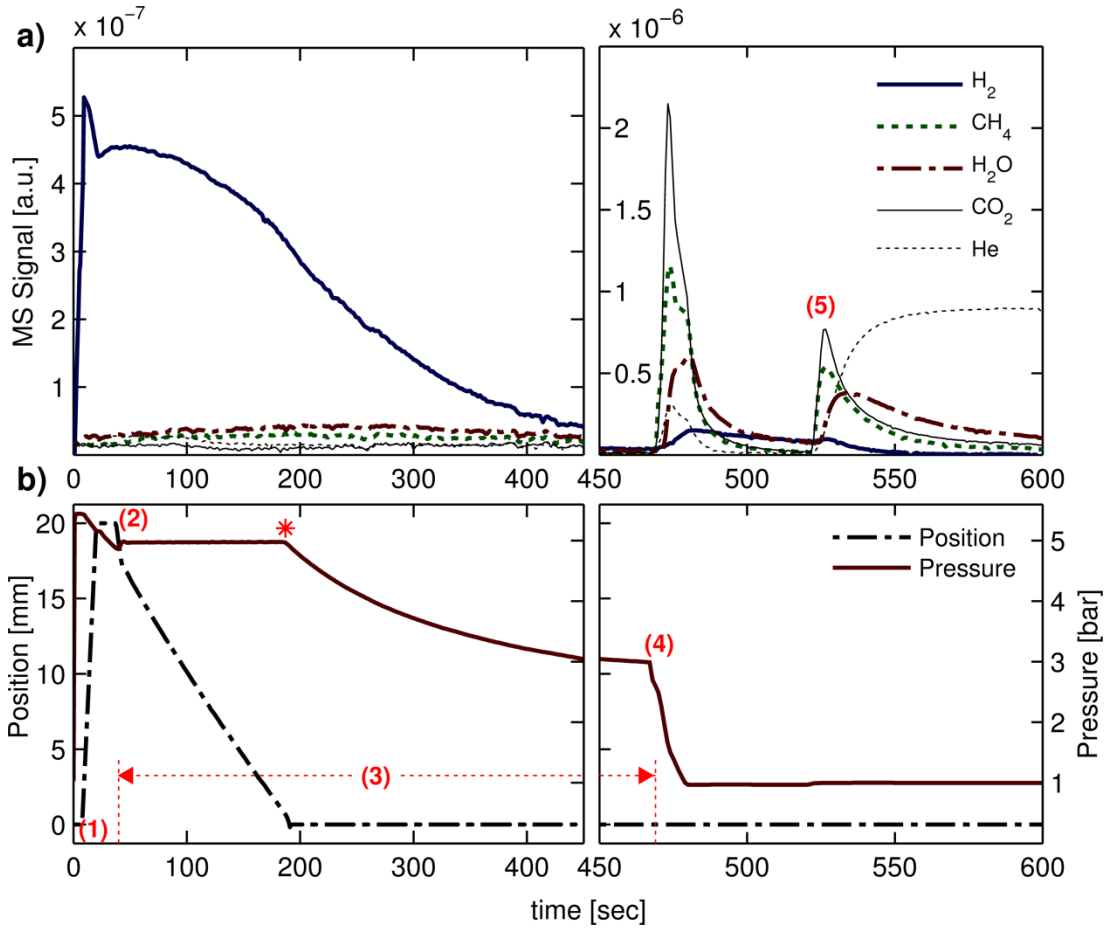

Figure 4.16: CHAMP-SORB testbed experimental results for a) effluent composition as measured by mass spectrometer (MS), and b) piston position and pressure. The asterisk in b) denotes the time at which the piston reached the top of the catalyst/sorbent bed, corresponding to the minimum (dead) reactor volume, and could no longer move to maintain constant pressure, and the steps labeled (1)-(5) indicate process steps described in the text. Note the change in y-axis scale on the top panels and the change in x-axis scale on the right panels (to better show the effluent MS signals).

The pressure evolution and piston position curves of Figure 4.16b illustrate one of the experimental limitations of the CHAMP-SORB testbed: presence of a substantial dead volume (as reported earlier, 45% of the volume at maximum reactor piston displacement). The closed-loop pressure control can reliably maintain the reactor at 5 bar for the first half of step (3), at which point the piston reached its minimum displacement

(marked by an asterisk on Figure 4.16b). The system volume is non-zero at this point, however, because of the valve volume and the void volume in the packed catalyst/sorbent bed. From this point onward, the pressure drops in the system as H_2 continues to permeate out of the reactor and no further compression can be applied.

Figure 4.17 reports the H_2 MS signal for three separate constant pressure CHAMP-SORB experiments. The same qualitative behavior is evident in all three experiments; the H_2 permeation rate remains elevated initially while the reactor can sustain constant pressure, until it tapers off when no more working volume is available in the system (at approximately $t = 150\ s$). Also shown in Figure 4.17 is a constant volume experiment for comparison, where the piston of the CHAMP-SORB reactor is fixed for the duration of the fuel batch residence time. Without compression provided during the beginning of the process, the permeation rate begins to decay immediately as pressure drops in the reactor and a reduction in reactor performance is clearly evident.

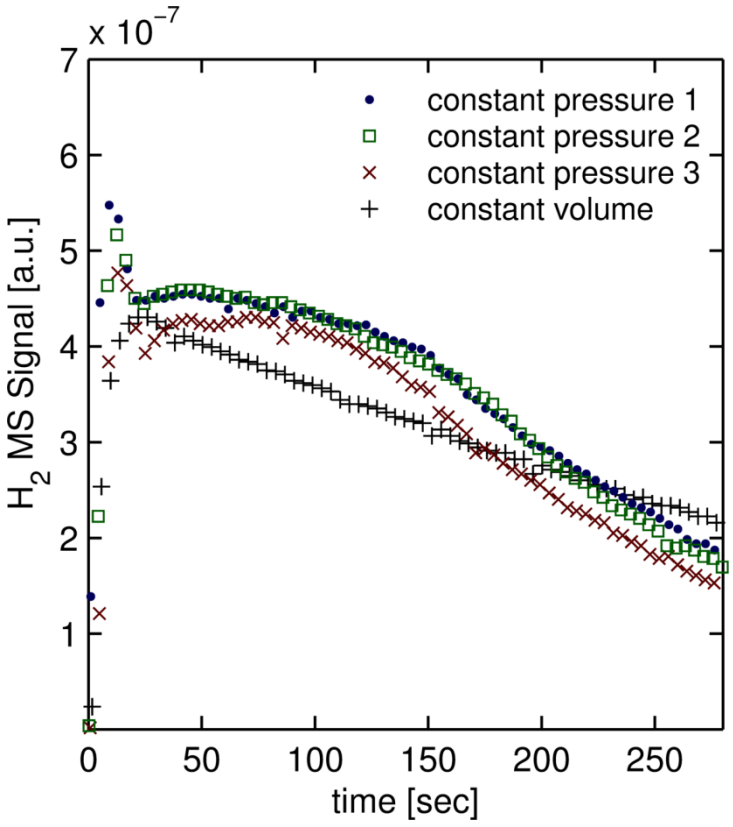

Figure 4.17: CHAMP-SORB experimental results showing reactor effluent H_2 MS signal for multiple constant pressure experiments, contrasted with the H_2 MS signal for a constant volume operation mode.

4.5 Conclusions

The experimental work presented in this chapter demonstrated that the SMR process can be accomplished by CHAMP-SORB reactor at temperatures as low as 400°C and at the stoichiometric 2:1 S/C ratio. Key findings of the experiments presented in this chapter are as follows:

- Experiments isolating individual sub-processes (i.e., H_2 membrane permeation, CO_2 adsorption kinetics, etc.) validated each respective sub-process model with minimal adjustment of material constants, which will have enabled a comprehensive kinetics and kinetics-transport modeling of

CHAMP-SORB reactor developed in Chapters 5 and 6 with minimum empiricism.

- No reduction in membrane permeation due to CO poisoning or material degradation was observed, as confirmed by comparison of pure H_2 permeation rates before and after several operating cycles; however long term membrane cyclic stability have not been assessed and should be a investigated in a separate study under conditions relevant to a specific practical implementation of CHAMP-SORB.
- No diminishment of catalytic activity due to coking or re-oxidation was observed over the course of multiple operating cycles, as indicated by the favorable comparison in performance between successive experiments. This is in agreement with a thermodynamic prediction of CHAMP-SORB's expected operation outside of the coking threshold, as substantiated in Chapter 2.
- Measurements of the effluent of the reactor (in the absence of any catalyst/sorbent) confirmed the operating robustness of the devised reactant "dosing" process , which can consistently fill the reactor at a precise S/C ratio (within the resolution limits of the mass spectrometer).
- The constant pressure mode of operation, demonstrated to be favorable in the baseline CHAMP-class of reactor that employed H_2 membrane separation only, has been shown to be even more important with the addition of CO_2 adsorption, as it is needed to sustain the driving force for adsorption and H_2 permeation.

The testbed limitations, namely the inability to reach near-complete CH_4 conversion and H_2 yield efficiency due to a substantial dead volume of the prototype reactor and a presence of the small, but non-negligible leak developed in the course of experiments, prevented collection of comprehensive performance data (e.g., fuel conversion and hydrogen production) for a broad range of operating conditions. Nevertheless, the detailed measurements of H_2 yield rate, reactor volume and pressure as function of time

provide fundamental information on the CHAMP-SORB behavior and are used in validation of the theoretical kinetic model developed next in Chapter 5.

CHAPTER 5

IDEAL KINETIC MODEL AND TIMESCALE ANALYSIS

In this chapter, an ideal reactor kinetic model is developed to establish basic understanding and quantify interactions among the key processes involved in the CHAMP-SORB reactor (*i.e.* reaction, permeation, and adsorption) in the limit of infinitely fast heat and mass transfer in the reactor bulk and porous catalyst/sorbent bed. The experimental data reported in the previous chapter is next used to establish validity of the ideal kinetic model. Lastly, timescale analysis is introduced and used in concert with the validated ideal kinetic model to better understand the impact of the rates of the individual reaction, permeation, and adsorption processes on the overall CHAMP-SORB system. This timescale analysis is used to identify the rate-limiting step for different reactor operational regimes and to assess the impact of operating variables, particularly reaction temperature and permeate side hydrogen partial pressure, on the CHAMP-SORB performance.

5.1 Model Development

Despite the significant simplifications made in a kinetic-only model which ignores heat and mass transfer limitations, it will be shown that the model appropriately captures the dominant chemical processes in the bench-scale reactor under the experimental operating conditions utilized in Chapter 4 and as such provides substantial insight into the performance of practical CHAMP-SORB systems. The following simplifying assumptions are made: (*i*) spatially uniform species concentration, (*ii*) isothermal conditions, and (*iii*) negligible intra-particle diffusion limitations (catalyst effectiveness

factor [79] of unity). The limits on the validity of the first two assumptions can be established by comparing the mass diffusion and thermal transport timescale ($H_0^2/\ D_{eff}$ and H_0^2/α_{eff}, respectively) to the reaction, adsorption and permeation timescales, which can be identified with help of the purely kinetic reaction-adsorption-permeation model. The negligible intra-particle diffusion assumption is justified through the use of small catalyst particles, as discussed in the previous chapter. Use of these very small, tightly packed particles is more viable in a CHAMP batch-type of reactors, as compared to a continuous flow arrangement, because viscous pressure drop due to flow is not as great of a concern for a batch mode of operation.

Figure 5.1 illustrates the control volume used in developing the ideal kinetic CHAMP-SORB model and highlights some of the relevant dimensions, including the membrane thickness (δ), catalyst/sorbent layer thickness (d), time varying reactor height ($H(t)$, defined as the distance from the top of the catalyst/sorbent layer to the bottom of the piston), and the membrane permeate side partial pressure of hydrogen ($P_{H_2}^{\infty}$). Because the CHAMP-SORB system is modeled as ideal, there are no internal transport limitations and the reactor total pressure (P_T), temperature (T), and mole fractions for all species j (x_j) are treated as spatially uniform.

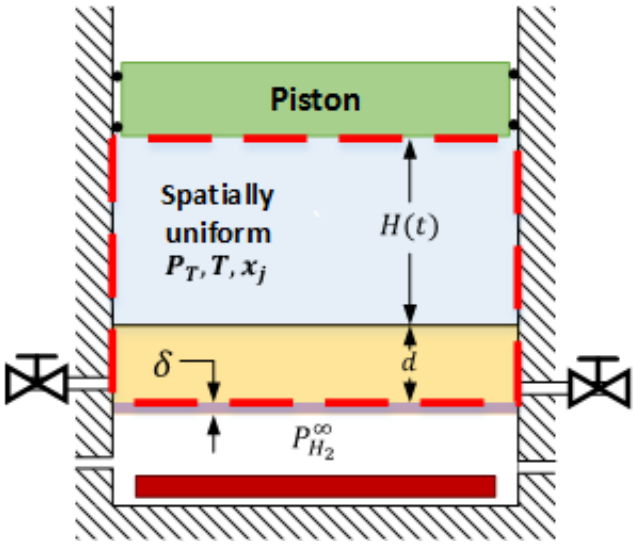

Figure 5.1: Schematic of control volume and dimensions for kinetic CHAMP-SORB model

5.1.1 Governing equations

For the control volume outlined in Figure 5.1, a species conservation equation can be written for each of the species present in the reactor (CH_4, H_2O, H_2, CO_2, CO).

$$\frac{dN_j}{dt} = \overline{\rho} dA_c \phi \sum_{i=1}^{3} \nu_{ij} r_i - \frac{dN_{j,perm}}{dt} - \overline{\rho} dA_c (1-\phi) \frac{dq_j}{dt} \tag{5.1}$$

where A_c is the cross-sectional area of the reactor, dN_j/dt is the time-rate of change of the number of moles of species j inside the reactor, $dN_{j,perm}/dt$ is the permeation rate of species j (non-zero only for j = H_2), and dq_j/dt is the rate of adsorption of species j per unit mass of sorbent (non-zero only for j = CO_2). The generation of species j due to reaction, the first term on the right side of equation (5.1), is the catalyst mass ($\overline{\rho} A_c d\phi$, where $\overline{\rho}$ is the average density of the sorbent/catalyst mixture and ϕ is the ratio of catalyst mass to total sorbent + catalyst mass) multiplied by the summation of the production rates for that species per unit catalyst mass. The mass-averaged density of the

sorbent/catalyst bed is calculated using the weighted harmonic mean, or $\overline{\rho} = [\phi/\rho_c + (1-\phi)/\rho_s]^{-1}$, of the individual component densities. The production rate term, $\nu_{ij} r_i$, is sum of products of the stoichiometric coefficient of species j for a given reaction i (ν_{ij}) and the per-unit-mass rate of that reaction (r_i). Reaction rates are calculated as functions of temperature and species concentration according to the kinetic model of Xu and Froment [28].

The molar permeation rate of hydrogen ($dN_{H_2,perm}/dt$) is modeled according to Sievert's Law [75]. The temperature-dependent membrane permeability is $D_{mem} = 4.1 \times 10^{-6}\, exp\{-1387.9/T\}$ $[mol \cdot m/(m^2 \cdot s \cdot bar^{1/2})]$, a value determined in a previous study [18] and validated in membrane characterization experiments (as discussed in Section 4.3.2). Carbon monoxide formation is suppressed by the CHAMP-SORB via a combination of continual CO_2 removal and the forward water gas shift reaction, leading to only trace quantities of CO in the reactor. As such, the rate of H_2 permeation from the reactor is unadjusted from Sievert's Law:

$$\frac{dN_{H_2,perm}}{dt} = A_c \frac{D_{mem}}{\delta}\left[\left(x_{H_2} P_T\right)^{1/2} - \left(P_{H_2}^{\infty}\right)^{1/2}\right] \tag{5.2}$$

The time rate of change of CO_2 adsorbed per unit of sorbent mass (dq_{CO_2}/dt) is the product of the temperature-dependent linear driving force coefficient (k_{ldf}) [80] and the driving difference between the sorbent equilibrium capacity (q_{eq}), which is a function of both temperature and CO_2 partial pressure, and the instantaneous amount of CO_2 adsorbed (q_{CO2}). The equilibrium capacity and linear driving force coefficient are taken from values reported in Lee, et al. [67].

$$\frac{dq_{CO_2}}{dt} = k_{ldf}\left[q_{eq} - q_{CO_2}\right] \tag{5.3}$$

The reaction rates are a function of pressure, which can be determined by the ideal gas equation of state, as a function of the total number of moles in the gas phase (summed over all N_s chemical species in the reactor), reactor temperature, piston position $H(t)$ defining the reactor extent above the catalyst/sorbent bed (as illustrated in Figure 5.1), the universal gas constant (R_u), and the reactor system dead volume (V_d):

$$P_T = \left[\frac{R_u T}{A_c H(t) + V_d}\right]\sum_{j=1}^{N_s} N_j \tag{5.4}$$

At a minimum, the dead volume is the space occupied by the porous voids in the catalyst/sorbent bed ($\bar{\varepsilon} A_c d$), however it can be greater due to volume occupied by valves/piping. Previous CHAMP studies have investigated various piston velocity profiles and determined that moving the piston in such a manner that the reactor pressure is held constant at the maximum allowable value (*e.g.*, an appropriate safety factor below membrane burst pressure) is the optimal operating mode [18]. The piston velocity (dH/dt) required to maintain constant pressure can also be determined by rearranging equation (5.4) and taking the time derivative (while holding T and P_T constant):

$$\frac{dH}{dt} = \left[\frac{R_u T}{A_c P_T}\right]\sum_{j=1}^{N_s} \frac{dN_j}{dt} \tag{5.5}$$

The solution of equations (5.1) – (5.5) is carried out in MATLAB using the ode15s routine, an implicit variable order differential equation solver with adaptive time stepping. This method is well suited for stiff systems of equations, which occur in the CHAMP-SORB due to the singularities created in the SMR kinetics when the partial pressure of H_2 approaches zero. During the simulation, the piston is moved according to

equation (5.5) to maintain constant total pressure as the number of moles of gas species in the reactor changes (due reaction, adsorption, and permeation), except when the piston reaches the sorbent/catalyst layer and further compression is not possible. When the piston reaches this position, its velocity is set to zero ($dH/dt = 0$) and the subsequent drop in reactor pressure is modeled according to equation (5.4). For properly designed reactor, reaching a state where there is no remaining working volume for compression should happen at or near the end of completion of the SMR reaction step, because both of the primary products of the SMR reaction (H_2 and CO_2) are being continually removed from the gas phase of the reactor leaving little gas to occupy the remaining reactor volume and necessitating maximum compression to maintain the target operating pressure.

5.1.2 Reaction kinetic model

The kinetic model proposed by Xu and Froment [28] is used to model the chemical reaction rates of the reverse methanation, water gas shift, and overall steam methane reforming reactions. The rate of reaction i is a function of the partial pressure of each species j in the reactor (P_j), the equilibrium constants for that reaction (K_i where $i = RM\ , WGS\ or\ SMR$), and of the adsorption equilibrium constant of each species j onto the catalyst surface (K_j where $j = CO, H_2, CH_4\ or\ H_2O$). The rate expressions for the three reactions are given in Table 5.1.

Table 5.1: Kinetic Rate Expressions for the SMR Process [28]

Reaction	Rate Expression $[mol/kg \cdot hr]$	Equilibrium Constant
$CH_4 + H_2O \rightleftharpoons 3H_2 + CO$	$r_{RM} = \frac{k_{RM}/P_{H_2}^{2.5}\left(P_{CH_4}P_{H_2O} - P_{H_2}^3 P_{CO}/K_{RM}\right)}{1 + K_{CO}P_{CO} + K_{H_2}P_{H_2} + K_{CH_4}P_{CH_4} + K_{H_2O}P_{H_2O}/P_{H_2}}$	$K_{RM} = exp\left\{30.11 - \frac{26{,}830}{T}\right\} \times 10^{-2}\ [bar^2]$
$CO + H_2O \rightleftharpoons H_2 + CO_2$	$r_{WGS} = \frac{k_{WGS}/P_{H_2}\left(P_{CO}P_{H_2O} - P_{H_2}P_{CO_2}/K_{WGS}\right)}{1 + K_{CO}P_{CO} + K_{H_2}P_{H_2} + K_{CH_4}P_{CH_4} + K_{H_2O}P_{H_2O}/P_{H_2}}$	$K_{WGS} = exp\left\{-4.036 - \frac{4{,}400}{T}\right\}\ [-]$
$CH_4 + 2H_2O \rightleftharpoons 4H_2 + CO_2$	$r_{SMR} = \frac{k_{SMR}/P_{H_2}^{3.5}\left(P_{CH_4}P_{H_2O}^2 - P_{H_2}^4 P_{CO_2}/K_{SMR}\right)}{1 + K_{CO}P_{CO} + K_{H_2}P_{H_2} + K_{CH_4}P_{CH_4} + K_{H_2O}P_{H_2O}/P_{H_2}}$	$K_{SMR} = K_{RM}K_{WGS}$

To avoid singularities in the rate expression, any time the partial pressure of H_2 in the reactor is below a minimum value of $P_{H_2,min} = 0.001\ bar$ during a reactor simulation, that minimum value is utilized (as opposed to $P_{H_2} = 0\ bar$) in calculating the rates r_{RM}, r_{WGS} and r_{SMR}. This is only necessary during the initial several milliseconds of the reactor simulation, where the reactor initially contains pure fuel (and no H_2).

The adsorption equilibrium constant for species j (K_j) is of the form $K_j = K_j^0 exp\{\Delta H_j/R_u T\}$, where K_j^0 is the pre-exponential factor and ΔH_j is the heat of chemisorption of species j onto the catalyst surface. The rate constant for reaction i (k_i) follows the form of the Arrhenius expression $k_i = k_i^0 exp\{E_{a,i}/R_u T\}$, where k_i^0 is the pre-exponential factor and $E_{a,i}$ is the activation energy of reaction i. The values of these parameters are given by Xu and Froment and are listed in Table 5.2.

Table 5.2: Kinetic Parameters for the SMR Process [28]

Parameter	Pre-Exponential Term k_i^0 or K_j^0	Activation Energy ($E_{a,i}$) or Heat of Chemisorption (ΔH_j)
k_{RM}	4.225×10^{18} $[mol \cdot bar^{1/2}/kg_{cat} \cdot hr]$	240.1 $[kJ/mol]$
k_{WGS}	1.955×10^{9} $[mol/kg_{cat} \cdot hr \cdot bar]$	67.13 $[kJ/mol]$
k_{SMR}	1.020×10^{18} $[mol \cdot bar^{1/2}/kg_{cat} \cdot hr]$	243.9 $[kJ/mol]$
K_{CO}	8.23×10^{-5} $[bar^{-1}]$	-70.65 $[kJ/mol]$
K_{H_2}	6.12×10^{-9} $[bar^{-1}]$	-80.29 $[kJ/mol]$
K_{CH_4}	6.65×10^{-4} $[bar^{-1}]$	38.28 $[kJ/mol]$
K_{H_2O}	1.77×10^{-5} $[-]$	88.68 $[kJ/mol]$

5.1.3 Sorbent equilibrium isotherm and kinetic models

The equilibrium and kinetic data of Lee et al. [67] is used for the adsorption model, as opposed to other studies on K_2CO_3-promoted hydrotalcite reported in the literature, because their work is the only study that measured the CO_2 adsorption isotherm up to the high CO_2 partial pressure range expected to be encountered during CHAMP-SORB operation [81]. According to the model proposed by Lee, CO_2 can be adsorbed to the surface of K_2CO_3-promoted hydrotalcite in two ways: (1) chemisorbed directly on a surface (S) site forming ($CO_2 - S$), or (2) as a surface complex (where a molecules of CO_2 in gas phase react with the chemisorbed CO_2 molecule to form a surface complex of the form $(CO_2)_{a+1}$):

$$CO_2(gas) + S \rightleftharpoons CO_2 - S \tag{5.6}$$

$$aCO_2(gas) + CO_2 - S \rightleftharpoons (CO_2)_{a+1} - S \tag{5.7}$$

This adsorption model results in an equilibrium isotherm describing the CO_2 adsorption capacity (q_{eq}) as a function of temperature (T) and CO_2 partial pressure (P_{CO_2}) of the form:

$$q_{eq}\left(P_{CO_2}, T\right) = \frac{mK_C P_{CO_2}\left[1 + (a+1)K_R P_{CO_2}^{a}\right]}{\left[1 + K_C P_{CO_2} + K_C K_R P_{CO_2}^{(a+1)}\right]} \tag{5.8}$$

where K_C (units $[bar^{-1}]$) and K_R (units $[bar^{-a}]$) are the equilibrium constants of the chemisorption (5.6) and chemical complexation (5.7) reactions, respectively, and m (units $[mol/kg]$) is the capacity of moles per unit mass available for chemisorbed CO_2 on the sorbent material. As such the maximum possible loading of CO_2 on the sorbent (in the limit of $P_{CO_2} \to \infty$) is $m(a+1)$ mol/kg. The rate at which the sorbent's specific CO_2 loading (q_{CO_2}) approaches the equilibrium value given by equation (5.8) is estimated using a linear driving force approach [80], where the rate of adsorption is directly proportional to the difference between equilibrium and instantaneous CO_2 loading at that point in time, as indicated by equation (4.10) in Section 4.3.3. The parameters K_C, K_R, a and k_{ldf} have an exponential dependence on the inverse of temperature of the form $y = y^0 exp\{\Delta E_y / R_u T\}$. Value of the pre-exponential factor (y^0) and activation parameter (ΔE_y) for K_C and K_R are given explicitly by Lee et al. The value of these parameters for a and k_{LDF} are estimated by fitting a line for $\ln\{a\}$ or $\ln\{k_{ldf}\}$ versus $1/T$ between data points given at two temperatures ($a = 2.5$, $k_{ldf} = 3\ min^{-1}$ at $T = 673K$, and $a = 1.8$, $k_{ldf} = 5\ min^{-1}$ at $T = 793K$). Determination of these parameters, listed in Table 5.3, allows for implementation of the adsorption model at temperatures other than the two values explicitly listed in Lee et al. [29, 67].

Table 5.3: Pre-Exponential Factor and Activation Parameter for K_2CO_3-Promoted Hydrotalcite Adsorption Model [29, 67]

Parameter	Parameter Expression	Pre-Exponential Factor	Activation Parameter
$K_C\ [bar^{-1}]$	$K_C = K_C^0 exp\{q_C/R_u T\}$	$K_C^0 = 0.8665\ [bar^{-1}]$	$q_C = 21.0\ [kJ/mol]$
$K_R\ [bar^{-a}]$	$K_R = K_R^0 exp\{\Delta H_R/R_u T\}$	$K_R^0 = 1.30 \times 10^{-3} [bar^{-a}]$	$\Delta H_R = 42.2\ [kJ/mol]$
$a\ [-]$	$a = a^0 exp\{\Delta E_a/R_u T\}$	$a^0 = 0.2821$	$\Delta E_a = 12.21\ [kJ/mol]$
$k_{ldf}\ [min^{-1}]$	$k_{ldf} = k_{ldf}^0 exp\{\Delta E_k/R_u T\}$	$k_{ldf}^0 = 87.4\ [min^{-1}]$	$\Delta E_k = -18.85\ [kJ/mol]$

5.2 Validation with Experimental Data

Figure 5.2 reports the comparison between experiment data and simulation results for the baseline case ($T = 400$℃, $P_T = 5\ bar$, $H_0 = 2\ cm$, $d = 1\ mm$). The molar H_2 flowrate reported in Figure 5.2a is calculated from the MS signal measurements from Figure 4.16a using the calibration function between metered H_2 and Ar flowrates and measured H_2/Ar MS signals reported in Figure 4.6. Error bars are calculated using a standard error propagation approach as discussed in Section 4.2.1.

For model validation simulations, the initial conditions are chosen to match the initial state during the experimental test procedure. In the experiment, the reactor is swept first with inert helium at atmospheric pressure with the piston fully down (minimum reactor volume). The reactor is then filled with H_2O/CH_4 from the accumulator while the piston moves from minimum to maximum displacement and the equilibrated accumulator/reactor pressure reaches the target initial pressure. The corresponding initial condition for simulations is that an initial quantity of $7.855 \times 10^{-4}\ moles$ is present in the reactor, with initial mole fractions of $x_{He}\big|_{t=0} = 0.090$, $x_{CH_4}\big|_{t=0} = 0.303$, and $x_{H_2O}\big|_{t=0} = 0.607$.

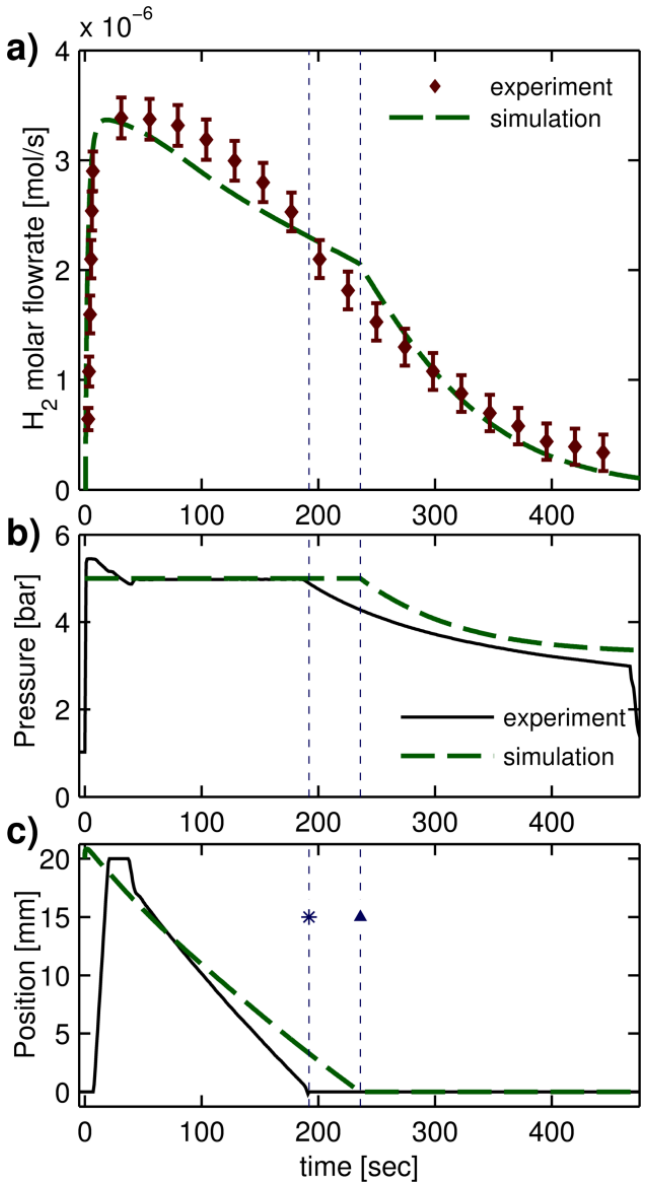

Figure 5.2: Model validation with experimental data, comparing a) H_2 molar flowrate from the reactor, *i.e.* H_2 yield rate, b) reactor total pressure and c) piston position. The time at which the piston reaches minimum displacement is marked with a vertical line (denoted by an asterisk or triangle for the experiment and simulation, respectively).

These initial condition values are determined by first calculating the total number of moles of fuel contained in the reactor at $5\ bar$ and 400°C at the maximum reactor volume ($8.79\ cm^3$) using the ideal gas equation of state, as well as the number of moles

of He contained in the reactor dead volume ($3.97\ cm^3$) at $1\ bar$ prior to filling with H_2O/CH_4 fuel. The ratio of these values is the initial mole fraction of He in the reactor, and the remainder is split between H_2O and CH_4 in a 2:1 ratio. A constant membrane permeate side H_2 partial pressure ($P_{H_2}^{\infty}$) of $0.2\ bar$ is utilized in the simulation, a value that is consistent with the average H_2 concentration in the sweep gas stream during the CHAMP-SORB baseline experiment. The model simulation utilizes the experimentally determined dead volume when determining pressure via equation (5.4).

As shown in Figure 5.2, the model accurately predicts the H_2 yield rate, reactor pressure, and piston trajectory as function of process time. The piston does reach its minimum volume position earlier in the experiment (marked by an asterisk in Figure 5.2) than is predicted by the model (marked by a triangle) due to a slow leak that was observed in the reactor (corresponding to an average $0.07\ bar/min$ drop in the reactor pressure in the absence of reactions and permeation). Both qualitative and quantitative agreement is observed in the shape of the H_2 yield rate evolution curve between experiments and simulations with several distinct features that can be related to the physics of the process: (1) prior to reaching the minimum volume compression helps prevent the H_2 yield rate from rapid drop, and (2) after the reactor volume can no longer be compressed, inflection point is observed, after which the H_2 yield rate decays exponentially.

5.3 Model Results and Discussion

Having validated the ideal kinetic CHAMP-SORB reactor model through its comparison with the experimental results, the model is next used to assess the impact of catalyst to sorbent mass ratio on the overall reactor system performance and to gain

insight into how the CHAMP-SORB reactor performance differs from that of the original CHAMP embodiment with only H_2 membrane separation.

5.3.1 Optimal catalyst to sorbent ratio

A series of simulations is performed with varying catalyst mass fraction ($\phi = m_{cat}/[m_{cat} + m_{sorb}]$) at a reaction temperature of 400°C, initial pressure of $5\ bar$, permeate side H_2 partial pressure of $0.2\ bar$, and a feed S/C ratio of 2:1 (no other species initially present). Because it is not possible to fully regenerate the sorbent during cyclic operation [81], an initial CO_2 loading of $0.25\ mol/kg$ is applied to the sorbent (corresponding to roughly 30% of the saturation loading of the sorbent). The height of the catalyst/sorbent bed is $1\ mm$, corresponding to 1/20 of the initial height of the reactor ($2\ cm$, to be consistent with the experimental reactor size). The piston trajectory is chosen such that pressure remains constant in the reactor until it reaches the top of the catalyst/sorbent layer, at which point the piston stops moving and the reactor operates at a constant volume, with pressure decaying as H_2 permeates and CO_2 adsorbs further. Lastly, the dead volume in balance-of-plant components (valves, lines, etc.) is neglected in ideal simulations, so that the reactor system dead volume, V_d, is taken to be only the void space in the catalyst/sorbent bed ($\bar{\varepsilon} A_c d$).

The temporal evolution of the H_2 yield efficiency (defined as the cumulative H_2 molar yield divided by the maximum possible yield, or $\eta_{H_2} \equiv N_{H_2,perm}/4N^0_{CH_4}$ according to the stoichiometry of the overall SMR process, $CH_4 + 2H_2O \rightleftharpoons 4H_2 + CO_2$) is reported in Figure 5.3 for varying values of catalyst mass fraction. With pure catalyst/no sorbent (as the value of ϕ approaches 1), the initial rate of H_2 yield, which is proportional to the slope of the curves in Figure 5.3 is higher than is achieved at lower values of ϕ; however,

the reaction becomes equilibrium limited such that the maximum possible yield efficiency is approximately 63%. At the other end of the spectrum, with predominately sorbent and little catalyst (as ϕ approaches 0) the system becomes kinetically limited; the reactor will eventually approach 100% H_2 yield efficiency, but it will take a sub-optimally long time to reach this state.

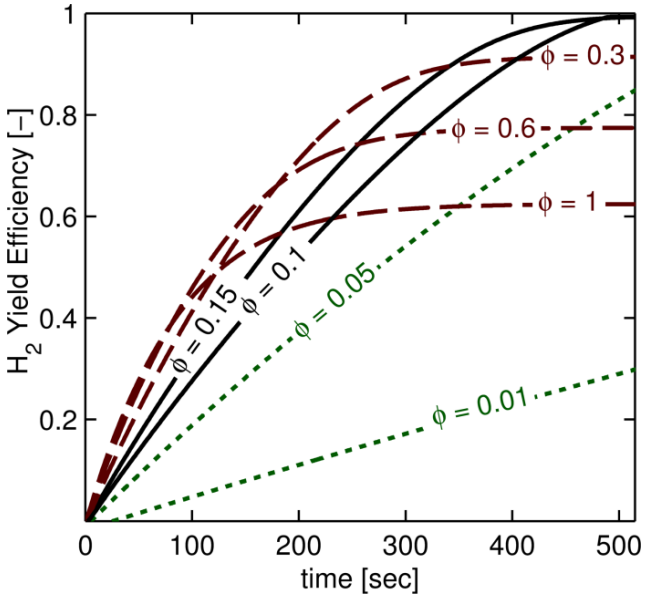

Figure 5.3: H_2 yield efficiency versus time for CHAMP-SORB with a fixed catalyst/sorbent bed height and constant reactor pressure (5 bar), temperature (400°C), steam-to-carbon ratio (2:1) and permeate side H_2 partial pressure (0. 2 bar). The two solid lines (ϕ ranging from 0.1-0.15) envelope the optimal catalyst mass fraction ratio. Dashed lines are equilibrium limited (insufficient sorbent to achieve full CH_4 conversion/H_2 yield) and dotted lines are kinetically limited (not enough catalyst to optimize reaction rate).

For the specific catalyst/sorbent bed height to initial reactor height ratio simulated, a mass fraction ratio of between ϕ = 0.1 and 0.15 is optimal. Values in this range balance the need for catalyst to promote the SMR reaction with sufficient CO_2 adsorption capacity to mitigate the equilibrium limitations on conversion. Within the optimal range of catalyst to sorbent ratio, due to a higher amount of catalyst the initial yield rate for ϕ =

0.15 is higher; however, the ultimate time required to reach 98% H_2 yield is approximately the same because an increased ability to adsorb CO_2 allows the ϕ = 0.10 scenario to proceed faster at the end of the cycle.

To better understand the relative importance of each component of the CHAMP-SORB process for both an optimal and equilibrium limited scenarios, Figure 5.4 reports rates for each of the three primary SMR reactions and for CO_2 adsorption.

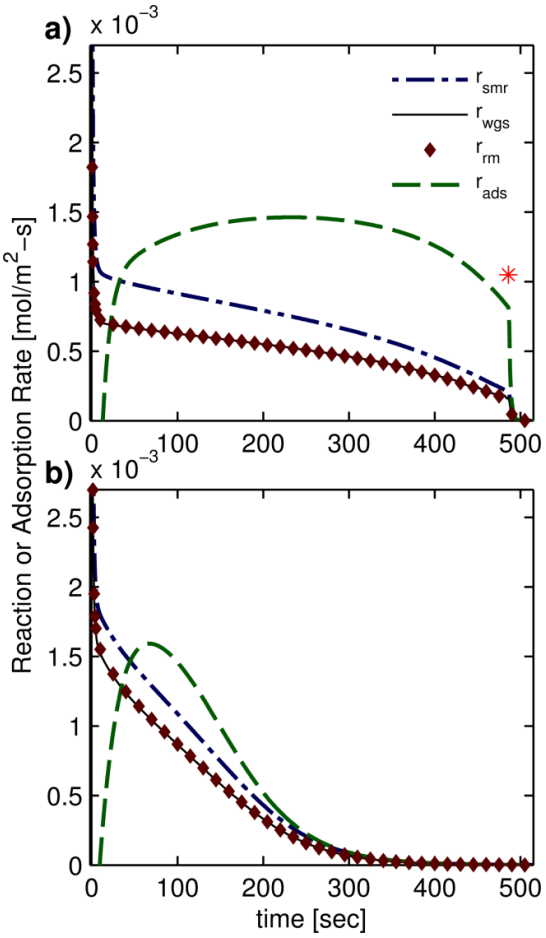

Figure 5.4: Reaction/adsorption rates for the a) optimal catalyst mass fraction (ϕ=0.1), and b) equilibrium limited mass fraction (ϕ=0.6). In both, the net rates of the reverse methanation and water gas shift reactions are approximately equal for the entire duration of the process, so any CO produced is essentially instantaneously consumed. For the optimal catalyst mass fraction case, the rates drop almost instantaneously to a near-zero level when the piston reaches the catalyst/sorbent bed and no further compression of the reactor volume possible (this time instant is denoted by an asterisk).

The temporal profiles of reaction/adsorption rates are dramatically different for each of the two cases considered: rates remain elevated in the optimal ϕ scenario until the piston reaches the top of the catalyst/sorbent bed (at $t \sim 490\ s$, marked with an asterisk in Figure 5.4a), whereas the rates decay asymptotically to zero once the sorbent capacity is reached in the equilibrium limited case (Figure 5.4b). In the equilibrium limited case and under the constraint of total pressure kept constant, the piston never reaches minimum displacement due to the presence of non-adsorbed CO_2 in the reactor. It is also important to note in both cases that the rate of RM and WGS trend together, yielding two significant conclusions: 1) the level of CO in the reactor remains near zero for the duration of the batch process (also having an important practical benefit, as carbon monoxide has a well-known poisoning effect on the Pd-based hydrogen separation membranes [82]), and 2) the stoichiometric ratio of 4 molecules of H_2 is produced for every molecule of CH_4 consumed, whether directly through the SMR reaction or in a parallel path through an initial RM step followed by the forward WGS reaction.

5.3.2 CHAMP-SORB comparison to the CHAMP-only approach

As this is the first kinetic study comparing the newly developed CHAMP-SORB approach to the original embodiment of the CHAMP reactor, it is informative to consider and understand the differences in operation between these two technologies. The original CHAMP only used H_2 removal to achieve full fuel conversion and maximum H_2 yield because methanol steam reforming is not nearly as endothermic, as methane steam reforming, and therefore is not severely equilibrium limited at relatively mild 200-300^{o}C operating temperatures [19]. In contrast, the CO_2 removal component of CHAMP-SORB was specifically introduced to circumvent the more severe equilibrium limitations

associated with highly endothermic steam methane reforming, while still maintaining operation at moderate temperatures of under 500^{o}C [81].

Figure 5.5 reports a comparison between CHAMP-SORB and a CHAMP reactor without CO_2 removal for the case of methane as a fuel. Because operating the CHAMP without CO_2 removal at 400°C would result in less than 70% CH_4 conversion and H_2 yield efficiency, which are not desirable for distributed fuel reforming, the simulation for the CHAMP-only scenario is performed at 600°C (*i.e.* the minimum temperature at which full CH_4 conversion can be reached without CO_2 sorption). To isolate the impact of CO_2 removal while comparing performance at different temperatures, the overall membrane permeance (D_{mem}/δ) is made consistent by increasing the membrane thickness for the 600°C simulation, the reaction timescale is made consistent by reducing the catalyst loading for the 600°C simulation by the same factor at which the SMR reaction rate constant increases between 400 and 600°C (as determined using the kinetic data of Xu and Froment [28]), and the initial total number of moles of fuel is made identical for each simulation by increasing the initial height (volume) of the reactor in the 600°C simulation from the baseline value of $2\ cm$, accounting for a reduction in molar density at elevated temperature.

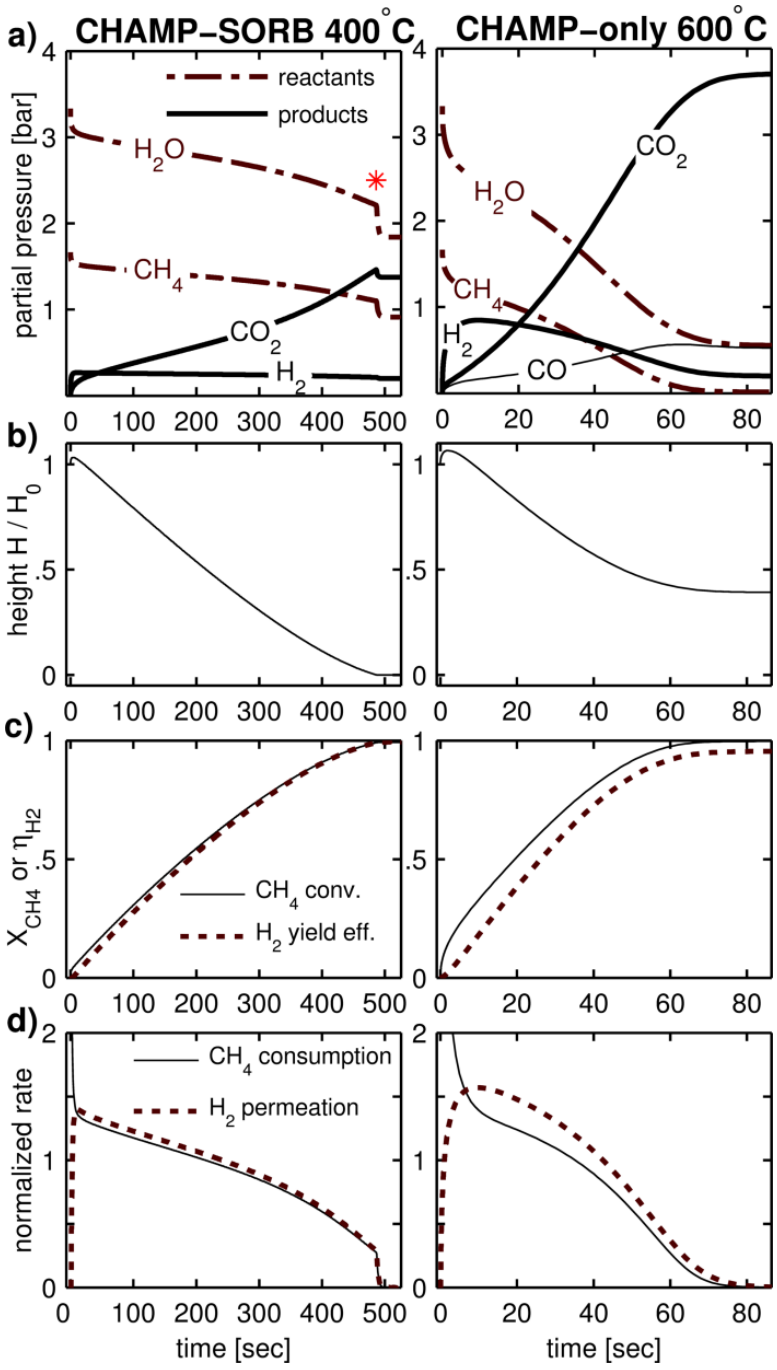

Figure 5.5: Temporal evolution of a) species partial pressure, b) reactor height (piston position), c) CH_4 conversion and H_2 yield efficiency, and d) CH_4 consumption and H_2 permeation rates (normalized by their average respective rates over the course of the cycle). Shown are simulation results for a CHAMP-SORB reactor operating at 400°C (left column) vs. a CHAMP reactor without sorbent operating at 600°C to circumvent equilibrium conversion limitations (right column).

Several important observations and conclusions can be drawn from comparison of the performance between these two scenarios. As expected, the partial pressure of CO_2 does not rise as high in the presence of a sorbent; however, it is important to note that there is even less CO_2 present in the CHAMP-SORB (relative to the CHAMP-only scenario) than it appears in Figure 5.5a when accounting for the late-cycle difference in reactor height (and thus volume) shown in Figure 5.5b, as the CO_2 content is proportional to the product of the CO_2 concentration and the reactor volume. Additionally, the concentration of the primary reactants (CH_4 and H_2O, highlighted by dash-dotted lines) remain much higher for the entire process duration in CHAMP-SORB, until the reactor reaches its minimum possible volume (again denoted by an asterisk in Figure 5.5a). The implication of maintaining elevated concentration of reactants is that the CHAMP-SORB reactor, relative to the CHAMP-only system, can sustain elevated reaction and hydrogen permeation rates throughout the entire process, as illustrated in Figure 5.5d (until the piston reaches the top of the porous bed and compression can no longer be applied, at which point near-100% H_2 yield is achieved and the subsequent exhaust step in the CHAMP-SORB cycle would begin). There is a gradual reduction in CHAMP-SORB reaction/permeation rates as the process proceeds, due to the unavoidable (but less dramatic than in the CHAMP-only scenario) rise in CO_2 concentration. This CO_2 concentration increase is due to a requirement for higher gas phase CO_2 partial pressure to facilitate further carbon dioxide uptake by the sorbent which has already been substantially loaded by CO_2, as dictated by the adsorption isotherm. In contrast, the exponential decay of the CHAMP-only reaction and permeation rates in later stages of the process points to the existence of a steep tradeoff between productivity (*i.e.* average

H_2 yield rate) and fuel utilization (*i.e.* H_2 yield efficiency). This tradeoff has been the traditional paradigm for fuel reforming reactors, and although it has been made less severe in advanced reactor designs such as membrane reactors [83], the combined CHAMP-SORB process is able to avoid this tradeoff entirely.

Two additional distinctions can be drawn from the comparison between CHAMP-SORB and CHAMP-only operation. First, the formation of CO in the CHAMP-SORB reactor is negligible, as was previously discussed. By comparison, the equilibrium CO mole fraction in the CHAMP-only reactor is approximately 5%. This is in part due to an unfavorable shift in equilibrium constant of exothermic WGS reaction (K_{WGS}) at the higher operating temperature; however, it is also due to relatively higher CO_2 and lower H_2O concentrations. The relationship between these parameters can be seen by noting that the final CO mole fraction (x_{CO}) must satisfy the equilibrium relationship for the WGS reaction ($x_{CO} = x_{H_2} x_{CO_2} / x_{H_2O} K_{WGS}$). Secondly, because CO_2 is not removed from the reaction space, it becomes by far the most concentrated gas species at the end of the CHAMP-only residence time and acts as a dilutant, thus lowering the H_2 partial pressure at a given reactor pressure and resulting in more unpermeated H_2 left inside the reactor at the end of the cycle. This, along with some proportion of hydrogen remaining in the form of H_2O due to incomplete conversion of the forward WGS reaction, results in a maximum H_2 yield efficiency of only 95% for the high temperature CHAMP-only reactor, whereas the CHAMP-SORB reactor is able to reach near 100% H_2 yield at much lower 400^{o}C temperature (as illustrated in Figure 5.5c).

Clearly the CHAMP-SORB and CHAMP-only scenarios each have unique benefits. For distributed reactors, where it is desired to achieve full conversion of CH_4 and to

operate at lower temperatures and near stoichiometric steam-to-carbon ratios [81], CHAMP-SORB offers significant advantages. It is easier to achieve a nearly ideal 4-to-1 yield of hydrogen relative to the methane fuel consumed during CHAMP-SORB operation because there is less dilution of H_2 with CO_2 in the reactor volume. Furthermore, the CHAMP-SORB is well suited to capture CO_2 if a low-carbon emission technology is desired. In cases where either energy-efficient CO_2 capture is not among the primary drivers, operating at a higher temperature is not prohibitive, or other fuels, such as methanol, are utilized which are not equilibrium limited even at fairly low temperatures (*ca.* 250^{o}C in the case of methanol), the simpler CHAMP-only reactor is capable of faster fuel conversion due to its ability to achieve higher H_2 concentrations (and thus increased driving force for permeation) during the early phase of the reforming reaction. This translates in higher volumetric power density of CHAMP-only reactors, which is an attractive feature for transportation or other mobile/portable applications of hydrogen-based power generation [84, 85].

5.4 Timescale Analysis

Timescale analysis is useful to better understand the interplay between the various processes in the CHAMP-SORB reactor. The rate of CH_4 consumption in the CHAMP-SORB reactor is determined by the slowest of five principal physical phenomena occurring concurrently: 1) kinetics of chemical reactions, 2) H_2 removal via permeation, 3) CO_2 removal via adsorption, 4) species transport to the catalyst/sorbent/membrane, and 5) heat transfer to maintain optimal temperature for the reaction/adsorption/ permeation processes.

5.4.1 Timescale determination

The timescale of a given processes can be determined by assuming that each of the other processes occurs at a significantly faster rate. For example, if the chemical reaction is rate limiting, transport is fast enough that there is a negligible spatial concentration gradient in the reactor, the membrane transport resistance is sufficiently low for the H_2 partial pressure in the reactor to approach the permeate side H_2 concentration, and adsorption rate is fast enough that the adsorbent is instantaneously loaded with the equilibrium amount of CO_2 according to the gas phase partial pressure. The prevailing species concentrations under these conditions can be determined and used to calculate the characteristic reaction rate ($\bar{r}_{CH_4}$) for the reaction-limited regime. This rate is then used to determine the reaction timescale (τ_{rxn}), or the time it would take to achieve full CH_4 conversion (with an initial amount of fuel, $N^0_{CH_4}$) if the process were strictly limited by resistance to reaction. A similar approach can be followed to determine the permeation timescale (τ_{perm}) and the adsorption timescale (τ_{ads}), using the following:

$$\tau_{process} = \frac{N^0_{CH_4}}{\bar{r}_{CH_4,process}} \tag{5.9}$$

To determine the characteristic reaction rate for each regime, it is necessary to first estimate the mole fraction for each of the species involved in the reaction network (H_2O, CH_4, CO, CO_2 and H_2) under the limiting conditions of that regime. Some observations can be made from the previous experimental and modeling work to simplify this process. First, when CO_2 adsorption is employed, the rates of RM and WGS reaction remain essentially equal, meaning that negligible CO is formed (or $x_{CO} \sim 0$). Additionally, this match in reaction rates means that regardless of the path that is followed (direct SMR, or

RM followed by WGS), CH_4 and H_2O are always consumed in a 2:1 ratio. As a result, if the initial S/C ratio is 2:1, then for the duration of the residence time these two species will remain in that proportion ($x_{H_2O} = 2x_{CH_4}$). The sum of the mole fractions in the reactor must also equal unity ($\sum x_j = 1$), leaving only two additional constraints required to determine all the approximate species mole fractions for a given regime.

These remaining two constraints depend on which timescale is under consideration. If the reaction is not limiting (*i.e.* when calculating either the permeation or adsorption timescale), the SMR reaction is at equilibrium:

$$K_{SMR}(T) = \frac{\left(x_{H_2}\right)^4 x_{CO_2}}{\left(x_{H_2O}\right)^2 x_{CH_4}} {P_T}^2 \tag{5.10}$$

For either the reaction or adsorption limited regime, the resistance to permeation is negligible such that the H_2 partial pressure on the retentate and permeate sides of the membrane are equal. As a result, the mole fraction of H_2 in the reactor is:

$$x_{H_2} = \frac{P_{H_2}^{\infty}}{P_T} \tag{5.11}$$

Lastly, in either the reaction or permeation limited regime, the adsorption kinetics are sufficiently fast such that there is instantaneous equilibrium between CO_2 in the gas phase and CO_2 adsorbed on the solid sorbent. As the cycle proceeds, the CO_2 gas-phase concentration must necessarily rise to continue loading more CO_2 onto the sorbent. For the purposes of timescale analysis it is possible, however, to determine an approximate "characteristic" CO_2 loading ($\bar{q}$) and CO_2 partial pressure ($\bar{P}_{CO_2}$). For an order-of-magnitude estimate, $\bar{q}$ is taken to be the arithmetic mean of the maximum possible (saturation) loading of the sorbent at the reaction temperature and the initial level of sorbent loading (q_0, as determined by the degree to which the sorbent was regenerated

from the previous cycle). The adsorption isotherm can then be used to determine $\bar{P}_{CO_2}$, or the corresponding equilibrium CO_2 partial pressure at $\bar{q}$ and T. Figure 5.6 illustrates a representative CO_2 isotherm, with an inflection point due to the chemical complexation reaction. The "carried over" CO_2 loading from the previous cycle (due to incomplete desorption/regeneration) is labeled P_{des}, and the saturation loading (or the highest possible sorbent loading in the limit that $P_{CO_2} \to \infty$) is labeled q_{sat}. For timescale analysis the "characteristic" CO_2 loading on the sorbent is taken to be the average of the initial loading (given by the isotherm when CO_2 pressure is P_{des}) and the final loading (assumed to reach saturation loading q_{sat}). The corresponding average CO_2 partial pressure ($\bar{P}_{CO_2}$) is then the CO_2 partial pressure at which the adsorption isotherm gives an equilibrium CO_2 loading equal to $\bar{q}$, as specified by equation (5.8).

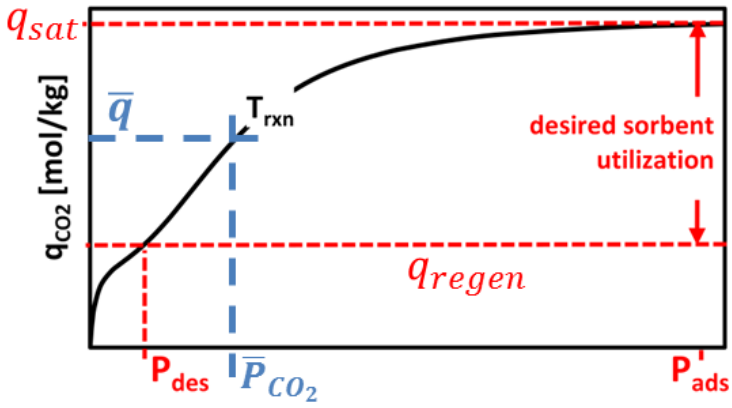

Figure 5.6: Determination of characteristic sorbent loading ($\bar{q}$) and CO_2 partial pressure ($\bar{P}_{CO_2}$) from the adsorption isotherm.

The mole fraction of CO_2 in the reactor for a regime that is not adsorption-rate limited is therefore:

$$x_{CO_2} = \frac{\bar{P}_{CO_2}(T, \bar{q})}{P_T} \tag{5.12}$$

Once the average "representative" species mole fractions are determined for each operating regime using the appropriate combination of equations (5.10) – (5.12), the approximate rate of fuel consumption for each process, $\bar{r}_{CH_4,process}$ in equation (5.9), can be determined and used to estimate the timescale of that process. The calculation of characteristic fuel consumption rate will vary depending on which process (reaction, adsorption or permeation) is limiting its rate of change. For the reaction timescale calculation, the kinetic model shows that the rates of the two parallel paths for H_2 production (reverse methanation followed by water gas shift, or direct steam methane reforming) are of similar magnitude. As such, only the rate of the (direct) steam methane reforming reaction (r_{SMR}) is calculated using the kinetic model from Xu and Froment and twice this value is used to determine the molar rate of CH_4 consumption in the reactor:

$$\bar{r}_{CH_4,rxn} = 2\bar{\rho}\phi A_c d \cdot r_{SMR} \tag{5.13}$$

For the permeation timescale, the rate of CH_4 consumption is balanced by the rate of H_2 permeation through the membrane. Stoichiometry of the SMR process ($2H_2O + CH_4 \rightleftarrows 4H_2 + CO_2$) dictates that these will occur in a 4:1 hydrogen to methane ratio. The characteristic CH_4 consumption rate for the permeation timescale calculation is then evaluated as one fourth of the hydrogen permeation rate:

$$\bar{r}_{CH_4,perm} = \frac{1}{4} \cdot A_c \frac{D_{mem}}{\delta} \left[\left(x_{H_2} P_T \right)^{1/2} - P_{H_2}^{\infty\,1/2} \right] \tag{5.14}$$

For the adsorption timescale, the rate of CH_4 consumption is balanced by the rate of CO_2 adsorption. In this case, the stoichiometry of (direct) steam reforming reaction dictates that these will occur in a 1:1 methane to carbon dioxide ratio, *i.e.*,

$$\bar{r}_{CH_4,ads} = \bar{\rho}(1-\phi)A_c d \cdot k_{ldf}\left[q_{eq}\left(x_{CO_2}, P_T\right) - \bar{q}\right] \tag{5.15}$$

The appropriate fuel consumption rate, as determined by either equation (5.13), (5.14), or (5.15), is used along with the total initial number of moles of fuel ($N^0_{CH_4}$), to estimate the time required to consume all of the initial quantity of fuel using equation (5.9). The initial quantity of fuel (for a given reactor height) will have a slight temperature dependence, as according to the ideal gas equation of state the molar density of a gas is inversely proportional to the reactor temperature T. Additionally, a small quantity of fuel is interspersed in the void volume of the porous bed. From the ideal gas equation of state, the initial number of moles of fuel is $x^0_{CH_4} P_T A_c (H_0 + \bar{\varepsilon} d_{cat})/R_u T$. Substituting this relationship for $N^0_{CH_4}$ into equation (5.9) yields the following expression for the timescale of a process:

$$\tau_{process} = \frac{x^0_{CH_4} P_T A_c (H_0 + \bar{\varepsilon} d_{cat})/R_u T}{\bar{r}_{CH_4,process}} \tag{5.16}$$

It is possible, however, to remove the temperature dependence and correct for the fuel located within the catalyst/sorbent layer by defining an effective initial height as $H_0^{eff} = (H_0 + \bar{\varepsilon} d_{cat}) \cdot T_{ref}/T$. To remain consistent with the baseline case for this chapter, 400°C is chosen as a reference temperature. Substituting H^0_{eff} into equation (5.16) yields an expression for timescale as a function of effective initial height, independent of operating temperature or amount of gas interspersed in the packed bed:

$$\tau_{process} = \frac{x^0_{CH_4} P_T A_c H_0^{eff}}{R_u T_{ref} \cdot \bar{r}_{CH_4,process}} \tag{5.17}$$

5.4.2 Timescale considerations for optimal catalyst to sorbent ratio

For the baseline case considered in Section 5.3.1, the calculated reaction, permeation and adsorption timescales are reported in Figure 5.7. The equilibrium reactor yield efficiency is also shown, and as before without a minimum amount of sorbent (in this case, $\phi < 0.15$) it is not possible to achieve full CH_4 conversion/H_2 yield.

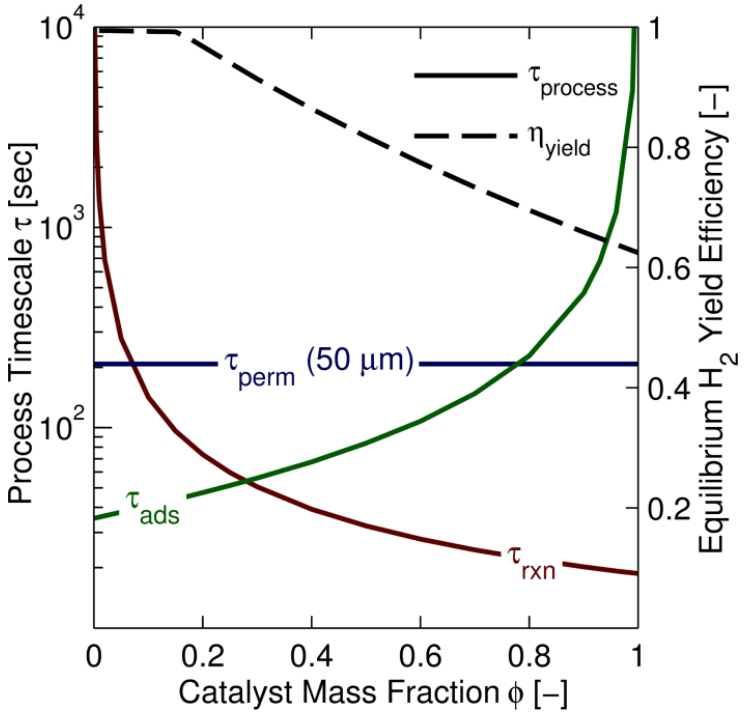

Figure 5.7: Reaction, permeation and adsorption timescales and equilibrium H_2 yield efficiency as a function of ϕ for baseline CHAMP-SORB reactor case ($T = 400$℃, $P = 5\ bar$, $P_{H_2}^{\infty} = 0.2\ bar$, $H_0 = 2\ cm$, $d = 1\ mm$, $q_0 = 0.25\ mol/kg$).

As the catalyst mass fraction of the bed approaches zero (all sorbent), the reaction timescale approaches infinity. Similarly, the adsorption timescale approaches infinity as the mass fraction approaches unity (all catalyst and no sorbent). In the optimal operating region (ϕ ranging from 0.1 to 0.15), the permeation timescale is greater than either the

reaction or adsorption timescale, meaning that the most effective way to improve performance in this scenario is to use a thinner membrane, rather than increase the thickness of the catalyst/sorbent bed. The permeation timescale governing the process ($\sim 200\ s$) is of the same order of magnitude as the actual cycle time from the ideal CHAMP-SORB model ($\sim 490\ s$). The reaction timescale is, however, within an order of magnitude of the permeation timescale, meaning that the time required for reaction does also contribute to the overall process time and is one reason why the overall cycle time is slightly greater than twice the permeation timescale.

The timescale predictions are useful in illustrating the reason that the hydrogen yield rate, proportional to the derivative of the H_2 yield efficiency curves shown in Figure 5.3, varies little within the range of optimal ϕ values ($\phi = 0.10 - 0.15$), yet is dramatically reduced for catalyst loadings below $\phi = 0.05$. In the optimal rage, the reaction timescale is still lower than the permeation timescale, meaning that the reactor performance is less sensitive to the catalyst loading. However, for lower values of ϕ, the reaction timescale is much greater than the permeation timescale and thus becomes overall rate limiting step; in turn, the overall reactor performance is strongly affected by a change in the catalyst loading, which directly impacts the rate of catalytic reaction and the overall transient dynamics of hydrogen generation.

The identified reaction, permeation and adsorption timescales can also be compared to the diffusion timescale ($H_0^2/\mathcal{D}_{eff}$) to determine if mass transfer resistance is expected to be a significant factor in the reactor performance. Our laboratory reactor has an initial height of $2\ cm$ and operates at 400 °C and $5\ bar$ total pressure. As calculated using the Chapman-Enskog theory [86], the average diffusion coefficient of the various species

present in the reactor at this temperature and pressure is approximately $\mathcal{D}_{eff} \sim 5 \times 10^{-5}\, m^2/s$. These values yield a diffusion timescale of approximately $8\, s$, which is much smaller than the permeation and reaction timescales for this reactor. It is expected that the thermal transport timescale is smaller than the mass diffusion timescale, as heat transfer is enhanced by the presence of the catalyst and the conducting walls of the reactor. Thermal behavior of the reactor may play a significant role in quantitatively capturing the fine features of the CHAMP-SORB dynamic behavior, in particular as the system is scaled up beyond the bench-sized testbed considered here. The impact of thermal effects on performance will require more elaborate analysis, which is the subject of Chapter 6.

5.4.3 Comparison of timescale analysis and reactor performance

To illustrate the utility of timescale analysis, Figure 5.8 compares the simulated performance of the ideal CHAMP-SORB reactor using the kinetics model with the estimated timescales for three catalyst loading values as a function of membrane thicknesses. The adsorption timescale is not shown because it is well below the reaction and permeation timescale in this region of ϕ. The reaction timescales for the catalyst loading values show up as horizontal lines (with a higher value of ϕ, or more catalyst, corresponding to a shorter reaction timescale) in Figure 5.8, as they are independent of the membrane transport resistance. The permeation timescale is a line with a slope of unity on the log-log plot, as the membrane permeation rate in the denominator of equation (5.9) scales as an inverse of the membrane thickness ($1/\delta$).

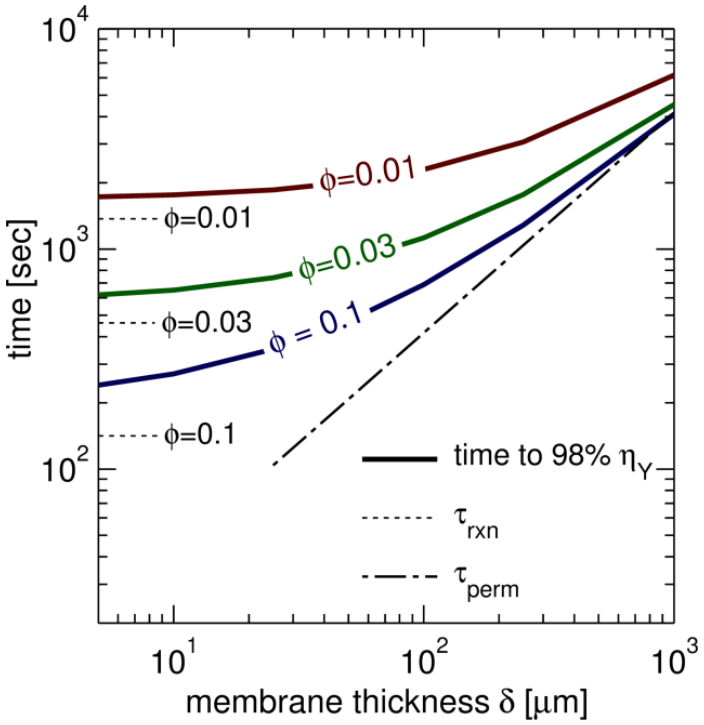

Figure 5.8: Comparison of CHAMP-SORB reactor performance (as represented by time to 98% H_2 yield efficiency) with reaction and permeation timescale at varying membrane thicknesses.

For very thin membranes, up to $10 - 20\ \mu m$, $\tau_{perm} \ll \tau_{rxn}$, indicating that the CHAMP-SORB is reaction-limited and the time to reach 98% H_2 yield is solely defined by the reaction timescale. Conversely, as the membrane becomes much thicker at $\sim 200\ \mu m$ and beyond, $\tau_{rxn} \ll \tau_{perm}$ and the system becomes permeation-limited. In this case, the time to 98% yield approaches the prediction of the permeation timescale. When reaction and permeation timescales are comparable, both the reaction and permeation dynamics influence the overall process transient, and since the reaction and permeation processes occur partially sequentially and partially in parallel, the time to achieve 98% yield is greater than either of the individual timescales.

5.4.4 Impact of operating temperatures and permeate side H_2 pressure

Having shown the utility of the timescale analysis in terms of predicting overall reactor performance and understanding the interplay between rate-limiting processes, timescales are next used explore the impact of other key operating parameters (including temperature, permeate side H_2 pressure, and reactor height) on the CHAMP-SORB process. For the geometry and configuration of the CHAMP-SORB reactor considered in this work, the reaction, permeation and adsorption timescales are directly proportional to the initial reactor height (H_0). For example, a doubling of H_0 while keeping the catalyst mass constant will result in a doubling of the reaction timescale because twice as much fuel must be consumed. In recognition of this fact, Damm and Fedorov proposed the division of timescale of CHAMP-related timescales by H_0 to remove the dependence on initial reactor height [18]. The resulting parameters, with units of [time/length], are termed the effective "resistances" for each process, which facilitate the generalization of the analysis by abstracting, at least partially, the reactor size from scaling considerations.

Maps of reaction and permeation resistances provide insight into the impact of operating parameters on the maximum possible performance envelope (in the absence of transport limitations). Figure 5.9 illustrates the impact of operating temperature and permeate side H_2 partial pressure on the effective reaction and permeation resistances, as defined in the previous paragraph. Temperatures of up to 520°C are considered because that is the maximum working temperature limit of K_2CO_3-promoted hydrotalcite [67], and this value is low enough to meet the desired attributes of a distributed H_2 production SMR system. To account for the slight gas density differences across the analyzed

operating temperature range, the timescale is divided by an effective initial reactor height (H_0^{eff}) rather than the true initial height H_0, as discussed in Section 5.4.1.

Rather than specifying the catalyst/sorbent layer thickness and then varying the catalyst mass fraction to assess different levels of catalyst loading, as was done in the Section 5.4.2, the catalyst mass (per unit reactor area) is specified directly in Figure 5.9. In light of the conclusions of the ideal model results presented in Figure 5.3, this method of determining catalyst loading is consistent with how the CHAMP-SORB reactor would be sized in practice: the required mass of sorbent is calculated by the amount of sorbent needed to fully adsorb the carbon present in the form of initial CH_4 that will be converted to CO_2 through the SMR process, and the appropriate mass of catalyst that will produce H_2 at an appropriate rate is then mixed with the sorbent. This appropriate rate, and thus the amount of catalyst, can be estimated using timescale analysis by ensuring that the reaction rate is not process-limiting, *i.e.*, its time scale is at least as small as those for permeation (based on membrane thickness) and adsorption (based on sorbent mass).

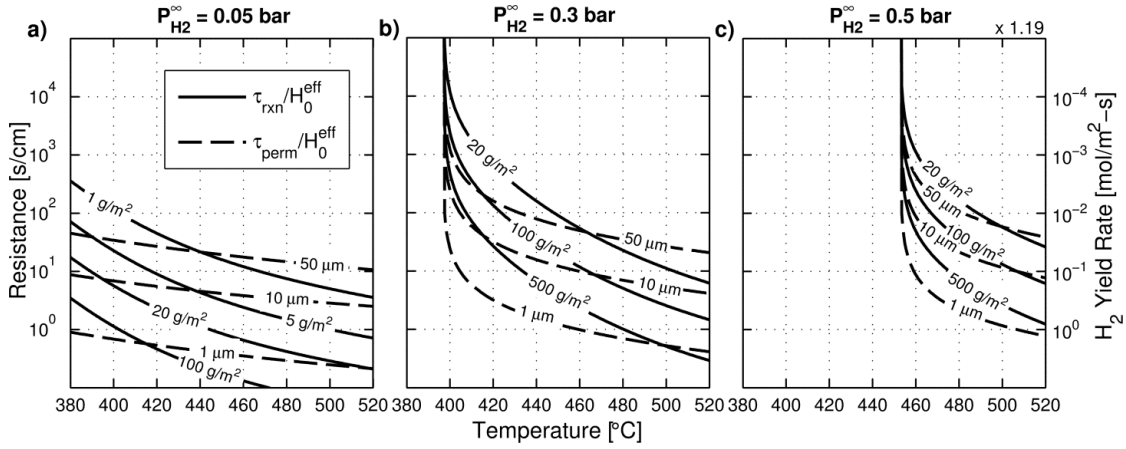

Figure 5.9: Timescale divided by reactor size, or effective "resistance," to the reaction and permeation processes as a function of temperature for permeate side H_2 partial pressures of a) $0.05\ bar$, b) $0.3\ bar$, and c) $0.5\ bar$. The resistances are mapped into an approximate maximum possible hydrogen yield rate on the secondary (right hand side) y-axis at a given process resistance level by recognizing that the rate of hydrogen yield is inversely proportional to the resistance.

Several important trends can be seen in Figure 5.9. As permeate side H_2 partial pressure ($P^{\infty}_{H_2}$) is reduced, it becomes easier for H_2 to exit the reactor, and as expected the permeation resistance decreases. However, the reaction resistance is also quite sensitive to changes in $P^{\infty}_{H_2}$, as the presence of H_2 in the reactor promotes the reverse direction of all three reactions that comprise the steam methane reforming process, necessitating significantly higher catalyst loadings to achieve levels of reaction resistance of comparable magnitude to the permeation resistance at low temperatures (in the 400-440°C range) as $P^{\infty}_{H_2}$ increases. The sensitivity to permeate side H_2 pressure can be seen most dramatically in Figure 5.9c where $P^{\infty}_{H_2} = 0.5\ bar$; at this elevated permeate side H_2 pressure, the reverse reaction rate actually approaches that of the forward direction at approximately 450°C, so the reaction timescale approaches infinity at this temperature. Obviously, from a pure reactor performance perspective it is desirable to minimize

permeate side H_2 partial pressure; however, maintaining a low $P_{H_2}^{\infty}$ comes at an economic cost. For example, if steam is used as a sweep gas, approximately an order of magnitude of additional steam (assuming only the cost of dilution) would be needed to reduce $P_{H_2}^{\infty}$ from the conditions illustrated in Figure 5.9c to those of Figure 5.9a. This steam comes at a considerable cost, as the enthalpy of vaporization of liquid water is approximately 25% of the heat of reaction for the overall steam methane reforming process [34].

In addition to highlighting the tradeoff at potential values of $P_{H_2}^{\infty}$, Figure 5.9 illustrates that in general, operating temperature has a more dramatic impact on the resistance to reaction than it does on permeation. The main exception to this observation is as the temperature reaches a sufficiently low value where the equilibrium H_2 mole fraction approaches the value of the permeate side H_2 partial pressure divided by the total reactor pressure, both the permeation and reaction resistance approach infinity. For temperatures above this "cutoff" value, the catalyst loading required to provide similar reaction resistance to the permeation resistance of a given membrane thickness can be determined using Figure 5.9 for any potential reactor temperature and $P_{H_2}^{\infty}$. Lastly, the secondary axis of Figure 5.9c reports the equivalent molar yield rate that would result from a CHAMP-SORB reactor producing H_2 at a given reaction or permeation resistance level if that process were fully dictating the overall reactor performance. For example, at a resistance level of $10\ s/cm$, one cm worth of fuel will be converted to H_2 during a $10\ s$ period, and the resulting hydrogen yield rate (per unit cross-sectional area) can be determined using the density of fuel at the operating conditions.

5.5 Cyclic Operation Considerations

The ideal, purely kinetic, model can also be used to assess the ideal reactor behavior during other steps in the CHAMP-SORB cycle, in particular to develop a basic understanding of how the pressure-swing regeneration approach would work in a variable volume reactor. Specifically of interest are two questions:

(i) Is it possible to achieve a substantial sorbent regeneration level of $q_0 = 0.25\ mol/kg$ using pressure swing via volume expansion alone, or would some complementary temperature swing also be necessary?

(ii) What fraction of the total cycle time is taken up by regeneration versus the reaction (H_2 producing) steps, with impact on expected power/hydrogen yield density of the CHAMP-SORB cycle?

To answer these questions, the ideal kinetic model developed in section 5.1 is employed to study the complete CHAMP-SORB regeneration cycle. The system starts with a reaction step governed by equations (5.1) – (5.5), followed by an exhaust step, then volume expansion to produce low pressure conditions favorable for CO_2 desorption and sorbent regeneration, then exhaust of the desorbed CO_2, and finally refilling of the reactor to begin a new cycle. For the exhaust step, the time rate of change of moles in the system decays proportional to a valve coefficient (k_V) and the difference between the total reactor pressure and ambient ($P_T - P_{atm}$),

$$\frac{dN_T}{dt} = -k_V(P_T - P_{atm}) \tag{5.18}$$

where the reactor pressure is calculated using the ideal gas equation of state, equation (5.4). Following with the ideal assumption of perfect mixing, the mixture composition at the outlet valve must be equal to the bulk composition in the reactor, and the time rate of change in number of moles of each individual species j during the exhaust step is equal to

the time rate of change of the total moles in the reactor, given by equation (5.18), multiplied by the mole fraction x_j of a given species ($dN_j/dt = x_j \cdot dN_T/dt$).

In modeling the desorption step, the piston is moved away from the catalyst/sorbent bed to expand the reactor volume at a velocity U_{max}^P ($dH/dt = U_{max}^P$) until it reaches the maximum volume (equal to that at the start of the reaction step), and the pressure varies according to equation (5.4). During desorption step, the inlets/outlets to the reactor are closed and $dN_j/dt = 0$ for all species other than CO_2, which may desorb into the gas volume, as favorable conditions for desorption occur due to pressure drop as the reactor volume expands:

$$\frac{dN_{CO_2}}{dt} = -\overline{\rho} dA_c (1 - \phi) \frac{dq_{CO_2}}{dt} \tag{5.19}$$

where the time rate of change of CO_2 loading is determined using the linear driving force kinetics (equation (5.3)). The desorption step is allowed to continue until the CO_2 loading on the sorbent approaches within 3% of its equilibrium value, at which point the piston begins to move downward to exhaust the desorbed CO_2 from the reactor. Because the pressure in the CHAMP-SORB is likely below atmospheric at the end of the desorption step, the CO_2 exhaust step first consists of a period of time where the piston moves downward (according to the schematic in Figure 5.1) at its maximum velocity ($dH/dt = -U_{max}^P$) and only CO_2 can begin to re-adsorb onto the sorbent, according to equation (5.19), as pressure in the reactor rises. Once atmospheric pressure is reached, the piston continues to move downward at $-U_{max}^P$, pushing all species out of the reactor at rates proportional to the mole fraction of each. Before the reactor can be refilled with CH_4 and H_2O to begin the next reaction step, the sorbent loading must reach its initial, periodic quasi-steady state loading value(q_0) for the cycle. If this does not occur after one

expansion/desorption followed by CO_2 exhaust step, the process can be repeated until the target sorbent loading is reached.

As a baseline case, conditions matching those of section 5.3.1 are chosen ($T = 400℃,\ P_T = 5\ bar,\ P_{H_2}^{\infty} = 0.2\ bar,\ q_0 = 0.25\ mol/kg,\ \delta = 50\ \mu m,\ H_0 = 2\ cm$). A catalyst loading of $0.1\ kg/m^2$ is utilized with a sorbent mass of $1.25\ kg/m^2$, a value calculated to ensure that a sufficient amount of CO_2 can be adsorbed to allow the reactor to reach full conversion when starting with a sorbent loading of $0.25\ mol/kg$. A valve coefficient of $0.004\ mol/bar - s$ is chosen such that the reactor depressurization during the first exhaust step takes $\sim 5\ s$, and a moderate piston velocity of $U_{max}^{P} = 3\ cm/s$ is utilized for the CO_2 desorption and exhaust steps. Figure 5.10 illustrates the transient rate of H_2 yield, reactor chamber extent (piston position), pressure and sorbent loading for 3 consecutive cycles.

In Figure 5.10, the H_2 production step lasts for approximately $500\ s$, with the CHAMP-SORB reactor sustaining elevated H_2 production rates until the piston can no longer provide compression (when the height reaches zero and the piston comes in contact with the packed bed, just after $t = 500\ s$). At this point, the reactor is first depressurized according to equation (5.18), then the piston moves upward to expand the reactor volume and create favorable conditions for CO_2 desorption. During this step, the reactor pressure first drops well below atmospheric level, but then begins to recover as CO_2 desorbs from the sorbent and enters the reaction chamber. When a pressure of approximately $0.6\ bar$ is reached, the sorbent is near equilibrium with the gas-phase CO_2 and the CO_2 exhaust step begins, during which the reactor is first compressed to atmospheric pressure and then CO_2 begins exiting the reactor chamber.

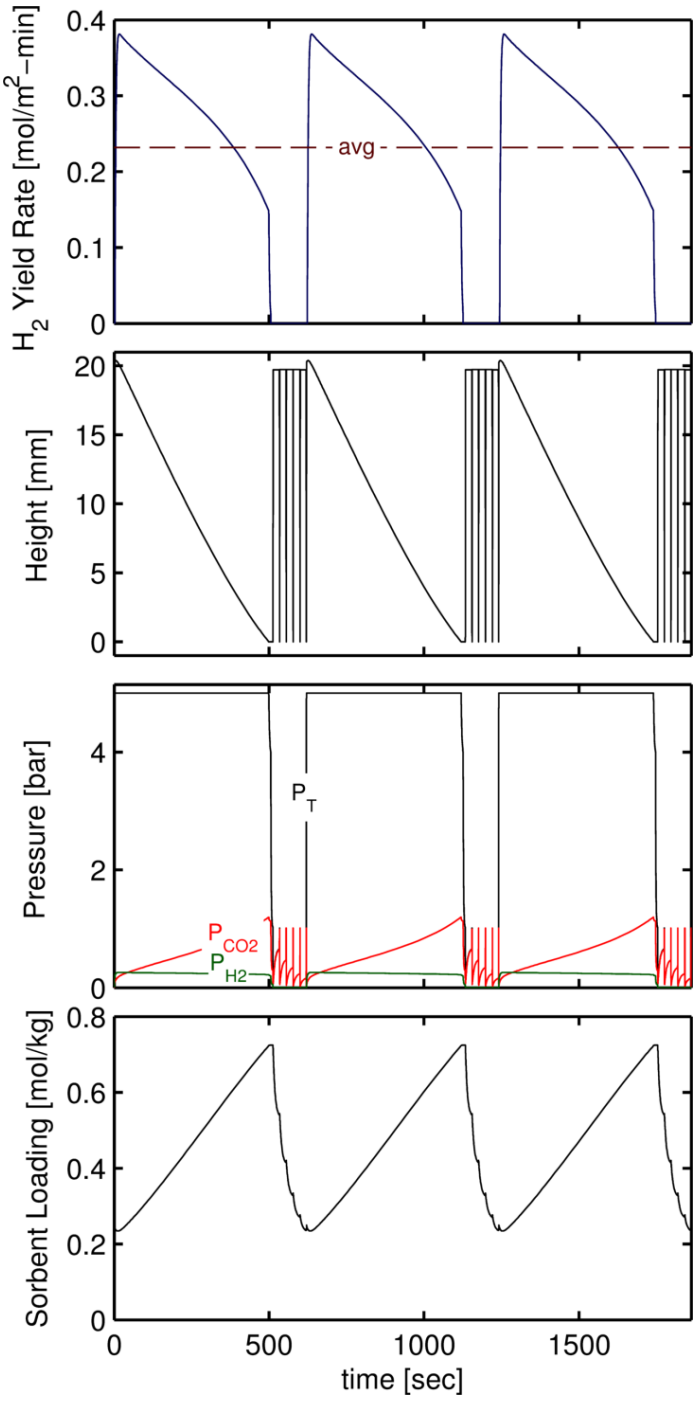

Figure 5.10: Time varying H_2 yield rate, reactor height, reactor pressure, and sorbent loading for three consecutive cycles of CHAMP-SORB operation with volume-expansion driven pressure-swing desorption. Five volume expansions are required to restore the CO_2 sorbent loading to its initial value, when the reactor is ready to start a new reaction cycle.

During the first CO_2 desorption step, the sorbent loading drops from a maximum value of $0.73\ mol/kg$ at the end of the reaction step to roughly $0.5\ mol/kg$ after completion of volume expansion and CO_2 desorption. In order to fully regenerate the sorbent to the $q_0 = 0.25\ mol/kg$ initial loading value, five repetitions of volume expansion step of CO_2 desorption followed by CO_2 exhaust are required with each successive step reducing the CO_2 loading further. The time required for this desorption, however is only approximately $110\ s$ out of the total $620\ s$ cycle time, or roughly 18% of the cycle time is spent exhausting and regenerating the reactor. The impact of sorbent regeneration on average H_2 production rate is illustrated in the top plot of Figure 5.10.

Figure 5.11 illustrates the piston position (reactor volume/height), pressure and sorbent loading for just the first desorption step, showing data from $500 \leq t \leq 550\ s$ in Figure 5.10. Here, the initial (first) exhaust step in the sequence, between the dotted vertical lines marked (1) and (2), can be clearly seen, followed by the volume expansion and subsequent CO_2 desorption (noted by a rise in reactor CO_2 partial pressure and drop in sorbent loading) that occurs between the lines marked (2) and (3).

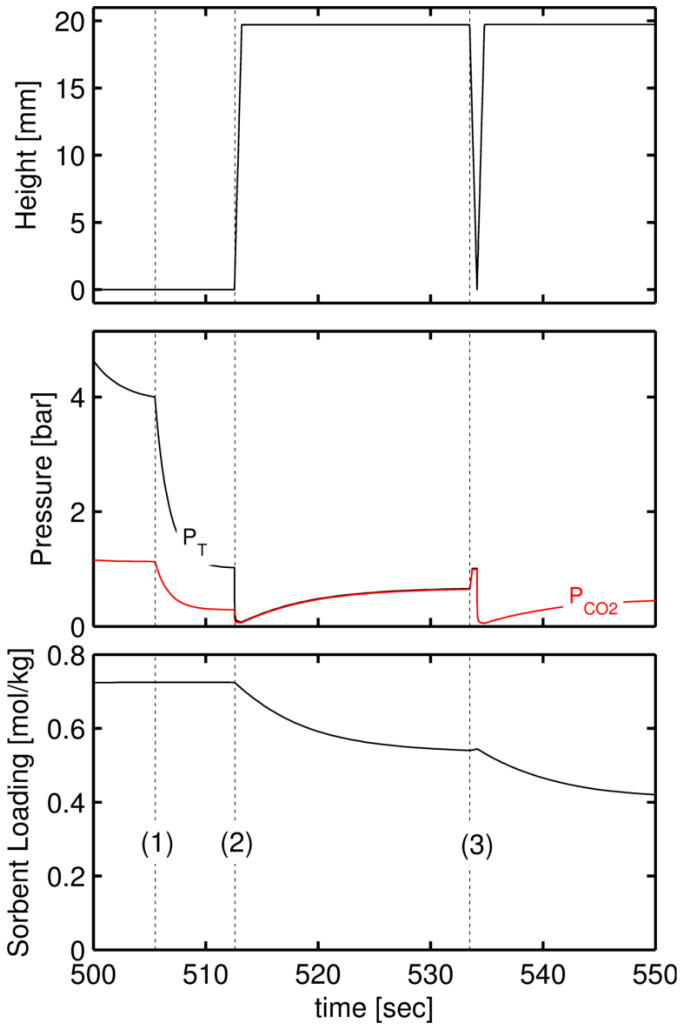

Figure 5.11: Time varying reactor height, reactor pressure, and sorbent loading for a single volume-expansion driven pressure-swing desorption step with a piston velocity of 3 cm/s.

The sorbent loading rises slightly just after the time instant marked (3), due to re-adsorption of CO_2 as the reactor is recompressed to atmospheric pressure to allow it to be exhausted, however the exhaust process is sufficiently quick relative to the adsorption timescale that a substantially quantity of CO_2 is not reloaded on the sorbent. A piston velocity of 3 cm/s is selected for volume expansion such that roughly 1 s is required for the piston to travel the height of the reactor, a time sufficiently short to avoid significant

desorption during the exhausting step (as predicted by the adsorption timescale of $1/k_{ldf} \sim 20\ s$).

While the analysis of this section shows that it is possible to regenerate the sorbent to a level of $q_0 = 0.25\ mol/kg$ using purely volume-expansion driven pressure swing adsorption, and that the time required to reach this value is less than 20% of the total cycle time, it may be desired to incorporate some temperature swing to minimize the number of expansion steps required to reach a suitable sorbent regeneration level without exposing the thin, hydrogen-permeable membrane to many pressure cycles, which may negatively impact its life time and reactor reliability. These simulations, conducted using an idealized kinetic model, neglect the mass transfer effect of CO_2 through the packed bed as well as any thermal effects. Mass transport is expected to be less significant in this part of the operating cycle (as compared to the combined reaction/permeation/adsorption step) because CO_2 is essentially the only species contained in the reactor and it is assumed that the CO_2 pressure will equilibrate via advection on the sonic timescale in the reactor. As such, the conclusions presented in this section are a good first pass at assessing the regeneration, and future work could account for all of these factors in a rigorous fashion to obtained refined predictions.

5.6 Conclusions

Building on the experimental work of Chapter 4, in this chapter a CHAMP-SORB ideal kinetic model was developed and validated through favorable qualitative and quantitative comparison between simulation results and experimental data at both the individual process (adsorption/permeation) and overall system performance levels. Though simplifications were employed in the model, most notably an assumption of

infinitely fast heat and mass transfer as compared to the reaction and sorption kinetics, the model successfully captures the key features of the CHAMP-SORB reaction/permeation/ sorption process exhibited in experiments. A negligible effect of heat and mass transfer in the experimental testbed under investigation was established through comparison of the relevant transport timescales to those of the reaction, sorption, and permeation processes.

The validated kinetic model was able to assess implications of scenarios that were not experimentally accessible; namely when the size of valves and piping is made small relative to the working volume of the system, full CH_4 conversion is possible. Further, using the kinetic model, we were able to explore the kinetic- and equilibrium conversion-related tradeoffs between the relative amount of sorbent to catalyst to identify the optimal catalyst mass fraction for a given catalyst/sorbent bed size, as well as to provide insights into fundamental underpinnings behind different performance of a CHAMP-style reactor with and without CO_2 capture. The key insights from the purely kinetic analysis are as follows:

- The CHAMP-SORB is able to maintain relatively high fuel (CH_4 and H_2O) concentrations for the duration of the residence time; the consumption of fuel is manifested as a decrease in *reactor volume* rather than a reduction in fuel species concentration. The CHAMP reactor with only H_2 removal cannot achieve this functionality, as CO_2 accumulates in the reactor and concentrations rise dramatically near the end of the process.
- Reaction and permeation rates are more uniform throughout the duration of the CHAMP-SORB batch process time, relative to the CHAMP-only, and the maximum achievable H_2 yield efficiency is increased due to less CO_2 dilution.
- Relatively higher H_2O and lower CO_2 concentrations of CHAMP-SORB (as compared to CHAMP-only) result in negligible CO formation due to a shift in

equilibrium of the water gas shift (WGS) reaction and a matching of reverse methanation (RM) and WGS reaction rates for the duration of the batch process.

A framework of timescale analysis was introduced to further elucidate the interactions between the rates of adsorption, permeation and chemical reaction. The time scale analysis identifies permeation, adsorption, and reaction limited regimes, leading to a conclusion that the optimal amount of catalyst in a CHAMP-SORB reactor is such that the reaction timescale does not exceed either the permeation or adsorption timescale. Further, timescale analysis shows that the appropriate quantity of sorbent is established by the required sorbent CO_2 capacity to reach full fuel conversion (*i.e.* sufficient capacity to adsorb all the carbon initially in the form of CH_4 as it is converted to CO_2), as opposed to the kinetics of adsorption.

To remove dependence on the initial reactor size, the process timescales were recast as effective resistances, which were used to estimate the maximum achievable H_2 yield rate per unit area at a given individual process resistance level (*i.e.* when the resistances of all other processes are significantly lower). Reaction and permeation process resistances were calculated for a range of operating temperature and permeate side H_2 partial pressures ($P_{H_2}^{\infty}$) to investigate the impact of these variables on the CHAMP-SORB performance. Interestingly, the reaction resistance is more sensitive to $P_{H_2}^{\infty}$ than the permeation timescale, as the SMR reaction rates depend heavily on the concentration of H_2 in the reactor. The ability to operate at lower temperatures depends upon the ability to remove H_2 effectively from the permeate side of the membrane to maintain sufficiently low $P_{H_2}^{\infty}$ values.

Having experimentally demonstrated the CHAMP-SORB concept and developed a basic understanding of the interplay between adsorption, permeation and reaction rates through a validated kinetic model and timescale analysis, scaling up the CHAMP-SORB process requires the development of a combined transport-kinetic model, accounting for the heat and mass transfer effects that will inevitably arise as the reactor becomes larger and the transport timescale becomes of similar (or greater) order of magnitude to the reaction, permeation and adsorption timescales. Additionally, the conclusions of idealized kinetics modeling and time scale analysis presented in Chapter 5 are limited to the porous bed in which the catalyst and sorbent are uniformly mixed, which may not be the most optimal arrangement, especially when heat and mass transfer effects become significant. The implications of the system scale-up and catalyst/sorbent bed composition considerations are addressed next in Chapter 6 through comprehensive heat/mass transfer, reactions/adsorption kinetics, and membrane separation modeling based on first principles formulation.

CHAPTER 6

TRANSPORT-KINETIC MODEL FOR CHAMP-SORB SCALE-UP

In this chapter, a comprehensive model is developed to investigate the effects of heat/mass transfer on reaction, adsorption and permeation processes in the CHAMP-SORB class of reactors. The model is applied to the most important, H_2 producing, compression step of the CHAMP-SORB cycle, during which accounting for interplay among the transport and reaction/separation processes is critical to performance. The simulations are used to assess the rate limiting process(es) for different reactor configurations and geometries and to develop the operation regime maps, resulting in guidelines for reactor scaling to achieve a desired hydrogen production level. Lastly, relative placement of the catalyst/sorbent in the porous bed is investigated to identify an optimal bed composition and benefits of layering.

6.1 Model Formulation

6.1.1 System schematic

The simulation domain for the problem formulation is illustrated in Figure 6.1 as the region surrounded by dotted red line. It consists of two distinct sub-domains: (1) a gas-phase only region; and, (2) the porous media region containing the sorbent/catalyst mixture of porosity $\bar{\varepsilon}$ filled with gas species in the void area. The domain is bordered on the top by an impermeable, well insulated piston that moves with a velocity of U^P to dynamically change the reactor volume (to maintain a constant operating pressure as temperature and gas mixture content and composition in the reactor change due to

reaction, permeation, and adsorption) and on the bottom by a Pd-Ag membrane of thickness δ that is selectively permeable to H_2 only.

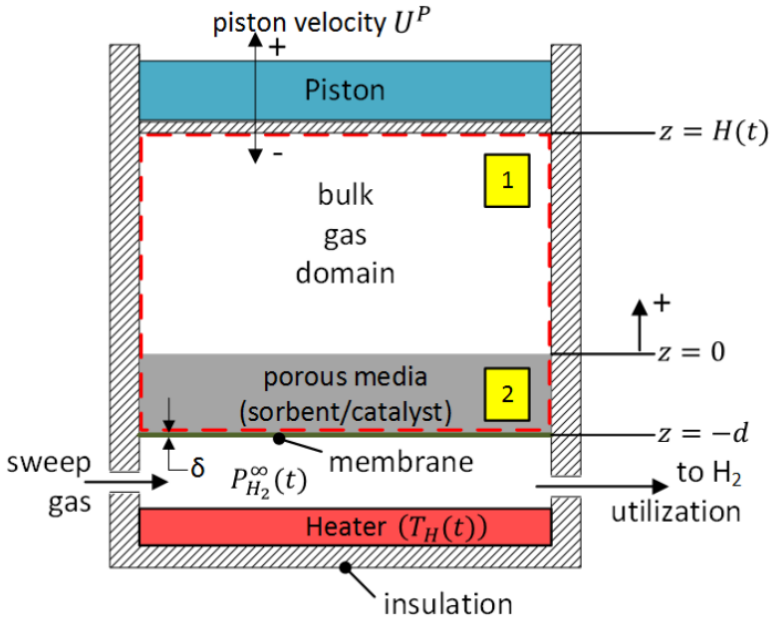

Figure 6.1: Schematic of CHAMP-SORB simulation domain. Two distinct regions are considered: (1) the gas-only volume between the porous media and the piston, and (2) the porous media consisting of a two phase mixture of gas interspersed within the solid catalyst/sorbent.

The permeate side of the membrane consists of a mixture of permeated H_2 with sweep gas at a H_2 partial pressure of $P^{\infty}_{H_2}$. The sweep gas H_2 partial pressure is a model parameter that can be changed to simulate conditions related to different approaches to downstream hydrogen collection and utilization. Heat is supplied to the system by a heat source, referred to as a heater in Figure 6.1 which is in close proximity to the membrane and catalyst layer, as these components require heating to a sufficient temperature T_H for carrying out the endothermic SMR reaction and for effective hydrogen permeation. In practice this heating could be via natural gas burners or combustion of residual fuel

leaving the reactor during the exhaust step. As radiation is expected to be a dominant mode of heat transfer at the elevated operating temperatures of the CHAMP-SORB, for the purpose of modeling, the heat transfer coefficient is estimated using the linearized radiation heat transfer coefficient between perfect radiation absorbers/black surfaces ($h_{eff} = \sigma \cdot [T_H^2 + T_{mem}^2] \cdot [T_H + T_{mem}] \approx 4\sigma T_0^3$) [87]. At a target operating temperature of 400℃ $(673\ K)$, this results in an effective heat transfer coefficient of $67\ W/m^2 - K$.

The H_2 partial pressure on the permeate side of the membrane is regulated by the flow of a sweep gas; choosing the optimal value for $P_{H_2}^{\infty}$ requires balancing the economic cost of introducing the sweep gas at a sufficient rate and the energetic cost of downstream separation with the performance benefit realized by a reduction in overall resistance to H_2 transport from the reactor to the collection stream [88]. For the purpose of this study, it is assumed that the flow of sweep gas can be regulated with a control strategy such that the partial pressure of H_2 on the permeate side of the membrane starts at zero and approaches a target value ($P_{H_{2,T}}^{\infty}$) exponentially with a time constant $\tau_{P_{H2}}$, yielding $P_{H_2}^{\infty}(t) = P_{H_{2,T}}^{\infty}\left[1 - e^{-t/\tau_{P_{H2}}}\right]$. This particular form is chosen in recognition of the fact that there will be some time delay before the H_2 permeating the membrane raises the permeate side H_2 partial pressure to its target value. The precise value of $\tau_{P_{H2}}$ will depend on the volume of the permeate side (between the heater and the membrane in Figure 6.1); for this study a value of $\tau_{P_{H2}} = 2\ s$ is chosen after considering values ranging from $0.1 - 20\ s$ and finding there is little impact on the overall time to reaction step completion (as the permeation time constant only impacts $P_{H_2}^{\infty}$ for a small percentage of the total residence time).

6.2.2 Modeling assumptions

To assess the general trends of CHAMP-SORB behavior as heat and mass transfer effects become significant, a reduced order transport-kinetic model is developed, with the system represented as one-dimensional with only variation in properties in z-direction (with reference to Figure 6.1). Three of the major assumptions inherent in this representation are that (*i*) side walls are well insulated and impermeable to any species, (*ii*) thermal effects of side walls (heat conduction along z-direction and thermal latency) are ignored, and (*iii*) the membrane temperature and $P_{H_2}^{\infty}$ are spatially uniform.

Additionally, the following modeling assumptions are made:

- All species behave as ideal gases.
- Pressure equilibrates quickly, on the sonic time scale of pressure wave propagation through the space volume, and is uniform throughout the reactor.
- Gas and solid in the porous media region are in local thermal equilibrium.
- Thermal contact resistance between the membrane and porous bed is negligible and variation in temperature across the membrane is small such that a single value, equal to the temperature at the bottom of the porous media region, can accurately represent the membrane temperature (*i.e.*, $T_{mem} = T|_{z=-d}$).
- Hydrogen permeation is diffusion limited and the rate can be described by Sievert's Law [75].
- Intra-particle diffusion resistance is negligible within the sorbent and catalyst.
- Membrane and sorbent are infinitely selective to uptake of hydrogen and carbon dioxide, respectively.
- Membrane, catalyst and sorbent poisoning and degradation effects are not considered.
- Soret (thermal diffusion or thermophoresis) effects are not considered.
- Radiation heat transfer in the both gas phase (domain 1) and porous media (domain 2) is ignored.

The assumption of ideal gas behavior is readily justified for all relevant species at the operating pressures and temperature. Of all chemical species present in the CHAMP-SORB reactor, steam (H_2O) is the most likely to exhibit non-ideal behavior and thus provides a good proxy for checking the validity of ideal gas approximation. At the target reactor operating temperature (T_0) and pressure (P_T), the reduced temperature $T_R = 1.04$ ($T_R = T_0/T_c = 673\ K/647.3\ K$) and pressure $P_R = 0.02$ ($P_R = P_T/P_c = 5\ bar/221\ bar$) yield a compressibility factor for steam of essentially unity thus validating the assumption of ideal gas behavior [89]. Quasi-steady and uniform pressure throughout the reactor is a sound treatment of momentum conservation in the reactor owing to fast pressure equilibration on the timescale of pressure wave propagation within the reactor domain, as is discussed in greater detail in prior studies [19, 90].

The assumption of local thermal equilibrium between gas and solid in the porous media region is checked by estimating the order of magnitude of the local temperature difference between gas and solid phases ($\Delta T = T_{solid} - T_{gas}$). This calculation, details of which are contained in Appendix C, predicts that the temperature difference is on the order of $\Delta T \sim 0.1\ K$ and is in agreement with a prior investigation of the porous media problem in the presence of an (electro)chemical reaction [91]. The membrane Biot number is calculated to ensure that the use of a single value to represent the membrane temperature is an appropriate approximation. Using the previously calculated effective heat transfer coefficient, the Biot number is on the order of 10^{-5} ($Bi = h_{eff} \cdot \delta/k_{Pd-Ag} = (67\ W/m^2 - K)(10^{-5}\ m)/71.8\ W/m - K$), indicating that the temperature variation (and heat transfer resistance) across the membrane is minimal. While it is possible that the effective heat transfer coefficient could be higher, due to the

contributions of forced or natural convection, any increase would likely not be sufficient to raise the Biot number to a level where temperature variations across the membrane thickness are significant. Detailed justification for the neglection of intraparticle diffusion limitations, Soret diffusion effects, catalyst/membrane poisoning, and radiation heat transfer within the reactor domains are provided in Appendix C.

6.2.3 Governing equations

Mass conservation for gas species j can be expressed using the 1-D scalar transport equation,

$$\frac{\partial c_j}{\partial t} + \frac{\partial}{\partial z}\left(c_j v_m\right) = -\frac{\partial}{\partial z}\left(J_{z,j}\right) + S_j \tag{6.1}$$

Equation (6.1) applies to both regions (1) and (2) in Figure 6.1, where c_j is the volumetric species concentration based on the *total* volume, which for porous media includes the volume occupied by the solid and not just the void space containing gas mixture, and v_m is the *molar* average velocity. The source term, S_j (with units $[mol/m^3 - s]$), is only non-zero in region (2) and represents volumetric species sources/sinks due to reaction and/or adsorption ($S_j = \overline{\rho}\phi\Sigma_i \nu_{ij} r_i - \bar{\rho}(1-\phi)\partial q_j/\partial t$), where $\bar{\rho}$ is the average density of the porous mixture, ϕ is the mass fraction of porous media that contains catalyst (as opposed to sorbent), ν_{ij} is the stoichiometric coefficient of species j for reaction i, and r_i is the rate of reaction i per unit mass of catalyst $[mol/kg - s]$. The time rate of change of adsorption of species j by the sorbent, $\partial q_j/\partial t$, is only non-zero for species j = CO_2 and is determined using an appropriate model for the specific adsorbent used. To facilitate comparison with results of the complimentary experimental study and ideal kinetic model, presented in Chapter 4 and

Chapter 5, the adsorption model for K_2CO_3-promoted hydrotalcite developed by Lee et al [67], is again used for the transport-kinetic model,

$$\frac{\partial q_{CO_2}}{\partial t} = k_{ldf}\left[q_{eq}(T, P_{CO_2}) - q_{CO_2}\right] \tag{6.2}$$

where k_{ldf} is the temperature-dependent linear driving force coefficient [80], q_{eq} is the sorbent equilibrium capacity at the temperature and CO_2 partial pressure, and q_{CO2} is the instantaneous amount of CO_2 adsorbed onto the sorbent, which are local quantities varying as functions of both time and position. Details of the sorption kinetic model and equilibrium isotherm calculations can be found in Section 5.1.3 of the previous chapter.

Reaction contributions to the source terms ($\overline{\rho}\phi\Sigma_i \nu_{ij} r_i$), in equation (6.1) are due to the three SMR reactions, with the individual rates (r_i) for reverse methanation (r_{RM}), water gas shift (r_{WGS}), and the combined steam methane reforming reaction (r_{SMR}), again determined using the intrinsic kinetics model of Xu and Froment [28] that can be found in Section 5.1.2 of the previous chapter.

The Maxwell-Stefan formulation is used to determine the diffusive flux in the z-direction of each species j ($J_{z,j}$) relative to the molar average velocity v_m in equation (6.1). The Maxwell-Stefan approach is adopted, as opposed to using a pseudo-binary Fickian approach [86], because it is rigorous in treating multiple component mixtures and has been found to be more accurate especially in the limit of large disparity in molecular weights of the mixture components [92]. In a previous study by Yun *et al.* [90], the use of Maxwell-Stefan was critical in achieving quantitative agreement between simulation and experimental results in a sorption-free CHAMP reactor with methanol as fuel. According to Maxwell-Stefan, the diffusive flux $\overrightarrow{\boldsymbol{J}_{z,J}} = -c_T[B]^{-1}\frac{\partial}{\partial z}\left(\overrightarrow{\boldsymbol{c}_J}/c_T\right)$, where $\overrightarrow{\boldsymbol{J}_{z,J}}$ is a column

vector representing the diffusive fluxes of $N_s - 1$ species and $[B]$ is an $(N_s - 1) \times (N_S - 1)$ matrix [93] with terms:

$$B_{lm} = \begin{cases} x_l \left(\dfrac{1}{\mathcal{D}_{lN_s}} - \dfrac{1}{\mathcal{D}_{lm}} \right) & l \neq m \\ \dfrac{1}{\mathcal{D}_{lN_s}} + \sum\limits_{\substack{k=1 \\ k \neq l}}^{N_s - 1} x_k \left(\dfrac{1}{\mathcal{D}_{lk}} - \dfrac{1}{\mathcal{D}_{lN_s}} \right) & l = m \end{cases} \tag{6.3}$$

where x_l is the mole fraction of species l and $\mathcal{D}_{lm}$ is the pair-wise binary diffusion coefficient of species l in species m. The binary diffusion coefficients used to populate the $[B]$ matrix are calculated by Chapman-Enskog theory [86]. In the porous media region, the binary gas-phase diffusion coefficients in the $[B]$ matrix are multiplied by the local porosity divided by the tortuosity (τ) to account for the impact of the packed bed on the gas diffusion path $\left(\mathcal{D}_{lm,eff} = \mathcal{D}_{lm} \cdot \bar{\varepsilon}/\tau\right)$ [94]. The diffusive flux of the remaining N_s^{th} species can be subsequently determined using that, by definition, the sum of the diffusive fluxes for all species must be zero.

The transient temperature distribution in the CHAMP-SORB reactor is determined by solving the 1D energy conservation equation for a packed bed reactor, in the limit of simplifying assumptions discussed in Section 6.2.2 [86],

$$\begin{aligned} &\frac{\partial}{\partial t}\left[\sum_{j=1}^{N_s}(c_j \overline{c}_{p,j} T) + \overline{\rho} c_{p,b} T\right] + \frac{\partial}{\partial z}\left[\sum_{j=1}^{N_s}\left(c_j v_m + J_{z,j}\right)\overline{c}_{p,j} T\right] \\ &= \frac{\partial}{\partial z}\left[k_{eff}\frac{\partial T}{\partial z}\right] + \bar{\varepsilon}\frac{dP_T}{dt} + S_h \end{aligned} \tag{6.4}$$

where $\overline{c}_{p,j}$ is the molar specific heat of gas species j, $c_{p,b}$ is the average specific heat of the catalyst/sorbent bed, and k_{eff} is the effective local value for thermal conductivity accounting for heat conduction through both gas and solid phases. With reference to

Figure 6.1, the generalized form of equation (6.4) is valid throughout the reactor in both of the simulation sub-domains 1 and 2; however the average solid mixture density ($\overline{\rho}$) is zero and the average packed bed porosity ($\overline{\varepsilon}$) is unity in the bulk gas domain (1). The thermal conductivity of the gas mixture is determined using a mole fraction-weighted method proposed by Mason and Saxena [95]. In the porous media region, the effective thermal conductivity is determined using a geometric mean [96] of the mole fraction-weighted gas mixture conductivity (k_{mix}) and the solid conductivity (k_s), or $k_{eff} = (k_{mix})^{\varepsilon}(k_s)^{1-\varepsilon}$. Additionally, S_h is the volumetric thermal energy generation/ consumption term due to reactions and CO_2 adsorption ($S_h = \bar{\rho}\phi\Sigma_i \Delta H_i r_i + \bar{\rho}(1-\phi)\Delta H_{ads} \cdot \partial q_{CO_2}/\partial t$, where ΔH_i is the heat of reaction i given in equations (2.1) – (2.3), and $\Delta H_{ads} = -42.2\ kJ/mol$ is the exothermic heat of adsorption for CO_2 on K_2CO_3-promoted hydrotalcite [67]). The thermal generation term is only non-zero in the catalyst/sorbent region.

To complete the model formulation, the system of species and energy conservation governing equations need to be supplemented by the closure relationships for the reactor pressure and total gas-phase molar concentration (mixture density). Total reactor pressure (P_T) is an unknown that must be solved as it impacts the reaction (r_i's), adsorption $\left(\partial q_{CO_2}/\partial t\right)$ and H_2 permeation rates ($J_{H_2,perm}$). The total molar concentration is an outcome of the continuity condition that needs to be satisfied locally everywhere, yielding the molar average velocity distribution in the reactor, which contributes to the advective terms in the species and energy conservation equations.

The total reactor pressure, assumed to be spatially uniform, is determined using the total number of moles (per unit area) of gas in the reactor at a given time (N_T'') and the

ideal gas equation of state modified (in porous media sub-domain 2) by the average packed bed porosity ($c_T = P_T\bar{\varepsilon}/R_uT$ where R_u is the universal gas constant). The total moles per unit area are equal to the total concentration integrated over the entire (gas bulk and porous media) reactor domain ($N_T'' = \int_{-d}^{H(t)} c_T dz$). Substituting the definition of total concentration from the ideal gas equation of state and solving for P_T yields the following relationship for total reactor pressure:

$$P_T = \frac{N_T'' R_u}{\int_{-d}^{H(t)} \bar{\varepsilon}\,[T(z)]^{-1} dz} \tag{6.5}$$

The total number of moles in the reactor (per unit area), N_T'', in equation (6.5) introduces an additional unknown that must be solved for by accounting for the change in total moles in the reactor due to reaction/adsorption ($\int S_j dz$) and permeation at the membrane surface ($J_{H_2,perm}$):

$$\frac{dN_T''}{dt} = \int_{-d}^{0} \left(\sum_{j=1}^{N_s} S_j \right) dz - J_{H_2,perm} \tag{6.6}$$

A governing equation for the molar average velocity can be derived by summing the species conservation equation over all species N_s, and recognizing that the sum of the diffusive fluxes is zero. This yields a continuity equation for the total molar concentration (mixture density):

$$\frac{\partial c_T}{\partial t} + \frac{\partial}{\partial z}(c_T v_m) = \sum_{j=1}^{N_s} S_j \tag{6.7}$$

Lastly, one final equation is necessary to close the problem (because only $N_s - 1$ species transport equations are independent): the sum of the individual concentrations must equal to the total concentration as determined using the ideal gas equation of state and the local

temperature/porosity. The spatial concentration profile of the remaining (any one can be chosen) N_s^{th} species is therefore found using:

$$c_{N_s}(z) = c_T(z) - \sum_{j=1}^{N_s-1} c_j\,(z) \tag{6.8}$$

6.2.4 Boundary conditions

The boundary conditions of species concentration in the CHAMP-SORB domain are given in equation (6.9). The membrane surface (at $z = -d$) is non-permeable to all species,

$$\left(c_j v_m\right)\big|_{z=-d} + J_{z,j}\big|_{z=-d} = 0 \tag{6.9a}$$

with the exception of H_2, which diffuses through the fully dense (i.e., no perspiration) solid membrane:

$$\left(c_{H_2} v_m\right)\big|_{z=-d} + J_{z,H_2}\big|_{z=-d} = -\frac{D_{mem}}{\delta}\left[\left(P_{H_2}\big|_{z=-d}\right)^{1/2} - P_{H_2,\infty}^{1/2}\right] \tag{6.9b}$$

The right side of equation (6.9b) represents the permeation flux ($J_{H_2,perm}$) through the H_2-selective Pd-Ag membrane, where $J_{H_2,perm} = \frac{D_{mem}}{\delta}\left[\left(P_{H_2}\big|_{z=-d}\right)^{1/2} - P_{H_2,\infty}^{1/2}\right]$, according to Sievert's Law for dissociative hydrogen diffusion with vanishing gas-phase mass transfer resistances on both sides of the membrane. The temperature-dependent membrane permeability is $D_{mem} = 4.1 \times 10^{-6}\, exp\{-1387.9/T\}$ $[mol \cdot m/(m^2 \cdot s \cdot bar^{1/2})]$, as was reported in the membrane characterization experiments in Section 4.3.2. The piston surface, at $z = H(t)$, is impenetrable to all species, resulting in the following species flux balance accounting for the boundary motion with a velocity of U^P :

$$\left(c_j v_m\right)\big|_{z=H(t)} + J_{z,j}\big|_{z=H(t)} = \left(c_j\big|_{z=H(t)}\right) U^P \tag{6.9c}$$

The temperature boundary conditions for the energy equation are given in equations (6.10a) and (6.10b) for the membrane and piston surfaces, respectively. At the membrane surface, the advective and conductive energy fluxes from top at the boundary of the domain ($z = -d$) are balanced by the heat supplied at the bottom on the permeate side of the membrane at the (potentially time-varying) temperature $T_H(t)$.

$$\left(J_{H_2,perm} \cdot \overline{c}_{p,H_2}\right)T|_{z=-d} - \left(k_{eff}\frac{\partial T}{\partial z}\right)\Big|_{z=-d} = h_{eff}[T_H(t) - T|_{z=-d}] \tag{6.10a}$$

To provide sufficient heat to the reaction, a proportional temperature control strategy is employed where the heater temperature (T_H) is varied to drive the reactor temperature to a target value (T_0): $T_H(t) = T_0 + k_p \cdot [T_0 - T|_{z=-d}(t)]$. At the opposite boundary, the piston is considered to be well insulated, and as such the heat flux (and temperature gradient) at $z = H(t)$ is zero:

$$\frac{\partial T}{\partial z}\Big|_{z=H(t)} = 0 \tag{6.10b}$$

The initial conditions for the reactor are that the temperature is uniform as the reactor is preheated to the nominal target operating temperature ($T(z)|_{t=0} = T_0$), the mixture is initially quiescent ($v_m(z)|_{t=0} = 0$), and the initial total molar concentration (mixture density) is determined using the ideal gas equation of state at the initial temperature (T_0) and pressure (P_T): $c_T(z)|_{t=0} = P_T\,\bar{\varepsilon}(z)/R_u T_0$. The reactor is filled primarily with H_2O and CH_4 in a ratio according to the operating S/C ratio. Trace amounts (only 0.01% of the total initial concentration) of each of the other species considered (H_2, CO_2, and CO) are included to avoid singularities in the Xu and Froment rate expressions. Because the sorbent cannot be fully regenerated from the previous operation cycle using reactor volume expansion-driven pressure swing adsorption, a spatially uniform initial sorbent

loading of $q_0 = 0.25\, mol/kg$ is employed as the sorbent initial condition, which is established after achieving a periodic quasi-steady state following CHAMP-SORB startup through several cycles (as was discussed in Section 5.5).

6.2 Solution Procedure

In solving the coupled set of partial differential and algebraic equations that govern the CHAMP-SORB reactor behavior, the equations are discretized using the Finite Volume Method [97]. The bulk gas region above the porous catalyst/sorbent must also account for the variable volume due to the piston motion and is simulated using a coordinate transformation similar to the variable domain height formulation used to solve boundary layers (see Appendix D for details) [98]. A fully implicit time discretization (*i.e.*, in determining source terms and advective/diffusive fluxes, values at each node at the *end*, as opposed to the *beginning*, of the timestep are utilized) is implemented. In order to adequately handle the stiff SMR reaction kinetics, an underrelaxation factor ranging from 0.3 – 0.5 is utilized to aid in numerical stability. The advective fluxes are treated using an upwinding methodology while diffusive fluxes are treated using central difference scheme with second order accuracy [97]. Figure 6.2 illustrates the iterative solution procedure used to solve the implicit set of discretized equations at each time step until convergence has been reached and the simulation can move on to the subsequent timestep.

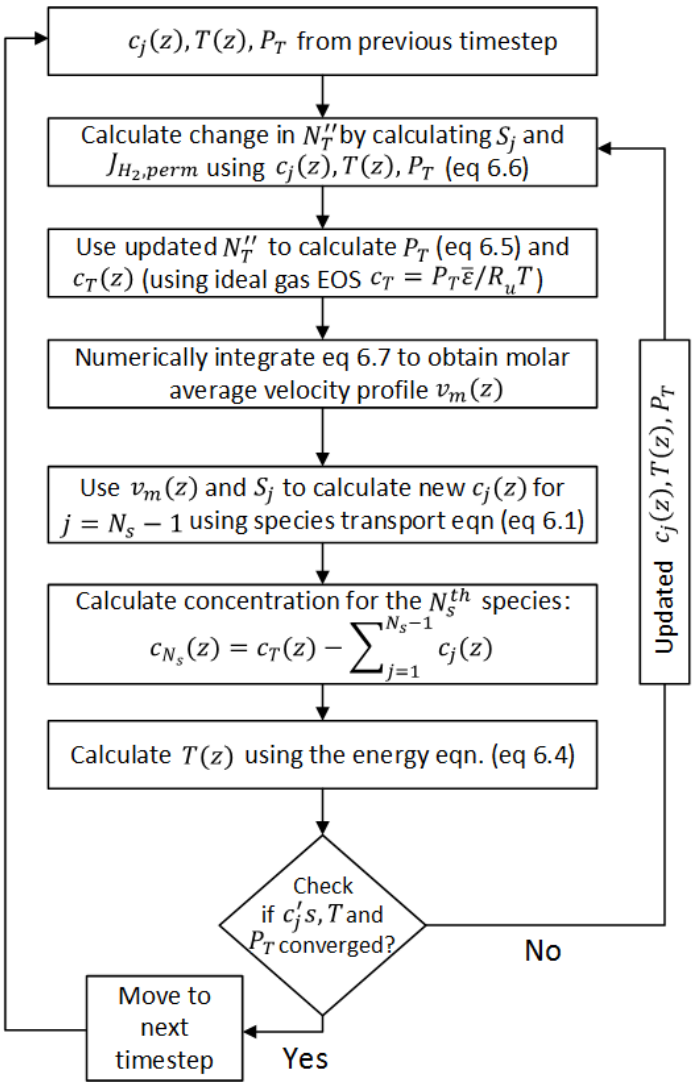

Figure 6.2: Flowchart of the iterative algorithm used to obtain solution of the CHAMP-SORB model at each time step.

In the flowchart presented in Figure 6.2, equation (6.7) is numerically integrated to find the velocity profile $v_m(z)$ at any given time required to maintain spatially uniform total pressure P_T in the reactor. This equation requires only one boundary condition, either at the membrane surface where the molar average velocity is determined by the H_2 permeation flux through the membrane ($c_{H_2} v_m\big|_{z=-d} = -J_{H_2,perm}$) or at the piston

surface where the velocity is determined by the piston trajectory ($v_m|_{z=H(t)} = U_p$). The use of either boundary condition, as has been shown in a previous study [18], leads to identical results due to self-consistency of the continuity condition. The values of total concentration (c_T) in equation (6.7) are not computed directly as the summation of concentration of each species j; rather, via the ideal gas equation of state at the local temperature and porosity ($c_T = P_T\bar{\varepsilon}/R_uT$).

Complete details on the coordinate transformation to account for the varying volume of the bulk gas region (due to piston motion), the discretization of the coupled governing equations, and the iterative solution procedure are provided in the Appendix D.

6.3 Baseline Model Results and Discussion

6.3.1 Operational case selection

The purely kinetic analysis of CHAMP-SORB reactor presented in Chapter 5 was shown to be fairly accurate in capturing experimentally observed behavior of a permeation-limited CHAMP-SORB prototype reactor discussed in Chapter 4. However, to assess the expected performance and trade-off associated with the CHAMP-SORB reactor's scale-up to higher hydrogen productivity levels relevant to practical applications, inclusion of heat and mass transfer effects is critical. To this end, two simulation cases are considered in detail: (1) a reactor with an initial height such that the transport resistances are on the order of 1/10th of the H_2 permeation and SMR reaction resistances, and (2) a taller reactor where the transport resistances are equal to the permeation and reaction resistances. For both cases, a consistent set of baseline operating

parameters and initial conditions are utilized (summarized in Table 6.1) to facilitate the performance comparison.

Table 6.1: Transport-Kinetic Model Baseline Parameters

Model Parameter	**Value [units]**
Target Operating Temperature (T_0)	400 [$^{\circ}C$]
Initial Sorbent Loading (q_0)	0.25 [mol/kg]
S/C Ratio	2 [$-$]
Reactor Pressure (P_T)	5 [$bar\ abs$]
Membrane thickness (δ)	10 [μm]
Permeate Side H_2 Partial Pressure ($P_{H_2}^{\infty}$)	0.2 [bar]
H_2 Permeate Conc. Time Constant ($\tau_{P_{H_2}}$)	2 [s]
Effective Heater Heat Transfer Coeff. (h_{eff})	67 [W/m^2-K]
Heater Proportionality Constant (k_p)	4 [$-$]
Sorbent Density (ρ_{sorb})	1300 [kg/m^3]
Sorbent Porosity (ε_{sorb})	0.24 [$-$]
Catalyst Density (ρ_{cat})	951 [kg/m^3]
Catalyst Porosity (ε_{cat})	0.5 [$-$]
Catalyst/Sorbent Specific Heat ($c_{p,b}$)	850 [$J/kg-K$]
Catalyst/Sorbent Thermal Conductivity (k_s)	0.3 [$W/m-K$]
Catalyst/Sorbent Tortuosity (τ)	3 [$-$]

The gaseous species properties used in the simulation are summarized in Table 6.2. Values for thermal conductivity (k_j) and molar specific heat ($\bar{c}_{P,j}$) for each species j are taken from the NIST WebBook [99]. The effective diffusivity of each species relative to the mixture ($\mathcal{D}_{j,mix}$) is calculated by first determining the binary diffusivity of species j with each of the other species present using Chapman-Enskog theory [86], then adjusting each binary diffusivity for pressure dependence ($D_{AB} \propto 1/P$), and finally calculating the ***effective*** diffusivity of species j with respect to the mixture using $\mathcal{D}_{j,mix} = (1-x_j)/\sum_{\substack{k=1 \\ k\neq j}}^{N_s}\left[x_k/\mathcal{D}_{jk}\right]$ [94]. The effective diffusivity values reported in Table

6.2 are only used for reference and for scaling analysis; in solving the coupled transport-kinetic equations, the Maxwell-Stefan relations are used to calculate diffusive fluxes.

Table 6.2: Species Gas Properties at 400℃, 5 bar for Baseline Transport-Kinetic Simulations

Species	$k_j\ [W/m-K]$	$\bar{c}_{P,j}\ [J/mol-K]$	$\mathcal{D}_{j,mix}\ [m^2/s]$
H_2	0.322	29.41	6.7×10^{-5}
CO_2	0.0463	48.85	1.6×10^{-5}
CO	0.0485	31.04	2.1×10^{-5}
CH_4	0.0978	53.97	2.3×10^{-5}
H_2O	0.0484	37.30	2.3×10^{-5}

The precise reactor dimensions and catalyst/sorbent loading for each case are determined using a methodology of time scale analysis introduced in Chapter 5. To estimate the mass transport resistance, the same definition of timescale presented in equation (5.9) is utilized, (*i.e.*,$\tau_{trans} = N^0_{CH_4}/\bar{r}_{CH_4,trans}$ where $N^0_{CH_4}$is the initial moles of CH_4 in the reactor and $\bar{r}_{CH_4,trans}$ is the rate of CH_4 consumption predicted to occur in the transport limited regime) and the resistance is simply the timescale divided by the reactor initial height (to normalize for the amount of fuel in the system). The initial amount of CH_4 in the reactor is determined using the ideal gas equation of state ($N^0_{CH_4} = \left(x^0_{CH_4} P_T A_c H_0^{eff}\right)/R_u T_0$) making use of the concept of "effective" initial height (H_0^{eff}) from Chapter 5 to account for the volume of fuel in the porous media region: $H_0^{eff} = (H_0 + \bar{\varepsilon} d)$.

To determine the expected rate of CH_4 consumption in the mass transport limited regime, expected values for the mole fractions of H_2 at the membrane surface ($x_{H_2,memb}$) and at the interface between the porous media and the bulk gas domain ($x_{H_2,int}$) are

calculated and the characteristic rate of H_2 transport ($\bar{r}_{H_2,trans}$) is then estimated to be the rate of H_2 diffusion across the porous media layer (using that the flux of species A in a binary mixture $N_A'' \sim c_T \mathcal{D}_{AB} \cdot [\Delta x_A / \Delta z]$):

$$\bar{r}_{H_2,trans} \sim c_T \left[\frac{\bar{\varepsilon}}{\tau}\mathcal{D}_{H_2,mix}\right] \frac{x_{H_2,int} - x_{H_2,memb}}{d} \tag{6.11}$$

Equation (6.11) makes use of the H_2 effective diffusivity from Table 6.2. The value of total concentration, c_T, is calculated using the ideal gas equation of state, and the porous media layer thickness (d) will vary with size of reactor, as a larger reactor contains more fuel and will require additional sorbent to adsorb all the produced CO_2. Because in the CHAMP-SORB all CH_4 is consumed and the H_2 yield efficiency is over 99%, according to the stoichiometry of the overall SMR reactions ($CH_4 + 2H_2O \rightleftarrows 4H_2 + CO_2$), the characteristic rate of H_2 production is $4x$ the rate of CH_4 consumption,

$$\bar{r}_{CH_4,trans} \sim \frac{1}{4} \cdot c_T \left[\frac{\bar{\varepsilon}}{\tau}\mathcal{D}_{H_2,mix}\right] \frac{x_{H_2,int} - x_{H_2,memb}}{d} \tag{6.12}$$

Equation (6.12) is used to estimate the characteristic CH_4 consumption rate in the mass transport limited regime, $\bar{r}_{CH_4,trans}$, which can then be used to determine the transport timescale (τ_{trans}) and resistance (τ_{trans}/H_0^{eff}) for a given reactor height (H_0^{eff}). The characteristic H_2 mole fractions in equations (6.11) and (6.12) are determined using a procedure similar to what is outlined in Section 5.4.1, where expected mole fractions under prevailing conditions of operation for each regime are determined. As was done in the reaction and adsorption timescale calculations, to determine the H_2 mole fraction at the membrane surface it is assumed that permeation resistance is negligible and the H_2 partial pressures on each side of the membrane are equal ($x_{H_2,memb} = P_{H_2}^{\infty}/P_T$). To determine the H_2 mole fraction at the interface between the

porous media and the bulk gas domain, it is assumed that: (*i*) $x_{CO} \sim 0$, (*ii*) $x_{CH_4} \sim 2x_{H_2O}$ based on 2:1 S/C ratio, (*iii*) the SMR reaction is locally at equilibrium according to equation (5.10), and (*iv*) the characteristic CO_2 mole fraction (x_{CO_2}) can be determined using the characteristic CO_2 partial pressure according to the sorbent utilization and sorption isotherm ($x_{CO_2} = \bar{P}_{CO_2}(T, \bar{q})/P_T$, where P_T is the total reactor pressure and $\bar{P}_{CO_2}(T, \bar{q})$ is the characteristic CO_2 partial pressure in the reactor as defined in Figure 5.6). These four assumptions, combined with the fact that the sum of the mole fractions must equal unity ($\sum x_j = 1$) provide enough information to solve the expected composition of the mixture at the porous media-bulk gas interface (including $x_{H_2.int}$).

Using the methodology outlined above to calculate the mass transport resistance, the following procedure is used to determine the exact reactor parameters for each of the two simulated cases aimed to assess the effect of mass transfer on performance:

1. The permeation resistance τ_{perm}/H_0^{eff} is calculated for the chosen membrane thickness ($\delta = 10\ \mu m$) at the target operating temperature, ($T_0 = 400$℃), reactor pressure ($P_T = 5\ bar$) and H_2 collection pressure ($P_{H_2}^{\infty} = 0.2\ bar$).
2. The amount of catalyst (per unit area) is chosen such that the reaction resistance is equal to the permeation resistance calculated in step 1.
3. The desired sorbent amount (per unit area) is determined as a function of effective reactor height (H_0^{eff}) by calculating the initial moles of CH_4 in the reactor and determining the required mass of sorbent to adsorb all of CO_2 that will be produced upon complete conversion of CH_4 through the SMR process. The required sorbent mass can be determined using the difference between the initial sorbent loading (q_0) and the saturation CO_2 loading q_{sat} (in the limit of high P_{CO_2}). An excess margin of 20% sorbent beyond the calculated value is utilized to ensure full CO_2 adsorption (as is required [81] to achieve full CH_4 conversion and near-100% H_2 yield).

4. For each effective reactor height (and thus initial total fuel input) considered, the fraction of catalyst mass relative to total mass of sorbent and catalyst (ϕ) is used to calculate the effective density and porosity of the porous media using the weighted harmonic mean: $\overline{\rho} = [\phi/\rho_{cat} + (1-\phi)/\rho_{sorb}]^{-1}$ and $\bar{\varepsilon} = \phi(\bar{\rho}/\rho_{cat})\varepsilon_{cat} + (1-\phi)(\bar{\rho}/\rho_{sorb})\varepsilon_{sorb}$, respectively.
5. The average density and porosity are used to calculate the catalyst/sorbent layer thickness (d) and required reactor initial height ($H_0 = H_0^{eff} - \bar{\varepsilon}d$) corresponding to each considered effective initial height.
6. The expected rate of CH_4 consumption in the transport limited regime ($\bar{r}_{H_2,trans}$) is estimated using equation (6.12), and this value is used to determine the mass transport timescale (τ_{trans}) and the transport resistance (τ_{trans}/H_0^{eff}) as a function of initial reactor size. Values of H_0^{eff} are determined that should result in mass transport resistances that are (*i*) 1/10th of the permeation and reaction resistance for case 1, and (*ii*) equal to the permeation and reaction resistance for case 2.

Following the procedure outlined in steps (1) – (6) above, the resulting values of values of effective reactor size H_0^{eff} and the corresponding sorbent/catalyst mass loadings and resistances are summarized in Table 6.3.

Table 6.3: Initial Reactor Height and Simulation Parameters for Baseline Cases

Parameter	Value [units]	
	(1) $H_0^{eff} = 2.8\ cm$	**(2) $H_0^{eff} = 29.5\ cm$**
Sorbent Loading (m_{sorb})	1.60 $[kg/m^2]$	16.98 $[kg/m^2]$
Catalyst Loading (m_{cat})	0.4275 $[kg/m^2]$	
Catalyst Mass Fraction (ϕ)	0.211 $[-]$	0.0246$[-]$
Average Density ($\bar{\rho}$)	1207 $[kg/m^3]$	1288 $[kg/m^3]$
Average Porosity ($\bar{\varepsilon}$)	0.310 $[-]$	0.249 $[-]$
Catalyst/Sorbent Layer Thickness	0.00168 $[m]$	0.0135 $[m]$
Actual Initial Height (H_0)	0.0273 $[m]$	0.292$[m]$
Reaction Resistance (τ_{rxn}/H_0^{eff})	20.8 $[s/cm]$	
Permeation Resistance ($\tau_{perm}/$	20.8 $[s/cm]$	
Transport Resistance (τ_{trans}/H_0^{eff})	2.08 $[s/cm]$	20.8 $[s/cm]$

6.3.2 Impact of heat and mass transfer effects on H_2 productivity

Each reactor size outlined in Table 6.3 is simulated using the modeling approach outlined in sections 6.1 and 6.2. The simulations are performed under conditions of constant pressure operation achieved via gradual compression of the reactor volume by piston, as this operational mode was shown previously to result in the best reactor performance achieving highest hydrogen yield rate/productivity [18]. Consistent with work in the previous chapters, the operating pressure is set at $5\ bar$, to maximize performance while recognizing the mechanical limitations of thin membranes. Figure 6.3 illustrates the H_2 yield efficiency, or the cumulative quantity of H_2 permeated from the reactor relative to the maximum possible value according to the overall stoichiometry of the SMR process ($\eta_{H_2,yield} \equiv N''_{H_2,perm}/4N''_{CH_4,ini}$), as a function of residence time for each case. To isolate the sole impact of mass transfer (vs. combined heat and mass transfer), the simulations have been performed in two ways: (*i*) considering only the

species conservation equations (assuming an isothermal reactor, labeled MT only in Figure 6.3), and (*ii*) solving the full set of coupled energy and species conservation equations (labeled as HT and MT in Figure 6.3).

The H_2 yield efficiency curves for an ideal (perfectly mixed and isothermal) reactor are also reported in Figure 6.3 for comparison. For case 1, shown in Figure 6.3a, the inclusion of heat and mass transfer effects results in a delay in the time required to reach 99% CH_4 conversion from approximately $150\ s$ to $450\ s$. As the final H_2 yield is identical for the ideal and transport-kinetic model simulations, this $3x$ increase in required residence time translates into a $3x$ reduction in H_2 yield rate or reactor productivity. Also of note, while mass transfer effects account for a larger portion of the performance gap between the ideal and real reactor, thermal effects do have a contribution that accounts for an additional $25\ s$ required to reach maximum H_2 yield efficiency. It is important to emphasize here that in the CHAMP-SORB reactor with multiple, tightly linked, interacting processes occurring concurrently, the observed significant ($\sim 3x$) reduction in H_2 yield rate is much greater than would be expected based purely on timescale analysis, as transport timescale for this reactor size is an order of magnitude smaller than that of reaction and permeation and transport effects should not play a very significant role to so negatively impact reactor performance. Reasons for this reduction are explored in detail in sections 6.3.3 and 6.3.4.

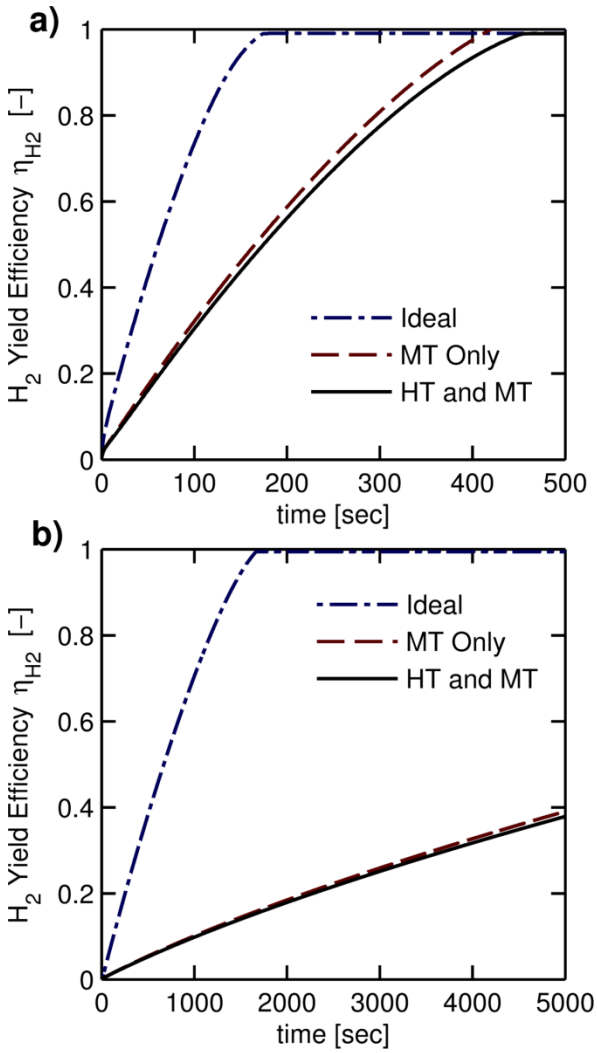

Figure 6.3: Comparison of reactor H_2 yield efficiency versus residence time for an ideal (perfectly mixed and isothermal) reactor model, an isothermal reactor model incorporating mass transfer effects using the Maxwell-Stefan diffusion model (MT), and a non-isothermal model accounting for both heat and mass transfer effects (HT and MT). Results reported for an a) $2.8\ cm$ initial height and b) $29.5\ cm$ initial height reactor, via reactor volume compression to maintain constant pressure of $5\ bar$.

For the larger reactor studied in case 2, the impact of heat and mass transfer is, as expected, even more significant. For the ideal reactor, the time required to reach 99% H_2 methane conversion scales directly with the height of the reactor (case 1 is approximately $10x$ smaller than case 2 and takes roughly $10x$ less time to achieve 99% H_2 yield); however, transport limitations cause a much more severe increase in required residence

time (and accordingly a drop in H_2 productivity). To better understand the reactor behavior that results in a performance reduction greater than would be predicted by the simplified timescale analysis alone, and identify possible methods to mitigate the detrimental effects of transport resistances, the discussion in the following sections examines closely the temporal evolution and coupling of the temperature, species concentration, and reaction/adsorption rate spatial profiles.

6.3.3 Case 1: Transport resistance 1/10th that of reaction and permeation

Figure 6.4 shows the evolution of the temperature and mole fraction distributions within a CHAMP-SORB reactor of effective initial height of $H_0^{eff} = 2.8\,cm$. The membrane is located at the left and the piston is located on the right side of each plot. The reactor volume is compressed to maintain constant pressure as H_2 permeates and CO_2 is adsorbed, and the required piston motion can be seen by the shift in location of the right-most point in the temperature and mole fraction profiles. Also shown are the spatial distributions of individual reaction rates (labeled "RM", "WGS" and "SMR" for the reactions listed in eqs 3-5) and adsorption rate (labeled "ADS") within the catalyst/sorbent porous layer (for dimensionless position ranging from $-d/H_0 < z/H_0 < 0$).

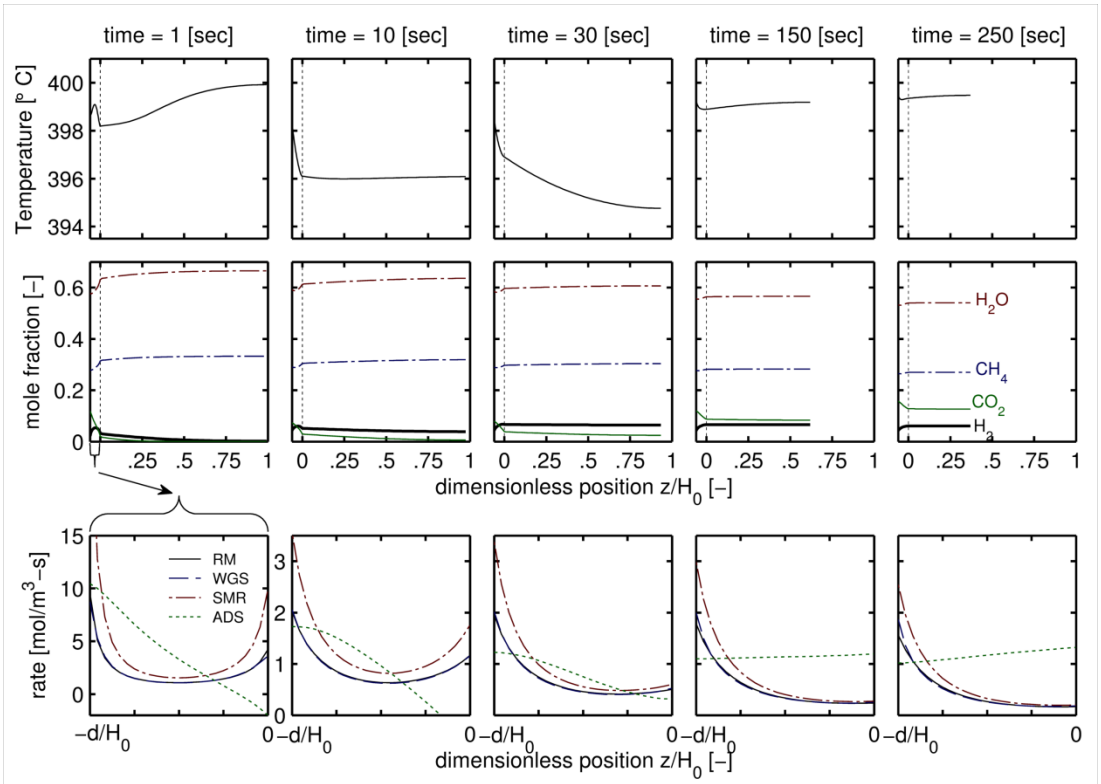

Figure 6.4: Temporal evolution of spatial temperature, species mole fraction and local reaction/adsorption rates (the rates are shown within the porous sorbent/catalyst layer only) for a CHAMP-SORB reactor with $H_0^{eff} = 2.8\ cm$ operated at constant pressure through compression of the reactor volume until the piston reaches the top of the catalyst/sorbent porous layer and cannot move further. To better show reaction/adsorption rates, the y-axis scale of the bottom row of plots is modified between the 1st and 2nd columns from the left (then held constant for subsequent plots moving rightward).

Several important aspects of the reactor behavior that impact the CHAMP-SORB performance can be observed in Figure 6.4. First of all, two distinct operating regimes can be identified: initially, up until $t \sim 30\ s$, a "start-up" regime exists where the H_2 and CO_2 that are produced in the porous media region loaded with catalyst diffuse into the gas region. During this time, the reaction rates are elevated at both the membrane surface and near the porous media-gas interface, due to an efficient removal of reactant products (H_2 and CO_2), thus locally shifting equilibrium and promoting forward reaction rates of

reversible RM and WGS reactions. As H_2 has a higher diffusivity, it more rapidly diffuses through the domain and reaches the impermeable piston surface quicker than CO_2. The bulk-gas diffusion timescale ($\tau_{diff,j} \sim H_0^2/\mathcal{D}_{j,mix}$ for each species j) does a good job predicting the time required for the H_2 and CO_2 concentration fronts to reach the piston. The H_2 bulk gas diffusion timescale is approximately $11\ s$ ($[0.0273\ m]^2/6.7 \times 10^{-5}\ m^2/s$), while the CO_2 diffusion timescale is roughly $5x$ larger due to CO_2's lower effective diffusivity. Also seen in Figure 6.4, the temperature profile within the porous region, initially spatially uniform at $T(z) = 400$℃, assumes a concave-down shape early in the process (evident in the $t = 1\ s$ time instant) because the endothermic reaction rates are highest at the boundaries of the porous zone where the H_2 concentration remains lowest due to removal by permeation at the left/membrane surface and diffusion to the bulk gas domain at the right interface. Interesting peculiarities of thr transient temperature behavior at the beginning of the CHAMP-SORB reaction step are discussed in greater detail later in this section, although an overall magnitude of the temperature drop is rather small (less than 5^oC at its maximum) throughout the entire reaction/compression process.

Once the H_2 concentration front reaches the piston surface, at times greater than $t \sim 30\ s$ in the $H_0^{eff} = 2.8\ cm$ reactor shown in Figure 6.4, the second operational regime begins. This regime is "quasi-steady" in the sense that within the bulk gas phase reactor domain the species mole fractions are essentially spatially uniform. As time progresses, the CO_2 concentration rises slowly (as an increasingly high CO_2 partial pressure is required to facilitate further adsorption on the K_2CO_3-promoted HTC sorbent, according the behavior of the sorption equilibrium isotherm) and the volume of the gas

region is slowly reduced via piston motion to maintain constant reactor pressure; yet these changes occur slow enough, as compared to time scale for species diffusion, for the distribution of species within the gas region to remain spatially uniform. As the CO_2 mole fraction rises, the CH_4, H_2O, and H_2 mole fractions all drop slightly to compensate, gradually slowing down the rate of reaction and H_2 permeation.

To better illustrate the evolution of H_2 and CO_2 concentration during the "start-up" regime of the CHAMP-SORB reaction step, Figure 6.5 illustrates the mole fraction of just the two most important species, H_2 and CO_2, with greater time resolution during the interval from $t = 0.05\ s$ to $t = 30\ s$, focused on the behavior in the porous media layer and the immediate near-interface region of the adjacent bulk gas phase domain ($-d/H_0 \leq z/H_0 \leq 0.27$). The mole fraction of both species is initially vanishingly small; however, the concentration of each quickly rises within the first $0.5\ s$ of operation when the SMR reaction rates are the fastest. The mole fraction of H_2 assumes a steeply concave-down profile due to transport away from the porous media region at the membrane surface (due to permeation across the membrane) and at the porous media-gas interface (due to diffusion into the bulk gas domain). The CO_2 concentration monotonically decreases from a maximum at the membrane surface (which is impermeable to any species other than H_2). The magnitude of the change in CO_2 concentration across the porous zone is greatest at $t = 0.5\ s$ and is cut by more than half at $t = 30\ s$. This is consistent with the CO_2 adsorption timescale (equal to $1/k_{LDF}$, which at 400℃ is $1/(3\ min^{-1}) = 20\ s$).

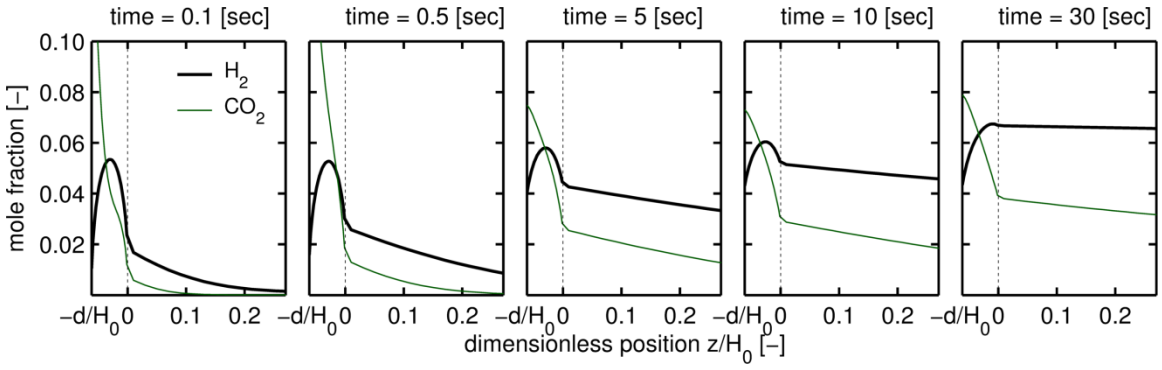

Figure 6.5: Temporal evolution of the H_2 and CO_2 mole fractions during the transient startup period of a CHAMP-SORB reactor with $H_0^{eff} = 2.8\ cm$. The selectively-permeable H_2 membrane is located at the left side of each figure (at the dimensionless position $-d/H_0$), and the transition between the porous media and gas-bulk only domain is denoted by a vertical dashed line. The simulations are for variable volume, constant pressure ($5\ bar$) operation under conditions listed in Table 6.1.

Looking closer at the transient temperature profile in Figure 6.4, somewhat counter-intuitive temperature distributions are observed; specifically, because there are no heat sinks in the bulk gas region and the piston is modeled as perfectly insulated, the temperature in the gas domain would have not been expected to drop below the temperature at the bulk gas-porous media interface (as energy is advected towards the porous media in the $-z$ direction as the reactor volume is compressed, and heat conduction must transfer thermal energy in a direction opposite the temperature gradient). At the $t = 30\ s$ time instant, however, the gas temperature at the piston surface reaches a minimum value that is below that of the bulk gas-porous media interface (whereas at $t = 10\ s$ these locations were at roughly the same temperature), indicating that between these two time instances, heat should have been transferred ***from*** the gas near the piston ***towards*** the porous media. The source of this seemingly anomalous heat transfer can be attributed to the Dufour effect, or the presence of a thermal gradient resulting from the counter-diffusion of gas species with different specific heats [100].

Specifically, the $\frac{\partial}{\partial z}\left[\sum_{j=1}^{N_s}\left(J_{z,j}\cdot\overline{c}_{p,j}T\right)\right]$ term in the energy conservation equation (6.4) that represents the divergence of the sum of the energy carried by the diffusive fluxes of all species $j = 1,2,\ldots N_s$, creates a net heat flux in the direction where species with higher specific heats are traveling, as a result of the fact that the sum of the diffusive fluxes is zero but each species carries a different amount of energy proportional to its specific heat. This curious effect has been experimentally demonstrated in a classical experiment where two gases, initially at thermal equilibrium but separated by an impenetrable barrier, develop a temperature difference on the order of 1℃ when the barrier is removed and the species diffuse into one another [101].

To isolate and prove that the observed behavior is caused by the Dufour effect, the transport-kinetic simulation for $H_0^{eff} = 2.8\,cm$ is conducted both *with* and *without* inclusion terms responsible for Dufour effects (*i.e.*, for the simulation without Dufour effects, the $\frac{\partial}{\partial z}\left[\sum_{j=1}^{N_s}\left(J_{z,j}\cdot\overline{c}_{p,j}T\right)\right]$ term is set to zero and only energy advected by the bulk velocity is considered). Figure 6.8 illustrates that in both cases the aforementioned concave down temperature profile is still seen within the catalyst layer, owing to the elevated endothermic reaction rates at the membrane surface and bulk gas-porous media interface. However, with Dufour effects considered, the drop in temperature at the bulk gas-porous media interface penetrates more rapidly into the bulk gas domain, and even locally drops below the interface temperature at $t = 0.1\,s$. During the transient start-up portion of the CHAMP-SORB reaction step, as illustrated in Figure 6.4, the H_2 that is produced by the SMR reaction diffuses in the $+z$ direction into the bulk gas region while CH_4 and H_2O diffuse in the $-z$ direction towards the catalyst to replace the fuel that is consumed in the reaction. As reported in Table 6.2, H_2 has a lower specific heat than CH_4

and H_2O and as such it carries less energy as it diffuses, thereby generating a net heat flux in the $-z$ direction. Overall, the time required for cycle completion is essentially identical regardless of whether simulation does or does not include Dufour effects, as the temperature in the catalyst region does not vary significantly enough between the two scenarios to impact reaction rates enough to create an appreciable performance difference.

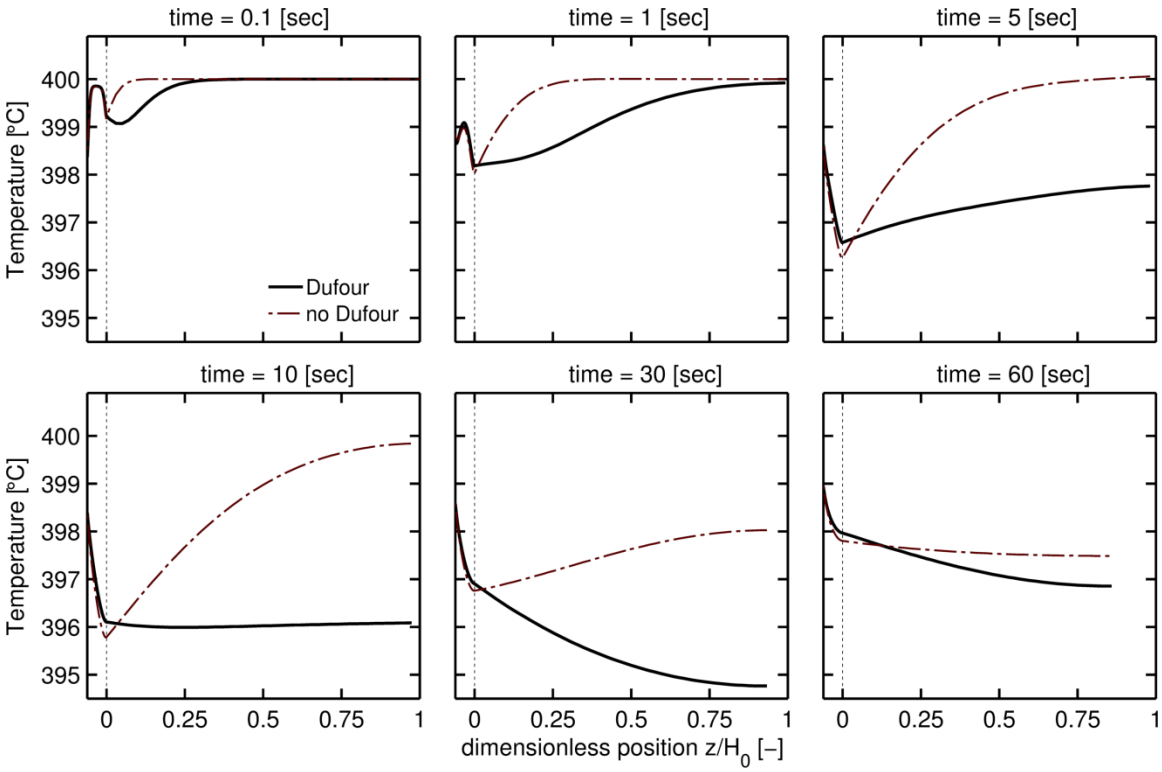

Figure 6.6: Temporal evolution of temperature profile during the transient startup period of a CHAMP-SORB reactor with $H_0^{eff} = 2.8\ cm$. The selectively-permeable H_2 membrane is located at the left side of each figure (at the dimensionless position $-d/H_0$), and the transition between the porous media and gas-bulk only domain is denoted by a vertical dashed line.

To further illustrate the impact that the spatial species concentration variations have on the reaction rates, Figure 6.7 shows the local CH_4 consumption rate per unit mass of catalyst (from either the reverse methanation followed by water gas shift, or the direct SMR path) at three different locations within the catalyst bed. Also shown for comparison are the CH_4 consumption rate for the ideal model (which is uniform due to the perfect mixing assumption), and the spatially average CH_4 consumption rate for the transport kinetic model. The local rate at the membrane surface ($z = -d$) is actually much higher than the rate observed in the ideal model predictions due to the "positive" effect of mass transfer resistance in the porous bed which limits hydrogen diffusion into the porous media bulk thus raising its local partial pressure which drives permeation through the membrane. However the rates are substantially lower both halfway between the membrane and at the bulk gas-porous media interface ($z = -d/2$) and at the interface ($z = 0$). As was demonstrated in Figure 6.4, during the transient "start-up" phase ($t < 30\ s$ for the $H_0^{eff} = 2.8\ cm$ reactor) the reaction rates at the interface remains elevated relative to the rates in the middle of the porous bed; however once the reactor transitions into the "quasi-steady" operational regime this behavior reverses and the local reaction rate is lowest at the interface. Overall, the average reaction rate as predicted by the transport-kinetic simulations is significantly lower than that of the ideal model simulation, which emphasize a significant negative effect played by heat and mass transfer resistances even in the reactor sized to keep the transport rates much below those for reaction and permeation.

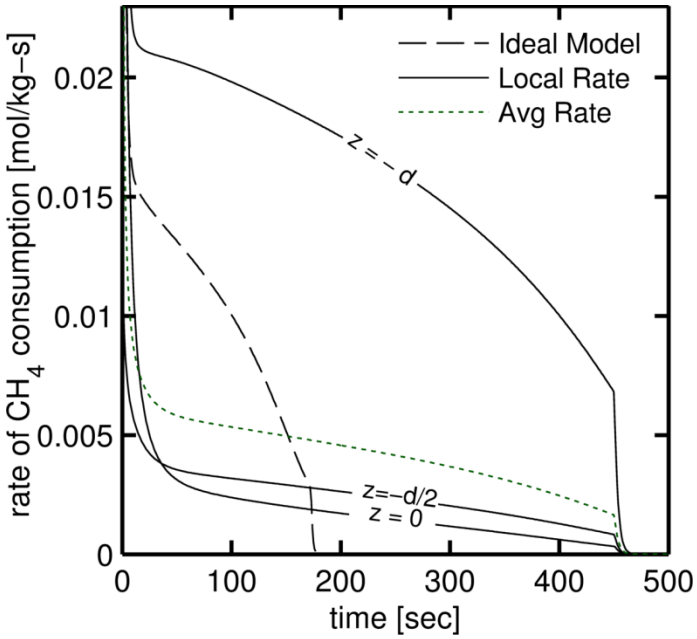

Figure 6.7: Temporal variation in local CH_4 consumption rate at three locations in the porous bed (at the membrane surface, at the bulk gas-porous media interface, and halfway between the membrane and the interface). Also shown for comparison are the CH_4 consumption rate for the ideal model simulation (the same at all three locations due to perfect mixing assumed in the ideal model) and the spatially averaged over the entire porous bed CH_4 consumption rate for the reactor as predicted by transport-kinetic simulations.

6.3.4 Case 2: Transport resistance equal to permeation and reaction resistance

When the size of reactor is increased by an order of magnitude, the transport limitations become much more significant contributors to the performance of the reactor, as compared to the permeation and reaction resistances. Figure 6.8 illustrates the impact that these limitations have on the time evolution of the spatial distribution of reactor temperature, species mole fractions, and reaction/adsorption rates. The same two regimes of operation are evident as in the $H_0^{eff} = 2.8\,cm$ case - the initial "start-up" and longer term "quasi-steady" behavior; however, the H_2 and CO_2 take substantially longer to diffuse towards the piston surface for the larger reactor, meaning that the "start-up" regime continues for a longer duration. Again, the time of this initial transient is well

predicted by the diffusion timescale for concentration front propagation into the reactor bulk volume; in this case $\tau_{diff,H_2} \sim 1250\ s$, or approximately $100x$ greater than that of case 1 because the reactor is $\sim 10x$ taller and the diffusion timescale scales with H_0^2.

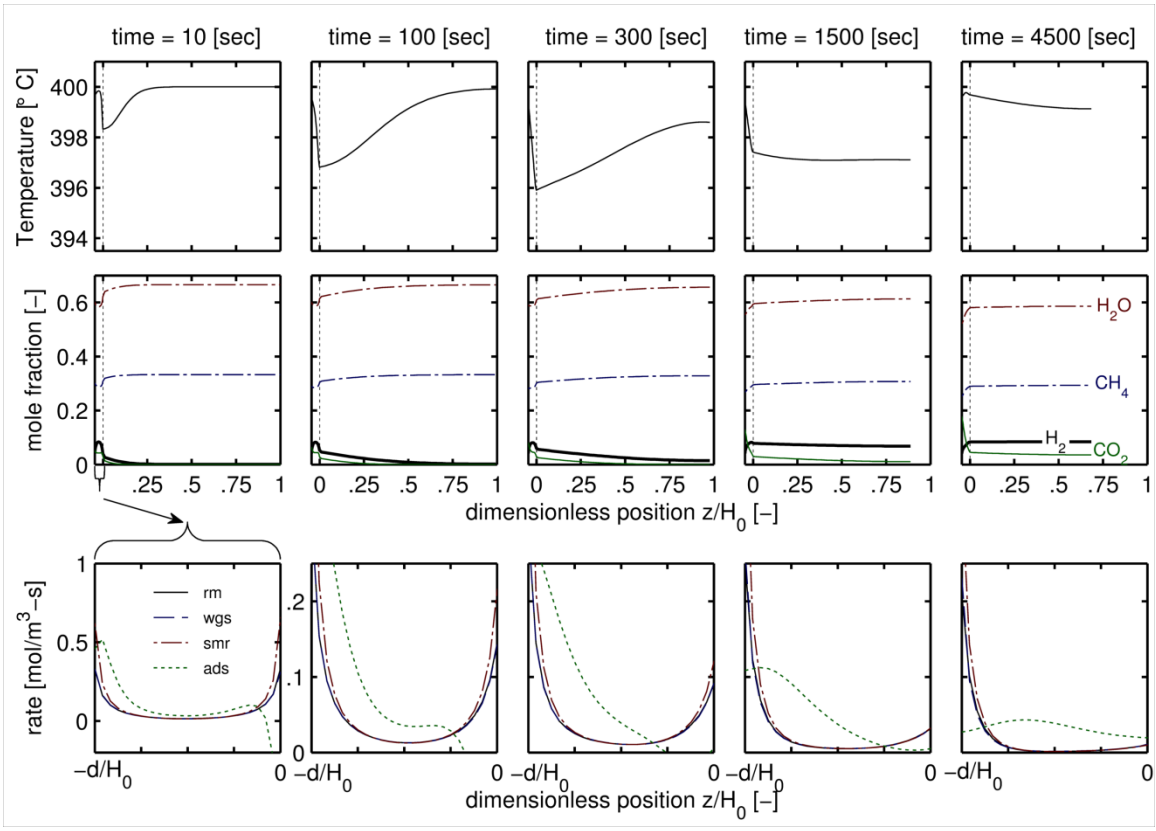

Figure 6.8: Temporal evolution of spatial temperature, species mole fractions and local reaction/adsorption rates (the rates are shown within the porous sorbent/catalyst layer only) for a CHAMP-SORB reactor with $H_0^{eff} = 29.5\ cm$ operated at constant (5 bar) pressure via volume compression. To better show reaction/adsorption rates, the y-axis scale of the bottom row of plots is modified between the 1st and 2nd column from the left (then held constant for subsequent plots moving rightward.

As a result of the increased transport resistance in the thicker catalyst/sorbent layer, there are larger H_2 and CO_2 gradients within the porous media layer for the $H_0^{eff} = 29.5\ cm$ case, resulting in larger relative variation in reaction rates across the porous

media layer in the bigger reactor. One significant implication of this concentration variation is that the reaction rates in approximately ¾ of the porous media layer are near-zero (*i.e.*, the mixture composition is at near-equilibrium values for each of the three SMR reactions), and the catalyst located in this region is effectively unutilized. As roughly 75% of the catalyst in the reactor is completely unutilized, it is not surprising that the required catalyst loading for the effective reaction timescale to match the permeation timescale is underpredicted by the purely kinetic analysis presented in Chapter 5.

6.4 Optimal Catalyst Placement to Mitigate Transport Limitations

Having noticed in Figures 6.4 and 6.8 that the catalyst furthest from the membrane is not effectively utilized, it is apparent that uniformly distributing the catalyst across the porous media layer (*i.e.*, constant ϕ everywhere throughout zone 2 in Figure 6.1) likely results in sub-optimal operating conditions, and that catalyst-sorbent stratification with catalyst concentrated near the membrane may be advantageous to improving performance. To test this hypothesis, the comprehensive transport-kinetic model simulations were performed for each of the two reactor sizes but with a layer of concentrated catalyst ($\phi = 0.75$) adjacent to the membrane surface, with the remainder of the sorbent located between this concentrated catalyst layer and the gas region (*i.e.*, a region of the porous media zone where $\phi = 0$). For a fair comparison, the total mass of the catalyst and sorbent, as well as the size of the packed bed, have been maintained the same between this case and the previous one with uniform distribution of catalyst and adsorbent across the porous layer.

6.4.1 Impact on species concentration and temperature profile

Figure 6.9 illustrates the time evolution of the temperature, species mole fractions and reaction/adsorption spatial profiles for the $H_0^{eff} = 2.8\ cm$ case, where ϕ is stratified as a piecewise function where $\phi = 0.75$ near the membrane (until all of the catalyst has been placed), then $\phi = 0$ for the remainder of the porous media region. The reaction rates are obviously zero in the sub-region of porous bed where $\phi = 0$, and the adsorption rates are lower in the region where only 25% by mass of the bed is sorbent. The resulting temperature and concentration profiles greatly impact the overall CHAMP-SORB reactor performance by allowing more effective use of the entire amount of catalyst and limiting the negative impact of temperature drop due to endothermic reaction on the reaction rates, since the heat input to the reactor from the membrane side is now more effectively delivered to the catalyst.

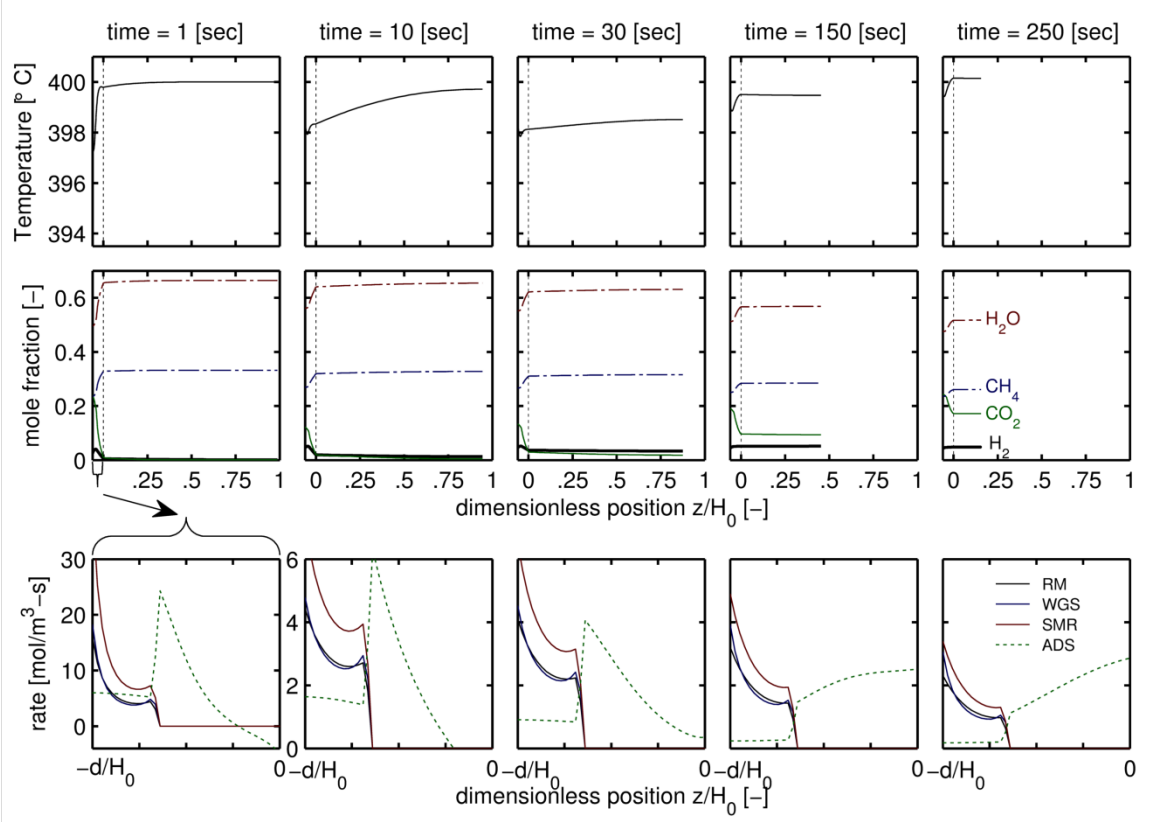

Figure 6.9: Temporal evolution of spatial temperature, species mole fractions and local reaction/adsorption rates (rates are shown only within the porous bed) for a CHAMP-SORB reactor with $H_0^{eff} = 2.8cm$ and a stratified catalyst mass fraction operated at constant ($5\ bar$) pressure via volume compression. The catalyst is loaded at 75% by weight (ϕ = 0.75) in the region of the porous bed closest to the membrane surface, with pure sorbent (ϕ = 0) placed outside of the catalyst zone.

As illustrated in the bottom row of Figure 6.9, the spatial variation in reaction rate for the reactor with catalyst concentrated closer to the membrane is much different than that for the uniformly distributed catalyst layer case of Figure 6.4. The major difference, leading to an increase in reactor performance, is that in the quasi-steady operating regime (for $t > 30\ s$), the reaction rates are more spatially uniform (and greater) across the entire region of the porous bed that contains catalyst.

The thermal behavior of the CHAMP-SORB reactor, in particular in the porous media layer, is also much different than that of the baseline (uniform ϕ) case; the temperature drop from the target value $T_0 = 400℃$ is consolidated closer to the membrane surface and is reduced in magnitude. Early in the cycle, at $t = 1\ s$, the temperature does drop slightly next to the porous media-bulk gas domain interface as some CO_2 desorbs from the sorbent (due to the initial sorbent loading of $q_0 = 0.25\ mol/kg$ as a carry-over after desorption step from the previous CHAMP-SORB cycle) and there is an associated heat consumption due to endothermic desorption; however this behavior reverses by the time instant of $t = 30\ s$ as CO_2 that is generated by the SMR process near the membrane diffuses through the porous layer and towards the piston, raising the local CO_2 partial pressure in this region and causing conditions favorable for exothermic CO_2 adsorption throughout the entire porous media zone. As a result, heat is actually applied to the area that contains catalyst (at $\phi = 0.75$) from ***both*** sides rather than predominately the membrane side in the case of uniform ϕ shown in Figure 6.4, and the temperature in the pure sorbent region of the porous layer actually slightly ***exceeds*** the target reactor operating temperature of 400℃. As a result, the reaction rates for the stratified ϕ case are not as negatively affected by the temperature drop within the porous bed as when the catalyst is uniformly distributed and intermixed with the sorbent.

6.4.2 Impact on H_2 yield efficiency

As a result of the temperature and species distribution profiles illustrated in Figure 6.9, the performance of a CHAMP-SORB reactor with a stratified ϕ is much improved relative to the baseline cases where the catalyst is uniformly distributed across the porous bed. Figure 6.10 captures this behavior by plotting the H_2 yield efficiency versus the

residence time divided by the reactor initial height (i.e., the volumetric hydrogen yield rate density, which is a proxy for volumetric productivity rate of the reactor). For the ideal simulation, the yield efficiency curve is the same regardless of initial size, indicating that the H_2 productivity rate is the same (*i.e.*, a $10x$ as tall reactor will take $10x$ as much longer time than a smaller reactor to reach complete fuel conversion, however it will produce $10x$ as much H_2 so the cycle average H_2 production rate is identical). When $H_0^{eff} = 2.8\,cm$, stratifying the catalyst closer to the membrane surface results in a nearly-half reduction in time/H_0^{eff} required to reach cycle completion, with a proportional increase in reactor productivity. The effect is even more profound in the case of a larger $H_0^{eff} = 29.5\,cm$ reactor, in which catalyst stratification near the membrane surface results in a more dramatic increase in reactor productivity.

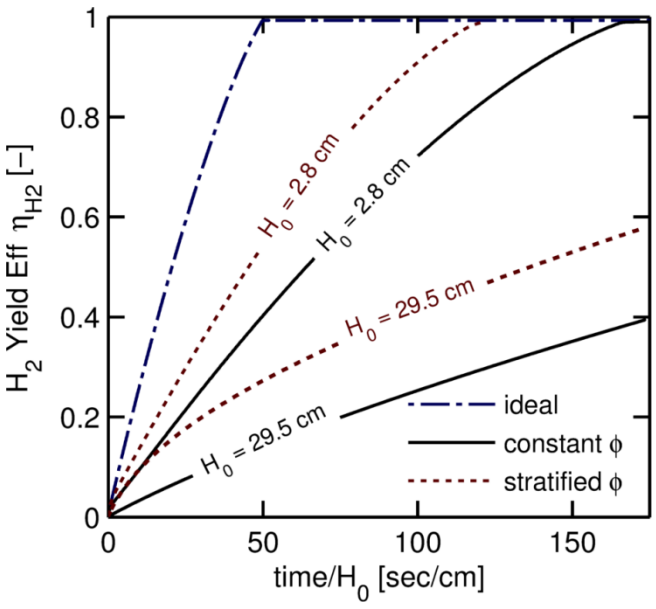

Figure 6.10: H_2 yield efficiency versus residence time (scaled by initial height H_0^{eff}) for the CHAMP-SORB reactor for varying initial heights. The reactor with catalyst concentrated closer to the membrane surface (stratified ϕ case) reduces the transport resistances, especially for heat transfer to support endothermic SMR reaction, as compared to the reactor with uniform ϕ and is much closer to the performance of an ideal reactor.

6.5 Conclusions

In this chapter, a comprehensive transport-kinetics model was developed to investigate the impact of heat and mass transfer on the CHAMP-SORB reactor performance with a particular focus on the key step of simultaneous compression-reaction-separation. It was found that, even for reactors with an average transport resistance one order of magnitude lower than the permeation and reaction resistances, significant reductions in performance occur because of the dramatic effect that local species concentration gradients and temperature drop due to endothermic reactions have on local and in turn global reaction rates. Specifically, if the catalyst is uniformly distributed within the porous media layer, which is an arrangement preferred for regular sorption-assisted SMR reactors [6, 36, 39], the catalyst near the bulk gas-porous media

interface is not effectively utilized except the very early time of the reaction cycle, and as the reactor is scaled up the reaction rates in this region approach zero. To mitigate this effect, it was demonstrated that stratifying the catalyst layer with a higher percentage of catalyst at the membrane surface, surrounded by pure sorbent to provide sufficient CO_2 adsorption capacity for complete uptake of carbon initially present in the reactor as fuel, significantly reduced the deleterious effects of concentration gradients, resulting in performance closer approaching that of an ideal reactor with no transport limitations.

In addition to mass transfer effects and concentration gradients, heat transfer effects play a role in the overall CHAMP-SORB reaction step performance; however, in the cases analyzed the temperature gradients in the system are not nearly as impactful on the reactor performance as the concentration gradients. Furthermore, stratifying the catalyst/sorbent bed with catalyst concentrated adjacent to the membrane reduces the temperature drop as the entire catalyst becomes closer to the source of external heating through the membrane interface and taking advantage of an exothermic adsorption process that supplies extra heat to the catalyst from the opposite side.

CHAPTER 7

CONCLUSIONS & DIRECTIONS OF FUTURE RESEARCH

The CHAMP-class of reactors enhanced with CO_2 adsorption is a promising approach for distributed production of hydrogen from the steam methane reforming process. Coupling *in situ* removal of H_2 via a selective membrane with CO_2 separation via adsorption enables operation of the SMR process at nearly 100% conversion at temperatures as low as 400℃ with a stoichiometric 2:1 ratio of H_2O:CH_4 in reactants/fuel mixture, which are arguably two most desirable attributes of chemical process suitable for distributed H_2 production. This chapter concludes the thesis by summarizing the original contributions made in this work, recapping the major conclusions, and discussing potential future research efforts.

7.1 Original Contributions

Several important contributions to the field of distributed fuel reforming, both to fundamental science and engineering practice, have been made as a result of this doctoral research.

7.1.1 Fundamental Science

1. Developed a first principle understanding of the interplay between catalytic reaction/adsorption kinetics, heat and mass transfer, and H_2 separation on the CHAMP-class variable volume batch-membrane reactors with CO_2 sorption.
2. Established the fundamental performance limits of a combined reaction-separation process natural gas derived feedstock, which utilizes simultaneous removal of multiple reaction products (both CO_2 and H_2) through the combination

of rigorous thermodynamic and transport-reaction analysis and supporting experiments.

3. Investigated the spatially-resolved, transient variations of reaction rate(s), species concentration, and temperature within the porous catalyst bed of the CHAMP-class of reactors, with and without CO_2 sorption, and established the critical importance of gradients in the bed to the accurate prediction of reactor performance.

7.1.2 Engineering Practice

1. Developed a new class of chemical reactors designed to meet the challenging requirements associated with distributed H_2 production; specifically, high levels of CH_4 conversion and H_2 yield at a steam-to-carbon ratio of 2:1 and a temperature of 400°C have been achieved, which substantially exceed the results that have ever been demonstrated before.
2. Identified operating regime maps and developed the design criteria for the ideal (transport limitation-free) CHAMP-SORB class of reactors using the framework of time scale analysis.
3. Identified the physical bases and quantified the relative impact of various heat and mass transport limitations on CHAMP-SORB reactor performance and provided practical recommendations to mitigate the detrimental impact on performance by appropriate spatial distribution and amount allocation of the catalyst and sorbent within the porous bed.

7.2 Summary of Conclusions

Based on the complementary theoretical and experimental results reported in this doctoral dissertation, several conclusions can be made about the potential for the CHAMP-SORB reactor for energy efficient hydrogen production via the SMR process in a distributed fashion:

- Both H_2 and CO_2 separation are required to reach suitable CH_4 conversion levels at temperatures as low as 400°C at a 2:1 S/C ratio, both of which are desirable for greater thermal efficiency and hydrogen yield density.
- Constant pressure operation, utilized in the original CHAMP-class of reactor which featured only H_2 membrane separation, is even more critical with the addition of CO_2 adsorption, as it is needed to sustain the driving force for adsorption and H_2 permeation. As a result, it is imperative for an optimally designed CHAMP-SORB reactor that the system dead volume (due to piping/valves/etc.) is minimized relative to the working volume of the system.
- Through concurrent separation of <u>both</u> of the primary products of the SMR reaction, the CHAMP-SORB reactor can maintain elevated levels of fuel (CH_4 and H_2O) concentrations throughout the entire reaction step of the operating cycle. In contrast, the baseline CHAMP reactor with hydrogen-separating membrane, but without adsorption, experiences a significant CO_2 concentration rise near the end of the reaction step throughout the entire reactor chamber, thus diluting both the fuel and H_2 in the reactor volume and causing respective reductions in the reaction and permeation rates.
- Formation of CO is suppressed in the CHAMP-SORB reactor due to a shift in equilibrium of the water gas shift (WGS) reaction and a matching of reverse methanation (RM) and WGS reaction rates for the duration of the reaction process. This provides numerous practical benefits, including (*i*) reduction of possibility for Pd-Ag membrane poisoning, (*ii*) increased levels of H_2 yield through the forward WGS reaction, and (*iii*) a reduced likelihood of catalyst coking by reducing likelihood of the Boudouard reaction.
- The concepts of permeation and reaction resistances (i.e., given by these processes' timescales normalized by reactor size) are excellent proxies to predict the CHAMP-SORB reactor performance in the absence of transport limitations; however, the mass transfer effects necessitate the use of additional catalyst beyond the amount predicted by timescale analysis owing to incomplete catalyst utilization due to an impedance to reactant transport.

7.3 Research Issues for Further Exploration

As this is the first in-depth study of the CHAMP-class of reactor combined with CO_2 adsorption, many questions remain to be answered to develop the CHAMP-SORB into a production-level system. Specifically, building a pilot-scale reactor would be useful to investigate the following areas:

- Experimental study of sorbent regeneration step using cyclic volume-expansion driven pressure swing regeneration of the sorbent. The bench-scale testbed used in this work did not have sufficiently low dead volume to experimentally assess this behavior; however, a pilot-scale system could be designed with valves and piping sufficiently small to enable utility of this concept. Also of interest is the investigation of coupling moderate temperature-swing regeneration with pressure-swing regeneration techniques.
- Extended duration testing to assess the impact of many operation cycles on (*i*) the capacity of the K_2CO_3-promoted hydrotalcite sorbent, (*ii*) membrane integrity and potential embrittlement due to cyclic operation, (*iii*) catalyst coking due to carbonaceous deposits (less likely to occur according to thermodynamic considerations, however still possible), and (*iv*) valve durability for sustained operation at elevated temperatures.
- Integration of heat sources other than electric resistance heaters to provide the endothermic heat of reaction required for the SMR process, potentially using off-gas from the process.
- Investigation of the impact of less-than-infinite membrane selectivity towards H_2 (*i.e.* some other species will pass through the membrane, what are the consequences?).
- Integration of several CHAMP-SORB reactors, operating out of phase with one another, into a coupled, multiple-unit stack capable of delivering a desired level of H_2 yield to a residential fuel cell or for compression and eventual use in a fuel cell vehicle.

Additionally, future work could include investigation of alternate CHAMP-SORB configurations to improve upon the performance of the basic embodiment considered in this dissertation, where the membrane area matches that of the piston cross-section. Figure 7.1 conceptualizes an alternative CHAMP-SORB embodiment where an increase in membrane surface area is achieved by running multiple H_2 collection tubes, surrounded by regions of increased catalyst concentration, through the sorbent bed.

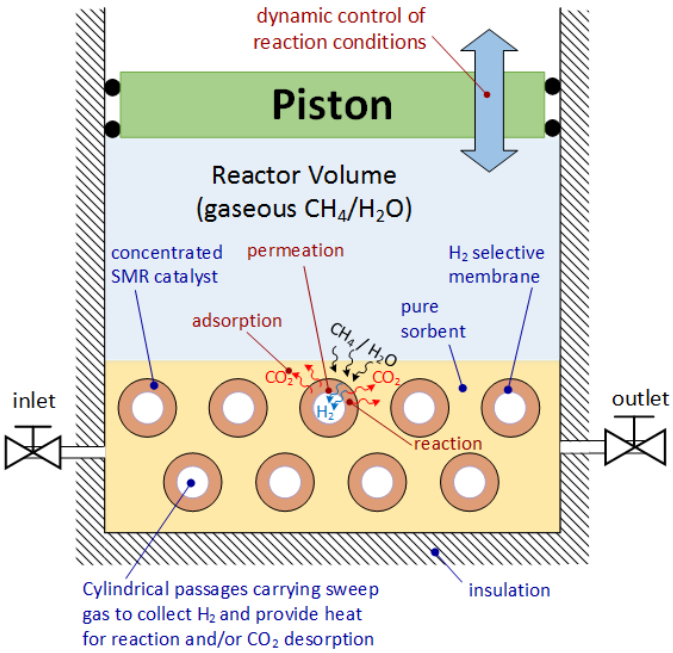

Figure 7.1: CHAMP-SORB arrangement with multiple passageways for H_2 collection (running into the page), increasing the effective membrane surface area per unit cross-sectional area of the reactor. Areas of concentrated SMR catalyst are located adjacent to the membrane surfaces, surrounded by pure sorbent.

From a theoretical standpoint, additional modeling efforts could be useful to incorporate multi-dimensional effects, in particular radial variations in temperature and membrane permeate-side partial pressure that could impact reactor performance. Also of interest is capturing the effect of radiation heat transfer within the porous bed.

Developing solutions to the engineering challenges highlighted in this section will be essential to establishing the commercial viability of the CHAMP-SORB reactor to meet the stringent demands of distributed H_2 production.

APPENDIX A: THERMODYNAMIC ANALYSIS OF CHAMP-SORB OPERATION CYCLE

To model the cyclic performance of the CHAMP-SORB reactor, species conservation is solved at each of the states (1) – (6) labeled in Figure 3.3. It is assumed that the reaction/permeation/adsorption and desorption steps both proceed fully to equilibrium and that sufficient heat is added to maintain isothermal conditions. It is also assumed that the filling processes (6) – (1) – (2) is fast enough that no CO_2 adsorption/desorption or SMR reaction occurs during this step. Similarly no change in sorbent loading is assumed to occur in the CO_2 exhaust step (5) – (6). Lastly, the system is modeled as if the chamber can be completely exhausted (i.e., neglecting any dead volume) at states (4) and (6) when the piston is fully extended and the top of the sorbent/catalyst mixture layer reaches the membrane; this assumption is valid with a thin layer of sorbent but as the sorbent volume increases the amount of gas contained within the sorbent void fraction may become significant.

In addition to solving the species balance, it is necessary to determine the required heat and work inputs for each step of the process to enable calculation of the overall thermal efficiency as a function of key process variables (temperature, pressure, S/C ratio, sorbent mass and recycle fraction). In doing so it is assumed that all expansion or compression steps are frictionless, quasi-equilibrium processes. The volume expansion during desorption step is assumed to occur slowly enough that the CO_2 loading of the sorbent remains in equilibrium with the surrounding gas. The entire thermodynamic system for the CHAMP-SORB cycle is illustrated in Figure A.1.

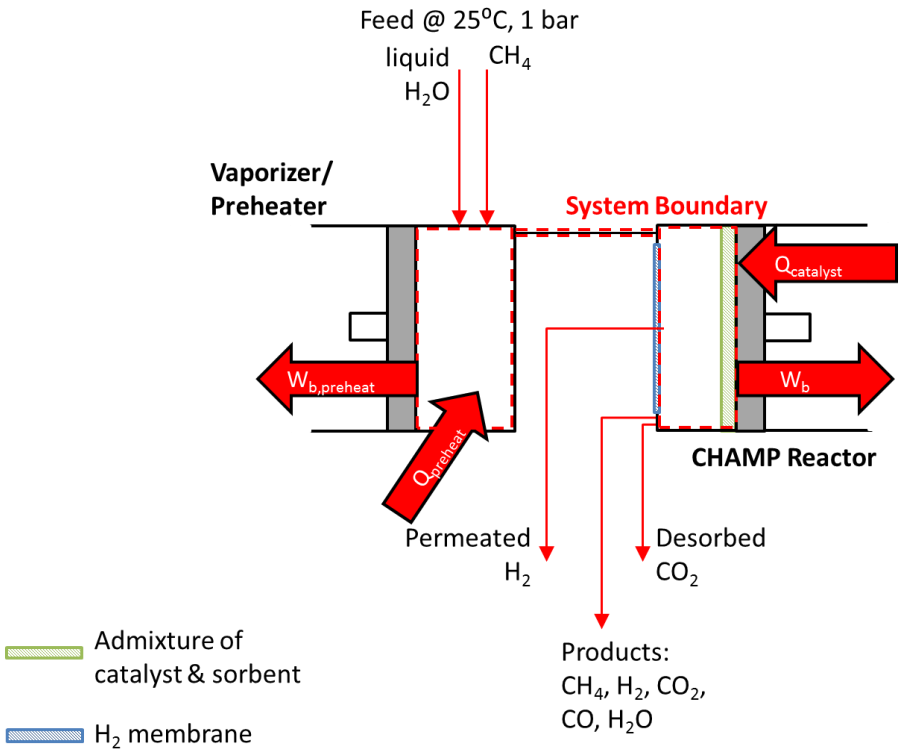

Figure A.1: Thermodynamic system for entire CHAMP-SORB cycle

Energy can cross the system boundary by heat transfer as well as boundary work into/out of either of the two chambers. By convention heat transfer in to the system and work done by the system on the surroundings are both positive. The overall CHAMP-SORB operation can be split up into two sub-processes:

a) **Preheating Stage:** The gaseous CH_4 and liquid H_2O initially at 1 bar, 25°C are brought to the reaction temperature and pressure in the vaporizer preheater.

b) **Reaction/Permeation/Adsorption Stage:** Methane steam reforming/water gas shift reactions produce H_2, CO, CO_2 while CO_2 is simultaneously adsorbed and pure H_2 permeates the selective membrane. Remaining species

are exhausted by bringing the piston to top dead center, after which the chamber is expanded to desorb CO_2 and regenerate the sorbent for the next step.

A.1 Preheating process heat and work inputs

During the entire preheating stage, there are no gas species in the CHAMP reactor chamber, and the sorbent/catalyst mixture are isolated so there are no changes in its internal energy or amount of adsorbed CO_2. As such, any changes in overall internal energy/enthalpy/entropy of the system are due only to changes in the properties of the gas species. Figure A.2 illustrates the thermodynamic system including boundaries and heat/work inputs during the preheating sub-process.

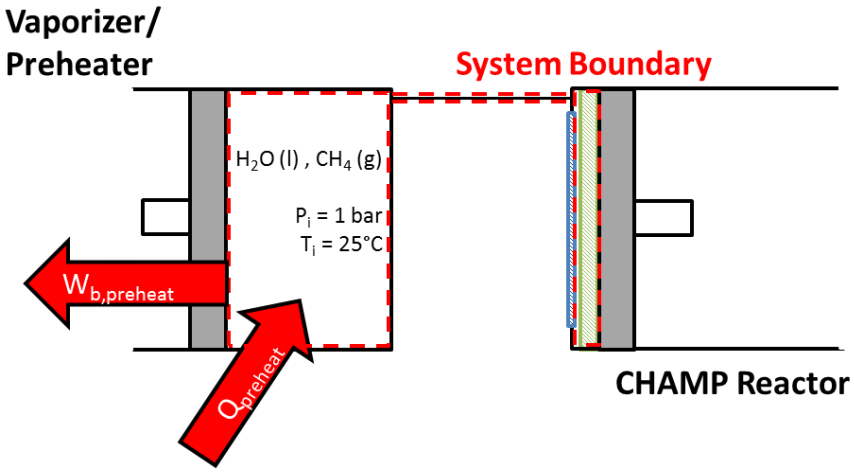

Figure A.2: Thermodynamic system schematic for preheating stage

Throughout the preheating process, the system is closed so the first law of thermodynamics can be taken in differential form $dU = \delta Q - \delta W$ and integrated from the initial state i to final state f:

$$U_f - U_i = Q_{preheat} - W_{b,preheat} \tag{A.1}$$

The left side of equation (A.1) involves only thermodynamic properties and can be determined without knowing anything about the path from the initial to final preheating state by summing the product of the number moles of each species *j* with the change in specific internal energy between the states:

$$U_f - U_i = \Sigma_j \left[N_j (u_{j,f} - u_{j,i}) \right] \tag{A.2}$$

Therefore, the sum of heat and work into the system during the preheating stage is fully defined by the number of moles of each species and the initial and final states. How much of this energy comes into this system as heat ($Q_{preheat}$) or work ($-W_{b,preheat}$) depends on the specific path. A practical path to minimize the volume required by the preheater is to first heat the mixture at a constant volume until the pressure rises from the initial pressure of 1 bar to the reaction pressure. Once the reaction pressure is reached, the system can be heated further at constant pressure to the reaction temperature. Alternatively, the system could be heated at constant pressure to an intermediate temperature and then compressed isentropically to the final temperature/pressure, but the intermediate state would require a larger volume at 1 bar than at the final reaction conditions.

If the constant volume heat addition to reaction pressure followed by constant pressure heat addition path is chosen, then boundary work only occurs during the constant pressure heat addition step. Assuming this expansion is done in a reversible manner, $W_{b,preheat} = \int P_b dV$ and because the boundary pressure is constant (and equal to the total pressure in the reactor P_T) it can be pulled out of the integral and the boundary work becomes:

$$W_{b,preheat} = P_T(V_f - V_i) \tag{A.3}$$

Because there is phase change of H_2O, the final volume at reaction temperature/pressure V_f will exceed V_i and therefore boundary work can be extracted from the system during the preheating process. With the boundary work specified, the heat input during preheating can also be determined by substituting equations (A.2) and (A.3) into the energy conservation relation given by equation (A.1):

$$Q_{preheat} = \Sigma_j\left[N_j(u_{j,f} - u_{j,i})\right] + P_T(V_f - V_i) \tag{A.4}$$

A.2 Cyclic reactor process heat and work inputs

Once the gas mixture is brought to the operating temperature and pressure in the preheating chamber, the valve between the chambers is opened and the gas is transferred at constant pressure from the preheater to the main CHAMP-SORB reactor. If losses are neglected and the transfer occurs adiabatically, the gas species will have the same temperature and pressure as at the end of the preheating stage and no heat or work inputs need to be calculated for the transfer process.

During the CHAMP-SORB reaction/permeation/adsorption sub-process, Figure A.3 shows energy transfers to/from the thermodynamic system:

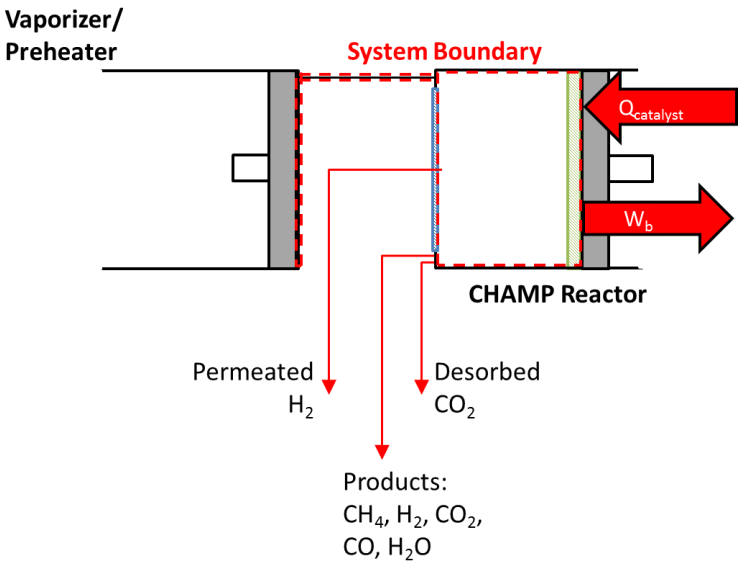

Figure A.3: Thermodynamic system during reaction/permeation/adsorption stage

Neglecting the dead volume in the line between the two chambers, the only part of the thermodynamic system which can change energy is the actual CHAMP reactor chamber, and the schematic can be simplified as shown in Figure A.4.

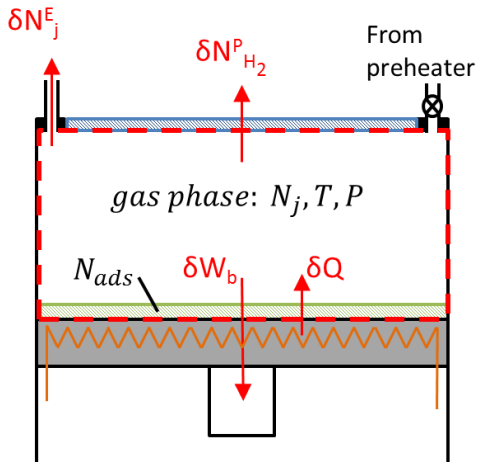

Figure A.4: Simplified thermodynamic representation for reaction/permeation/adsorption stage

Mass can be transported across the system boundary by exiting the chamber through the exhaust port (δN_j^E) or by H_2 permeation through the Pd/Ag membrane ($\delta N_{H_2}^P$). There are a total of 5 gas species (N_j where j = CH_4, H_2O, CO_2, H_2, CO) as well as an adsorbed CO_2 species (denoted N_{ads}). The catalyst is heated by a resistance cartridge heater in the piston, although in principle some/all of this heat could be supplied by combustion of residual unconverted CH_4 or unpermeated H_2. The thermodynamic states considered are as follows:

(1) CH_4 (g) and H_2O (g) at P_{rxn}, T_{rxn} is fed into the reactor from the preheater.
(2) A fraction of additional species from the previous CHAMP-SORB cycle, $f \cdot N_{j,3}$, is added to the initial feed CH_4 and H_2O if fuel recycling is incorporated.
(3) Gas species N_j in chemical equilibrium at the end of the reaction/permeation/ adsorption step. Additionally, the partial pressure of H_2 in the chamber is equal to the H_2 partial pressure on the permeate side of the membrane, and the gaseous CO_2 is in equilibrium with the adsorbed CO_2 according to the equilibrium isotherm.
(4) Chamber volume is fully exhausted so that $N_{j,4} = 0$ and only $N_{ads,4}$ present in system.
(5) Chamber expanded with pressure of CO_2 in equilibrium according to the sorption isotherm
(6) Chamber volume is fully exhausted so that $N_{j,6} = 0$ and only $N_{ads,6}$ present in system.

The processes (1) – (2) and (2) – (3) are isothermal and isobaric. The processes (3) – (4) and (5) – (6) occur adiabatically and at constant gas pressure until all species are exhausted. Process (4) – (5) occurs in sufficiently slowly so that as the chamber expands,

the desorbed CO_2 gas is at all times in equilibrium with the adsorbed CO_2. Assumptions made in the modeling process are as follows:

- Boundary work in any process is quasi-equilibrium and can be represented by $\delta W_b = -PdV$.
- No H_2 permeation occurs during the processes from states (4) – (6): either the membrane is sealed off or zero H_2 partial pressure is held on the backside of the membrane.
- The exhaust steps (3) – (4) and (5) – (6) are sufficiently fast that no appreciable adsorption/desorption occurs.

Process (1) – (2):

This step allows for some of the unpermeated products from the previous reaction step to be recycled. In this case δN_j^E as depicted in Figure A.4 is negative. Expressing the incoming recycled gas species as $\delta N_j^I = -\delta N_j^E$, on a differential basis, the change in extensive energy in the system can be written using the first law of thermodynamics:

$$dE = \delta Q - \delta W + \Sigma_j \delta N_j^I h_j^I \tag{A.5}$$

Assuming there are negligible changes in kinetic or potential energy $dE = dU = \Sigma_j d(u_j N_j)$. Using the assumption that boundary work is reversible ($\delta W = P_T dV$), and expanding $d(u_j N_j)$ using product rule, equation (A.5) can be rewritten as:

$$\Sigma_j \left(N_j du_j + u_j dn_j\right) = \delta Q - P_T dV + \Sigma_j \delta N_j^I h_j^I \tag{A.6}$$

If the process is isothermal, specific internal energy is constant and therefore $du_j = 0$. Bringing the enthalpy term associated with the transport of recycled species into the reactor control volume to the left hand side of equation (A.6):

$$\Sigma_j \left(u_j dN_j - \delta N_j^I (u_j^I + (P_T v)_j^I\right) = \delta Q - P_T dV \tag{A.7}$$

The recycled gas is at the same temperature and pressure as the current contents of the chamber, therefore $u_j^I = u_j$. Also without any reaction, by species conservation $\delta N_j^I = dN_j$, and equation (A.7) can be simplified by noting the first two terms in the summation on the left side are of equal magnitude and opposite sign:

$$\Sigma_j\left(-dN_j(P_T v)_j^I\right) = \delta Q - P_T dV \tag{A.8}$$

The inlet gases are at the same temperature and pressure as the contents of the reactor, so the inlet superscript can be dropped from the pressure term and pulled out of the integral and summation. Because all species are all assumed to exhibit ideal gas behavior at the same temperature and total pressure, the inlet specific volume is the same as the specific volume of the species inside the reactor and the superscript on v_j^I can be dropped. Making these modifications, equation (A.8) becomes:

$$-P_T d(\Sigma_j N_j v_j) = \delta Q - P_T dV \tag{A.9}$$

Finally, recognizing that the total volume V is equal to the sum of the specific volume of each species multiplied by that species molar quantity ($\Sigma_j N_j v_j$), it is apparent that $\delta Q = 0$ throughout step (1) – (2). By integrating over the process, the total heat input during this step is $Q_{12} = 0$. To calculate the boundary work done by the system, recognizing the process (1) – (2) is isobaric,

$$W_{12} = P_T(V_2 - V_1) \tag{A.10}$$

Process (2) – (3):

In this step, the reaction chamber is held at constant pressure and the system is open because H_2 can permeate through the Pd/Ag membrane. Also the number of moles of

each of the gas species can change due to chemical reaction. The first law of thermodynamics for this open system can be written on a differential basis as:

$$dU = \delta Q - PdV - \delta N_{H_2}^{P} h_{H_2} \tag{A.11}$$

The differential change in extensive internal energy (dU) can be related to the differential change in enthalpy (dH) using the definition of enthalpy and the product rule: $dU = d(H - PV) = dH - PdV - VdP$. Making this substitution into equation (A.11), and noting that pressure is constant, the differential form of the first law for process (2) – (3) becomes:

$$dH - V\cancel{dP} = \delta Q - \delta N_{H_2}^{P} h_{H_2} \tag{A.12}$$

The change in total (extensive) enthalpy is the sum of the enthalpy of each individual species ($dH = d\left[\Sigma_j N_j h_j + N_{ads} h_{ads}\right]$). Expanding this relationship using product rule and substituting into (A.12),

$$\Sigma_j N_j dh_j + \Sigma_j h_j dN_j + N_{ads} dh_{ads} + h_{ads} dN_{ads} = \delta Q - \delta N_{H_2}^{P} h_{H_2} \tag{A.13}$$

Because the process is isothermal the enthalpy of each gas species h_j is constant. Assuming that the enthalpy of adsorption is constant then h_{ads} must be constant as well, making $dh_{ads} = 0$. Further, the differential change in number of moles of a particular gas species dN_j is not independent of the change in moles of the other species. The changes are linked by the reaction stoichiometry and by the incremental amount of permeation/adsorption of each species, or $dN_j = \Sigma_i v_{ij} d\varepsilon_i - dN_{ads,j} - \delta N_j^{P}$ where v_{ij} is the stoichiometric coefficient and $d\varepsilon_i$ is the incremental change in extent of each reaction. Because the three SMR reactions are not thermodynamically independent, only

two of the three reactions must be considered in determining change in composition. Substituting the relation for dN_j into the energy balance:

$$\Sigma_j\left[h_j\left(\Sigma_i \upsilon_{ij} d\varepsilon_i - dN_{ads,j} - \delta N_j^P\right)\right] + h_{ads} dN_{ads} = \delta Q - \delta N_{H_2}^P h_{H_2} \qquad \text{(A.14)}$$

However δN_j^P is only non-zero for j = H_2, and $dN_{ads,j}$ is only non-zero for j = CO_2, so those terms can be pulled out of the summation and equation (A.14) can be expressed as:

$$\Sigma_j\left[h_j\left(\Sigma_i \upsilon_{ij} d\varepsilon_i\right)\right] - h_{CO_2} dN_{ads} - h_{H_2} \delta N_{H_2}^P + h_{ads} dN_{ads} = \delta Q - \delta N_{H_2}^P h_{H_2} \qquad \text{(A.15)}$$

The first term on the left side of equation (A.15) is recognized as the product of the enthalpy and extent of reaction $\left(\Sigma_j\left[h_j\left(\Sigma_i \upsilon_{ij} d\varepsilon_i\right)\right] = \Sigma_i \Delta H_i d\varepsilon_i\right)$. Also two terms on the left involving dN_{ads} can be grouped together using $h_{ads} - h_{CO_2} = \Delta H_{ads}$. Finally, the differential form of the first law energy balance for process (2) – (3) becomes:

$$\Sigma_i \Delta H_i d\varepsilon_i - \Delta H_{ads} dN_{ads} = \delta Q \qquad \text{(A.16)}$$

If ΔH_{ads} is independent of sorbent loading, it can be held constant while integrating from state (2) – (3) and the total heat input during the process is:

$$Q_{23} = \Delta H_1 \varepsilon_1 + \Delta H_2 \varepsilon_2 + \Delta H_{ads}(N_{ads,3} - N_{ads,2}) \qquad \text{(A.17)}$$

Because process (2) – (3) is isobaric and assumed to be reversible, the required boundary work during the reaction step is

$$W_{23} = P_T(V_3 - V_2) \qquad \text{(A.18)}$$

If the number of additional moles created by the reaction is less than those that leave the gas phase due to permeation and adsorption, this work will be negative (meaning that work input is required to compress the cylinder during the process).

Process (3) – (4):

The process of exhausting the chamber by moving the piston is modeled to occur adiabatically and at a constant pressure. The chamber is also assumed to be well mixed such that the properties at the boundary are equal to the properties at any point in the chamber, and that the mole fraction of each gas species in the chamber remains constant because equal proportions of each gas in the mixture is exhausted. Beginning with the 1st law of thermodynamics for an open system:

$$dU = \cancel{\delta Q} - PdV - \Sigma_j \delta N_j^E h_j^E \tag{A.19a}$$

$$dH = -\Sigma_j \delta N_j^E h_j^E \tag{A.19b}$$

The extensive enthalpy H is the sum of the individual components specific enthalpy multiplied by the number of moles of each component. Expanding the differential of this summation using the product rule yields $dH = d\left[\Sigma_j\left(N_j h_j\right)\right] = \Sigma_j N_j dh_j + \Sigma_j h_j dN_j$. By conservation, because no reaction or adsorption is occurring $dN_j = -\delta N_j^E$ and the 1st law expression can be rewritten:

$$\Sigma_j N_j dh_j - \Sigma_j h_j \delta N_j^E = -\Sigma_j \delta N_j^E h_j^E \tag{A.20}$$

Because the gases in the chamber are well mixed, $h_j = h_j^E$ and, as a result equation (A.20) simplifies to $\Sigma_j N_j dh_j = 0$. The only way this can be satisfied is if $\boldsymbol{dh_j = 0}$ for every individual gas component, because the specific enthalpy h_j for each species is a monotonically increasing function of temperature only and the gases remain in thermal equilibrium with one another. It is therefore not possible for the enthalpy of one species to increase while another decreases to satisfy $\Sigma_j N_j dh_j = 0$; hence the specific enthalpies of <u>all</u> species must remain unchanged. With the pressure, enthalpy, and mole fraction of

each species remaining constant, the gas in the cylinder undergoes a **constant property process** (*e.g.* specific entropy, temperature, etc. are all unchanged). This result can be used to show that the process does not violate the 2nd law of thermodynamics and is, in fact, ideal ($\sigma_{gen} = 0$):

$$dS = \Sigma_j\left(s_j dN_j + N_j \cancel{ds_j}\right) = \delta\sigma_{gen} - \Sigma_j \delta N_{j,e} s_{j,e} \tag{A.21a}$$

$$\delta\sigma_{gen} = \Sigma_j\left(s_j \delta N_{j,e}\right) - \Sigma_j \delta N_{j,e} s_{j,e} = 0 \tag{A.21b}$$

The reversible boundary work of the process is $\delta W_b = -PdV$. Because pressure is constant (equal to reaction pressure P_T) and the process goes to zero dead volume at state 4:

$$W_{34} = P_T(\cancel{V_4} - V_3) = -P_T V_3 \tag{A.22}$$

Again the work is negative, meaning that work will have to be done on the system to exhaust the chamber.

Process (4) – (5)

In state 5, the system comprises only the solid adsorbent with adsorbed CO_2, and zero dead volume (e.g. no gaseous CO_2). It is assumed that during the entire expansion process the adsorbed and gaseous species are in quasi-equilibrium. Because the process is reversible (quasi-equilibrium), $\delta\sigma_{gen} = 0$ and therefore the 2nd law of thermodynamics for the closed system in differential form is:

$$TdS = \delta Q \tag{A.23}$$

The extensive entropy of the system S is the sum of the entropy of the gaseous and adsorbed CO_2. During this step, N_j for all species other than $j = CO_2$ is zero and

therefore $dS = d\left[N_{ads}s_{ads} + N_{CO_2}s_{CO_2}\right]$. Expanding the expression for dS using the product rule, $dS = s_{ads}dN_{ads} + s_{CO_2}dN_{CO_2} + N_{ads}ds_{ads} + N_{CO_2}ds_{CO_2}$. Because the system is closed, by species conservation $dN_{CO_2} = -dN_{ads}$, and the quantity $s_{ads}dN_{ads} + s_{CO_2}dN_{CO_2}$ can be expressed more compactly as $\Delta S_{ads}dN_{ads}$ (where $\Delta S_{ads} = s_{CO_2} - s_{ads}$). Inserting this relationship into equation (A.23):

$$T\left(\Delta S_{ads}dN_{ads} + N_{ads}ds_{ads} + N_{CO_2}ds_{CO_2}\right) = \delta Q \tag{A.24}$$

If ΔS_{ads} does not change during the process, then $ds_{ads} = ds_{CO_2}$ because the specific entropy of the adsorbed species is offset from to the specific entropy of the gas species by a fixed ΔS_{ads}. This is consistent with the earlier assumption that ΔH_{ads} is constant, because if the adsorption occurs reversibly then the change in Gibbs free energy along the equilibrium isotherm must be zero throughout the process ($\Delta G_{ads} = 0 = \Delta H_{ads} - T\Delta S_{ads}$). It then follows that $T\Delta S_{ads} = \Delta H_{ads}$, and because the process is isothermal if ΔH_{ads} is constant, then ΔS_{ads} must also be constant. It is then possible to express the incremental heat addition as:

$$\delta Q = T\left[\Delta S_{ads}dN_{ads} + (N_{ads} + N_{CO_2})ds_{CO_2}\right] \tag{A.25}$$

By species conservation, the total CO_2 in the reactor in the form of adsorbed and gas species $\left(N_{ads} + N_{CO_2}\right)$ must remain unchanged throughout the process (4) – (5), so both this quantity and the temperature can be held constant during the integration (and equal to $N_{ads,4}$). Integrating equation (A.25), over the process (4) – (5) yields the total heat addition required during the process:

$$Q_{45} = T\left[\Delta S_{ads}\left(N_{ads,5} - N_{ads,4}\right) + N_{ads,4}(s_{CO_2,5} - s_{CO_2,4})\right] \tag{A.26}$$

At state 4 there is no gas present in the reactor, but the specific entropy of gas-phase CO_2 at state 4 ($s_{CO_2,4}$) is the specific entropy corresponding to the system temperature and the equilibrium CO_2 pressure at the initial sorbent loading. Using the relation for entropy change of an ideal gas at constant temperature and recognizing that $T\Delta S_{ads} = \Delta H_{ads}$, equation (A.26) can be rewritten as:

$$Q_{45} = \Delta H_{ads}\left(N_{ads,5} - N_{ads,4}\right) + N_{ads,4}RTln\left(\frac{P_{CO_2,4}}{P_{CO_2,5}}\right) \quad \text{(A.27)}$$

The first term on the right side of equation (A.27) represents the necessary heat input to remain isothermal under constant pressure conditions, while the second term is a correction for non-constant CO_2 pressure. Next, the 1st law of thermodynamics can be used to calculate the work done in the process. Starting with $\Delta U_{45} = Q_{45} - W_{45}$ and expanding the change in extensive internal energy U to be the sum of the change of each individual component $\left(\Delta U = N_{ads,5}u_{ads,5} + N_{CO_2,5}u_{CO_2,5} - N_{ads,4}u_{ads,4}\right)$, the 1st law can be further simplified by noting that by species conservation $N_{CO_2,5} = N_{ads,5} - N_{ads,4}$ and that because the process is isothermal $u_{ads,5} = u_{ads,4}$. As such, the 1st law expression becomes

$$\Delta U_{ads}\left(N_{ads,5} - N_{ads,4}\right) = Q_{45} - W_{45} \quad \text{(A.28)}$$

where ΔU_{ads} is the change in internal energy upon adsorption $\left(\Delta U_{ads} = u_{CO_2}(g) - u_{ads}\right)$ and unchanged throughout the process of moving from state (4) to state (5). It is possible to relate enthalpy of adsorption to entropy of adsorption, according to Ruthven [46] as $\Delta U_{ads} = \Delta H_{ads} + RT$. The work done by the system on the environment in process (4) – (5) is therefore:

$$W_{45} = \Delta H_{ads}\left(N_{ads,5} - N_{ads,4}\right) + N_{ads,4}RTln\left(\frac{P_{CO_2,4}}{P_{CO_2,5}}\right) - (\Delta H_{ads} + RT)(N_{ads,5} - N_{ads,4}) \quad \text{(A.29a)}$$

$$W_{45} = RT\left[N_{ads,4}ln\left(\frac{P_{CO_2,4}}{P_{CO_2,5}}\right) - (N_{ads,5} - N_{ads,4})\right] \quad \text{(A.29b)}$$

Process (5) – (6):

This process is essentially identical to the previous chamber exhaust step (3) – (4), and a similar analysis can be used to show that the intensive properties of all components of the system remain constant. As such no heat input is required to maintain the process as adiabatic, and the work done by the process is:

$$W_{56} = P_{CO_2,5}(\cancel{V_6} - V_5) = -P_{CO_2,5}V_5 \quad \text{(A.30)}$$

APPENDIX B: ENGINEERING DRAWINGS OF CHAMP-SORB TESTBED COMPONENTS

The following figures contain assembly and part-level drawings of the CHAMP-SORB reactor used for the experimental work presented in Chapter 4. The drawings presented are not to scale, as the pages (originally 8.5" x 11") are resized to fit the thesis document format. Unless otherwise specified, all dimensions are in inches.

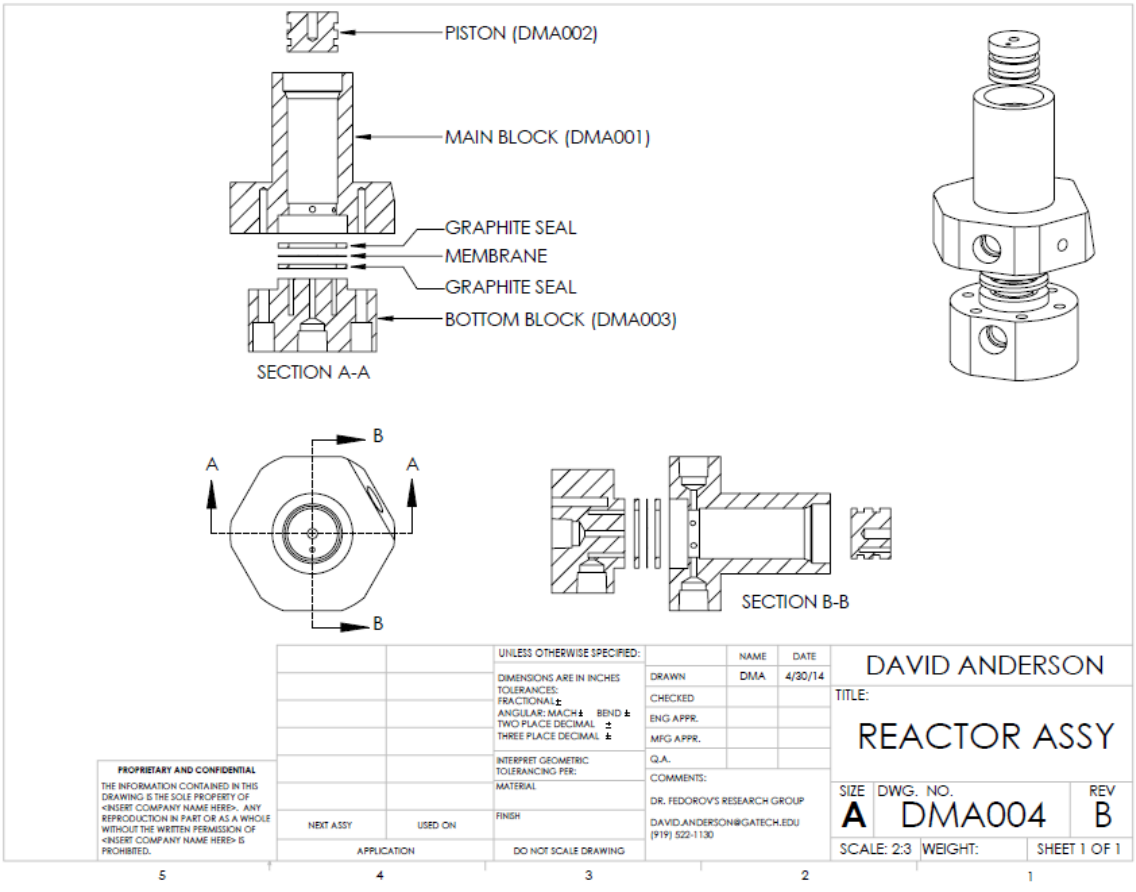

Figure B.1: CHAMP-SORB Reactor Assembly Drawing

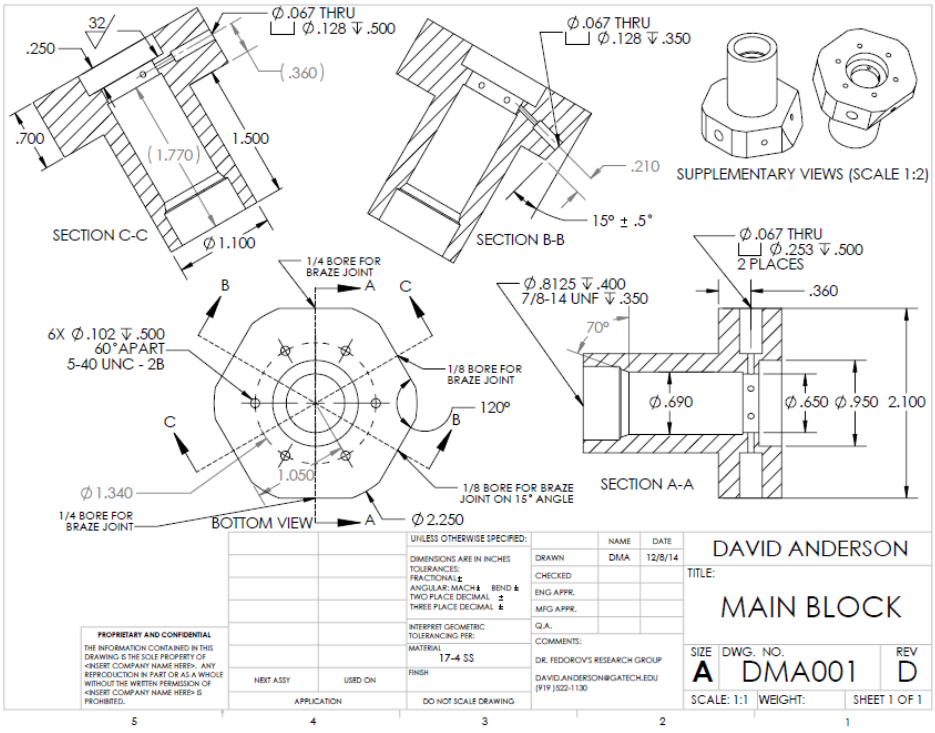

Figure B.2: CHAMP-SORB Reactor Block Part Drawing

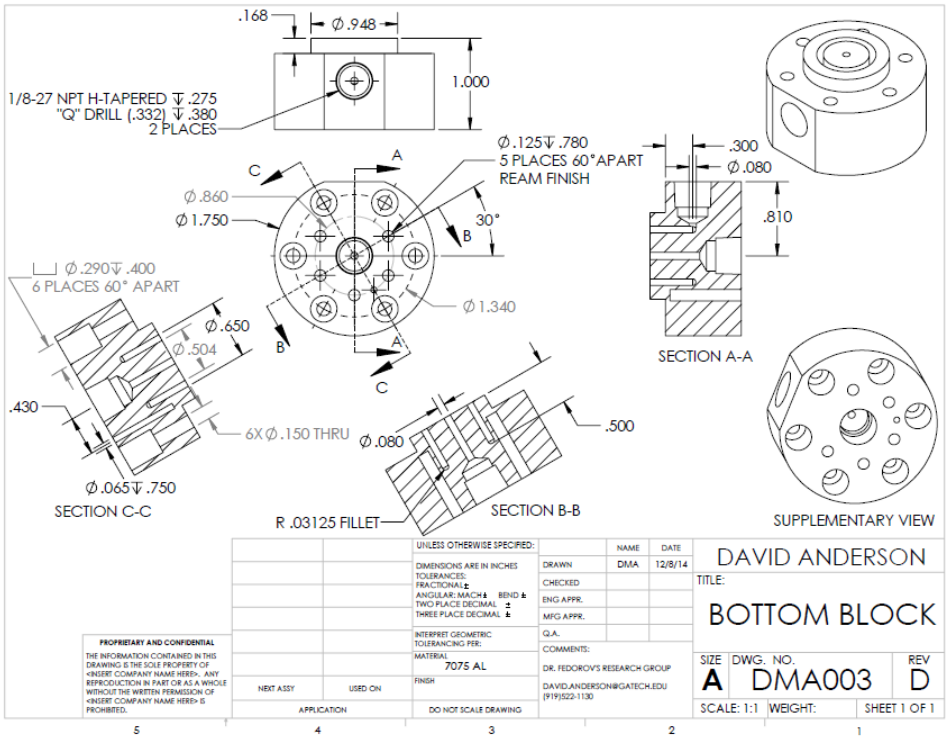

Figure B.3: CHAMP-SORB Reactor Bottom Block Part Drawing

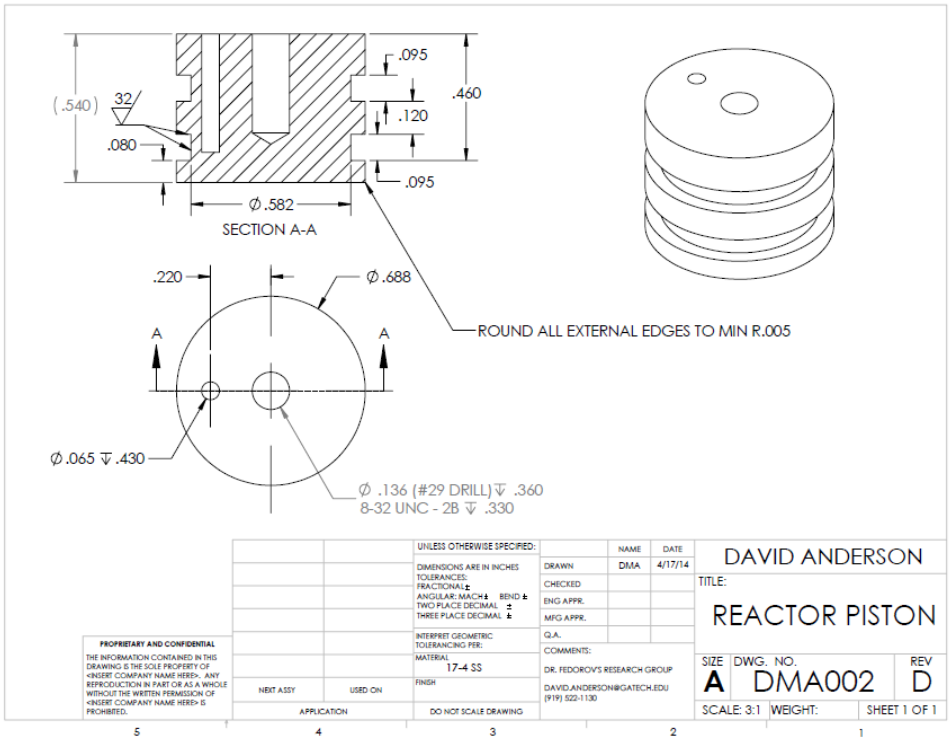

Figure B.4: CHAMP-SORB Reactor Piston Part Drawing

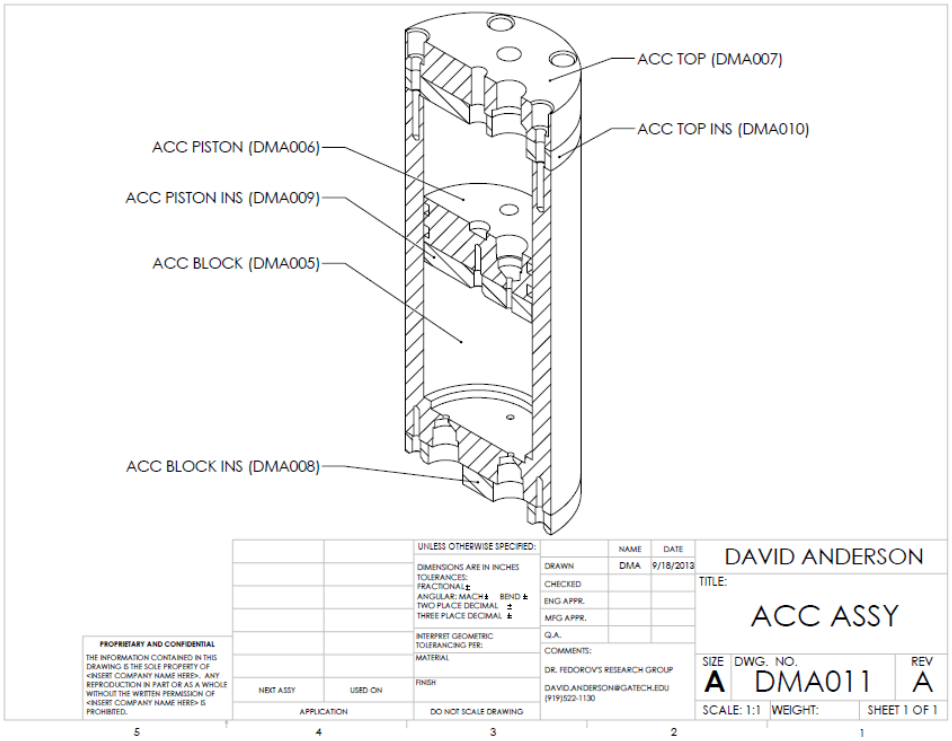

Figure B.5: Fuel Accumulator Assembly Drawing

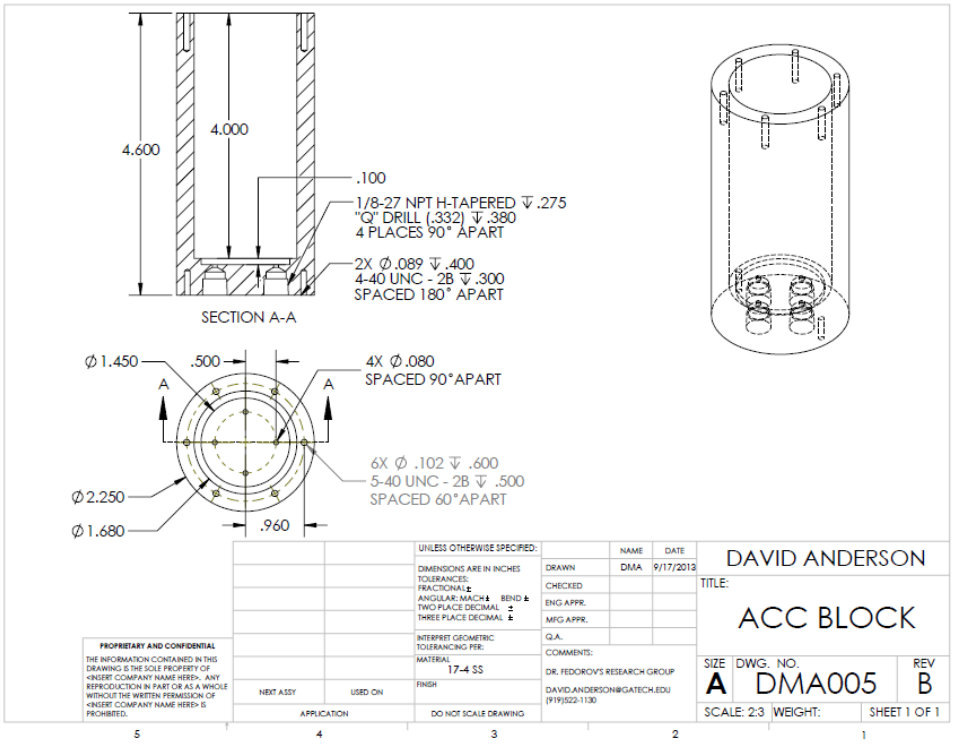

Figure B.6: Fuel Accumulator Block Part Drawing

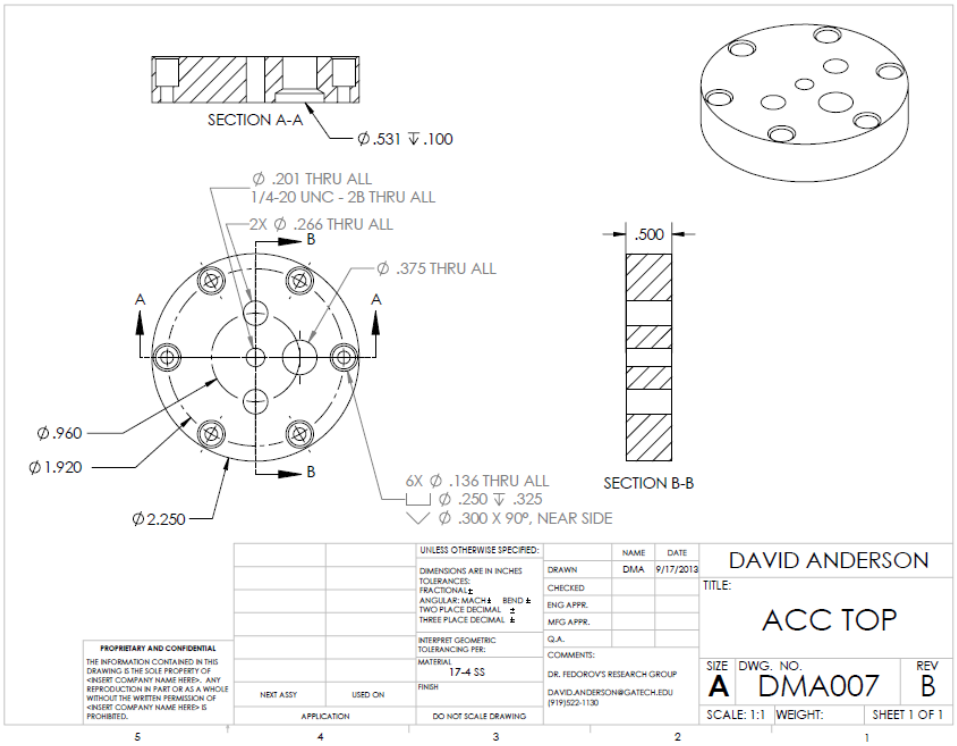

Figure B.7: Fuel Accumulator Top Part Drawing

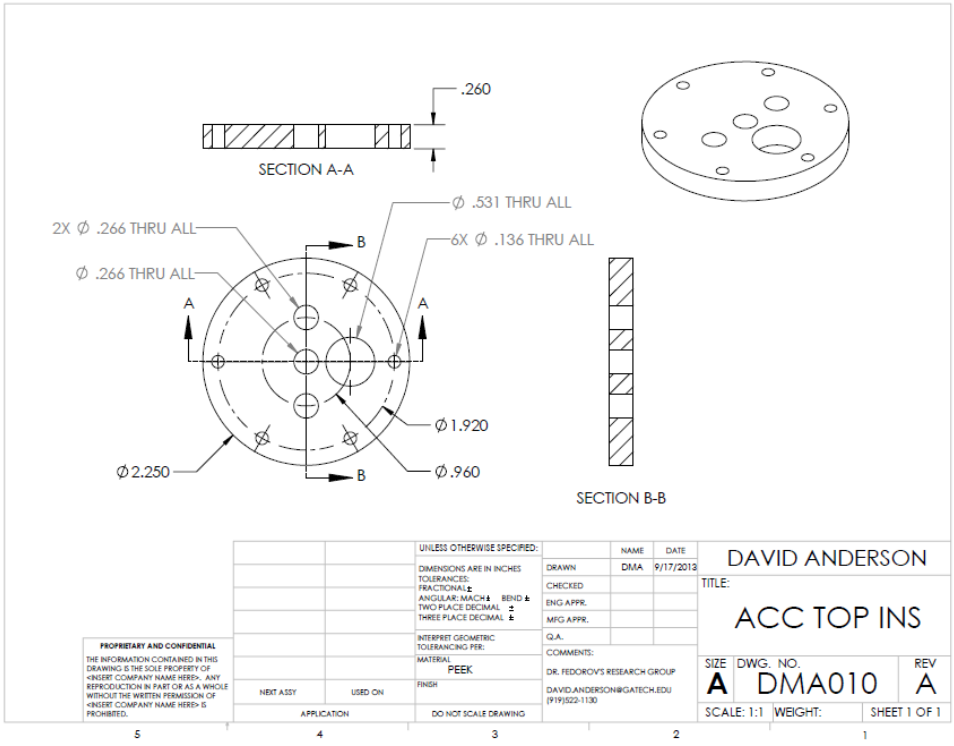

Figure B.8: Fuel Accumulator Top Insulation Part Drawing

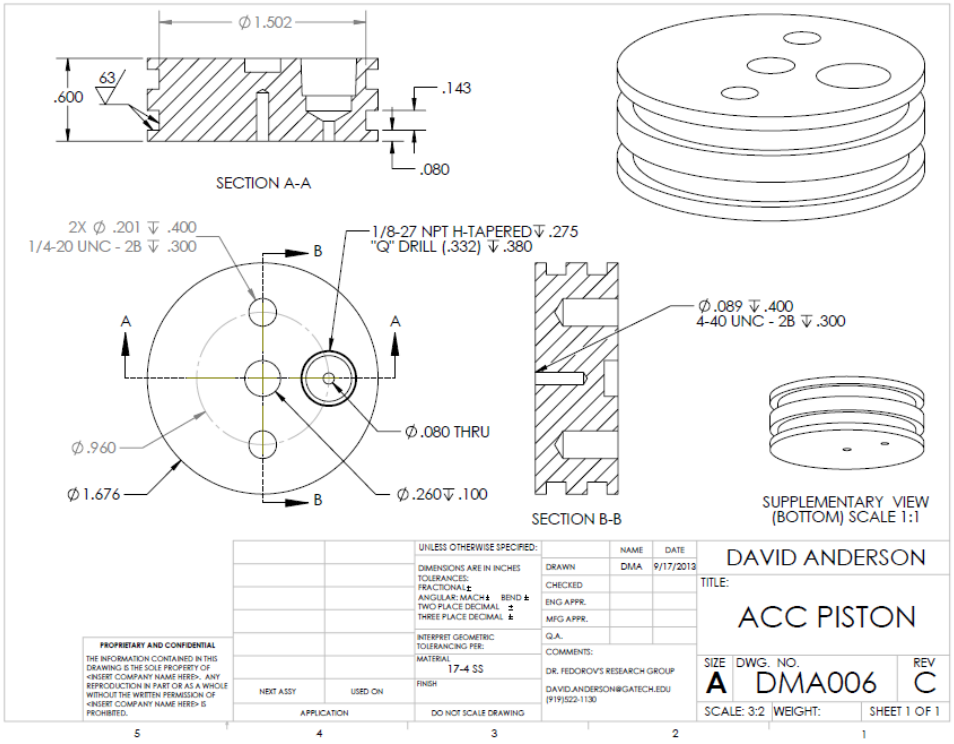

Figure B.9: Fuel Accumulator Piston Part Drawing

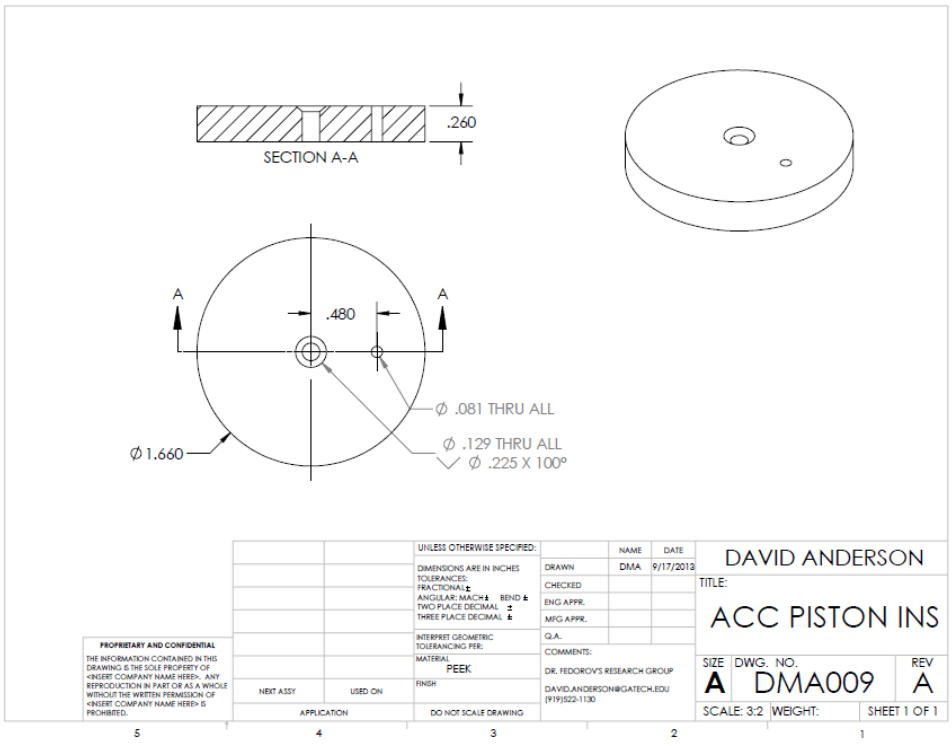

Figure B.10: Fuel Accumulator Piston Insulation Part Drawing

APPENDIX C: JUSTIFICATION OF TRANSPORT-KINETIC MODELING ASSUMPTIONS

C.1 Assumption of Local Thermal Equilibrium

The energy conservation equation (6.4) is valid when the gas and solid phases of the porous medium are in local thermal equilibrium, an assumption that can be justified by estimating the order of magnitude of the local temperature difference between gas and solid phases ($\Delta T = T_{solid} - T_{gas}$). Scaling of the energy conservation equation for the gas and solid phases yields an order of magnitude estimate for the maximum temperature difference to be $\Delta T \sim Q'''_{gen}/(\dot{h}_{eff} \cdot a_s)$, where Q'''_{gen} is the heat generation term per unit mass in the solid phase $[W/kg]$ that drives the temperature difference between phases, h_{eff} is the effective convection coefficient between the two phases $[W/m^2 \cdot K]$, and a_s is the specific surface area of the porous media $[m^2/kg]$ [91]. The maximum local reaction rate observed for the net SMR reaction (with $\Delta H_{net} = 165\ kJ/mol$) during CHAMP-SORB operation is $2 \times 10^{-2}\ mol/kg \cdot s$, as seen in Figure 6.7. This local reaction rate yields an approximate endothermic heat of reaction of $3.3\ kW/kg$. Using the reported value for specific surface area of K_2CO_3-promoted hydrotalcite of $5000\ m^2/kg$ from Halabi et al. [37], along with a conservative estimate for h_{eff} of $5\ W/m^2 \cdot K$, results in an estimated temperature difference between solid and gas phase of $\Delta T \sim 0.1\ K$. This is an agreement with a similar analysis previously performed for electrochemically-reacting solid oxide fuel cell (SOFC) electrodes [91], and as such, the assumption of local thermal equilibrium is justified in the energy conservation equation.

C.2 Assumption of Negligible Intra Particle Diffusion Resistance

The assumption of negligible intra particle diffusion resistance is justified by calculation of the Weisz-Prater criterion [102],

$$C_{W-P} = R_v \cdot R_p^2 / c_s \mathcal{D}_{eff} \tag{C.1}$$

where R_v is the local volumetric reaction rate, R_p is the catalyst pellet radius, c_s is the surface concentration, and $\mathcal{D}_{eff}$ is the effective mass diffusivity in the catalyst). If $C_{W-P} \ll 1$, intra particle diffusion effects are expected to be negligible, and the use of a catalyst effectiveness factor of unity is appropriate. The maximum value of local volumetric reaction rate observed in Chapter 6 is $R_v = 30\ mol/m^3$ −s, with typical local reaction rates $R_v < 5\ mol/m^3$ −s. Using a characteristic concentration at the surface of $10\ mol/m^3$ (the approximate value of concentration for an ideal gas at 400℃ and $5\ bar$ total pressure) and a effective diffusivity of $6.5 \times 10^{-5}\ m^2/s$, for C_{W-P} to be less than 0.1 the catalyst radius must be $R_p \leq 1.5\ mm$. In the experimental study of Chapter 4, catalyst pellets of diameter $\leq 0.3\ mm$, a full order of magnitude less than the threshold criteria calculated using the Weisz-Prater criteria, were used to be consistent with the size at which intra particle transport limitations were experimentally observed in the Xu and Froment kinetic study [28].

C.3 Assumption of Negligible Membrane and Catalyst Poisoning

Membrane and catalyst poisoning is not considered in this study because CO, the species that competitively adsorbs onto these surfaces and degrades performance, is kept at near-zero concentration levels through the equilibrium shift enabled by CO_2 adsorption

[88], and because the reduction in membrane permeation at the expected operating temperature of 400℃ is minimal, as can be seen in Figure C.1.

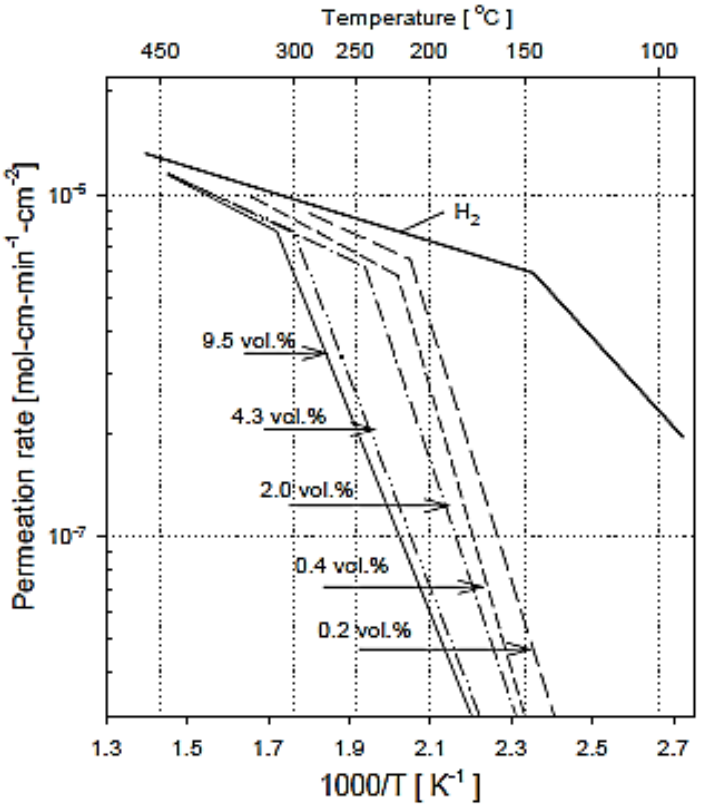

Figure C.1: Inhibiting effect of CO (at various concentration levels) on H_2 permeation rate through a Pd-Ag membrane (reproduced from Chabot, et al. [103])

C.4 Assumption to Neglect Soret Thermal Diffusion

To justify neglecting the Soret effect in the species flux terms of the conservation equations, the order of magnitude of Soret diffusion is estimated by comparison of the diffusive flux due to the concentration gradient to the flux induced by the temperature

gradient. In a binary mixture of A and B, the general form of diffusive flux (J_A) with the Soret effect is:

$$J_A = -c_T \mathcal{D}_{AB} \cdot \Big(\underbrace{\nabla x_A}_{\substack{concentration \\ gradient-driven \\ diffusive\ flux}} + \underbrace{k_T \nabla \ln T}_{\substack{temperature \\ gradient-driven \\ diffusive\ flux}} \Big) \tag{C.2}$$

where k_T is the thermal diffusion ratio, a parameter which depends on temperature and species composition. For most gaseous species, $k_T < 0.1$ [86]. If the characteristic length for thermal diffusion and mass diffusion are similar (which can be assumed to be true for gases where the Lewis number is typically of order 1), the Soret effect can be neglected if $T\Delta x_A/(k_T \Delta T) \gg 1$. Recognizing that mole fraction changes Δx_A are of order 1, the maximum ΔT in this study is $\sim 5\ K$, and the work is conducted at $T \sim 700K$, the quantity $T\Delta x_A/(k_T \Delta T) \sim 1400$ and the neglection of the Soret effect in the species conservation equations is well justified.

C.5 Decision to Neglect Radiation Heat Transfer in the CHAMP-SORB Reactor

At elevated temperatures, radiation heat transfer become increasingly important, as the emissive power, or the rate of energy released by a surface $[W/m^2]$ is proportional to T^4 [87]. In solid oxide fuel cells (SOFCs), operating from between $600 - 1000$℃, radiation effects have been shown to be significant in thermal management efforts and in materials development [91]. While the target operating temperature range of the CHAMP-SORB reactor is not quite as high as SOFCs (limited to $400 - 500$℃), radiation effects could be important in modeling the system thermal behavior.

For the purpose of this dissertation, however, radiation heat transfer is neglected because (*i*) inclusion of the radiative effects will introduce additional complexity and non-linearity into the system, and (*ii*) any radiative heat transfer effects would serve to diminish the spatial temperature variations across the porous bed. As can be seen in Figure 6.4 and Figure 6.8, even in the conservative case where enhancement of heat transfer due to radiative effects is not considered, the heat transfer limitations play much less of a role than mass transfer limitations. Spatial temperature variation across the catalyst layer is even less significant in the case of a stratified catalyst, as shown in Figure 6.9, as the region of the porous bed where the endothermic reaction takes place is concentrated closer to the membrane surface (at the location of heat input to the reactor), and additional heat can be supplied to the catalyst by the surrounding pure sorbent region as it undergoes exothermic CO_2 adsorption.

APPENDIX D: TRANSPORT-KINETIC MODEL DISCRETIZATION

D.1 Coordinate Transformation

The domain to be simulated is shown in Figure D.1, including definition of the mesh and relevant dimensions and properties used for numerical discretization.

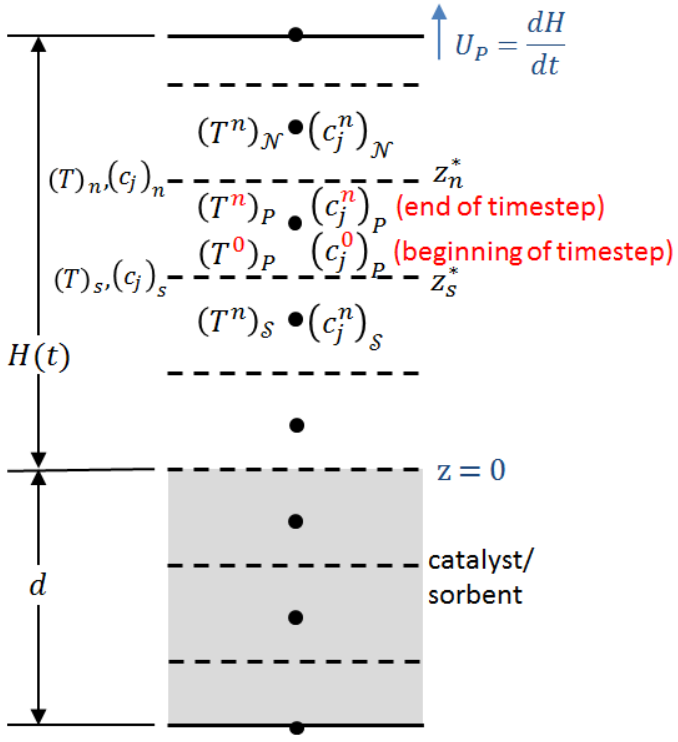

Figure D.1: Discretization schematic and nomenclature

The set of governing equations describing transient, one-dimensional species transport and energy conversation in the reactor (applicable both to the gas phase bulk and porous catalyst/sorbent bed) is as follows:

$$\underbrace{\frac{\partial c_j}{\partial t}}_{\substack{Time\ rate\ of\ change\ of\ species\ j's\ concentration}} + \underbrace{\frac{\partial}{\partial z}\left(c_j v + J_{z,j}\right)}_{\substack{Net\ rate\ of\ species\ transport\ from\ CV\ due\ to\ advection\ and\ diffusion}} = \underbrace{S_j}_{\substack{Net\ production\ rate\ of\ species\ j\ in\ CV\ due\ to\ rxn}} \tag{D.1}$$

$$\underbrace{\frac{\partial}{\partial t}\left[\sum_{j=1}^{N}\left(c_j \overline{c}_{p,j} T\right) + \overline{\rho} c_{p,b} T\right]}_{\substack{Time\ rate\ of\ change\ of\ energy\ stored\ in\ CV}} + \underbrace{\frac{\partial}{\partial z}\left[\sum_{j=1}^{N}\left(c_j v + J_{z,j}\right)\overline{c}_{p,j} T\right]}_{\substack{Net\ rate\ of\ energy\ leaving\ CV\ due\ to\ species\ transport}}$$

$$= \underbrace{\frac{\partial}{\partial z}\left[k_{eff}\frac{\partial T}{\partial z}\right]}_{\substack{Net\ rate\ of\ energy\ into\ CV\ due\ to\ conduction}} + \underbrace{\overline{\varepsilon}\frac{dp_T}{dt} + S_h}_{\substack{Net\ rate\ of\ energy\ gain\ in\ CV\ due\ to\ compression/\ rxn\ sources}} \tag{D.2}$$

$$\underbrace{\frac{\partial c_T}{\partial t}}_{\substack{Time\ rate\ of\ change\ of\ total\ concentration\ in\ CV}} + \underbrace{\frac{\partial}{\partial z}\left(c_T v\right)}_{\substack{Net\ rate\ of\ total\ species\ transport\ due\ to\ advection}} = \underbrace{\sum_{j=1}^{N} S_j}_{\substack{Net\ rate\ of\ total\ molar\ species\ prod.\ due\ to\ rxn}} \tag{D.3}$$

The coordinate system is transformed into t^* and z^* space where $t^* = t$ and $z^* = z/H(t)$ to facilitate discretization and numerical integration of governing equations as the transformed domain remains fixed in size even though the physical domain continuously changes with the piston motion. Using chain rule:

$$\frac{\partial t^*}{\partial t} = 1 \tag{D.4a}$$

$$\frac{\partial t^*}{\partial z} = 0 \tag{D.4b}$$

$$\frac{\partial z^*}{\partial z} = \frac{1}{H(t)} \tag{D.4c}$$

$$\frac{\partial z^*}{\partial t} = \frac{-z}{[H(t)]^2}\cdot\frac{dH(t)}{dt} = \frac{-z^* U_p}{H(t)} \tag{D.4d}$$

where the equation for $\partial z^*/\partial t$ is simplified by recognizing that $z = z^* \cdot H(t)$ and that $dH/dt = U_p$ where U_p is the piston velocity. As a result, the partial derivatives for each

term in the governing equations can be transformed in the following manner using the chain rule:

$$\frac{\partial}{\partial t}\left(\ \right) = \frac{\partial}{\partial t^*}\left(\ \right)\cdot\frac{\partial t^*}{\partial t}^{1} + \frac{\partial}{\partial z^*}\left(\ \right)\cdot\frac{\partial z^*}{\partial t} \tag{D.5a}$$

$$\frac{\partial}{\partial t}\left(\ \right) = \frac{\partial}{\partial t^*}\left(\ \right) - \frac{z^* U_p}{H(t)}\cdot\frac{\partial}{\partial z^*}\left(\ \right) \tag{D.5b}$$

and for the spatial derivatives:

$$\frac{\partial}{\partial z}\left(\ \right) = \frac{\partial}{\partial z^*}\left(\ \right)\cdot\frac{\partial z^*}{\partial z} + \frac{\partial}{\partial t^*}\left(\ \right)\cdot\frac{\partial t^*}{\partial z}^{0} \tag{D.6a}$$

$$\frac{\partial}{\partial z}\left(\ \right) = \frac{1}{H(t)}\cdot\frac{\partial}{\partial z^*}\left(\ \right) \tag{D.6b}$$

$$\frac{\partial^2}{\partial z^2}\left(\ \right) = \frac{1}{H(t)}\cdot\frac{\partial}{\partial z}\left[\frac{\partial}{\partial z^*}\left(\ \right)\right] \tag{D.6c}$$

$$\frac{\partial^2}{\partial z^2}\left(\ \right) = \frac{1}{[H(t)]^2}\cdot\frac{\partial^2}{\partial z^{*2}}\left(\ \right) \tag{D.6d}$$

D.2 Discretization for Species Conservation in the Bulk Gas Only Domain (Outside of Porous Bed)

Prior to modeling the complex reactor domain illustrated in Figure D.1, with energy and species concentration considered in two separate regions of different grid size and properties (*i.e.* one is pure gas, the other is a porous media/gas mixture), the discretized equations are first developed for species conservation alone in a simplified case with only the gas region (no porous bed) and spatially uniform (but temporally varying due to piston motion) grid size. In developing these equations, the temperature is allowed to vary spatially to enable future use in non-isothermal simulations; however, for the time being an arbitrary temperature profile is assumed *a priori* for developing a general

framework for numerical solution of the species transport equations, which would be applicable for future incorporation of the temperature field from the solution of the energy conservation equation. The simulation domain of this simplified case is illustrated in Figure D.2.

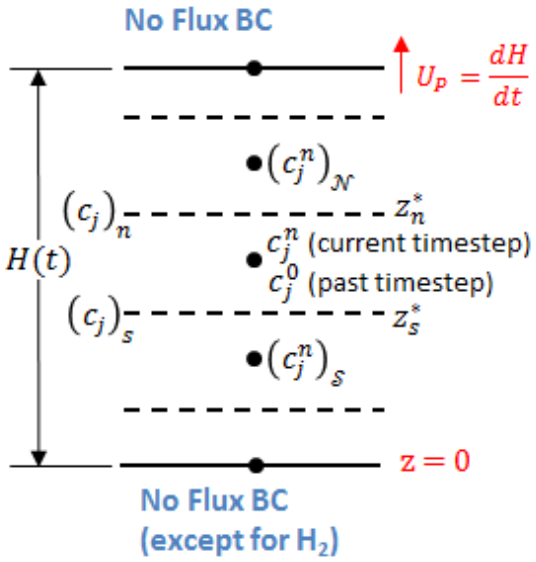

Figure D.2: Simplified simulation domain for species conservation equations consisting of one (gas-only) region with no porous media

D.2.1 Species concentration discretization

Following the transformation process outlined in equations (D.5) and (D.6), the species conservation equation for species j (D.1), becomes:

$$\frac{\partial c_j}{\partial t^*} - \frac{z^* U_p}{H(t)} \cdot \frac{\partial c_j}{\partial z^*} + \frac{1}{H(t)} \cdot \frac{\partial}{\partial z^*}\left(c_j v + J_{z,j}\right) = S_j \tag{D.7}$$

Or multiplying through by $H(t)$ and replacing t^* with t (because as defined, $t = t^*$):

$$\frac{\partial c_j}{\partial t^*} - \frac{z^* U_p}{H(t)} \cdot \frac{\partial c_j}{\partial z^*} + \frac{1}{H(t)} \cdot \frac{\partial}{\partial z^*}\left(c_j v + J_{z,j}\right) = S_j \tag{D.8}$$

Two modifications are made to (D.8) to make the equation more readily discretized using the finite volume method (FVM). First, because by the chain rule $\partial(Hc_j)/\partial t = H(\partial c_j/\partial t) + c_j(\partial H/\partial t)$ and making the substitution that by definition $U_p = \partial H/\partial t$:

$$H\frac{\partial c_j}{\partial t} = \frac{\partial}{\partial t}(Hc_j) - U_p c_j \tag{D.9}$$

Secondly, also using chain rule $\partial(z^* U_p c_j)/\partial z^* = z^* U_p \partial c_j/\partial z^* + U_p c_j \cancel{\partial z^*/\partial z^*}^{1}$, yielding:

$$z^* U_p \frac{\partial c_j}{\partial z^*} = \frac{\partial}{\partial z^*}(U_p z^* c_j) - U_p c_j \tag{D.10}$$

Substituting (C.9) and (C.10) into the transformed species conservation equation (C.8) yields:

$$\left[\frac{\partial}{\partial t}(Hc_j) - U_p c_j\right] - \left[\frac{\partial}{\partial z^*}(U_p z^* c_j) - U_p c_j\right] + \frac{\partial}{\partial z^*}(c_j v + J_{z,j}) = H \cdot S_j \tag{D.11}$$

The $U_p c_j$ terms inside the first and second brackets on the left side of eq S11 cancel one another out, and the first term inside the second bracket can be combined with the divergence of the advective flux in the third element of the left side:

$$\frac{\partial}{\partial t}(Hc_j) + \frac{\partial}{\partial z^*}\left[c_j(v - U_p z^*) + J_{z,j}\right] = H \cdot S_j \tag{D.12}$$

Equation (D.12) can be further simplified by recognizing that $v - U_p z^*$ is simply the average molar velocity relative to the motion of the coordinate system's local velocity and defining this relative velocity to be $v^* = v - U_p z^*$. Next, FVM discretization is applied by integrating the governing equation from $z_s^* \rightarrow z_n^*$ and from $t^0 \rightarrow t^n$. First the spatial integration is carried out:

$$\int_{z_s^*}^{z_n^*} \frac{\partial}{\partial t}(Hc_j)dz^* + \int_{z_s^*}^{z_n^*} \cancel{\frac{\partial}{\partial z^*}}(c_j v^* + J_{z,j})\,\cancel{dz^*} = \int_{z_s^*}^{z_n^*} [HS_j]dz^* \tag{D.13}$$

Assuming a constant c_j and S_j profile throughout the infinitesimally small control volume, the equation can be readily integrated (where $\left(c_j v^* + J_{z,j}\right)_n$ and $\left(c_j v^* + J_{z,j}\right)_s$ are the advective and diffusive fluxes at the north and south face of the CV, respectively):

$$\frac{\partial}{\partial t}\left(Hc_j\right)\Delta z^* + \left(c_j v^* + J_{z,j}\right)_n - \left(c_j v^* + J_{z,j}\right)_s = HS_j\Delta z^* \tag{D.14}$$

Next, carrying out the integration over the time step from $t^0 \rightarrow t^n$:

$$\int_{t^0}^{t^n}\left[\Delta z^* \frac{\partial}{\partial t}\left(Hc_j\right)\right]dt + \int_{t^0}^{t^n}\left[\left(c_j v + J_{z,j}\right)_n - \left(c_j v + J_{z,j}\right)_s\right]dt = \int_{t^0}^{t^n} HS_j\Delta z^*\, dt \tag{D.15}$$

In the source term on the right side of equation (D.15), H is approximated as constant over the integration time, $\bar{H} = [H(t^0) + H(t^n)]/2$. A fully implicit scheme (*i.e.*, all of the c_j's used to calculate the advective and diffusive fluxes are taken at the end of the timestep t^n, not at the beginning t^0) is also implemented to aid in numerical stability:

$$\Delta z^*\left(H^n\left(c_j^n\right)_P - H^n\left(c_j^0\right)_P\right) + \left(c_j^n v^* + J_{z,j}\right)_n\Delta t - \left(c_j^n v^* + J_{z,j}\right)_s\Delta t = \bar{H}S_j\Delta z^*\Delta t \tag{D.16a}$$

or, dividing through by $\Delta t = (t^n - t^0)$ and noting the physical meaning of each parameter:

$$\underbrace{\frac{\Delta z^*}{\Delta t}\left(H^n\left(c_j^n\right)_P - H^n\left(c_j^0\right)_P\right)}_{\substack{time\ rate\ of\ change\ of \\ species\ j\ stored\ in\ CV}} + \underbrace{\left(c_j^n\right)_n v_n^* - \left(c_j^n\right)_s v_s^*}_{\substack{net\ advective\ flux\ of \\ species\ j\ out\ of\ CV}} + \underbrace{\left(J_{z,j}\right)_n - \left(J_{z,j}\right)_s}_{\substack{net\ diffusive\ flux \\ of\ species\ j\ from\ CV}} = \underbrace{\bar{H}S_j\Delta z^*}_{\substack{rate\ of\ production \\ of\ species\ j\ due\ to \\ reaction/adsorption}} \tag{D.16b}$$

The parameters in (D.16b) all are on a per-unit area basis (units $[mol/m^2 \cdot s]$) for the 1-D simulation geometry under consideration. Figure D.3 illustrates the advective/diffusive fluxes for a representative grid-point cluster described by the discretized equation (D.16b).

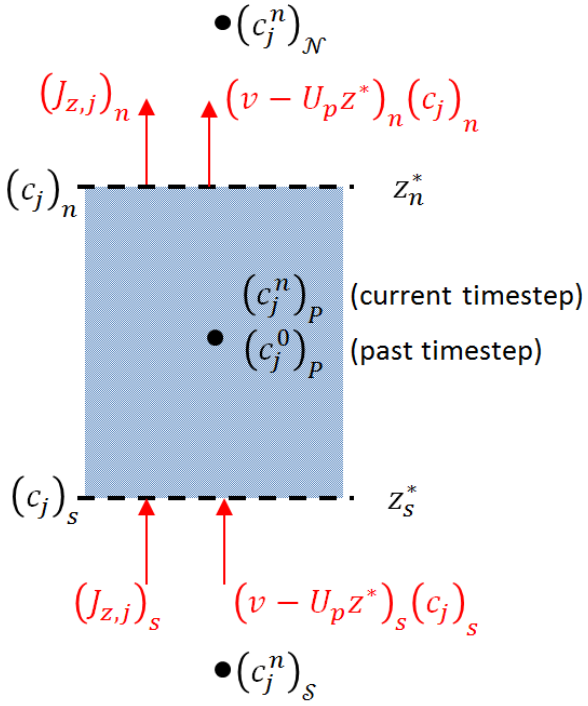

Figure D.3: Advective/diffusive fluxes for a representative grid-point cluster corresponding to the discretized governing equation for species conservation. Three spatial elements are denoted with subscript $\mathcal{N}, \mathcal{S}$ and P for north, south, and present node, respectively. The values at the north and south boundary are denoted with a n and s subscript, respectively. The point in time for a concentration value is noted with a superscript of n or 0 for new/previous time step, respectively.

Applying an upwinding scheme, if the average relative molar velocity at the north CV face is positive, the value of the concentration of species j at the north face, $(c_j^n)_n$, is equal to the value at the center of the node, $(c_j^n)_P$. Conversely, if the average relative

molar velocity at the north CV face is negative, the value of $\left(c_j^n\right)_n$ is the concentration at the center of the node above it, or $\left(c_j^n\right)_{\mathcal{N}}$[97]. In other words:

$$\left(c_j^n\right)_n = \begin{matrix} \left(c_j^n\right)_P & \text{If } v_n^* > 0 \\ \left(c_j^n\right)_{\mathcal{N}} & \text{If } v_n^* < 0 \end{matrix} \tag{D.17a}$$

and the boundary value at the south face is similarly upwinded according to the direction of the advective flux:

$$\left(c_j^n\right)_s = \begin{matrix} \left(c_j^n\right)_S & \text{If } v_s^* > 0 \\ \left(c_j^n\right)_P & \text{If } v_s^* < 0 \end{matrix} \tag{D.17b}$$

Using the notation that $[\![A, B]\!]$ is the maximum of A or B and letting $\left(J_{z,j}\right)_s^n = \left(J_{z,j}\right)_n - \left(J_{z,j}\right)_s$:

$$\begin{aligned} \frac{\Delta z^*}{\Delta t}\left(H^n\left(c_j^n\right)_P - H^0\left(c_j^0\right)_P\right) + \left(c_j^n\right)_P [\![v_n^*, 0]\!] - \left(c_j^n\right)_{\mathcal{N}} [\![-v_n^*, 0]\!] \\ - \left(c_j^n\right)_S [\![v_s^*, 0]\!] + \left(c_j^n\right)_P [\![-v_s^*, 0]\!] + \left(J_{z,j}\right)_s^n = \bar{H} S_j \Delta z^* \end{aligned} \tag{D.18}$$

Next the term $\left(J_{z,j}\right)_s^n$, representing the divergence of the diffusive flux, must be determined using a constitutive relation. The Maxwell-Stefan formulation is used because it is rigorous in treating multiple component mixtures and has been found to be more accurate especially in the limit of large disparity in molecular weights of the mixture components,[92] whereas the Fickian representation strictly applies only to binary systems.[86] According to Maxwell-Stefan, $\overrightarrow{\boldsymbol{J}_{z,J}} = -c_T [B]^{-1} \frac{\partial}{\partial z}\left(\overrightarrow{\boldsymbol{c}_J}/c_T\right)$ where $\overrightarrow{\boldsymbol{J}_{z,J}}$ is a column vector of length N-1 representing the diffusive fluxes of N-1 species and $[B]$ is an $(N-1) \times (N-1)$ matrix with terms [93]:

$$B_{lm} = \begin{cases} x_l\left(\frac{1}{D_{lN}} - \frac{1}{D_{lm}}\right) & l \neq m \\ \frac{1}{D_{lN}} + \sum_{\substack{k=1 \\ k\neq l}}^{N-1} x_k\left(\frac{1}{D_{lk}} - \frac{1}{D_{lN}}\right) & l = m \end{cases} \tag{D.19}$$

Non-dimensionalizing z in a similar fashion as before yields:

$$\overrightarrow{\boldsymbol{J}_{z,\boldsymbol{J}}} = \frac{-c_T[B]^{-1}}{H(t)} \frac{\partial}{\partial z^*}\left(\frac{\overrightarrow{\boldsymbol{c}_{\boldsymbol{J}}}}{c_T}\right) \tag{D.20}$$

The diffusive flux for a single species *j* is then given by

$$J_{z,j} = \frac{-c_T}{H(t)}\left[\sum_{k=1}^{N-1} B_{jk}^{-1} \frac{\partial(c_k/c_T)}{\partial z^*}\right] \tag{D.21}$$

where B_{jk}^{-1} is the j,k component of the inverted B matrix. This constitutive relationship for diffusive flux can be calculated at the north and south faces, respectively, by approximating the gradient term as:

$$\left(\frac{\partial(c_k/c_T)}{\partial z^*}\right)_n \sim \frac{(c_k^n)_{\mathcal{N}}/\left(c_T^{n'}\right)_{\mathcal{N}} - (c_k^n)_P/\left(c_T^{n'}\right)_P}{\Delta z^*} \tag{D.22a}$$

$$\left(\frac{\partial(c_k/c_T)}{\partial z^*}\right)_s \sim \frac{(c_k^n)_P/\left(c_T^{n'}\right)_P - (c_k^n)_{\mathcal{S}}/\left(c_T^{n'}\right)_{\mathcal{S}}}{\Delta z^*} \tag{D.22b}$$

In order to make the set of equations linear, the total concentration term from the previous iteration (n') is used when calculating the mole fractions rather than the current iteration (n), *i.e.* $\left(c_j^n\right)_{\mathcal{N}}/\left(c_T^{n'}\right)_{\mathcal{N}}$. Using these gradient terms, the discretized term representing the divergence of the diffusive flux $\left(J_{z,j}\right)_s^n$ is:

$$\left(J_{z,j}\right)_s^n = \frac{-1}{\bar{H}}\left[\sum_{k=1}^{N-1}\left(\left(c_T^{n'}B_{jk}^{-1}\right)_n \frac{(c_k^n)_{\mathcal{N}}/\left(c_T^{n'}\right)_{\mathcal{N}} - (c_k^n)_P/\left(c_T^{n'}\right)_P}{\Delta z^*} - \left(c_T^{n'}B_{jk}^{-1}\right)_s \frac{(c_k^n)_P/\left(c_T^{n'}\right)_P - (c_k^n)_{\mathcal{S}}/\left(c_T^{n'}\right)_{\mathcal{S}}}{\Delta z^*}\right)\right] \tag{D.23a}$$

Or grouping terms of the same node together and pulling terms involving j out of the summation:

$$\left(J_{z,j}\right)_s^n = \frac{-1}{\bar{H}}\left[\frac{\left(c_T^{n'}B_{jj}^{-1}\right)_n}{\Delta z^*\left(c_T^{n'}\right)_{\mathcal{N}}}\left(c_j^n\right)_{\mathcal{N}} - \frac{\left(c_T^{n'}B_{jj}^{-1}\right)_n + \left(c_T^{n'}B_{jj}^{-1}\right)_s}{\Delta z^*\left(c_T^{n'}\right)_P}\left(c_j^n\right)_P + \frac{\left(c_T^{n'}B_{jj}^{-1}\right)_s}{\Delta z^*\left(c_T^{n'}\right)_{\mathcal{S}}}\left(c_j^n\right)_{\mathcal{S}} + \sum_{\substack{k=1\\k\neq j}}^{N-1}\left(\frac{\left(c_T^{n'}B_{jk}^{-1}\right)_n}{\Delta z^*\left(c_T^{n'}\right)_{\mathcal{N}}}(c_k^n)_{\mathcal{N}} - \frac{\left(c_T^{n'}B_{jk}^{-1}\right)_n + \left(c_T^{n'}B_{jk}^{-1}\right)_s}{\Delta z^*\left(c_T^{n'}\right)_P}(c_k^n)_P + \frac{\left(c_T^{n'}B_{jk}^{-1}\right)_s}{\Delta z^*\left(c_T^{n'}\right)_{\mathcal{S}}}(c_k^n)_{\mathcal{S}}\right)\right] \tag{D.23b}$$

In equation (D.23), the time varying term $H(t)$ is approximated as $\bar{H}$ (the average height during the timestep), continuing with the assumption made in the earlier discretization of the source term. Finally, the fully discretized equation for concentration of a given species at a given ***internal*** node is:

$$\left[\frac{\Delta z^* H^n}{\Delta t} + [\![v_n^*, 0]\!] + [\![-v_s^*, 0]\!] + \frac{\left(c_T^{n'} B_{jj}^{-1}\right)_n + \left(c_T^{n'} B_{jj}^{-1}\right)_s}{\bar{H}\Delta z^* \left(c_T^{n'}\right)_P}\right] \left(c_j^n\right)_P$$

$$- \left[[\![-v_n^*, 0]\!] + \frac{\left(c_T^{n'} B_{jj}^{-1}\right)_n}{\bar{H}\Delta z^* \left(c_T^{n'}\right)_{\mathcal{N}}}\right] \left(c_j^n\right)_{\mathcal{N}} - \left[[\![v_s^*, 0]\!] + \frac{\left(c_T^{n'} B_{jj}^{-1}\right)_s}{\bar{H}\Delta z^* \left(c_T^{n'}\right)_{\mathcal{S}}}\right] \left(c_j^n\right)_{\mathcal{S}}$$

$$- \sum_{\substack{k=1 \\ k\neq j}}^{N-2} \left[\frac{\left(c_T^{n'} B_{jk}^{-1}\right)_n}{\bar{H}\Delta z^* \left(c_T^{n'}\right)_{\mathcal{N}}} \left(c_k^n\right)_{\mathcal{N}}\right] - \sum_{\substack{k=1 \\ k\neq j}}^{N-2} \left[\frac{\left(c_T^{n'} B_{jk}^{-1}\right)_n + \left(c_T^{n'} B_{jk}^{-1}\right)_s}{\bar{H}\Delta z^* \left(c_T^{n'}\right)_P} \left(c_k^n\right)_P\right] \tag{D.24}$$

$$- \sum_{\substack{k=1 \\ k\neq j}}^{N-2} \left[\frac{\left(c_T^{n'} B_{jk}^{-1}\right)_s}{\bar{H}\Delta z^* \left(c_T^{n'}\right)_{\mathcal{S}}} \left(c_k^n\right)_{\mathcal{S}}\right] = \bar{H} S_j \Delta z^* + \frac{\Delta z^* H^0}{\Delta t} \left(c_j^0\right)_P$$

The discretized equations for nodes on the boundaries will have slightly different terms due to the boundary conditions. In the case of the CHAMP-SORB geometry, the node at the top boundary will have no flux, whereas the node at the bottom boundary will have no flux with the exception of hydrogen permeating through the membrane. Revisiting the governing species conservation equation after FVM integration (equation (D.16b)), but modifying to note that the bottom boundary nodes are a "half width" and that the flux at the south face is zero for all non-H_2 species, *i.e.* $\left(c_j^n\right)_s v_s^* + \left(J_{z,j}\right)_s = 0$, and adding in a south face permeation "source" term $N''_{perm,j}$ (=0 for all j except $j = H_2$):

$$\frac{(\Delta z^*/2)}{\Delta t}\left(H^n\left(c_j^n\right)_P - H^0\left(c_j^0\right)_P\right) + \left(c_j^n\right)_n v_n^* - \cancel{\left(c_j^n\right)_s v_s^*} + \left(J_{z,j}\right)_n - \cancel{\left(J_{z,j}\right)_s}$$

$$= \bar{H} S_j \Delta z^* - N''_{perm,j} \tag{D.25}$$

The permeation flux for species j (only non-zero for $j = H_2$ because the membrane is hydrogen selective) is given by Sieverts' Law, where $\left(c_j^{n'}\right)_b$ and $\left(c_T^{n'}\right)_b$ are the species j and total concentrations, respectively, at the boundary node adjacent to the membrane :

$$N''_{perm,j} = \frac{D_{mem,j}}{\delta}\left[\left(P_T \frac{\left(c_j^{n'}\right)_b}{\left(c_T^{n'}\right)_b}\right)^{1/2} - P_{j,\infty}^{1/2}\right] \tag{D.26}$$

where $D_{mem,j}$ is the permeance of the membrane for species j and is only non-zero for $j = H_2$.

To keep the system of equations linear, the permeation term is treated explicitly, using hydrogen concentration at the ***beginning*** of the current timestep (*i.e.*, at $t = t^0$) to determine the permeation flux, meaning that it will be solved as a source term on the right-hand side of the discretized equation. Applying the constitutive relations for the diffusive flux at the north face and shorthand notation for average molar velocity relative to the CV boundary, the discretized equation for a node of species *j* at the bottom of the domain is:

$$\begin{aligned}\left[\frac{\Delta z^* H^n}{2\Delta t} + [\![v_n^*, 0]\!] + \frac{\left(c_T^{n'} B_{jj}^{-1}\right)_n}{\bar{H}\Delta z^* \left(c_T^{n'}\right)_P}\right]\left(c_j^n\right)_P - \left[[\![-v_n^*, 0]\!] + \frac{\left(c_T^{n'} B_{jj}^{-1}\right)_n}{\bar{H}\Delta z^* \left(c_T^{n'}\right)_{\mathcal{N}}}\right]\left(c_j^n\right)_{\mathcal{N}} \\ - \sum_{\substack{k=1 \\ k\neq j}}^{N-2}\left[\frac{\left(c_T^{n'} B_{jk}^{-1}\right)_n}{\bar{H}\Delta z^* \left(c_T^{n'}\right)_{\mathcal{N}}}\left(c_k^n\right)_{\mathcal{N}}\right] - \sum_{\substack{k=1 \\ k\neq j}}^{N-2}\left[\frac{\left(c_T^{n'} B_{jk}^{-1}\right)_n}{\bar{H}\Delta z^* \left(c_T^{n'}\right)_P}\left(c_k^n\right)_P\right] \\ = \bar{H} S_j \frac{\Delta z^*}{2} + \frac{\Delta z^* H^0}{2\Delta t}\left(c_j^0\right)_P - \frac{D_{mem,j}}{\delta}\left[\left(P_T \frac{\left(c_j^{n'}\right)_b}{\left(c_T^{n'}\right)_b}\right)^{1/2} - P_{H_2,\infty}^{1/2}\right]\end{aligned} \tag{D.27}$$

Applying a similar approach to the one used in developing equation (D.26) to the node at the top of the domain (piston face), where the flux at the north face is zero, *i.e.* $\left(c_j^n\right)_n v_n^* + \left(J_{z,j}\right)_n = 0$, and there is no membrane permeation, yields:

$$\frac{(\Delta z^*/2)}{\Delta t}\left(H^n\left(c_j^n\right)_P - H^0\left(c_j^0\right)_P\right) + \cancel{\left(c_j^n\right)_n v_n^*} - \left(c_j^n\right)_s v_s^* + \cancel{\left(J_{z,j}\right)_n} - \left(J_{z,j}\right)_s = \bar{H} S_j \Delta z^* \tag{D.28}$$

Applying the constitutive relations for the diffusive flux at the south face and shorthand notation for average molar velocity relative to the CV boundary, the discretized equation for a node of species j at the top of the domain is:

$$\left[\frac{\Delta z^* H^n}{2\Delta t} + [\![-v_s^*, 0]\!] + \frac{\left(c_T^{n\prime} B_{jj}^{-1}\right)_s}{\bar{H}\Delta z^*\left(c_T^{n\prime}\right)_P}\right]\left(c_j^n\right)_P - \left[[\![v_s^*, 0]\!] + \frac{\left(c_T^{n\prime} B_{jj}^{-1}\right)_s}{\bar{H}\Delta z^*\left(c_T^{n\prime}\right)_S}\right]\left(c_j^n\right)_S$$
$$- \sum_{\substack{k=1 \\ k\neq j}}^{N-2}\left[\frac{\left(c_T^{n\prime} B_{jk}^{-1}\right)_s}{\bar{H}\Delta z^*\left(c_T^{n\prime}\right)_P}\left(c_k^n\right)_P\right] - \sum_{\substack{k=1 \\ k\neq j}}^{N-2}\left[\frac{\left(c_T^{n\prime} B_{jk}^{-1}\right)_s}{\bar{H}\Delta z^*\left(c_T^{n\prime}\right)_S}\left(c_k^n\right)_S\right] \tag{D.29}$$
$$= \bar{H} S_j \frac{\Delta z^*}{2} + \frac{\Delta z^* H^0}{2\Delta t}\left(c_j^0\right)_P$$

Lastly, to determine the molar average velocity at each node, the total concentration equation must be discretized and numerically integrated. Summing the discretized equation for an internal node (equation D.16b) over all species j and noting that, by definition, the sum of the diffusive fluxes is zero:

$$\frac{\Delta z^*}{\Delta t}[H^n(c_T^n)_P - H^0(c_T^0)_P] + (c_T^n)_n v_n^* - (c_T^n)_s v_s^* + \sum_{j=1}^{N}\cancel{\left(J_{z,j}\right)_s^n} = \left[\sum_{j=1}^{N} S_j\right]\bar{H}\Delta z^* \tag{D.30a}$$

or, grouping "known" source terms on the right side and coefficients of the unknown velocity on the right left side:

$$(c_T^n)_n v_n^* - (c_T^n)_s v_s^* = \left[\sum_{j=1}^{N} S_j\right]\bar{H}\Delta z^* - \frac{\Delta z^*}{\Delta t}[H^n(c_T^n)_P - H^0(c_T^0)_P] \tag{D.30b}$$

where the value of c_T^n at the north and south face is upwinded based on the direction of the relative velocity v^* (which can be determined by using the previous iteration's velocity).

The discretized equation (D.30b) for the first node must be modified because it is only a half-width and has a molar flux at the south face equal to the rate of H_2 permeation:

$$(c_T^n)_n v_n^* = \left[\sum_{j=1}^{N} S_j\right] \bar{H} \frac{\Delta z^*}{2} - \frac{\Delta z^*}{2\Delta t}[H^n(c_T^n)_P - H^0(c_T^0)_P] - N''_{perm,H_2} \tag{D.31}$$

Continuity at the top node (adjacent to the moving piston surface) can be checked by verifying that the following equation is satisfied (v_n^* must equal zero because the piston is impenetrable):

$$0 = \left[\sum_{j=1}^{N} S_j\right] \bar{H} \frac{\Delta z^*}{2} - \frac{\Delta z^*}{2\Delta t}[H^n(c_T^n)_P - H^0(c_T^0)_P] + (c_T^n)_s v_s^* - \cancel{(c_T^n)_n v_n^{*0}} \tag{D.32}$$

The values of total concentration used in the discretized equations (D.30) – (D.32) are not computed directly as the summation of concentration of each species j; rather, the new cumulative total number of moles (per unit area) in the reactor ($N_T^n = N_T^0 + \Delta N_{rxn} - \Delta N_{perm}$) is calculated from the molar balance by taking the number of moles at the beginning of the time step and subtracting the loss of moles per unit area due to permeation ($\Delta N_{perm} = N''_{perm,H_2} \cdot \Delta t$ obtained via equation (D.26)) and adding the net number of moles due to reactions ($\Delta N_{rxn} = \sum_{z=1}^{N_{nodes}} \left[\sum_{j=1}^{N_{species}} S_j H \Delta z^*\right] \cdot \Delta t$) during the timestep. The new number of moles per unit area is then used to calculate a new total reactor pressure (per unit area) at the conclusion of the timestep, P_T^n (where $P_T^n =$

$(N_T^n R_u)/\int_0^{H(t)}(T^n)^{-1}dz$ because, according to the ideal gas equation of state $N_T^n = \int_0^{H(t)} c_T^n dz = (P_T^n/R_u)\cdot\int_0^{H(t)}(T^n)^{-1}dz$). The total reactor pressure at the conclusion of the timestep is then used to determine the local total concentration at each node based on the temperature profile using the ideal gas equation of state ($(c_T^n)_z = P_T^n/[R_u(T^n)_z]$).

The discretized species conservation equations, (D.24) for interior nodes and (D.27) and (D.29) for the nodes adjacent to the membrane and the piston, respectively, can be arranged into a system of equations in matrix form by inputting each equation as a row, resulting in a form $[\boldsymbol{a}]\overrightarrow{c_j^n} = \overrightarrow{RHS}$. In this system of equations, $\overrightarrow{c_j^n}$ is an array of the new concentration values of each species at each node (arranged starting with the concentration of species 1 at nodes $\{1,2,3 \ldots N_{nodes}\}$, followed by the concentration for species 2 at nodes $\{1,2,3 \ldots N_{nodes}\}$, etc. up through $\{N_s - 1\}$ species). Only $\{N_s - 1\}$ species are solved directly because only that quantity of diffusive flux relations is independent. The coefficient matrix $[\boldsymbol{a}]$ and right hand side vector $\overrightarrow{RHS}$ are populated similarly, where the value of each comes from the general form of equation (D.27) $(a_{j,P}(c_j^n)_P + a_{j,\mathcal{N}}(c_j^n)_{\mathcal{N}} + a_{j,\mathcal{S}}(c_j^n)_{\mathcal{S}} + \sum_{\substack{k=1 \\ k\neq j}}^{N_s-1}[\, a_{k,P}(c_k^n)_P + a_{k,\mathcal{N}}(c_k^n)_{\mathcal{N}} + a_{k,\mathcal{S}}(c_k^n)_{\mathcal{S}}] =$ $RHS_{j,P}$, where j is the species being conserved in the equation and k can take the value of any species not equal to j). Figure D.4 illustrates the resulting matrix form of this system of equations for a simulation domain consisting of $N_{species} = 4$ and $N_{nodes} = 6$, where the coefficients for the equation representing conservation of species 2 at node 3 are explicitly shown.

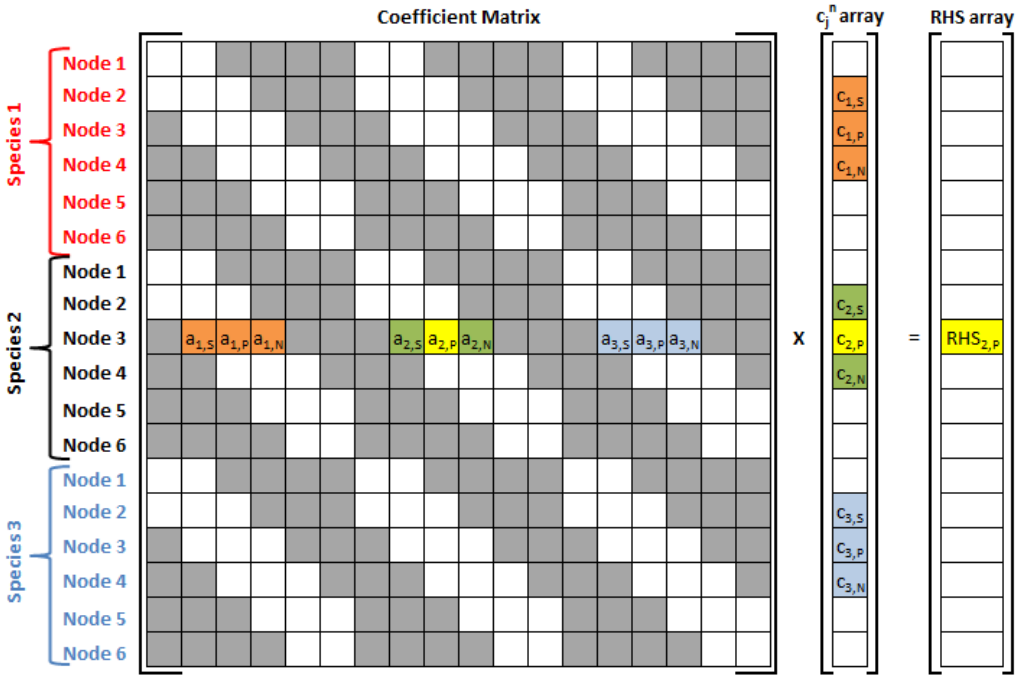

Figure D.4: Illustration of system of species concentration equations in matrix form, with the coefficients and species involved in the conservation of species 2 at node 3 highlighted. All grey cells in the matrix have a value of zero, while the white cells are non-zero (but involved only in the conservation equations at other nodes).

The $[\boldsymbol{a}]$ coefficient matrix that results from the arrangement of the system of equations into matrix form is sparse and banded, with all grey cells in Figure D.4 having a value of zero. The matrix is not tri-diagonal, however, due to the influence of gradients of other species (k) on the diffusive flux of a given species (j), and as such an efficient matrix solver such as the Thomas algorithm cannot be used to solve the system of equations [97]. Instead, the solution of these equations is determined directly using MATLAB's right hand divide functionality to calculate the solution $\overrightarrow{c_j^n} = [\boldsymbol{a}]^{-1}\overrightarrow{RHS}$. Because an implicit discretization is employed, an iterative solution technique (illustrated in Figure 6.2) is employed.

As previously mentioned, species conservation can only be directly solved for $\{N_s - 1\}$ species due to the lack of linear independence in the diffusive flux relationship for the final species. The concentration of that final species is determined by instead calculating the total number of moles of all species in the reactor at the end of the timestep by determining the net change in total moles due to reaction, permeation and adsorption during the timestep, then using this number to determine the pressure and species concentration distribution inside the reactor using the ideal gas equation of state. Once the total concentration distribution at the end of the timestep is known, the concentration for the first $\{N_s - 1\}$ species is found via solution of the matrix $\overrightarrow{c_j^n} = [\boldsymbol{a}]^{-1}\overrightarrow{RHS}$, the concentration of the final species is determined by subtracting the sum of the other species concentrations from the total concentration ($c_{N_s}^n = c_T^n - \sum_{j=1}^{N_s-1} c_j^n$).

C.3 Full Domain (Bulk Gas & Porous Bed) Discretized Species Transport Equations

Generalizing the discretized species conservation equation for the gas domain, equation (C.16b) to include the possibility of different size nodes in different regions:

$$\frac{\Delta z_\alpha^*}{\Delta t}\left(\alpha^n c_j^n - \alpha^0 c_j^0\right) + \left(c_j^n\right)_n v_n^* - \left(c_j^n\right)_s v_s^* + \left(J_{z,j}\right)_n - \left(J_{z,j}\right)_s = \bar{\alpha} S_j \Delta z_\alpha^* \qquad \text{(D.33)}$$

where α is the total height (which could be time dependent) of the particular region of the domain being simulated ($\alpha = H = H(t)$ for the gas region and $\alpha = d = constant$ for the porous catalyst/sorbent region). Also accounting for the fact that there may be a different number of nodes in the porous region, Δz_α^* represents the non-dimensionalized height of the node in the region under consideration. The diffusive fluxes at the north and south faces are, respectively:

$$\left(J_{z,j}\right)_n = -(c_T)_n \left[\sum_{k=1}^{N-1} \left(B_{jk}^{-1}\right)_n \frac{(c_k^n)_{\mathcal{N}} / \left(c_T^{n'}\right)_{\mathcal{N}} - c_k^n / c_T^{n'}}{\delta z_n}\right] \tag{D.34a}$$

$$\left(J_{z,j}\right)_s = -(c_T)_s \left[\sum_{k=1}^{N-1} \left(B_{jk}^{-1}\right)_s \frac{c_k^n / c_T^{n'} - (c_k^n)_{\mathcal{S}} / \left(c_T^{n'}\right)_{\mathcal{S}}}{\delta z_s}\right] \tag{D.34b}$$

where the "diffusion distance" from the center of a given node to the center of its adjacent node to the north (δz_n) or to the south (δz_s) will depend on the location of the particular node being analyzed. In regions where the north, south and center nodes all have equal spacing (*i.e.* a uniform node cell width equal to $\alpha \cdot \Delta z_\alpha^*$), the north and south diffusion distances are both equal to the width of the center node cell; however, the diffusional distance differs from the node cell width at the transition between the porous and gas-only regions which have different node widths.

Within the porous domain, gas species concentrations are defined with respect to the ***total*** volume of the solid and pore void, not just the volume available for gas inside the pores. As such, there will be a step discontinuity in total concentration across the border between gas only and porous medium regions (defining concentration based on the total, rather than just void, volume results in a generalized form of the ideal gas equation of state $c_T = P_T \bar{\varepsilon} / [R_u T]$, where the average porosity is a weighted average of the catalyst/sorbent properties in the porous region, $\overline{\varepsilon} = \phi \frac{\bar{\rho}}{\rho_c} \varepsilon_{cat} + (1 - \phi) \frac{\bar{\rho}}{\rho_s} \varepsilon_{sorb}$, and is $\bar{\varepsilon} = 1$ in the gas-only region). This impacts the determination of the average molar velocity in equations (D.30) – (D.32), as the total pressure at the conclusion of the timestep must be determined by $P_T^n = (N_T^n R_u) / \int_{-d}^{H(t)} \bar{\varepsilon} (T^n)^{-1} dz$ where $\bar{\varepsilon} < 1$ from $-d < z < 0$ and $\bar{\varepsilon} = 1$ from $0 < z < H(t)$. The resulting average molar velocity, along with above definition for species concentration in the porous media, allows for

continuity of the advective fluxes across the interface between gas only and porous medium domains, which are calculated identically using the product of the average molar velocity and the individual species concentration ($c_j v^*$) at either side of the interface. The diffusive flux is calculated in a similar fashion regardless of the domain, using equations (D.34a) and (D.34b), however, the individual binary diffusion coefficients between species l and m (D_{lm}) used in calculating the individual elements of the $[B]$ matrix are modified by the porosity and tortuosity (τ) in the porous region to account for transport impediment, yielding the "effective binary diffusion coefficients" ($\mathcal{D}_{lm,eff} = \mathcal{D}_{\ lm} \cdot \bar{\varepsilon}/\tau$) [94].

Using the above definitions for node width and diffusion distance, the discretized equation for an internal node can be written as:

$$\begin{aligned}
&\left[\frac{\Delta z_\alpha^* \alpha^n}{\Delta t} + [\![v_n^*, 0]\!] + [\![-v_s^*, 0]\!] + \frac{\left(c_T^{n'} B_{jj}^{-1}\right)_n}{\delta z_n c_T^{n'}} + \frac{\left(c_T^{n'} B_{jj}^{-1}\right)_s}{\delta z_s c_T^{n'}}\right]\left(c_j^n\right)_P \\
&\quad - \left[[\![-v_n^*, 0]\!] + \frac{\left(c_T^{n'} B_{jj}^{-1}\right)_n}{\delta z_n \left(c_T^{n'}\right)_{\mathcal{N}}}\right]\left(c_j^n\right)_{\mathcal{N}} - \left[[\![v_s^*, 0]\!] + \frac{\left(c_T^{n'} B_{jj}^{-1}\right)_s}{\delta z_s \left(c_T^{n'}\right)_{\mathcal{S}}}\right]\left(c_j^n\right)_{\mathcal{S}} \\
&\quad - \sum_{\substack{k=1 \\ k\neq j}}^{N-2}\left[\frac{\left(c_T^{n'} B_{jk}^{-1}\right)_n}{\delta z_n \left(c_T^{n'}\right)_{\mathcal{N}}}\left(c_k^n\right)_{\mathcal{N}}\right] - \sum_{\substack{k=1 \\ k\neq j}}^{N-2}\left[\left(\frac{\left(c_T^{n'} B_{jk}^{-1}\right)_n}{\delta z_n c_T^{n'}} + \frac{\left(c_T^{n'} B_{jk}^{-1}\right)_s}{\delta z_s c_T^{n'}}\right)\left(c_k^n\right)_P\right] \\
&\quad - \sum_{\substack{k=1 \\ k\neq j}}^{N-2}\left[\frac{\left(c_T^{n'} B_{jk}^{-1}\right)_s}{\delta z_n \left(c_T^{n'}\right)_{\mathcal{S}}}\left(c_k^n\right)_{\mathcal{S}}\right] = \bar{\alpha} S_j \Delta z_\alpha^* + \frac{\Delta z_\alpha^* \alpha^0}{\Delta t} c_j^0
\end{aligned} \tag{D.35}$$

Equation (D.35) represents a general discretized species transport equation and can be used in either the porous or gas-phase region, as long as the correct domain size α, diffusion distance δz, and dimensionless node distance Δz_α^* are used. Additionally, a modified version of equation (D.35) analogous to equation (D.27), can be used for the

bottom node (porous region adjacent to membrane) by using a half-node width for the storage term, adding a term for the hydrogen flux leaving the domain through the membrane to the right-hand side of the equation for H_2, and setting v_s^* and $\left(c_T^{n'} B_{jj}^{-1}\right)_s$ equal to zero because the advective or diffusive flux through the south face are replaced by the specified permeation flux. Similarly, a modified version of equation (D.35), this time analogous to the discretized equation for the node adjacent to the piston (equation (D.29)), can be used for the north face with the exception that there is no permeation term, *i.e.*, the total flux for all species through the north face is identically zero.

Table D.1 shows different equivalent distances used in the discretization of species transport equation (C.35). The source term S_j (only non-zero in the catalyst/sorbent region) is $S_j = \overline{\rho}\phi\Sigma_i \nu_{ij} r_i - \bar{\rho}(1-\phi)\partial q_j/\partial t$, where the rates of SMR reaction for $i = 1, 2, 3$ are determined using Xu and Froment kinetics as a function of reactor temperature, pressure and species mole fractions. The partial derivative of sorbent loading with respect to time ($\partial q_{CO_2}/\partial t$) is represented by the linear driving force model, in discretized form $\partial q_{CO_2}/\partial t \sim k_{ldf}\left(q^*(T, P_{CO_2}) - q_{CO_2}\right)$, where the equilibrium CO_2 loading $q^*(T, P_{CO_2})$ and linear driving force coefficient (k_{ldf}) are determined using equilibrium and kinetic data from Lee et al [67].

Table D.1: Distances for Use in General Discretization Equation

Simulation domain	Node	δz_n	δz_s	α	Δz_α^*	S_j
Porous domain (nodes $1:n_c$ where n_c is # of nodes in porous region)	1	$d\Delta z_c^*$	n/a	d	$\Delta z_c^*/2$	According to Xu/Froment [28] SMR and Lee et al. [67] sorption kinetics
	2:n_c -1		$d\Delta z_c^*$		Δz_c^*	
	n_c	$d\frac{\Delta z_c^*}{2} + \bar{H}\frac{\Delta z_g^*}{2}$				
Gas-only domain (nodes $n_c+1:n_T$ where n_T is total # of nodes in both domains)	n_c+1	$\bar{H}\Delta z_g^*$	$d\frac{\Delta z_c^*}{2} + \bar{H}\frac{\Delta z_g^*}{2}$	$\bar{H}$	Δz_g^*	0
	n_c+1: n_T-1		$\bar{H}\Delta z_g^*$			
	n_T	n/a			$\Delta z_g^*/2$	

It is also important to use the correct effective "interface conductance," $\left(c_T B_{jk}^{-1}\right)^{int}$, for the diffusive flux, because the value of the inverse $[B]$ matrix as well as individual and total concentrations is only known at the particular nodes. For the situation illustrated in Figure D.5, according to Maxwell Stefan the diffusive flux is:

$$J_{z,j} = -\left[\sum_{k=1}^{N-1}\left(c_T B_{jk}^{-1}\right)^{int}\frac{\partial}{\partial z}\left(\frac{c_j^{int}}{c_T^{int}}\right)\right] \tag{D.36}$$

where the superscript int represents the value at the interface.

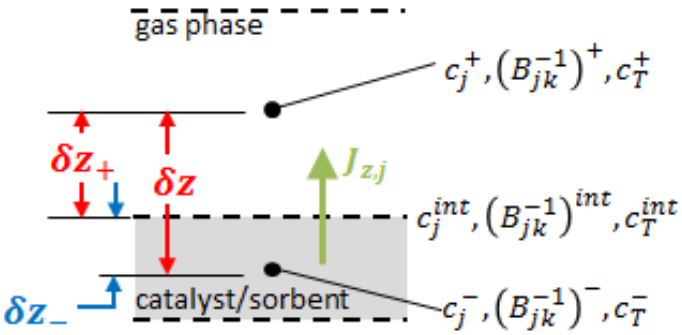

Figure D.5: Interface conductance schematic for diffusive flux calculation

By approximating the gradients in equation (D.36) linearly using the values at the nodes adjacent to the interface, $J_{z,j}$ from the interface to the "+" node and to the "–" node becomes, respectively:

$$J_{z,j}^{+} = -\sum_{k=1}^{N-1}\left[\left(c_T B_{jk}^{-1}\right)^{+} \cdot \frac{\left(\frac{c_k}{c_T}\right)^{+} - \left(\frac{c_k}{c_T}\right)^{int}}{\delta z^{+}}\right] \tag{D.37a}$$

$$J_{z,j}^{-} = -\sum_{k=1}^{N-1}\left[\left(c_T B_{jk}^{-1}\right)^{-} \cdot \frac{\left(\frac{c_k}{c_T}\right)^{int} - \left(\frac{c_k}{c_T}\right)^{-}}{\delta z^{-}}\right] \tag{D.37b}$$

However, the flux must be continuous at the interface so these must be equal and also equivalent to the overall flux using just the concentrations at each adjacent node and the effective interface conductance, leading to the following relationship:

$$\begin{aligned}\left(c_T B_{jk}^{-1}\right)^{+} \cdot \frac{\left(\frac{c_k}{c_T}\right)^{+} - \left(\frac{c_k}{c_T}\right)^{int}}{\delta z^{+}} &= \left(c_T B_{jk}^{-1}\right)^{-} \cdot \frac{\left(\frac{c_k}{c_T}\right)^{int} - \left(\frac{c_k}{c_T}\right)^{-}}{\delta z^{-}} \\ &= \left(c_T B_{jk}^{-1}\right)^{int} \cdot \frac{\left(\frac{c_k}{c_T}\right)^{+} - \left(\frac{c_k}{c_T}\right)^{-}}{\delta z}\end{aligned} \tag{D.38}$$

The relationship contained in equation (D.38) leads to the following definition of effective interface conductance:

$$J_{z,j} = -\sum_{k=1}^{N-1}\left[\underbrace{\left(\frac{\delta z_- / \delta z}{\left(c_T B_{jk}^{-1}\right)^-} + \frac{\delta z_+ / \delta z}{\left(c_T B_{jk}^{-1}\right)^+}\right)^{-1}}_{\left(c_T B_{jk}^{-1}\right)^{int}} \cdot \frac{\left(\frac{c_k}{c_T}\right)^+ - \left(\frac{c_k}{c_T}\right)^-}{\delta z}\right] \tag{D.39}$$

D.4 Discretization of Energy Equation

Recognizing that the quantity $\sum_{j=1}^{N}(c_j \overline{c}_{p,j}) + \overline{\rho} c_{p,b}$ (where the average density in the porous domain, $\bar{\rho}$,is a weighted harmonic mean of the component densities $\overline{\rho} = [\phi/\rho_{cat} + (1-\phi)/\rho_{sorb}]^{-1}$, $c_{p,b}$ is the specific heat at constant pressure per unit mass of the catalyst/sorbent bed, and $\overline{c}_{p,j}$ is the molar constant pressure specific heat of species j in the gas phase) in the energy conservation equation (D.2) is the average volumetric heat capacity ($\bar{C}_p$, units $[J/m^3 \cdot K]$) of the gas/porous media mixture (or pure gas in the domain above the catalyst/sorbent bed, where the solid density $\bar{\rho} = 0$), equation (C.2) can be rewritten in more compact notation as:

$$\frac{\partial}{\partial t}\left[\bar{C}_p T\right] + \frac{\partial}{\partial z}\left[\sum_{j=1}^{N}(c_j v + J_{z,j})\overline{c}_{p,j} T\right] = \frac{\partial}{\partial z}\left[k_{eff}\frac{\partial T}{\partial z}\right] + \overline{\varepsilon}\frac{dp_T}{dt} + S_h \tag{D.40}$$

Applying the transformations outlined in equations (D.5) and (D.6) to transform into z^* space, where the total height of the domain under consideration is α (using a general form that can be applied to either domain where $\alpha = H(t)$ in the gas-only region and $\alpha = d$ in the porous media region) and the moving velocity at the top boundary of the domain under consideration is U_d (where $U_d = U_p$ in the gas region and $U_d = 0$ in the porous region that does not get compressed during operation), equation (D.40) becomes:

$$\frac{\partial}{\partial t^*}\left[\bar{C}_p T\right] - \frac{z^* U_d}{\alpha}\cdot\frac{\partial}{\partial z^*}\left[\bar{C}_p T\right] + \frac{1}{\alpha}\cdot\frac{\partial}{\partial z^*}\left[\sum_{j=1}^{N}\left(c_j v + J_{z,j}\right)\overline{c}_{p,j} T\right] = \frac{1}{\alpha}\cdot\frac{\partial}{\partial z^*}\left[k_{eff}\frac{1}{\alpha}\frac{\partial T}{\partial z^*}\right] + \overline{\varepsilon}\left(\frac{dp}{dt^*} - \frac{z^* U_p}{H(t)}\cdot\frac{\partial p_T}{\partial z^*}^{0}\right) + S_h \tag{D.41}$$

Or multiplying through by α and replacing t^* with t (because as defined, $t = t^*$):

$$\alpha\frac{\partial}{\partial t}\left[\bar{C}_p T\right] - z^* U_p\frac{\partial}{\partial z^*}\left[\bar{C}_p T\right] + \frac{\partial}{\partial z^*}\left[\sum_{j=1}^{N}\left(c_j v + J_{z,j}\right)\overline{c}_{p,j} T\right] = \frac{\partial}{\partial z^*}\left[k_{eff}\frac{1}{\alpha}\frac{\partial T}{\partial z^*}\right] + \alpha\left(\overline{\varepsilon}\frac{dp_T}{dt} + S_h\right) \tag{D.42}$$

To modify equation (D.42) in order to make FVM discretization more straightforward, chain rule is used:

$$\frac{\partial}{\partial t}\left[\alpha\bar{C}_p T\right] = \alpha\frac{\partial}{\partial t}\left[\bar{C}_p T\right] + \bar{C}_p T\frac{\partial\alpha}{\partial t} = \frac{\partial}{\partial t}\left[\bar{C}_p T\right] + U_d\bar{C}_p T \tag{D.43a}$$

and

$$\frac{\partial}{\partial z^*}\left[z^* U_d\bar{C}_p T\right] = z^* U_d\frac{\partial}{\partial z^*}\left[\bar{C}_p T\right] + U_d\bar{C}_p T\frac{\partial z^*}{\partial z^*}^{1} \tag{D.43b}$$

Again using the fact that $\partial\alpha/\partial t = U_d$, substituting equations (D.43a) and (D.43b) into equation (C.42) yields:

$$\frac{\partial}{\partial t}\left[\alpha\bar{C}_p T\right] - \bar{C}_p T U_d - \frac{\partial}{\partial z^*}\left[z^* U_d\bar{C}_p T\right] + U_d\bar{C}_p T + \frac{\partial}{\partial z^*}\left[\sum_{j=1}^{N}\left(c_j v + J_{z,j}\right)\overline{c}_{p,j} T\right] = \frac{\partial}{\partial z^*}\left[\frac{k_{eff}}{\alpha}\frac{\partial T}{\partial z^*}\right] + \alpha\left(\overline{\varepsilon}\frac{dp_T}{dt} + S_h\right) \tag{D.44}$$

The second and fourth terms on the left side of equation (D.44) cancel identically. Substituting the definition for $\bar{C}_p$ into the advective term in equation (D.44) and

separating out the gas ($\sum_{j=1}^{N} c_j \overline{c}_{p,j}$) and porous media ($\overline{\rho} c_{p,b}$) volumetric heat capacity terms:

$$\frac{\partial}{\partial t}\left[\alpha \bar{C}_p T\right] - \frac{\partial}{\partial z^*}\left[z^* U_d \left(\overline{\rho} c_{p,b}\right) T\right] - \frac{\partial}{\partial z^*}\left[z^* U_d \left(\sum_{j=1}^{N} c_j \overline{c}_{p,j}\right) T\right] + \frac{\partial}{\partial z^*}\left[\sum_{j=1}^{N} \left(c_j v + J_{z,j}\right) \overline{c}_{p,j} T\right] = \frac{\partial}{\partial z^*}\left[\frac{k_{eff}}{\alpha}\frac{\partial T}{\partial z^*}\right] + \alpha\left(\overline{\varepsilon}\frac{dp_T}{dt} + S_h\right) \tag{D.45}$$

As was done in the species transport equation discretization, it is possible to group the third and fourth terms on the left side of equation (D.45) together by recognizing that the average molar velocity relative to the motion of the coordinate system's local velocity is $v^* = v - U_p z^*$:

$$\frac{\partial}{\partial t}\left[\alpha \bar{C}_p T\right] - \frac{\partial}{\partial z^*}\left[z^* U_d \left(\overline{\rho} c_{p,b}\right) T\right] + \frac{\partial}{\partial z^*}\left[\sum_{j=1}^{N} \left(c_j v^* + J_{z,j}\right) \overline{c}_{p,j} T\right] = \frac{\partial}{\partial z^*}\left[\frac{k_{eff}}{\alpha}\frac{\partial T}{\partial z^*}\right] + \alpha\left(\overline{\varepsilon}\frac{dp_T}{dt} + S_h\right) \tag{D.46}$$

The porous domain (the region where the solid density $\overline{\rho} \neq 0$) cannot be compressed (*i.e.*, only the pure gas domain volume varies with the piston motion), so either $\overline{\rho}$ or U_d will be zero in the second term on the left of equation (D.46) in each and every simulation domain (and therefore the entire $\frac{\partial}{\partial z^*}\left[z^* U_d \left(\overline{\rho} c_{p,b}\right) T\right]$ term is always zero). Following the FVM discretization approach, integrating the governing equation (D.46) first from $z_s^* \rightarrow z_n^*$ ($\Delta z_\alpha^* = z_n^* - z_s^*$) and then from $t^0 \rightarrow t^n$ ($\Delta t = t^n - t^0$) yields:

$$\Delta z_\alpha^*\left(\alpha^n \bar{C}_p^n (T^n)_P - \alpha^0 \bar{C}_p^0 (T^0)_P\right)$$

$$+\left[\sum_{j=1}^{N}\left[\left(c_j v^* + J_{z,j}\right)\overline{c}_{p,j}T\right]_n - \sum_{j=1}^{N}\left[\left(c_j v^* + J_{z,j}\right)\overline{c}_{p,j}T\right]_s\right]^n \Delta t \qquad \text{(D.47)}$$

$$= \left[\left(\frac{k_{eff}}{\bar{\alpha}}\frac{\partial T}{\partial z^*}\right)_n - \left(\frac{k_{eff}}{\bar{\alpha}}\frac{\partial T}{\partial z^*}\right)_s\right]^n \Delta t + \bar{\alpha}\Delta z_\alpha^* \bar{\varepsilon}(P_T^n - P_T^0) + \bar{\alpha} S_h^n \Delta z_\alpha^* \Delta t$$

where an implicit approach is used, similar to that used in discretizing the species conservation equation, such that values at the current timestep t^n are used in determining advective and conduction fluxes, as noted by the n superscript on the outer brackets of each term. Dividing through equation (D.47) by Δt and noting the physical meaning of each term underneath it with braces:

$$\underbrace{\frac{\Delta z_\alpha^*}{\Delta t}\left(\alpha^n \bar{C}_p^n (T^n)_P - \alpha^0 \bar{C}_p^0 (T^0)_P\right)}_{\substack{\text{rate change of thermal} \\ \text{energy stored in CV}}} + \underbrace{\left[\sum_{j=1}^{N}\left[\left(c_j v^* + J_{z,j}\right)\overline{c}_{p,j}T\right]_n - \sum_{j=1}^{N}\left[\left(c_j v^* + J_{z,j}\right)\overline{c}_{p,j}T\right]_s\right]^n}_{\text{net rate of energy transport from CV due to species flux}}$$

$$= \underbrace{\left[\left(\frac{k_{eff}}{\bar{\alpha}}\frac{\partial T}{\partial z^*}\right)_n - \left(\frac{k_{eff}}{\bar{\alpha}}\frac{\partial T}{\partial z^*}\right)_s\right]^n}_{\substack{\text{net rate of energy} \\ \text{conducted into CV}}} + \underbrace{\bar{\alpha}\Delta z_\alpha^* \bar{\varepsilon}\frac{(P_T^n - P_T^0)}{\Delta t}}_{\substack{\text{rate of energy change} \\ \text{due topressure change}}} + \underbrace{\bar{\alpha} S_h \Delta z_\alpha^*}_{\substack{\text{rate of heat} \\ \text{input due to} \\ \text{reaction/} \\ \text{adsorption}}} \qquad \text{(D.48)}$$

The units of each term in equation (D.48) are $[W/m^2]$, as the rate of energy change is calculated on a per unit of reactor cross sectional area basis for the 1-D geometry under consideration. The temperature gradient terms in the conduction terms of equation (D.48) are approximated as:

$$\left(\frac{\partial T}{\partial z^*}\right)_n \sim \frac{(T^n)_N - (T^n)_P}{\delta z_n^*} \qquad \text{(D.49a)} \qquad\qquad \left(\frac{\partial T}{\partial z^*}\right)_s \sim \frac{(T^n)_P - (T^n)_S}{\delta z_s^*} \qquad \text{(D.49b)}$$

Additionally, the sum of the advective and diffusive flux terms (relative to the moving CV boundary) can be grouped together as the total species flux ($N_j^* = c_j v^* +$

$J_{z,j}$). Making this substitution as well as the ones for the approximated temperature gradients yields:

$$\frac{\Delta z_\alpha^*}{\Delta t}\left(\alpha^n \bar{C}_p^n (T^n)_P - \alpha^0 \bar{C}_p^0 (T^0)_P\right) + \sum_{j=1}^{N}\left[N_j^* \, \bar{c}_{p,j} T^n\right]_n - \sum_{j=1}^{N}\left[N_j^* \, \bar{c}_{p,j} T^n\right]_s$$

$$= k_{eff,n}\frac{(T^n)_{\mathcal{N}} - (T^n)_P}{\bar{\alpha}\delta z_n^*} - k_{eff,s}\frac{(T^n)_P - (T^n)_{\mathcal{S}}}{\bar{\alpha}\delta z_s^*} \qquad \text{(D.50)}$$

$$+ \bar{\alpha}\Delta z_\alpha^* \bar{\varepsilon}\frac{(P^n - P^0)}{\Delta t} + \bar{\alpha}\, S_h^n \Delta z_\alpha^*$$

The fluxes, temperature values, and distances referenced in equation (D.50) are illustrated in Figure D.6.

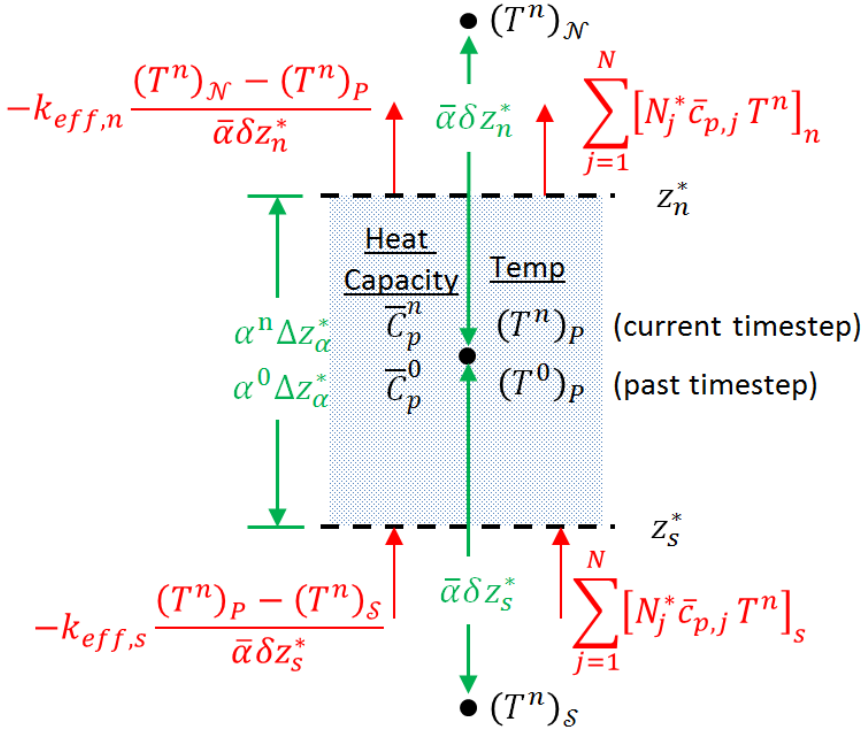

Figure D.6: Pictorial representation of dependent variables and flux values relevant to the discretized energy equation for a cluster of three points (labeled $\mathcal{N}$, P, and $\mathcal{S}$ for north, present, and south nodes, respectively) at the current (superscript n) and prior (superscript 0) time step. Distances for storage and conduction flux terms are also illustrated for reference.

An upwinding approach is employed to determine the appropriate values of specific heat and temperature for energy transport via species transport (advection and diffusion) at the interface $\left[N_j^* \, \bar{c}_{p,j} T^n\right]_{interface}$ in equation (D.50). Similar to the upwinding of concentration in the species conservation equation, the value of T at the interface is treated as equal to the value at the adjacent grid point in the upstream direction (based on the direction of total species flux N_j^*). Implementing this upwind scheme, the term describing energy transport due to species flux becomes:

$$\sum_{j=1}^{N} \left[N_j^* \, \bar{c}_{p,j} T^n\right]_n - \sum_{j=1}^{N} \left[N_j^* \, \bar{c}_{p,j} T^n\right]_s$$

$$= \left[\sum_{j=1}^{N} \left[\bar{c}_{p,j} \left[\left[\left(N_j^*\right)_n, 0\right]\right]\right] + \sum_{j=1}^{N} \left[\bar{c}_{p,j} \left[\left[-\left(N_j^*\right)_s, 0\right]\right]\right]\right] (T^n)_P \qquad \text{(D.51)}$$

$$- \left[\sum_{j=1}^{N} \left[\bar{c}_{p,j} \left[\left[-\left(N_j^*\right)_n, 0\right]\right]\right]\right] (T^n)_N - \left[\sum_{j=1}^{N} \left[\bar{c}_{p,j} \left[\left[\left(N_j^*\right)_s, 0\right]\right]\right]\right] (T^n)_S$$

Inserting equation (C.51) into (C.50) and regrouping coefficient terms for temperature nodes together on the left side of the equation and the terms that do not depend on the temperatures at the current timestep as a source on the right side yields the final discretized energy equation for an ***internal*** node:

$$\left[\frac{\Delta z_\alpha^*}{\Delta t}\alpha^n \bar{C}_p^n + \sum_{j=1}^{N}\left[\bar{c}_{p,j}\left[\left[\left(N_j^*\right)_n, 0\right]\right]\right] + \sum_{j=1}^{N}\left[\bar{c}_{p,j}\left[\left[-\left(N_j^*\right)_s, 0\right]\right]\right] + \frac{k_{eff,n}}{\bar{\alpha}\delta z_n^*} + \frac{k_{eff,s}}{\bar{\alpha}\delta z_s^*}\right](T^n)_P$$

$$-\left[\sum_{j=1}^{N}\left[\bar{c}_{p,j}\left[\left[-\left(N_j^*\right)_n, 0\right]\right]\right] + \frac{k_{eff,n}}{\bar{\alpha}\delta z_n^*}\right](T^n)_{\mathcal{N}}$$

$$-\left[\sum_{j=1}^{N}\left[\bar{c}_{p,j}\left[\left[\left(N_j^*\right)_s, 0\right]\right]\right] + \frac{k_{eff,s}}{\bar{\alpha}\delta z_s^*}\right](T^n)_{\mathcal{S}} \tag{D.52}$$

$$= \frac{\Delta z_\alpha^*}{\Delta t}\alpha^0 \bar{C}_p^0 (T^0)_P + \bar{\alpha}\Delta z_\alpha^* \bar{\varepsilon}\frac{(P^n - P^0)}{\Delta t} + \bar{\alpha}\, S_h^n \Delta z_\alpha^*$$

where, as in the species conservation equation discretization, the specific values of the distance parameters ($\alpha, \Delta z_\alpha^*$, $\delta z_n = \bar{\alpha}\cdot\delta z_n^*$, and $\delta z_s = \bar{\alpha}\cdot\delta z_s^*$) vary depending on the domain under consideration (*i.e.* whether in the gas or porous media region). For a review of these specific values, reference Table D.1. The source term (S_h^n) in equation (D.52) is only non-zero in the porous domain, and consists of the enthalpy of reaction and adsorption at the rates predicted in the species transport equation according to the Xu and Froment [28] SMR or Lee et al. [67] sorption kinetics ($S_h = \bar{\rho}\phi\Sigma_i \Delta \mathrm{H_i} r_i + \Delta H_{ads}\bar{\rho}(1-\phi)\partial q_{CO_2}/\partial t$). The n superscript in the S_h^n term designates that the heat of reaction/adsorption during a timestep is determined implicitly (*i.e.*, based on values at the end of the timestep) rather than explicitly.

For the node adjacent to the membrane surface, the node width is $d\cdot\Delta z_c^*/2$ and there is only hydrogen flux through the "south" face of the node, denoted N''_{perm,H_2} and determined using equation (D.26) from Sievert's Law. A convective boundary condition is applied for heat input to this node, with an overall heat transfer coefficient of U_s (accounting for resistance to heat transfer due to convection and conduction across the

membrane). Using this definition, the heat flux per unit area is $q''_{in} = U_s\left[T_{\infty,s} - (T^n)_P\right]$ and the discretized equation for the half-width node adjacent to the membrane surface is:

$$\left[\frac{\Delta z_c^*}{\Delta t}\left(\frac{d}{2}\right)\bar{C}_p^n + \sum_{j=1}^{N}\left[\bar{c}_{p,j}\left[\left[\left(N_j^*\right)_n, 0\right]\right]\right] + \bar{c}_{p,H_2}\cdot N''_{perm,H_2} + \frac{k_{eff,n}}{d\cdot\delta z_n^*} + U_s\right](T^n)_P$$

$$-\left[\sum_{j=1}^{N}\left[\bar{c}_{p,j}\left[\left[-\left(N_j^*\right)_n, 0\right]\right]\right] + \frac{k_{eff,n}}{d\cdot\delta z_n^*}\right](T^n)_{\mathcal{N}} \tag{D.53}$$

$$= \left[\frac{\Delta z_c^*}{\Delta t}\left(\frac{d}{2}\right)\bar{C}_p^0\right](T^0)_P + \frac{d}{2}\Delta z_c^*\bar{\varepsilon}\frac{(P^n - P^0)}{\Delta t} + \frac{d}{2}S_h^n\Delta z_c^* + U_s\cdot T_{\infty,s}$$

For the node adjacent to the piston, the node width is $H\cdot\ \Delta z_g^*/2$ and there is no flux of any species through the "north" face of the node. To keep the most general form possible, a convective boundary condition with an overall heat transfer coefficient of U_n is utilized in the discretization; however, the best case in terms of reactor design is for this interface to be perfectly insulated (*i.e.* $U_n = 0$). Allowing for there to be some heat loss through the piston, the discretized equation for the half-width node at the top of the gas-only domain is:

$$\left[\frac{\Delta z_g^*}{\Delta t}\left(\frac{H^n}{2}\right)\bar{C}_p^n + \sum_{j=1}^{N}\left[\bar{c}_{p,j}\left[\left[-\left(N_j^*\right)_s, 0\right]\right]\right] + \frac{k_{eff,s}}{\bar{H}\delta z_s^*} + U_n\right](T^n)_P$$

$$-\left[\sum_{j=1}^{N}\left[\bar{c}_{p,j}\left[\left[\left(N_j^*\right)_s, 0\right]\right]\right] + \frac{k_{eff,s}}{\bar{H}\delta z_s^*}\right](T^n)_{\mathcal{S}} \tag{D.54}$$

$$= \frac{\Delta z_g^*}{\Delta t}\left(\frac{H^0}{2}\right)\bar{C}_p^0(T^0)_P + \frac{\bar{H}}{2}\Delta z_g^*\bar{\varepsilon}\frac{(P^n - P^0)}{\Delta t} + \frac{\bar{H}}{2}S_h^n\Delta z_g^* + U_n\cdot T_{\infty,n}$$

In solving the discretized equations (D.52) – (D.54), the appropriate effective thermal conductivity of the bulk gas is determined using the method proposed by Mason and Saxena for a low-density gas mixture (*i.e.* pressure below 10 bar) consisting of N species [95]:

$$k_{mix} = \sum_{j=1}^{N} \left[\frac{x_j k_j}{\sum_{k=1}^{N} (x_k \Phi_{jk})} \right] \tag{D.55}$$

where k_j and x_j are the thermal conductivity and mole fraction, respectively of an individual species j and the coefficients Φ_{jk} are determined using the following equation:

$$\Phi_{jk} = \frac{1}{\sqrt{8}} \cdot \left(1 + \frac{MW_j}{MW_k}\right)^{-1/2} \left[1 + \left(\frac{\mu_j}{\mu_k}\right)^{-1/2} \cdot \left(\frac{MW_k}{MW_j}\right)^{1/4}\right]^2 \tag{D.56}$$

where MW is the molecular weight and μ is the viscosity of each individual species (j or k). Values of k and μ are assumed to be constant and taken at a nominal temperature of 400°C using data from the NIST Chemistry WebBook [99]. Where data is not available at the precise temperature, thermal conductivity and viscosity values are scaled according to their dependence on temperature ($\propto T^{1/2}$) [86]. For the portion of the simulation domain where there is gas interspersed within porous media, the effective thermal conductivity is determined using a geometric mean of the gas mixture conductivity (k_{mix}) and the solid conductivity (k_s) [96]:

$$k_{eff} = (k_{mix})^{\varepsilon} (k_s)^{1-\varepsilon} \tag{D.57}$$

REFERENCES

[1] K. S. Thorne, "John Achibald Wheeler (1911-2008)," *Science,* vol. 320, p. 1603, 2008.

[2] V. Rao, *Shale Gas, The Promise and the Peril*: RTI Press, 2012.

[3] S. Paltsev, H. D. Jacoby, J. M. Reilly, Q. J. Ejaz, J. Morris, F. O'Sullivan, *et al.*, "The future of US natural gas production, use, and trade," *Energy Policy,* vol. 39, pp. 5309-5321, 2011.

[4] D. M. Kargbo, R. G. Wilhelm, and D. J. Campbell, "Natural gas plays in the Marcellus shale: Challenges and potential opportunities," *Environmental Science & Technology,* vol. 44, pp. 5679-5684, 2010.

[5] L. Barreto, A. Makihira, and K. Riahi, "The hydrogen economy in the 21st century: a sustainable development scenario," *International Journal of Hydrogen Energy,* vol. 28, pp. 267-284, Mar 2003.

[6] K. B. Lee, M. G. Beaver, H. S. Caram, and S. Sircar, "Novel thermal-swing sorption-enhanced reaction process concept for hydrogen production by low-temperature steam−methane reforming," *Industrial & Engineering Chemistry Research,* vol. 46, pp. 5003-5014, 2007/07/01 2007.

[7] W. F. Baade, U. N. Parekh, and V. S. Raman, "Hydrogen," in *Kirk-Othmer Encyclopedia of Chemical Technology*, ed: John Wiley & Sons, Inc., 2000.

[8] J. R. Rostrup-Nielsen, "Production of Synthesis Gas," *Catalysis Today,* vol. 18, pp. 305-324, Dec 31 1993.

[9] D. P. Harrison, "Sorption-enhanced hydrogen production: A review," *Industrial & Engineering Chemistry Research,* vol. 47, pp. 6486-6501, Sep 2008.

[10] M. J. Varady and A. G. Fedorov, "Fuel reformation and hydrogen generation with direct droplet impingement reactors: model formulation and validation," *Industrial & Engineering Chemistry Research,* vol. 50, pp. 9502-9513, 2011.

[11] Y. Ding and E. Alpay, "Adsorption-enhanced steam-methane reforming," *Chemical Engineering Science,* vol. 55, pp. 3929-3940, Sep 2000.

[12] J. R. Hufton, S. Mayorga, and S. Sircar, "Sorption-enhanced reaction process for hydrogen production," *AIChE Journal,* vol. 45, pp. 248-256, Feb 1999.

[13] M. Saric, Y. C. van Delft, R. Sumbharaju, D. F. Meyer, and A. de Groot, "Steam reforming of methane in a bench-scale membrane reactor at realistic working conditions," *Catalysis Today,* vol. 193, pp. 74-80, Oct 15 2012.

[14] P. Marin, Y. Patino, F. V. Diez, and S. Ordonez, "Modelling of hydrogen perm-selective membrane reactors for catalytic methane steam reforming," *International Journal of Hydrogen Energy,* vol. 37, pp. 18433-18445, Dec 2012.

[15] M. H. Halabi, M. H. J. M. de Croon, J. van der Schaaf, P. D. Cobden, and J. C. Schouten, "A novel catalyst-sorbent system for an efficient H_2 production with in-situ CO_2 capture," *International Journal of Hydrogen Energy,* vol. 37, pp. 4987-4996, Mar 2012.

[16] M. H. Halabi, M. H. J. M. de Croon, J. van der Schaaf, P. D. Cobden, and J. C. Schouten, "Kinetic and structural requirements for a CO_2 adsorbent in sorption enhanced catalytic reforming of methane - Part I: Reaction kinetics and sorbent capacity," *Fuel,* vol. 99, Sep 2012.

[17] J. Shu, B. P. A. Grandjean, and S. Kaliaguine, "Methane steam reforming in asymmetric Pd-Ag and Pd-Ag/porous SS membrane reactors," *Applied Catalysis A-General,* vol. 119, pp. 305-325, Nov 24 1994.

[18] D. L. Damm and A. G. Fedorov, "Batch reactors for hydrogen production: Theoretical analysis and experimental characterization," *Industrial & Engineering Chemistry Research,* vol. 48, pp. 5610-5623, Jun 17 2009.

[19] D. L. Damm and A. G. Fedorov, "Comparative assessment of batch reactors for scalable hydrogen production," *Industrial & Engineering Chemistry Research,* vol. 47, pp. 4665-4674, Jul 16 2008.

[20] N. L. Garland, D. C. Papageorgopoulos, and J. M. Stanford, "Hydrogen and Fuel Cell Technology: Progress, Challenges, and Future Directions," *Energy Procedia,* vol. 28, pp. 2-11, // 2012.

[21] N. A. Kelly, T. L. Gibson, M. Cai, J. A. Spearot, and D. B. Ouwerkerk, "Development of a renewable hydrogen economy: Optimization of existing technologies," *International Journal of Hydrogen Energy,* vol. 35, pp. 892-899, 2// 2010.

[22] M. A. Rosen, "Advances in hydrogen production by thermochemical water decomposition: A review," *Energy,* vol. 35, pp. 1068-1076, 2// 2010.

[23] B. D. Adams and A. Chen, "The role of palladium in a hydrogen economy," *Materials Today,* vol. 14, pp. 282-289, 6// 2011.

[24] A. Züttel, A. Borgschulte, and L. Schlapbach, *Hydrogen as a future energy carrier*: John Wiley & Sons, 2011.

[25] J. Fletcher and V. Callaghan, "Evaluation Cost of Distributed Production of Hydrogen from Natural Gas–Independent Review," NREL/BK-150-40382, October2006.

[26] W. C. Lattin and V. P. Utgikar, "Transition to hydrogen economy in the United States: A 2006 status report," *International Journal of Hydrogen Energy,* vol. 32, pp. 3230-3237, Oct 2007.

[27] D. L. Damm and A. G. Fedorov, "Conceptual study of distributed CO_2 capture and the sustainable carbon economy," *Energy Conversion and Management,* vol. 49, pp. 1674-1683, Jun 2008.

[28] J. G. Xu and G. F. Froment, "Methane steam reforming, methanation and water-gas shift 1. Intrinsic kinetics," *AIChE Journal,* vol. 35, pp. 88-96, Jan 1989.

[29] K. B. Lee, M. G. Beaver, H. S. Caram, and S. Sircar, "Reversible chemisorbents for carbon dioxide and their potential applications," *Industrial & Engineering Chemistry Research,* vol. 47, Nov 5 2008.

[30] O. Okada and K. Yokoyama, "Development of polymer electrolyte fuel cell cogeneration systems for residential applications," *Fuel Cells,* vol. 1, pp. 72-77, May 2001.

[31] L. Barelli, G. Bidini, F. Gallorini, and S. Servili, "Hydrogen production through sorption-enhanced steam methane reforming and membrane technology: A review," *Energy,* vol. 33, pp. 554-570, Apr 2008.

[32] J. A. Ritter and A. D. Ebner, "State-of-the-art adsorption and membrane separation processes for hydrogen production in the chemical and petrochemical industries," *Separation Science and Technology,* vol. 42, pp. 1123-1193, 2007/04/01 2007.

[33] S. Uemiya, N. Sato, H. Ando, T. Matsuda, and E. Kikuchi, "Steam reforming of methane in a hydrogen-permeable membrane reactor," *Applied Catalysis,* vol. 67, pp. 223-230, Jan 3 1991.

[34] H. T. J. Reijers, S. E. A. Valster-Schiermeier, P. D. Cobden, and R. W. van den Brink, "Hydrotalcite as CO_2 sorbent for sorption-enhanced steam reforming of methane," *Industrial & Engineering Chemistry Research,* vol. 45, pp. 2522-2530, 2006/04/01 2005.

[35] K. B. Lee, M. G. Beaver, H. S. Caram, and S. Sircar, "Effect of reaction temperature on the performance of thermal swing sorption-enhanced reaction process for simultaneous production of fuel-cell-grade H_2 and compressed CO_2 from synthesis gas," *Industrial & Engineering Chemistry Research,* vol. 47, pp. 6759-6764, 2008/09/03 2008.

[36] M. G. Beaver, H. S. Caram, and S. Sircar, "Sorption enhanced reaction process for direct production of fuel-cell grade hydrogen by low temperature catalytic steam-methane reforming," *Journal of Power Sources,* vol. 195, pp. 1998-2002, Apr 2 2010.

[37] M. H. Halabi, M. H. J. M. de Croon, J. van der Schaaf, P. D. Cobden, and J. C. Schouten, "High capacity potassium-promoted hydrotalcite for CO_2 capture in H_2 production," *International Journal of Hydrogen Energy,* vol. 37, Mar 2012.

[38] A. Harale, H. T. Hwang, P. K. T. Liu, M. Sahimi, and T. T. Tsotsis, "Experimental studies of a hybrid adsorbent-membrane reactor (HAMR) system for hydrogen production," *Chemical Engineering Science,* vol. 62, pp. 4126-4137, 8// 2007.

[39] A. Harale, H. T. Hwang, P. K. T. Liu, M. Sahimi, and T. T. Tsotsis, "Design aspects of the cyclic hybrid adsorbent-membrane reactor (HAMR) system for hydrogen production," *Chemical Engineering Science,* vol. 65, pp. 427-435, Jan 1 2010.

[40] B. Fayyaz, A. Harale, B. G. Park, P. K. T. Liu, M. Sahimi, and T. T. Tsotsis, "Design aspects of hybrid adsorbent-membrane reactors for hydrogen production," *Industrial & Engineering Chemistry Research,* vol. 44, pp. 9398-9408, Dec 7 2005.

[41] M.-B. Andrés, T. Boyd, J. R. Grace, C. J. Lim, A. Gulamhusein, B. Wan, *et al.*, "In-situ CO_2 capture in a pilot-scale fluidized-bed membrane reformer for ultra-pure hydrogen production," *International Journal of Hydrogen Energy,* vol. 36, pp. 4038-4055, 2011.

[42] Y. Chen, A. s. Mahecha-Botero, C. J. Lim, J. R. Grace, J. Zhang, Y. Zhao, *et al.*, "Hydrogen Production in a Sorption-Enhanced Fluidized-Bed Membrane Reactor: Operating Parameter Investigation," *Industrial & Engineering Chemistry Research,* vol. 53, pp. 6230-6242, 2014.

[43] Z. Chen, F. Po, J. R. Grace, C. J. Lim, S. Elnashaie, A. Mahecha-Botero, *et al.*, "Sorbent-enhanced/membrane-assisted steam-methane reforming," *Chemical Engineering Science,* vol. 63, pp. 170-182, 2008.

[44] B. T. Carvill, J. R. Hufton, M. Anand, and S. Sircar, "Sorption-enhanced reaction process," *AIChE Journal,* vol. 42, pp. 2765-2772, Oct 1996.

[45] K. B. Lee, M. G. Beaver, H. S. Caram, and S. Sircar, "Production of fuel-cell grade hydrogen by thermal swing sorption enhanced reaction concept," *International Journal of Hydrogen Energy,* vol. 33, pp. 781-790, 2008.

[46] D. M. Ruthven, "Principles of adsorption and adsorption processes," 1984.

[47] S. Uemiya, "Brief review of steam reforming using a metal membrane reactor," *Topics in Catalysis,* vol. 29, pp. 79-84, 2004.

[48] S. Adhikari and S. Fernando, "Hydrogen membrane separation techniques," *Industrial & Engineering Chemistry Research,* vol. 45, pp. 875-881, 2006.

[49] Y. Cheng, M. Pena, J. Fierro, D. Hui, and K. Yeung, "Performance of alumina, zeolite, palladium, Pd–Ag alloy membranes for hydrogen separation from Towngas mixture," *Journal of Membrane Science,* vol. 204, pp. 329-340, 2002.

[50] J. M. van de Graaf, E. van der Bijl, A. Stol, F. Kapteijn, and J. A. Moulijn, "Effect of operating conditions and membrane quality on the separation performance of composite silicalite-1 membranes," *Industrial & Engineering Chemistry Research,* vol. 37, pp. 4071-4083, 1998.

[51] Y. L. A. Leung and K. Yeung, "Microfabricated ZSM-5 zeolite micromembranes," *Chemical Engineering Science,* vol. 59, pp. 4809-4817, 2004.

[52] S. Steward, "Review of hydrogen isotope permeability through materials," Lawrence Livermore National Lab., CA (USA)1983.

[53] Ø. Hatlevik, S. K. Gade, M. K. Keeling, P. M. Thoen, A. Davidson, and J. D. Way, "Palladium and palladium alloy membranes for hydrogen separation and production: history, fabrication strategies, and current performance," *Separation and Purification Technology,* vol. 73, pp. 59-64, 2010.

[54] S. Uemiya, T. Matsuda, and E. Kikuchi, "Hydrogen permeable palladium-silver alloy membrane supported on porous ceramics," *Journal of Membrane Science,* vol. 56, pp. 315-325, 1991.

[55] L. McLeod, F. Degertekin, and A. Fedorov, "Effect of microstructure on hydrogen permeation through thermally stable, sputtered palladium-silver alloy membranes," *Applied Physics Letters,* vol. 90, pp. 261905-261905-3, 2007.

[56] L. McLeod, F. Degertekin, and A. Fedorov, "Determination of the rate-limiting mechanism for permeation of hydrogen through microfabricated palladium–silver alloy membranes," *Journal of Membrane Science,* vol. 341, pp. 225-232, 2009.

[57] S. Tosti, "Development and application of self-supported palladium membranes," in *Palladium Membrane Technology for Hydrogen Production, Carbon Capture and Other Applications,* A. Doukelis, K. Panopoulos, A. Koumanakos, and E. Kakaras, Eds., ed: Woodhead Publishing, 2015, pp. 101-152.

[58] S. Paglieri and J. Way, "Innovations in palladium membrane research," *Separation & Purification Reviews,* vol. 31, pp. 1-169, 2002.

[59] S. Yun and S. T. Oyama, "Correlations in palladium membranes for hydrogen separation: a review," *Journal of Membrane Science,* vol. 375, pp. 28-45, 2011.

[60] N. Al-Mufachi, N. Rees, and R. Steinberger-Wilkens, "Hydrogen selective membranes: A review of palladium-based dense metal membranes," *Renewable and Sustainable Energy Reviews,* vol. 47, pp. 540-551, 2015.

[61] A. G. Fedorov and D. L. Damm, "Hydrogen-generating reactors and methods," U.S. Patent 7,981,171, 2011.

[62] M. Twigg, *Catalyst Handbook*. London: Manson Publishing Ltd, 1996.

[63] S. Brunauer, L. S. Deming, W. E. Deming, and E. Teller, "On a theory of the van der Waals adsorption of gases," *Journal of the American Chemical Society,* vol. 62, pp. 1723-1732, Jul-Dec 1940.

[64] S. Choi, J. H. Drese, and C. W. Jones, "Adsorbent materials for carbon dioxide capture from large anthropogenic point sources," *ChemSusChem,* vol. 2, pp. 796-854, 2009.

[65] E. L. G. Oliveira, C. A. Grande, and A. E. Rodrigues, "CO_2 sorption on hydrotalcite and alkali-modified (K and Cs) hydrotalcites at high temperatures," *Separation and Purification Technology,* vol. 62, pp. 137-147, Aug 2008.

[66] Y. Ding and E. Alpay, "Equilibria and kinetics of CO_2 adsorption on hydrotalcite adsorbent," *Chemical Engineering Science,* vol. 55, pp. 3461-3474, Sep 2000.

[67] K. B. Lee, A. Verdooren, H. S. Caram, and S. Sircar, "Chemisorption of carbon dioxide on potassium-carbonate-promoted hydrotalcite," *Journal of Colloid and Interface Science,* vol. 308, pp. 30-39, Apr 2007.

[68] A. D. Ebner, S. P. Reynolds, and J. A. Ritter, "Nonequilibrium kinetic model that describes the reversible adsorption and desorption behavior of CO_2 in a K-promoted hydrotalcite-like compound," *Industrial & Engineering Chemistry Research,* vol. 46, pp. 1737-1744, 2007/03/01 2007.

[69] H. Du, A. D. Ebner, and J. A. Ritter, "Pressure dependence of the nonequilibrium kinetic model that describes the adsorption and desorption behavior of CO_2 in K-promoted hydrotalcite like compound," *Industrial & Engineering Chemistry Research,* vol. 50, pp. 412-418, 2011/01/05 2010.

[70] N. D. Hutson and B. C. Attwood, "High temperature adsorption of CO_2 on various hydrotalcite-like compounds," *Adsorption-Journal of the International Adsorption Society,* vol. 14, pp. 781-789, Dec 2008.

[71] A. E. Lutz, R. W. Bradshaw, J. O. Keller, and D. E. Witmer, "Thermodynamic analysis of hydrogen production by steam reforming," *International Journal of Hydrogen Energy,* vol. 28, pp. 159-167, Feb 2003.

[72] C. H. Bartholomew, "Mechanisms of catalyst deactivation," *Applied Catalysis A: General,* vol. 212, pp. 17-60, 2001.

[73] J. R. Rostrup-Nielsen, J. Anderson, and M. Boudart, "Catalysis science and technology, vol. 5," *by JR Anderson and M. Boudart, Springer, Berlin,* 1984.

[74] J. W. Snoeck, G. F. Froment, and M. Fowles, "Steam/CO_2 reforming of methane. Carbon filament formation by the boudouard reaction and gasification by CO_2, by H_2, and by steam: Kinetic study," *Industrial & Engineering Chemistry Research,* vol. 41, pp. 4252-4265, Aug 2002.

[75] A. Sieverts, "Palladium and Hydrogen I," *Z Phys. Chem,* vol. 88, pp. 103-127, 1914.

[76] A. Sieverts, "Palladium and Hydrogen II," *Z Phys. Chem,* vol. 88, pp. 121-122, 1914.

[77] J. R. Dormand and P. J. Prince, "A family of embedded Runge-Kutta formulae," *Journal of Computational and Applied Mathematics,* vol. 6, pp. 19-26, 1980.

[78] S. Walspurger, L. Boels, P. D. Cobden, G. D. Elzinga, W. G. Haije, and R. W. van den Brink, "The Crucial Role of the K+–Aluminium Oxide Interaction in K+-Promoted Alumina-and Hydrotalcite-Based Materials for CO2 Sorption at High Temperatures," *ChemSusChem,* vol. 1, pp. 643-650, 2008.

[79] J. B. Rawlings and J. G. Ekerdt, *Chemical Reactor Analysis and Design Fundamentals*: Nob Hill Pub, Llc, 2002.

[80] S. Sircar and J. R. Hufton, "Why does the Linear Driving Force model for adsorption kinetics work ?," *Adsorption-Journal of the International Adsorption Society,* vol. 6, pp. 137-147, Jan 2000.

[81] D. M. Anderson, P. A. Kottke, and A. G. Fedorov, "Thermodynamic analysis of hydrogen production via sorption-enhanced steam methane reforming in a new class of variable volume batch-membrane reactor," *International Journal of Hydrogen Energy,* vol. 39, pp. 17985-17997, 10/22/ 2014.

[82] S. H. Israni and M. P. Harold, "Methanol steam reforming in Pd− Ag membrane reactors: effects of reaction system species on transmembrane hydrogen flux," *Industrial & Engineering Chemistry Research,* vol. 49, pp. 10242-10250, 2010.

[83] M. P. Harold, B. Nair, and G. Kolios, "Hydrogen generation in a Pd membrane fuel processor: assessment of methanol-based reaction systems," *Chemical Engineering Science,* vol. 58, pp. 2551-2571, 2003.

[84] T. M. Yun, P. A. Kottke, D. M. Anderson, and A. G. Fedorov, "Power density assessment of variable volume batch reactors for hydrogen production with dynamically modulated liquid fuel introduction," *Industrial & Engineering Chemistry Research,* vol. 53, pp. 18140-18151, 2014.

[85] T. M. Yun, P. A. Kottke, D. M. Anderson, and A. G. Fedorov, "Experimental investigation of hydrogen production by variable volume membrane batch reactors with modulated liquid fuel introduction," *International Journal of Hydrogen Energy,* 2015.

[86] R. B. Bird, W. E. Stewart, and E. N. Lightfoot, *Transport phenomena*, 2nd ed. New York: John Wiley & Sons, 2007.

[87] F. Incropera and D. DeWitt, *Introduction to Heat Transfer*, 4th ed. New York: John Wiley & Sons, 2001.

[88] D. Anderson, T. Yun, P. Kottke, and A. Fedorov, "Sorption-Enhanced Variable Volume Batch-Membrane Steam Methane Reforming at Low Temperature: Experimental Demonstration and Kinetic Modeling," *Industrial & Engineering Chemistry Research*, vol. Under Review - Revision Requested, 2015.

[89] E. F. Obert, *Concepts of Thermodynamics*. New York: McGraw-Hill, 1960.

[90] T. M. Yun, P. A. Kottke, D. M. Anderson, and A. G. Fedorov, "Theoretical analysis of hydrogen production by variable volume membrane batch reactors with direct liquid fuel injection," *International Journal of Hydrogen Energy*, vol. 40, pp. 8005-80019, 2015.

[91] D. L. Damm and A. G. Fedorov, "Local thermal non-equilibrium effects in porous electrodes of the hydrogen-fueled SOFC," *Journal of Power Sources*, vol. 159, pp. 1153-1157, 2006.

[92] A. Shigarov and V. Kirillov, "Comparison of external mass transfer approaches for heterogeneously catalyzed hydrogenation of vaporized hydrocarbons," *Chemical Engineering Journal*, vol. 154, pp. 120-130, 2009.

[93] R. Krishna and J. Wesselingh, "The Maxwell-Stefan approach to mass transfer," *Chemical Engineering Science*, vol. 52, pp. 861-911, 1997.

[94] A. Hines and R. Maddox, *Mass Transfer: Fundamentals and Applications. 1985*. New Jersey: Prentice-Hall, Inc.

[95] E. Mason and S. Saxena, "Approximate formula for the thermal conductivity of gas mixtures," *Physics of Fluids (1958-1988)*, vol. 1, pp. 361-369, 1958.

[96] M. Kaviany, *Principles of Heat Transfer in Porous Media*. New York: Springer-Verlag Inc., 1991.

[97] S. V. Patankar, *Numerical Heat Transfer and Fluid Flow*. New York: CRC Press, 1980.

[98] R. H. Pletcher, J. C. Tannehill, and D. Anderson, *Computational Fluid Mechanics and Heat Transfer*, 3rd ed. New York: CRC Press, 2013.

[99] E. W. Lemmon, M. O. McLinden, and D. G. Friend, "Thermophysical Properties of Fluid Systems," in *NIST Chemistry WebBook, NIST Standard Reference Database Number 69* P. J. Linstrom and W. G. Mallard, Eds., ed.

[100] R. G. Mortimer and H. Eyring, "Elementary transition state theory of the Soret and Dufour effects," *Proceedings of the National Academy of Sciences,* vol. 77, pp. 1728-1731, 1980.

[101] R. Rastogi and G. Madan, "Cross-phenomenological coefficients. Part 6.—Dufour effect in gases," *Transactions of the Faraday Society,* vol. 62, pp. 3325-3330, 1966.

[102] P. Weisz and C. Prater, "Interpretation of measurements in experimental catalysis," *Adv. Catal,* vol. 6, pp. 143-196, 1954.

[103] J. Chabot, J. Lecomte, C. Grumet, and J. Sannier, "Fuel clean-up system: poisoning of palladium-silver membranes by gaseous impurities," *Fusion Science and Technology,* vol. 14, pp. 614-618, 1988.